

Universitat Autònoma de Barcelona
Institut de Biotecnologia i de Biomedicina

Parc Científic de Barcelona
Computer Simulation and Modeling Laboratory
Institut de Química Teòrica i Computacional

**ESTUDI DE LA
REACTIVITAT DE CATALASES
MITJANÇANT DINÀMICA MOLECULAR *AB INITIO***

TESI DOCTORAL
Mercedes Alfonso Prieto

Barcelona, desembre de 2009

ELECTRONIC STATE OF
THE MOLECULAR OXYGEN
RELEASED BY CATALASE

M. Alfonso-Prieto, P. Vidossich, A. Rodríguez-Fortea,
X. Carpena, I. Fita, C. Rovira, and P. C. Loewen.

Electronic state of molecular oxygen released by catalase

J. Phys. Chem. A **2008**, 112 (50), pp 12842–12848

1. INTRODUCTION

In the previous chapters we have already explained that Compound I (Cpd I), the main intermediate of the catalase reaction, is reduced back to the resting state generating molecular oxygen and a water molecule (Nicholls, 2001):



In reaction 1 (i.e. the *catalatic* reaction), H₂O₂ serves as a two-electron reductant. Formally one electron reduces the porphyrin cation radical and the other one contributes to the change of oxidation state of the iron atom, from Fe^{IV} to Fe^{III}. The transfer of these two electrons is associated to the transfer of two protons from H₂O₂ to the ferryl oxygen, forming water. As a result, H₂O₂ is converted into an O₂ molecule, as demonstrated by isotope labeling kinetic studies (Jarnagin, 1958; Vlasits, 2007). Nevertheless, it is not known how H₂O₂ loses these two electrons and two protons (Figure 1): transfer of a proton and a hydride ion (H⁺ / H⁻), double transfer of a hydrogen atom (H[•] / H[•]) or other mechanisms.

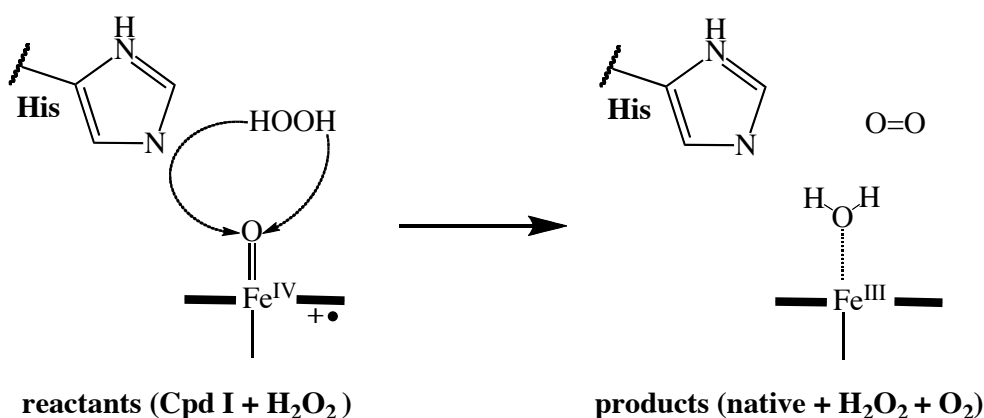
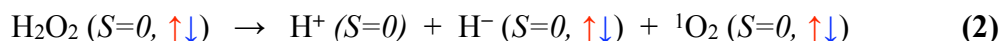


Figure 1. Schematic representation of Cpd I reduction by hydrogen peroxide in catalase. The porphyrin is depicted as a bold line.

As shown in Figure 1, the active site of catalase contains a distal His, which has been shown to be essential for the catalase reaction (Nicholls, 2001). It is generally accepted that this conserved His acts as a general acid-base catalyst in Cpd I formation. Besides, it has been proposed by Fita and Rossmann (Fita & Rossmann, 1985), and recently supported by Watanabe et al. (Kato, 2004; Watanabe, 2007), that the distal His is also involved in Cpd I reduction. Hence, the catalatic reaction (reaction 1) has been assumed to occur by a H⁺ / H⁻ scheme, in which the transfer of the proton is mediated by the distal His and the hydride ion is transferred directly to the oxoferryl unit (Figure 1).

Some authors (Khan, 1983; Lledías, 1998; Michán, 2002; Jakopitsch, 2003) have suggested that such H⁺ / H⁻ mechanism generates singlet oxygen, invoking spin conservation of the H₂O₂ molecule:



where S is the spin quantum number, \uparrow represent the α spin (spin-up electron) and \downarrow the β spin (spin-down electron). In contrast, simultaneous uptake of two hydrogen atoms from H₂O₂ (i.e. a H[•] / H[•] mechanism) would generate triplet oxygen:



In other words, a “pairwise movement of electrons” produces singlet oxygen, whereas “two single electron movements” lead to triplet oxygen. For instance, these arguments have been used to propose reaction mechanisms in catalases and catalase-peroxidases (Jakopitsch, 2003). Therefore, a priori it might seem that the mechanism involving proton transfer to the distal His (the H⁺ / H⁻ mechanism) generates singlet oxygen in catalase.

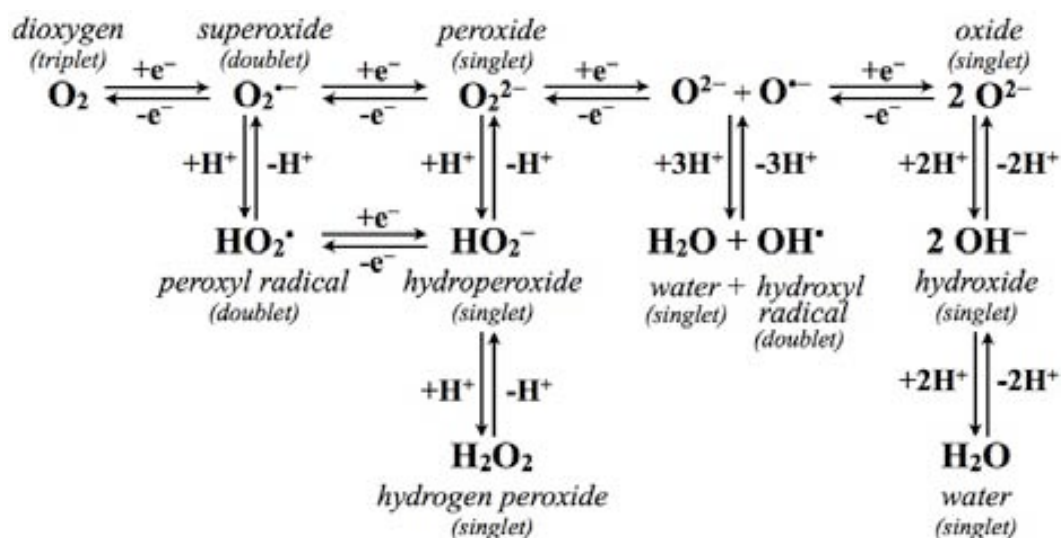
Indeed, production of singlet oxygen by catalase has been observed. In particular, several experiments have detected oxidation of catalase by singlet oxygen (Lledías, 1998; Michán, 2002) or chemiluminescence assigned to ¹O₂ emission (Khan, 1983; Kanofsky, 1984). However, as pointed out by Jakopitsch et al. (Jakopitsch, 2003) it would not make biological sense to release large amounts of singlet oxygen out of the heme pocket, because molecular oxygen in the singlet state is a very powerful oxidant. Its damaging action in a variety of biological processes has been well recognized (Alia, 2001; Adam, 2005) and it has been shown to inactivate enzymes (Jones & Suggett, 1968).

In this chapter, we assess the validity of the arguments that are used to predict the spin state of the molecular oxygen released by catalase. First we analyze all the possible spin states for the reactants (Cpd I + H₂O₂) and products (i.e. Por-Fe^{III} + H₂O + O₂) of the catalytic reaction (reaction 1) in catalase. We also figure out the possible reaction schemes for the transfer of two electrons and two protons from H₂O₂ to Cpd I, and qualitatively examine the spin state of the species involved within the spin conservation formalism. To complement this analysis, the electronic structures of the reactants and products are calculated for gas phase models of the active site by means of density functional theory (DFT).

2. SPIN STATE ANALYSIS

2.1. Reactants and products

Generation of O₂ from H₂O₂ is part of the known Latimer series (Latimer, 1938, Petlicki & van de Ven, 1998) going from O₂ to H₂O formation and reverse:



This series passes across species with triplet (O₂), doublet (O₂^{•-}, HO₂[•] and HO[•]) and singlet (H₂O, H₂O₂, OH⁻ and HO₂⁻) ground spin states, raising the question of how these a priori spin-forbidden reactions can take place. Nevertheless, the restrictions imposed by the spin conservation rule may be circumvented by the presence of a paramagnetic transition metal (Taube, 1965; Wagnerová, 2001), which increases the multiplicity of the overall system, thus increasing the number of spin-allowed reactions. For instance, whereas isolated H₂O₂ can only be a singlet, the global spin state of Cpd I + H₂O₂ (i.e. the reactants) can be a priori a doublet, quartet or sextet, based on the possible multiplicities of the separate fragments (see Appendix C, section 3). Likewise, the overall spin state of the products (i.e. Por-Fe^{III} + H₂O + O₂) can be a doublet, quartet, sextet or octuplet.

All the possible electronic configurations of the reactants (i.e. Cpd I + H₂O₂) and the products (i.e. Por-Fe^{III} + H₂O + O₂) of the catalytic reaction in monofunctional catalases are depicted in Figure 2. To facilitate the analysis, we have classified each species according to the total spin ($S_{total} = 1, 3/2, 5/2$ and $7/2$).

	reactants	products		
$S_{total} = 1$	$S_{His} = 0$ His $S_{H_2O_2} = 0$ HOOH O ↑↑ $S_{heme} = 1/2$ — Fe^{IV} — ↓	$S_{His} = 0$ His $S_{O_2} = 0$ O₂ HOH ↑····· $S_{heme} = 1/2$ — Fe^{III} —	$S_{His} = 0$ His $S_{O_2} = 1$ O₂↑↑ HOH ↓····· $S_{heme} = 1/2$ — Fe^{III} —	$S_{His} = 0$ His $S_{O_2} = 1$ O₂↓↓ HOH ↑↑↑····· $S_{heme} = 3/2$ — Fe^{III} —
	²R	²P_a	²P_b	²P_c
$S_{total} = 3/2$	$S_{His} = 0$ His $S_{H_2O_2} = 0$ HOOH O ↑↑ $S_{heme} = 3/2$ — Fe^{IV} — ↑	$S_{His} = 0$ His $S_{O_2} = 1$ O₂↑↑ HOH ↑····· $S_{heme} = 1/2$ — Fe^{III} —	$S_{His} = 0$ His $S_{O_2} = 0$ O₂ HOH ↑↑↑····· $S_{heme} = 3/2$ — Fe^{III} —	$S_{His} = 0$ His $S_{O_2} = 1$ O₂↓↓ HOH ↑↑↑↑····· $S_{heme} = 5/2$ — Fe^{III} —
	⁴R	⁴P_a	⁴P_b	⁴P_c
$S_{total} = 5/2$	$S_{His} = 0$ His $S_{H_2O_2} = 0$ HOOH O ↑↑↑ $S_{heme} = 5/2$ — Fe^{IV} — ↑	$S_{His} = 0$ His $S_{O_2} = 1$ O₂↑↑ HOH ↑↑↑····· $S_{heme} = 3/2$ — Fe^{III} —	$S_{His} = 0$ His $S_{O_2} = 0$ O₂ HOH ↑↑↑↑····· $S_{heme} = 5/2$ — Fe^{III} —	
	⁶R	⁶P_a	⁶P_b	
$S_{total} = 7/2$	$S_{His} = 0$ His $S_{H_2O_2} = 0$ HOOH O ↑↑↑↑ $S_{heme} = 7/2$ — Fe^{III} — ↑↑	$S_{His} = 0$ His $S_{O_2} = 1$ O₂↑↑ HOH ↑↑↑↑····· $S_{heme} = 5/2$ — Fe^{III} —		
	⁸R	⁸P		

Figure 2. Possible electronic configurations of the reactants (R, i.e. Cpd I + H₂O₂) and products (P, i.e. Por-Fe^{III} + H₂O + O₂) of the catalytic reaction in monofunctional catalases. The number in the left upper side (2, 4, 6 or 8) denotes the multiplicity and the letter in the right lower side (a, b or c) indicates the different electronic configurations compatible with the overall multiplicity. The α spin (spin-up electron) is represented by ↑ and the β spin (spin-down electron) by ↓.

It follows from Figure 2 that, when the spin state of all the species involved in the reaction is taken into account (and not only H₂O₂), the catalytic reaction could a priori generate both types of oxygen spin configurations, singlet (¹O₂) and triplet (³O₂). Let us now analyze the reactants and products in each possible spin state.

- *Quartet spin state*

The ground state of the reactants is expected to be a quartet, with a doublet state very close in energy, because this is the situation in Cpd I (de Visser, 2006). Therefore, we assume that the spin state does not change when H₂O₂ enters the distal pocket.

In the quartet state (an excess of three more unpaired electrons of a given spin, either α or β), there are three possible electron configurations of the products that are compatible with a global quartet state (Figure 2, $S_{tot} = 3/2$). Configuration ⁴P_a contains triplet oxygen and a doublet, low spin Fe^{III}-heme, both with parallel spins. In configuration ⁴P_c, the oxygen is also in a triplet spin state, but its two unpaired spins are antiparallel with the ones of the heme iron, which is in a quintuplet, high spin state. By contrast, in configuration ⁴P_b, the oxygen molecule is in a singlet state and all unpaired spins are localized on the heme iron, which is locally in a quartet, intermediate spin state. Therefore, the catalytic reaction in the quartet surface could a priori generate any type of oxygen spin configuration.

- *Doublet spin state*

Since the doublet state of catalase Cpd I is almost degenerated with the quartet state (de Visser, 2006), it is reasonable that at room temperature both spin states can coexist in equilibrium. An analogous analysis starting with Cpd I in the doublet state (Figure 2, $S_{tot} = 1$) also gives one configuration with singlet oxygen (²P_a) and two with triplet oxygen (²P_b and ²P_c). In configuration ²P_a there is only one unpaired electron, localized on the heme iron (i.e. it is locally in a doublet, low spin state), and the oxygen molecule is in a single state. By contrast, configuration ²P_b contains a triplet oxygen, whose two unpaired spins are antiparallel with the one on the heme iron (i.e. a doublet, low spin Fe^{III}), and thus it is the antiferromagnetic counterpart of ⁴P_a. In configuration ²P_c the oxygen is also in a triplet state, but the iron heme is now in a quartet, intermediate spin state.

Therefore, as for the quartet, in the doublet state any of the two types of oxygen spin configurations is possible.

- *Sextet and octuplet spin states*

The sextet (de Visser, 2006) and octuplet spin states of Cpd I are expected to be higher in energy, because they contain a {d⁴} iron and a strong field oxo ligand (i.e. Fe^{IV}=O, see Appendix C, section 3.1.). Nevertheless, in the products the sextet and octuplet states probably decrease in energy, because they will bear a {d⁵} iron and a weak field water molecule ligand (i.e. Fe^{III}-OH₂, see Appendix C, section 3.1.). In other words, once the products are reached, reorganization of the d-electrons of the iron may change the local spin state of the heme and thus the overall spin state.

Even though the spin state of the products of the catalytic reaction is not known experimentally, let us first assume that it is the same as in the resting state of the enzyme, i.e. a high-spin iron ($S_{heme} = 5/2$) (Sharma, 1989). This only happens in configurations ⁴P_c, ⁶P_b and ⁸P (Figure 2). Both configurations ⁴P_c and ⁸P contain triplet oxygen, whereas ⁶P_b involves singlet O₂. On the other hand, if we assume that iron can adopt any local spin configuration (not only sextet), both singlet and triplet oxygen are again found.

In summary, *when the spin state of all the species involved in the reaction is taken into account (and not only H₂O₂), it turns out that the catalytic reaction could a priori generate both types of oxygen spin configurations (singlet and triplet).*

2.2. Possible reaction schemes

In the catalytic reaction (reaction 1), two hydrogen atoms are formally transferred from hydrogen peroxide to Cpd I. It has been proposed that the distal His also participates in this transfer (as an acid-base catalyst), as it does in Cpd I formation (Fita & Rossmann, 1985; Kato, 2004; Watanabe, 2007). Assuming the distal His is involved in the reaction, three main reaction schemes may be envisioned to describe how two protons and two electrons are transferred to Cpd I.

(a) *H⁺ / H⁻ reaction scheme*

In this scheme, the distal His mediates the transfer of a proton to the oxoferryl unit, and a hydride ion is transferred to Fe=O, as shown in Figure 3.

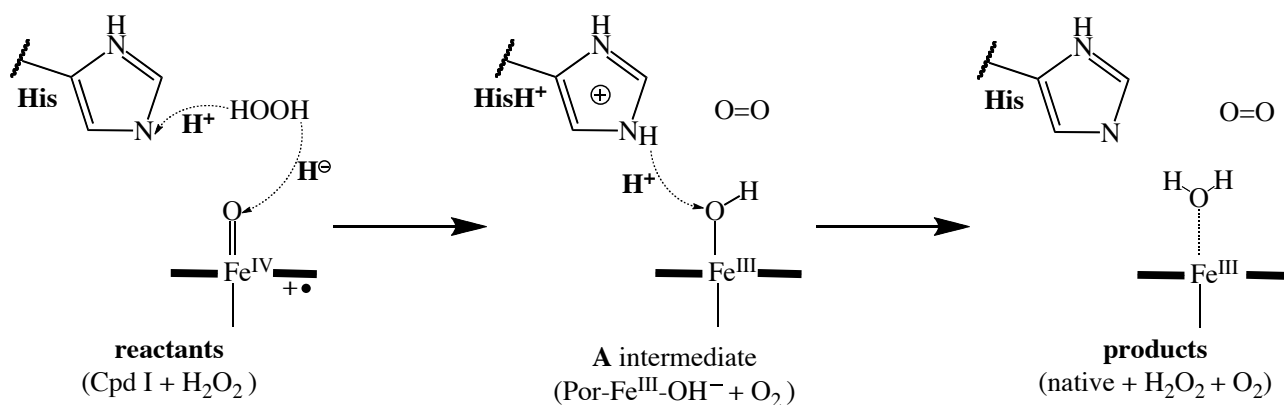


Figure 3. Schematic representation of the H⁺/H⁻ mechanism (assuming simultaneous transfers).

Given the pK_a of His and H₂O₂ in water solution (6.5 and 11.6), proton transfer from H₂O₂ to His appears to be unfavourable (Jones & Dunford, 2005). However, the binding of hydrogen peroxide to both His and Fe=O probably decreases its pK_a, thus enabling proton transfer to the His and yielding HisH⁺. On the other hand, hydride ion transfer to Cpd I renders Por-Fe^{III}-OH⁻, i.e. one of the two electrons of the hydride ion reduces the porphyrin cation radical and the other decreases the iron oxidation state. Assuming both transfers occur simultaneously, the **A** intermediate (shown in Figure 3) is formed. In the next reaction step, HisH⁺ gives a proton to the hydroxoferryl group, forming a water molecule and dioxygen.

$S_{total}=1$	$S_{His}=0$ HisH⁺ $S_{O_2}=0$ O₂	$S_{His}=0$ HisH⁺ $S_{O_2}=1$ O₂ ↑↑	$S_{His}=0$ HisH⁺ $S_{O_2}=1$ O₂ ↓↓
	$\ominus\text{OH}$ \uparrow $S_{schem}=1/2$ Fe^{III}	$\ominus\text{OH}$ \downarrow $S_{schem}=1/2$ Fe^{III}	$\ominus\text{OH}$ $\uparrow\uparrow\uparrow$ $S_{schem}=3/2$ Fe^{III}
	²A_a	²A_b	²A_c
$S_{total}=3/2$	$S_{His}=0$ HisH⁺ $S_{O_2}=1$ O₂ ↑↑	$S_{His}=0$ HisH⁺ $S_{O_2}=0$ O₂	$S_{His}=0$ HisH⁺ $S_{O_2}=1$ O₂ ↓↓
	$\ominus\text{OH}$ \uparrow $S_{schem}=1/2$ Fe^{III}	$\ominus\text{OH}$ $\uparrow\uparrow\uparrow$ $S_{schem}=3/2$ Fe^{III}	$\ominus\text{OH}$ $\uparrow\uparrow\uparrow\uparrow$ $S_{schem}=5/2$ Fe^{III}
	⁴A_a	⁴A_b	⁴A_c

Figure 4. Possible electronic configurations of the intermediate in the H⁺/H⁻ mechanism (**A**).

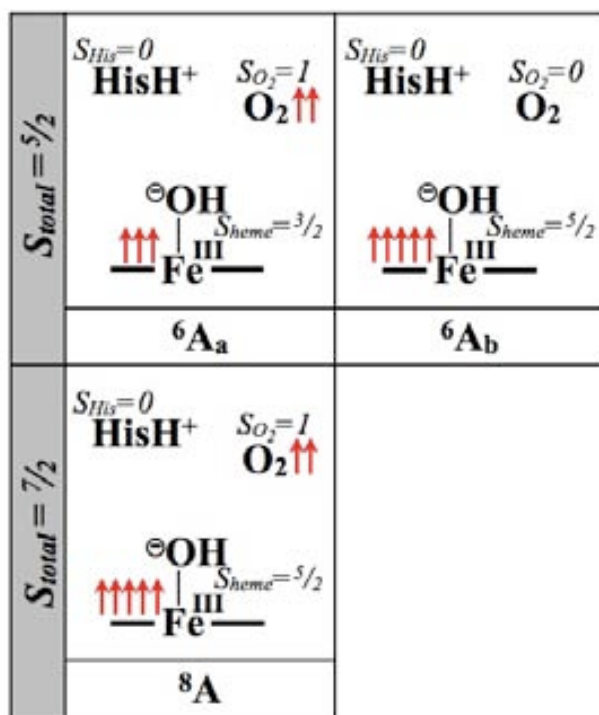


Figure 4 (cont.). Possible electronic configurations of the intermediate in the H⁺/H⁻ mechanism (**A**). The number in the left upper side (2, 4, 6 or 8) denotes the multiplicity and the letter in the right lower side (a, b or c) indicates the different electronic configurations compatible with the overall multiplicity. The α spin (spin-up electron) is represented by \uparrow and the β spin (spin-down electron) by \downarrow .

Figure 4 shows the possible electronic configurations of the **A** intermediate, which we will now use to analyze the H⁺/H⁻ reaction scheme in each possible spin state.

- *Reaction in the quartet state*

Because the ground state of Cpd I is a quartet, we will first analyze the quartet surface (Figure 4, $S_{total} = 3/2$). In the ⁴A_a configuration, one of two electrons of the hydride ion couples with the unpaired spin on the porphyrin cation radical, and the second with one of the two unpaired spins on the oxoferryl, resulting in a local doublet state at the Por-Fe^{III}-OH⁻ heme ($S_{heme} = 1/2$). Thus, the product oxygen molecule must be in a triplet state ($S_{O_2} = 1$) in order to conserve the global spin. Alternatively, the iron d-electrons could reorganize in a quartet ($S_{heme} = 3/2$, ⁴A_b) or a sextet ($S_{heme} = 5/2$, ⁴A_c) heme, and thus the molecular oxygen must be in a singlet or a triplet state, respectively, to conserve the overall spin state.

In the next reaction step, HisH⁺ gives a proton to the hydroxoferryl group, forming a water molecule and leading to products (Figure 2): ⁴P_a (from ⁴A_a), ⁴P_b (from ⁴A_b) and ⁴P_c (from ⁴A_c). Configurations ⁴P_a and ⁴P_c contain triplet oxygen, whereas ⁴P_b involves singlet oxygen. Therefore, *in contrast to the commonly used argument that the H⁺ / H⁻ mechanism (i.e. a pairwise movement of electrons) generates singlet oxygen* (Khan, 1983, Lledías, 1998, Michán, 2002; Jakopitsch, 2003), *both triplet and singlet oxygen can be the product of the catalytic reaction when one takes into account the spin state of all the species in the active center (and not only H₂O₂).*

• *Reaction in the other spin states*

As mentioned above, the doublet state of Cpd I is very close in energy to the quartet. In the doublet state surface (Figure 4, $S_{total} = 1$), proton transfer to the His and hydride ion transfer to the heme renders either ²A_a or ²A_b (the antiferromagnetic counterpart of ⁴A_a). Besides, reorganization of the iron d-electrons leads to ²A_c. Subsequent proton transfer from HisH⁺ to Fe^{III}-OH⁻ unit yields the products (²P_a, ²P_b and ²P_c, respectively, see Figure 2). Therefore, as in the quartet surface, the released molecular oxygen can be both triplet and singlet.

The sextet and octuplet states are expected to be very high energy for the reactants, as for Cpd I. They are also expected to be high-energy configurations of the **A** intermediate, because the ground state of catalase Por-Fe^{III}-OH⁻ has been found to be a doublet (Yshida, 1970; Rydberg, 2004). Nevertheless, as mentioned in section 2.1., the sextet and octuplet states probably decrease in energy in the products, and hence they are also considered here. Analysis of the sextet and octuplet surfaces (Figure 4, $S_{total} = 5/2$ and $S_{total} = 7/2$) leads to the same conclusions as for the lower spin states. Therefore, *regardless of the spin state surface, the H⁺ / H⁻ mechanism can generate both triplet and singlet oxygen.*

(b) H[•] / H[•] reaction scheme

Even though the H⁺ / H⁻ scheme is considered to be the most likely mechanism, other mechanisms are compatible with the catalytic reaction (reaction 1). One of them involves hydrogen transfer to both His and Cpd I (H[•] / H[•] scheme), resulting in the **B** intermediate shown in Figure 5. The distal histidine acquires spin density ($S_{His} = 1/2$) and the heme adopts a Compound II-like configuration (Cpd II-like), due to the one-electron reduction of Cpd I (see Chapter I, section 4.2.). Two electromers are possible for the Cpd II-like species, as reported for *Horse radish peroxidase*

(HRP) (Derat, 2006b), cytochrome P450 (P450) (Filatov, 1999; Shaik, 2005) or chloroperoxidase (CPO) (Lai, 2009). In case the electron that transfers to Cpd I couples with the unpaired porphyrin radical, the Por-Fe^{IV}-OH electromer is formed. Alternatively, if the transferred electron couples with one of the unpaired electrons localized on the oxoferryl unit, the Por^{+•}-Fe^{III}-OH electromer is formed.

From B1, the next step is the transfer of a hydrogen atom from HisH[•] to the hydroxoferryl Cpd II, releasing a water molecule and an oxygen molecule.

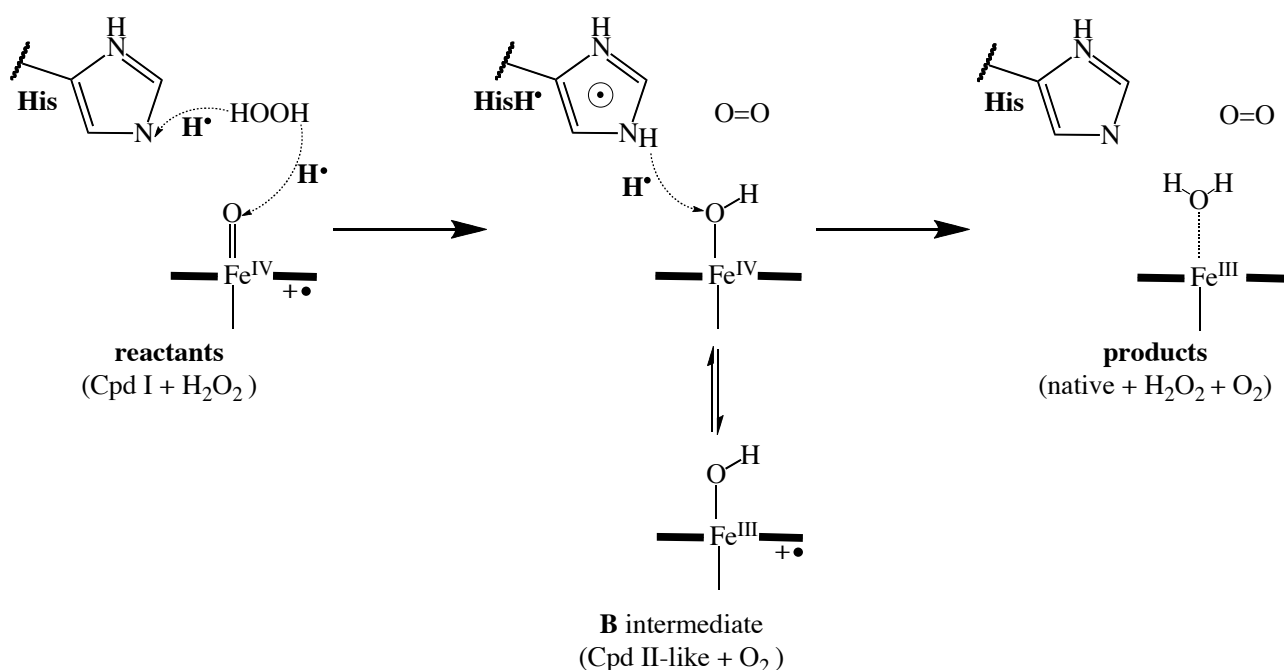


Figure 5. Schematic representation of the H[•] / H[•] mechanism (assuming simultaneous transfers).

- *Reaction in the quartet spin state*

As shown in Figure 6, there are five possible configurations of the **B** intermediate that are compatible with the overall quartet multiplicity ($S_{tot} = 3/2$). ⁴B_a and ⁴B_b contain the Por-Fe^{IV}-OH electromer, in which iron is in a triplet local state. Therefore, to conserve the total spin, the oxygen molecule must be either a singlet (in ⁴B_a) or a triplet (in ⁴B_b), depending on whether the spin on the distal HisH[•] is parallel or antiparallel to the two unpaired electrons on the hydroxoferryl group, respectively. From ⁴B_a and ⁴B_b, transfer of a hydrogen atom from HisH[•] to the hydroxoferryl Cpd II leads to ⁴P_b (from ⁴B_a) or ⁴P_a (from ⁴B_b).

By contrast, configurations 4B_c , 4B_d and 4B_e bear the $\text{Por}^{+\bullet}\text{-Fe}^{\text{III}}\text{-OH}$ electromer (Figure 5). Depending on the coupling of the unpaired electrons on the porphyrin and the hydroxoferryl unit, the local spin state of the heme can be either a singlet (4B_b) or a triplet (4B_c and 4B_e). Therefore, to conserve the total spin, the oxygen molecule must be a triplet (in 4B_c and 4B_d) or a singlet (in 4B_e), depending on the orientation of the HisH^\bullet unpaired spin. In the next reaction step, hydrogen atom transfer from HisH^\bullet to the heme would generate the products, 4P_a (from 4B_c and 4B_d) or 4P_b (from 4B_e). Alternatively, reorganization of the d-electrons of the iron could also yield 4P_c (i.e. a high spin Fe^{III}). This reorganization is unlikely to occur in the **B** intermediate, because the quintuplet state of Cpd II is higher in energy than the singlet or the triplet (Filatov, 1999), but it is more probable in the products, because water is a weak field ligand (see Appendix C, section 3.1.). Overall, *unlike the common assumption that the H^\bullet / H^\bullet scheme (i.e. two single electron movements) leads to triplet oxygen, both triplet and singlet oxygen products are compatible with this reaction scheme.*

- *Reaction in the other spin states*

The doublet surface (Figure 6, $S_{tot} = 1$) also shows five possible configurations for the **B** intermediate. All of them are very similar to their quartet state counterparts, except that the coupling between the unpaired spins of the HisH^\bullet and the heme is antiferromagnetic, instead of ferromagnetic. Therefore, the conclusions regarding the spin state of the released oxygen in the quartet surface also hold for the doublet.

The possible configurations of the **B** intermediate in the sextet and the octuplet state surfaces are also shown in Figure 6 ($S_{tot} = 5/2$ and $S_{tot} = 7/2$). Most of the sextet and all the octuplet configurations contain a $S_{heme} = 2$ or $S_{heme} = 3$ Cpd II-like species, and thus they are expected to be higher in energy than the quartet, as found for P450 (Filatov, 1999; Altun, 2007). Only 6B_c and 6B_f have a local triplet heme, and thus they may be energetically accessible. Indeed, 6B_c and 6B_f can be seen as the ferromagnetic counterparts of 4B_c or 4B_d , respectively. 6B_c and 4B_c only differ on the unpaired spin on the His being parallel or antiparallel to the triplet hydroxoferryl heme. For 6B_f and 4B_d the difference is just the local spin state of the heme (doublet or singlet $\text{Por}^{+\bullet}\text{-Fe}^{\text{III}}\text{-OH}$, depending on the coupling, ferro- or antiferromagnetic, of the unpaired spins of the porphyrin and the ferric ion). Hence, 6B_c and 6B_f are expected to be close in energy to 4B_c and 4B_d , respectively. In all four configurations, the released molecular oxygen is in a triplet state (Figure 6).

$S_{total} = 1$	$S_{His} = 1/2$ HisH• ↓ $S_{O_2} = 0$ O₂	$S_{His} = 1/2$ HisH• ↑ $S_{O_2} = 1$ O₂ ↓↓	$S_{His} = 1/2$ HisH• ↑ $S_{O_2} = 1$ O₂ ↓↓	$S_{His} = 1/2$ HisH• ↓ $S_{O_2} = 1$ O₂ ↓↓	$S_{His} = 1/2$ HisH• ↓ $S_{O_2} = 1$ O₂ ↑↑	$S_{His} = 1/2$ HisH• ↓ $S_{O_2} = 0$ O₂
	$S_{Scheme} = 1$ OH ↑↑ — Fe — IV	$S_{Scheme} = 1$ OH ↑↑ — Fe — IV	$S_{Scheme} = 1$ OH ↑↑ — Fe — IV	$S_{Scheme} = 1$ OH ↑↑ — Fe — IV	$S_{Scheme} = 1$ OH ↑↑ — Fe — IV	$S_{Scheme} = 0$ OH ↑ — Fe — III
	²B_a	²B_b	²B_c	²B_c	²B_d	²B_e
$S_{total} = 3/2$	$S_{His} = 1/2$ HisH• ↑ $S_{O_2} = 0$ O₂	$S_{His} = 1/2$ HisH• ↓ $S_{O_2} = 1$ O₂ ↑↑	$S_{His} = 1/2$ HisH• ↓ $S_{O_2} = 1$ O₂ ↑↑	$S_{His} = 1/2$ HisH• ↓ $S_{O_2} = 1$ O₂ ↑↑	$S_{His} = 1/2$ HisH• ↑ $S_{O_2} = 1$ O₂ ↑↑	$S_{His} = 1/2$ HisH• ↑ $S_{O_2} = 0$ O₂
	$S_{Scheme} = 1$ OH ↑↑ — Fe — IV	$S_{Scheme} = 1$ OH ↑↑ — Fe — IV	$S_{Scheme} = 1$ OH ↑↑ — Fe — IV	$S_{Scheme} = 1$ OH ↑↑ — Fe — IV	$S_{Scheme} = 1$ OH ↑↑ — Fe — IV	$S_{Scheme} = 0$ OH ↑ — Fe — III
	⁴B_a	⁴B_b	⁴B_c	⁴B_c	⁴B_d	⁴B_e

Figure 6. Possible electronic configurations of the intermediate in the H•/H• mechanism (**B**). The number in the left upper side (2, 4, 6 or 8) denotes the multiplicity and the letter in the right lower side (a, b or c) indicates the different electronic configurations compatible with the overall multiplicity. The α spin (spin-up electron) is represented by ↑ and the β spin (spin-down electron) by ↓.

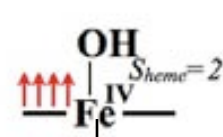
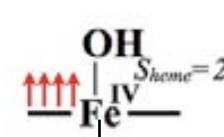
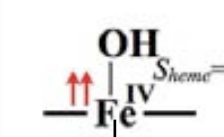
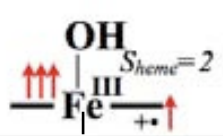
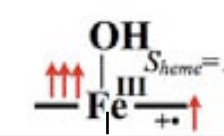
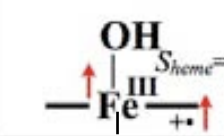
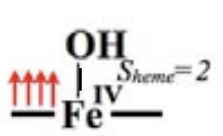
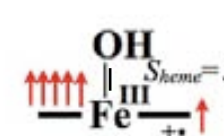
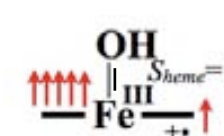
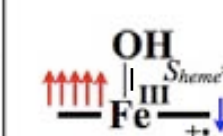
$S_{total} = 5/2$	$S_{His} = 1/2$ $HisH^{\bullet\uparrow}$ $S_{O_2} = 0$ O_2	$S_{His} = 1/2$ $HisH^{\bullet\downarrow}$ $S_{O_2} = 1$ $O_2\uparrow\uparrow$	$S_{His} = 1/2$ $HisH^{\bullet\uparrow}$ $S_{O_2} = 1$ $O_2\uparrow\uparrow$	
				
	6B_a	6B_b	6B_c	
	$S_{His} = 1/2$ $HisH^{\bullet\uparrow}$ $S_{O_2} = 0$ O_2	$S_{His} = 1/2$ $HisH^{\bullet\downarrow}$ $S_{O_2} = 1$ $O_2\uparrow\uparrow$	$S_{His} = 1/2$ $HisH^{\bullet\uparrow}$ $S_{O_2} = 1$ $O_2\uparrow\uparrow$	
				
	6B_d	6B_e	6B_f	
$S_{total} = 7/2$	$S_{His} = 1/2$ $HisH^{\bullet\uparrow}$ $S_{O_2} = 1$ $O_2\uparrow\uparrow$	$S_{His} = 1/2$ $HisH^{\bullet\uparrow}$ $S_{O_2} = 0$ O_2	$S_{His} = 1/2$ $HisH^{\bullet\downarrow}$ $S_{O_2} = 1$ $O_2\uparrow\uparrow$	$S_{His} = 1/2$ $HisH^{\bullet\uparrow}$ $S_{O_2} = 1$ $O_2\uparrow\uparrow$
				
	8B_a	8B_b	8B_c	8B_d

Figure 6 (cont). Possible electronic configurations of the intermediate in the H^{\bullet}/H^{\bullet} mechanism (**B**). The number in the left upper side (2, 4, 6 or 8) denotes the multiplicity and the letter in the right lower side (a, b or c) indicates the different electronic configurations compatible with the overall multiplicity. The α spin (spin-up electron) is represented by \uparrow and the β spin (spin-down electron) by \downarrow .

(c) $H^{\bullet}/H^{\bullet} + ET$ reaction scheme

Even though a $H^{\bullet}/H^{\bullet} + ET$ mechanism has not previously considered, it is also a possible reaction scheme. Here, proton transfer (H^{\bullet}) through the distal His occurs, together with the transfer of a hydrogen atom (H^{\bullet}) and an electron (ET). Hydrogen atom transfer to Cpd I yields a peroxy radical (HOO^{\bullet}) and a Cpd II-like species. Because the pKa of HOO^{\bullet} (4.8) is lower than that of His (6.5), it is expected that the peroxy radical donates a proton to the His, resulting in a superoxide radical anion ($O_2^{\bullet-}$) and a protonated His ($HisH^{\bullet+}$). The resulting $\{Cpd\ II\text{-like} + O_2^{\bullet-} + HisH^{\bullet+}\}$

intermediate (hereafter **C**) is shown in Figure 7. As explained above, two different electromers are possible for the Cpd II-like species (i.e. Por-Fe^{IV}-OH or Por⁺-Fe^{III}-OH), depending on which orbital from Cpd I “receives” the electron transferred by H₂O₂.

It should be pointed out that the whole H[•] / H⁺ process is a single electron transfer, whereas the catalytic reaction (reaction 1) is a two-electron process. It is thus expected that, in the next step, not only the proton on the His but also a second electron from O₂⁻ is transferred to the Cpd II, yielding a water molecule and dioxygen. This process, namely proton transfer (PT) from the distal His to the ferryl oxygen and electron transfer (ET) from superoxide to the heme, could possibly proceed via proton-coupled electron transfer (PCET), as found in other hemeproteins (Derat, 2007; Cho, 2007).

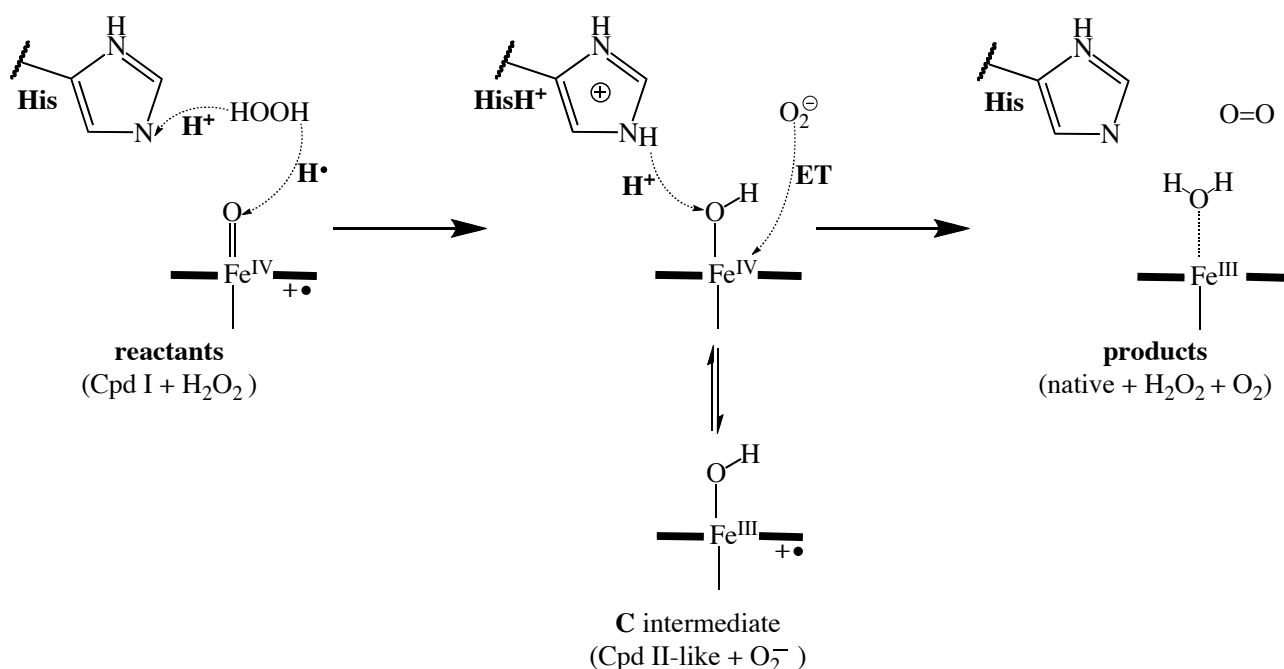


Figure 7. Schematic representation of the H[•] / H⁺ mechanism (assuming simultaneous transfers).

- *Reaction in the quartet state*

The **C** intermediate may have four different electronic configurations in the quartet surface (Figure 8, $S_{tot} = 3/2$). Both ⁴C_a and ⁴C_b contain a doublet superoxide anion radical coupled ferromagnetically to a triplet Cpd II (Por-Fe^{IV}-OH in ⁴C_a and Por⁺-Fe^{III}-OH in ⁴C_b). Considering electronic reorganization at the iron atom, other electronic configurations are also possible (⁴C_c and ⁴C_d). However, they are expected to be higher in energy, because they bear a quintuplet Cpd II (Filatov, 1999; Altun, 2007).

In the next step, Cpd II receives one proton from HisH⁺ and one electron from O₂⁻, leading to products ⁴P_a (from ⁴C_a and ⁴C_b), in which triplet oxygen is produced, or ⁴P_b (from ⁴C_c and ⁴C_d), in which singlet oxygen is formed. Therefore, as for the previous schemes, a *H[•] / H⁺+ET mechanism can lead to either triplet or singlet oxygen as reaction product.*

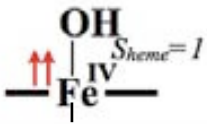
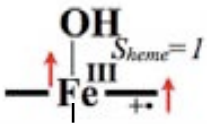
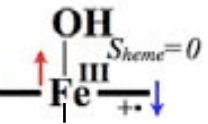
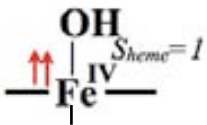
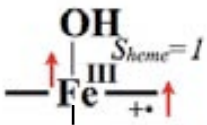
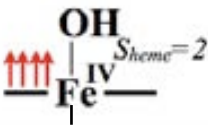
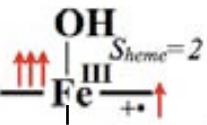
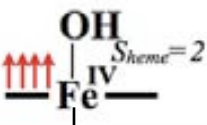
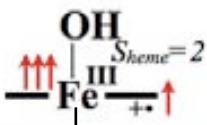
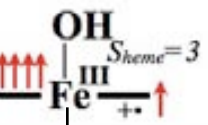
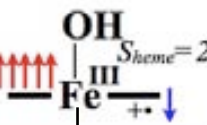
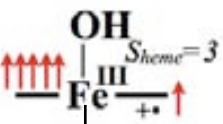
$S_{total}=1$	$S_{His}=0$ HisH ⁺ $S_{O_2}=1/2$ O ₂ ⁻ ↓	$S_{His}=0$ HisH ⁺ $S_{O_2}=1/2$ O ₂ ⁻ ↓	$S_{His}=0$ HisH ⁺ $S_{O_2}=1/2$ O ₂ ⁻ ↑	
				
	² C _a	² C _b	² C _c	
$S_{total}=3/2$	$S_{His}=0$ HisH ⁺ $S_{O_2}=1/2$ O ₂ ⁻ ↑	$S_{His}=0$ HisH ⁺ $S_{O_2}=1/2$ O ₂ ⁻ ↑	$S_{His}=0$ HisH ⁺ $S_{O_2}=1/2$ O ₂ ⁻ ↓	$S_{His}=0$ HisH ⁺ $S_{O_2}=1/2$ O ₂ ⁻ ↓
				
	⁴ C _a	⁴ C _b	⁴ C _c	⁴ C _d
	$S_{total}=5/2$	$S_{His}=0$ HisH ⁺ $S_{O_2}=1/2$ O ₂ ⁻ ↑	$S_{His}=0$ HisH ⁺ $S_{O_2}=1/2$ O ₂ ⁻ ↑	$S_{His}=0$ HisH ⁺ $S_{O_2}=1/2$ O ₂ ⁻ ↓
				
⁶ C _a		⁶ C _b	⁶ C _c	⁶ C _d
$S_{total}=7/2$		$S_{His}=0$ HisH ⁺ $S_{O_2}=1/2$ O ₂ ⁻ ↑		
	⁸ C _a			

Figure 8. Possible electronic configurations of the intermediate in the H[•] / H⁺ mechanism (C). The number in the left upper side (2, 4, 6 or 8) denotes the multiplicity and the letter in the right lower side (a, b or c) indicates the different electronic configurations compatible with the overall multiplicity. The α spin (spin-up electron) is represented by \uparrow and the β spin (spin-down) by \downarrow .

- *Reaction in the other spin states*

The analysis in the doublet surface shows very similar results (Figure 8, $S_{tot} = 1$). 2C_a and 2C_b are the antiferromagnetic counterparts of 4C_a and 4C_b (i.e. the unpaired spin on the superoxide is antiparallel or parallel to the triplet Cpd II). By contrast, 2C_c bears a singlet Cpd II and the only unpaired spin is on the superoxide. From **C**, proton transfer (PT) from HisH⁺ and electron transfer (ET) from O₂⁻ yields the products (2P_a or 2P_b).

All sextet and octuplet intermediates contain a local quintuplet or septuplet Cpd II (Figure 8, $S_{tot} = 5/2$ and $S_{tot} = 7/2$), and, therefore, they are expected to be too high in energy (Filatov, 1999; Altun, 2007) to participate in the reaction. In case they do, again both singlet (6P_b from 6C_c and 6C_d) and triplet (6P_b from 6C_a and 6C_b , or 8P from 8C) oxygen can be produced.

2.3. Implications for the mechanism of the catalatic reaction

Even though the generation of O₂ from H₂O₂ is basically part of the known Latimer series (Latimer, 1938, Petlicki & van de Ven, 1998), the spin state of the oxygen molecule generated in the catalatic reaction (reaction **1**) is not clear in the literature (Khan, 1983; Lledías, 1998; Michán, 2002; Jakopitsch, 2003). Based on the spin conservation of the singlet state of hydrogen peroxide, it has been claimed that the H⁺ / H⁻ mechanism should generate singlet oxygen, whereas the H[•] / H[•] mechanism would generate triplet oxygen. Nevertheless, we have demonstrated that, *when the spin of all the species involved in the reaction is taken into account (not only H₂O₂), both H⁺ / H⁻ and H[•] / H[•] mechanisms can produce molecular oxygen in the singlet as well as in the triplet state* (Figures 4 and 6, respectively). In other words, the commonly assumed association of the H⁺ / H⁻ mechanism with singlet oxygen production is not justified.

Apart from the two previously proposed mechanisms, we have suggested a third possible reaction scheme (Figure 7), in which superoxide anion radical is formed. *This H[•] / H⁺ + ET mechanism can also lead to either singlet or triplet oxygen as reaction product (Figure 8), similar to the H⁺ / H⁻ and H[•] / H[•] mechanisms.* Therefore, the spin state of the released molecular oxygen does not depend on the mode how the two electrons and two protons of hydrogen peroxide are transferred to Cpd I.

Although in this analysis we have considered that the global spin state is conserved, reactions of high-valent iron-oxo species are known to involve multistate reactivity (MSR) (Shaik, 2007), i.e. they involve at least two spin states that either crisscross or remain in proximity. In the catalytic reaction, the ground state of the reactants (Cpd I + H₂O₂) is most likely a quartet, because Cpd I has been found to be a quartet, with a close-in-energy doublet state (de Visser, 2006). The **A** intermediate (Figure 4) contains a Fe^{III}-OH heme, which is known to be a doublet (Rydberg, 2004; Yshida, 1970), and an oxygen molecule, which can be either a singlet or a triplet. As a result, the overall spin state of the **A** intermediate could be a quartet or a doublet (Figure 4). Both **B** and **C** intermediates (Figures 6 and 8) contain a Cpd II-like species, which is expected to have a local triplet state with a nearly degenerated singlet (Filatov, 1999; Derat, 2006b; Altun, 2007; Lai, 2009), together with an additional unpaired spin on the His (**B**) or the superoxide (**C**). As a result, the overall spin state of the **B** and **C** intermediates could be either a quartet or a doublet (Figures 6 and 8).

Therefore, *the catalytic reaction probably happens in the quartet surface for all three mechanisms considered, with a nearby doublet surface.* The participation of the higher spin states (i.e. sextet and octuplet) in the reaction is unlikely, because their corresponding intermediates are expected to be higher-in-energy configurations.

Once the products are reached, the iron d-electrons may reorganize from a doublet Fe^{III} to a quartet or even a sextet ferric ion, because water is a weak field ligand. As a consequence, the overall spin state would also increase. In other words, *spin crossing to the sextet or the octuplet states may occur in the products.*

3. GAS PHASE CALCULATIONS

To complement our spin state analysis, we have calculated the electronic structures of the reactants (Cpd I + H₂O₂) and products (Por-Fe^{III} + H₂O + O₂) of the catalytic reaction by means of density functional theory (DFT) (Hohenberg, 1964; Kohn & Sham, 1965). A reduced model of the catalase active site was used (Figure 9), and therefore these calculations should be regarded as preliminary. The computational details are described in Appendix C (section 1). We have not attempted to rank in energy all the possible electronic configurations discussed so far (Figures 4, 6 and 8), but we have only analyzed the most stable electronic configuration for a given total spin.

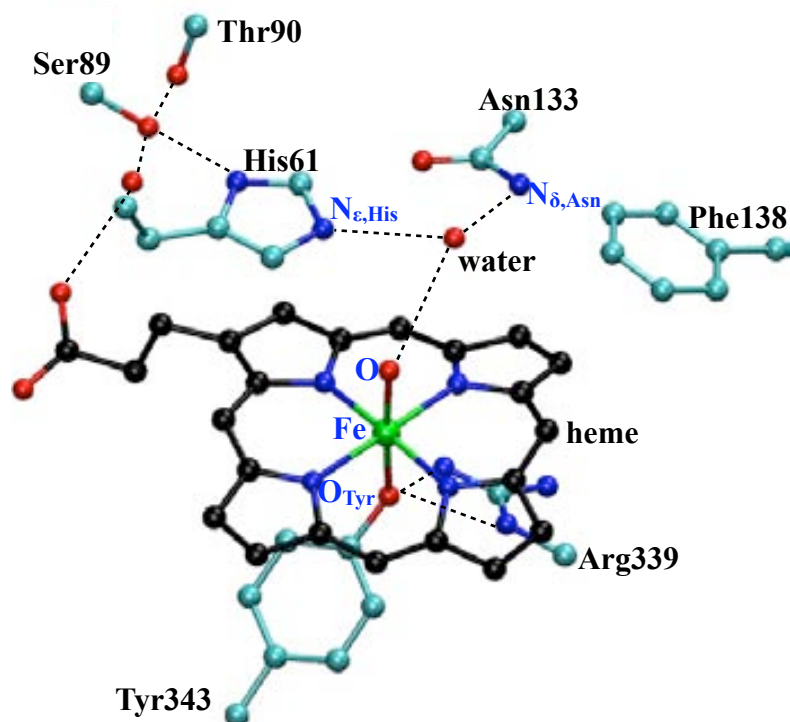
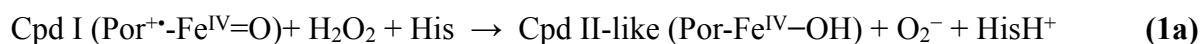


Figure 9. Model of the catalase active site used in the calculations (see Appendix C, section 1). The residue numbering corresponds to *Micrococcus luteus* catalase (MLC, PDB entry 1GWF) (Murshudov, 2002). The hydrogen atoms are omitted for clarity¹.

3.1. Reactants (Cpd I + H₂O₂)

The reactants of the catalytic reaction, i.e. the Michaelis complex Cpd I : H₂O₂, were optimized in both the doublet and quartet states, because the ground state of catalase Cpd I is known to be a quartet, with a doublet state very close in energy (de Visser, 2006). As mentioned in section 2.1., the sextet and octet states are expected to be high-energy configurations, and thus they are not considered in the calculations.

Upon geometry optimization, hydrogen peroxide is found to be not stable, but it spontaneously initiates the reaction (Figure 10):



Analysis of the optimized structures (Table 1) and spin density distributions (Figure 11 and Table 2) demonstrates that one proton has been transferred (PT) to the distal His, whereas hydrogen atom transfer (HAT) to Cpd I has been taken place, resulting in a superoxide radical anion and a Cpd II-

¹ As explained in Appendix C, section 1.1, the propionate side chain of the heme is taken as protonated. The influence of the protonation state of the propionate is investigated in Appendix C, section 4

like species. Therefore, based on a simplified model, *our preliminary calculations indicate a first step of the catalytic reaction consistent with the $H^\bullet / H^+ + ET$ reaction scheme* (Figure 7).

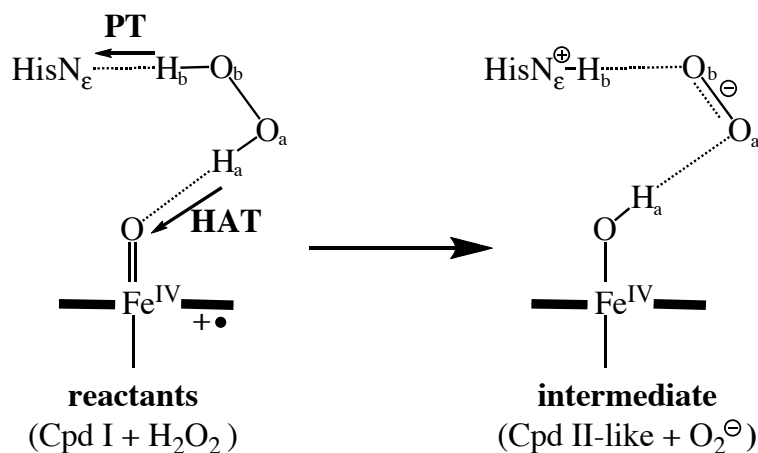


Figure 10. Atomic and electronic reorganization upon structure optimization of the reactants of the catalytic reaction (i.e. Cpd I + H_2O_2). PT = proton transfer, HAT = hydrogen atom transfer.

Table 1 shows the main distances defining the optimized structure of the intermediate species formed (i.e. Cpd II-like + O_2^-). The Fe-O distance (1.75-1.74 Å) is very similar to that reported for hydroxoferryl Cpd II (1.77 Å) (Rovira, 2005), and the O_a - O_b distance (1.30-1.31 Å) is consistent with a superoxide radical anion (1.32 Å, see Appendix C, section 2). As shown in Figure 11, the spin density on the porphyrin has disappeared along with the emergence of unpaired spin density on the O_a - O_b moiety. This is consistent with the reduction of the porphyrin cation radical by the O_a - O_b moiety. Indeed, integration of the spin density (Table 2) results in approximately two unpaired electrons on the oxoferryl unit (i.e. a Cpd II-like species, $^3[\text{Fe}^{\text{IV}}=\text{O}]$) and one unpaired spin on the dioxygen moiety (i.e. a superoxide anion radical, $^2\text{O}_2^-$). The only difference between the quartet and doublet states is the coupling between $^3[\text{Fe}^{\text{IV}}=\text{O}]$ and $^2\text{O}_2^-$, ferromagnetic in the quartet state and antiferromagnetic in the doublet state.

Table 1. Selected distances ^a defining the optimized structure of the intermediate species of the catalytic reaction (i.e. Cpd II-like + O₂⁻) in the quartet and doublet spin states.

distance (Å)	quartet	doublet
Fe-O	1.75	1.74
Fe-O _{Tyr}	2.04	2.04
Fe-N _{Por}	1.99-2.03	2.00-2.03
Fe out-of-plane	0.07	0.08
O _a -O _b	1.30	1.31
O _a -H _a	1.62	1.56
O-H _a	1.03	1.04
O _b -H _b	1.62	1.55
N _{ε,His} -H _b	1.07	1.08
O _b -H _{δ,Asn}	2.01	1.99

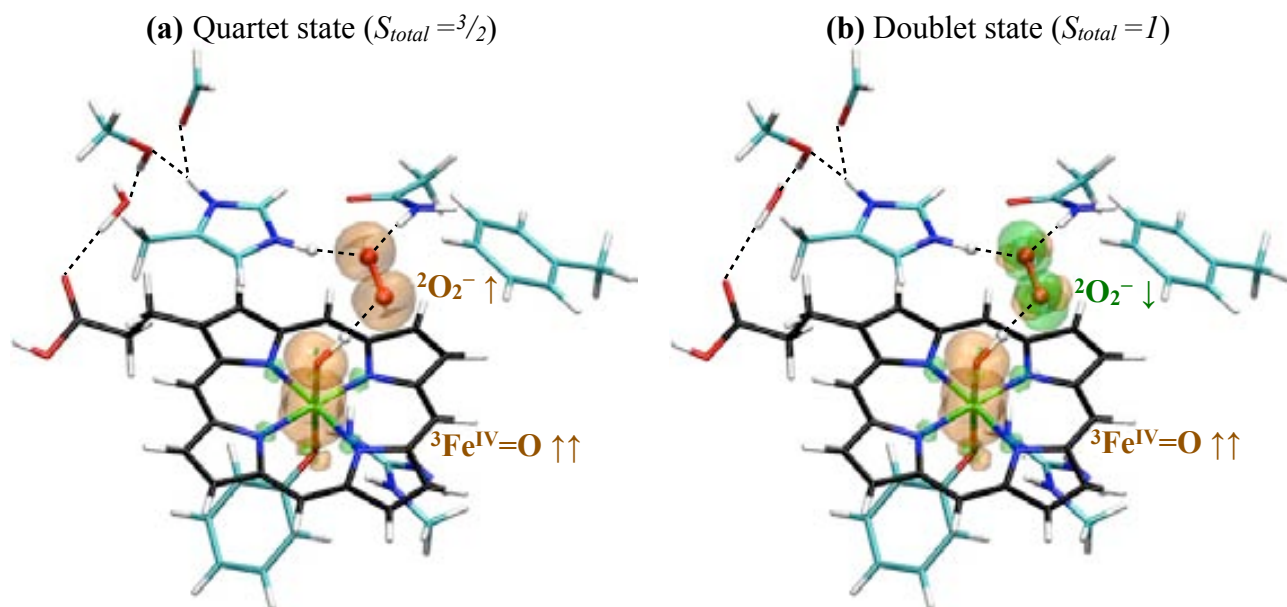
^a For atom names see Figures 9 and 10.**Figure 11.** Optimized structure and spin density distribution of the intermediate species of the catalytic reaction (i.e. Cpd II-like + O₂⁻). Spin isodensity surfaces at 0.004 e Å⁻³ are plotted in orange (spin-up) and green (spin-down). The atoms of H₂O₂ are represented in ball and stick.

Table 2. Number of unpaired electrons on relevant fragments^a of the intermediate species of the catalytic reaction (i.e. Cpd II-like + O₂⁻). The spin density distributions (Figure 11) were integrated using Bader's Atoms-In-Molecules theory (Bader, 1990).

number of unpaired electrons	quartet	doublet
Fe	1.45 [↑]	1.54 [↑]
O	0.26 [↑]	0.28 [↑]
FeO	1.71 [↑]	1.82 [↑]
O_{Tyr}	0.03 [↑]	0.03 [↑]
O_a-O_b	1.28 [↑]	0.80 [↓]
N_{Por}	0.05 [↓]	0.07 [↓]

^a For atom names see Figures 9 and 10.

Therefore, the electronic configuration of the intermediate species of the catalytic reaction (i.e. Cpd II-like + O₂⁻) is consistent with configurations ⁴C_a and ²C_a (Figure 8). It should be noted that the number of unpaired electrons on FeO is somewhat less than 2, indicating some degree of charge transfer from superoxide. Complete electron transfer (from superoxide to Cpd II-like) will require the transfer of the proton on the His to the ferryl oxygen (see section 3.2.)

The ground state of the {Cpd II-like + O₂⁻} intermediate species turns out to be the same as Cpd I (de Visser, 2006): a quartet, with a doublet state very close in energy (within 3 kcal/mol). This small energy difference between quartet and doublet is consistent with the optimized structures in both spin states being very similar (Table 1), and suggests that the coupling between the π^*_{FeO} orbitals and the $\pi_{\text{O}_a\text{-O}_b}$ orbital is small.

It could be argued that the well-known self-interaction error (SIE) associated to DFT could affect the results obtained (for instance, the hydrogen atom transfer from H₂O₂ to Cpd I to generate hydroxoferryl Cpd II). Because the inclusion of Hartree-Fock (HF) exchange part in the exchange-correlation functional decreases the SIE (Lundberg & Siegbahn, 2005), we performed additional B3LYP/PW single-point calculations of the reactants, which gave the same electronic distribution (i.e. Cpd II-like + superoxide, see Appendix C, section 5). This result does not exclude completely that the SIE could be present in our calculation. Nevertheless, Cpd I of heme b-containing catalases

(such the one studied here) can be spontaneously reduced to Cpd II by a residue of the protein in the absence of hydrogen peroxide (Ivancich, 1997; Alfonso-Prieto, 2007), and catalase Cpd II is expected to be protonated (Rovira 2005; Horner, 2006 & 2007). Moreover, catalases also exhibit peroxidatic activity, in which Cpd I is one-electron reduced to Cpd II by an exogenous organic substrate (see Chapter I, section 3.3.). Therefore, it should not be surprising that Cpd II is formed via hydrogen atom transfer from H₂O₂ to Cpd I.

3.2. Products (Por-Fe^{III} + H₂O + O₂)

As described in section 2.2., the subsequent step of the catalytic reaction is expected to be the transfer of the proton (PT) from the His to the ferryl oxygen, as well as the transfer of one electron (ET) from the superoxide to Fe^{IV} (Figure 12), forming the products (i.e. Por-Fe^{III} + H₂O + O₂), i.e.:

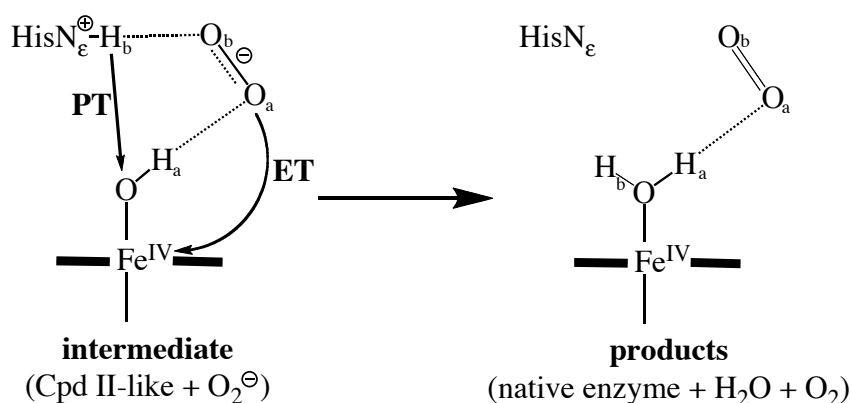


Figure 12. Schematic representation of the evolution of the intermediate species of the catalytic reaction (i.e. Cpd II-like + O₂⁻) into the products (i.e. Por-Fe^{III} + H₂O + O₂). PT = proton transfer, ET = electron transfer.

The optimized structures of the products of the catalase reaction in different spin states are shown in Figure 13 and Table 3 lists the main structural parameters. The side chain of the distal His has moved slightly with respect to its position in the intermediate {Cpd II-like + O₂⁻} species (Figure 13) and forms a hydrogen bond to the pocket water (N_{ε,His}-H_b = 1.91-1.94 Å), indicating a putative proton transfer pathway from the distal His to the ferryl oxygen. The O_a-O_b distance (1.23-1.24 Å) is consistent with a neutral oxygen molecule. Overall, these results suggest that *the*

last step of the catalytic reaction consists of a proton transfer from the distal His to the ferryl oxygen, accompanied by electron transfer from superoxide to the iron, forming an oxygen molecule.

Table 3. Selected distances ^a defining the optimized structure of the products of the catalytic reaction (Por-Fe^{III} + H₂O + O₂) in all the possible overall spin states.

distance (Å)	quartet	doublet	sextet	octuplet
Fe-O	2.05	2.06	2.45	2.33
Fe-O _{Tyr}	1.96	1.96	2.10	2.04
Fe-N _{Por}	2.00-2.02	2.00-2.02	1.99-2.01	2.06-2.08
Fe out-of-plane	0.04	0.04	0.09	0.13
O _a -O _b	1.24	1.24	1.23	1.23
O-(H _a ,H _b)	0.99-1.03	0.99-1.03	0.98-1.01	0.98-1.02
N _{ε,His} -H _b	1.91	1.94	1.93	1.91
O _a -H _a	1.99	2.10	2.23	2.18
O _b -H _{δ,Asn}	2.72	2.97	2.78	2.81

^a For atom names see Figures 9 and 12.

Table 4. Number of unpaired electrons on relevant fragments^a of the products of the catalytic reaction (Por-Fe^{III} + H₂O + O₂). The spin density distributions (Figure 13) were integrated using Bader's Atoms-In-Molecules theory (Bader, 1990).

number of unpaired electrons	quartet	doublet	sextet	octuplet
Fe	1.06 [↑]	1.00 [↓]	2.67 [↑]	4.09 [↑]
O	0.02 [↑]	0.01 [↑]	0.07 [↑]	0.08 [↑]
FeO	1.08 [↑]	0.99 [↓]	2.74 [↑]	4.17 [↑]
O _{Tyr}	0.02 [↑]	0.02 [↓]	0.14 [↑]	0.16 [↑]
O _a -O _b	1.89 [↑]	1.94 [↑]	1.95 [↑]	1.95 [↑]
N _{Por}	0.02 [↓]	0.03 [↑]	0.03 [↓]	0.46 [↑]

^a For atom names see Figures 9 and 12.

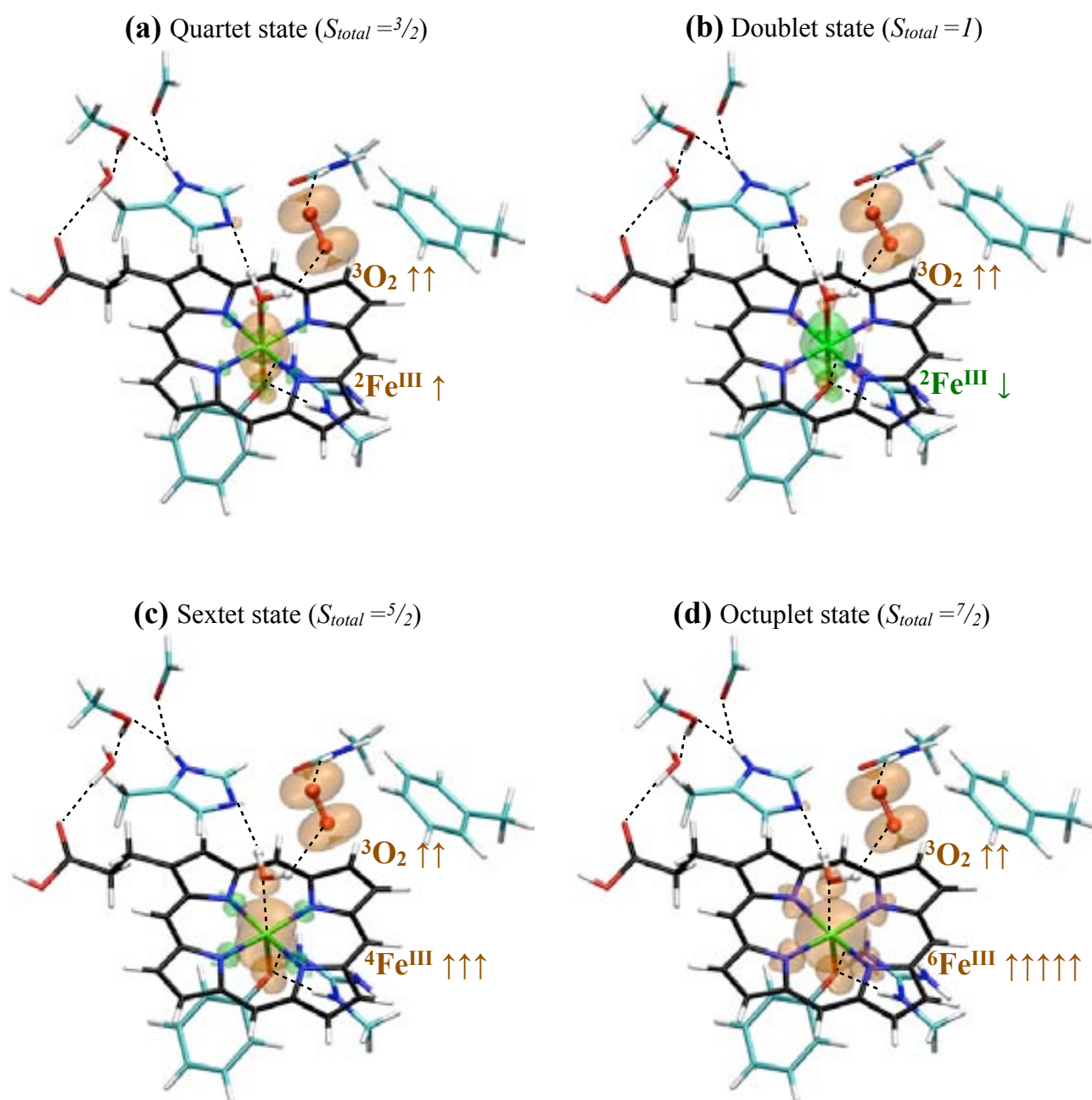


Figure 13. Optimized structure and spin density distribution of the products of the catalytic reaction (Por-Fe^{III} + H₂O + O₂). Spin isodensity surfaces at 0.004 e Å⁻³ are plotted in orange (spin-up) and green (spin-down). The atoms of H₂O₂ are represented in ball and stick.

Analysis of the spin density distributions (Figure 13 and Table 4) shows that *the oxygen molecule is in the triplet state (³O₂) in all cases*. The only difference among the different overall spin states is the local spin state of Fe^{III}: low-spin (²Fe^{III}) in the doublet and quartet states, intermediate-spin (⁴Fe^{III}) in the sextet state and high-spin (⁶Fe^{III}) in the octuplet state. It should be noted that in the sextet state the number of unpaired spins on Fe^{III} is somewhat less than 3 (Table 4), owing to charge transfer from the proximal Tyr. Likewise, in the octet state the number of unpaired

spins on Fe^{III} is slightly less than 5 (Table 4), owing to charge transfer from the proximal Tyr and the porphyrin nitrogen atoms.

The newly formed water molecule remains coordinated to the iron atom in the lower spin states (Fe-O = 2.05 Å, quartet, and 2.06 Å, doublet), whereas in the higher spin states they only interact weakly (Fe-O = 2.45 Å, sextet, and 2.33 Å, octuplet). Nevertheless, the Fe-O distance is even longer in the X-Ray structure of the native enzyme (Fe-O ~ 3 Å) (Murshudov, 2002). This discrepancy is probably due to the presence of the oxygen molecule in the distal pocket. In the products state the pocket water is hydrogen bonded to the distal His and the oxygen molecule (Figure 13). By contrast, in the crystal structure (Murshudov, 2002) it is hydrogen bonded not only to the distal His but also to the distal Asn. Most likely, the exit of O₂ results in more space in the pocket, and thus the water molecule can move further away from the iron and become hydrogen bonded to both distal residues.

Even though the spin state of the products is not known experimentally, we can assume it is the same as that of the resting state of the enzyme, i.e. a high spin iron (⁶Fe^{III}, see section 2.1.). However, our calculations show that the doublet and quartet states (²Fe^{III}) and the sextet state (⁴Fe^{III}) are very close in energy (all within 3 kcal/mol), with the octuplet (⁶Fe^{III}) lying higher in energy (9 kcal/mol above the quartet). The fact that the spin state of the products is not well reproduced in the calculations could be due to the well-known drawback of DFT in describing high spin states of the iron atom in porphyrin systems (Rovira, 1997; Ghosh, 2001). Alternatively, it could be that the spin state changes when O₂ is still in the active site. The exit of the oxygen molecule from the active site might allow the water molecule to break the bond with the iron, yielding a pentacoordinated Fe^{III}. The change in the coordination number of the iron will decrease the splitting of the d-orbitals of the iron, further stabilizing the higher spin states (see Appendix C, section 3.1.). Indeed, the optimized structures in the sextet and octuplet states exhibit the longest iron-water distance (2.45 and 2.33 Å).

4. SUMMARY AND CONCLUSIONS

In catalases, the reduction of the high redox intermediate Cpd I by hydrogen peroxide (i.e. the catalytic reaction) involves the transfer of two electrons and two protons from H₂O₂ to the oxoferryl porphyrin cation radical, restoring the heme resting state with the release of a water molecule and molecular oxygen (reaction **1**). The actual mechanism of this reaction is not known and two possible reaction schemes has been proposed (Fita & Rossmann, 1985; Kato, 2004; Watanabe, 2007), **(a)** H⁺ / H⁻ and **(b)** H[•] / H[•] mechanisms. On the basis of an analysis of the nature and the geometry of the active site, the H⁺ / H⁻ scheme (transfer of a proton to the distal His and a hydride to the ferryl oxygen) has been assumed as more favorable than the H[•] / H[•] scheme (double transfer of one hydrogen atom), because of the ability of the nearby His as a proton driver.

The electronic state of the oxygen released in the catalytic reaction has been related to the way in which the two electrons and the two protons are transferred. To conserve the initial singlet state of H₂O₂, the H⁺ / H⁻ transfer has been associated with the release of singlet oxygen (reaction **2**), which has indeed been detected (Khan, 1983; Kanofsky, 1984; Lledías, 1998; Michán, 2002). By contrast, using the same arguments, the H[•] / H[•] transfer would yield triplet oxygen (reaction **3**). This poses a biological question, because the most favourable H⁺ / H⁻ mechanism would generate large amounts of singlet oxygen that would inactivate the enzyme.

In this work we have qualitatively analyzed the electronic configuration of the oxygen released in catalases, taking into account the spin state of all active species (and not only H₂O₂). It is shown that, *in contrast to what has been often assumed, the H⁺ / H⁻ scheme does not necessarily generate singlet oxygen, but a priori it can generate both singlet and triplet oxygen.* Likewise, the assumption that the H[•] / H[•] scheme leads to triplet oxygen is not justified. Besides, *we have proposed a third possible mechanism for the catalytic reaction, (c) H[•] / H⁺ + ET*, which is also compatible with the conservation of the total spin. This stepwise scheme involves first proton and hydrogen atom transfer (reaction **1a**), then proton and electron transfer (possibly in a concerted fashion, reaction **1b**). *As for the two previously proposed mechanisms, the H[•] / H⁺ scheme can lead to either triplet or singlet oxygen as a reaction product.*

In order to complement this qualitative analysis of the spin states, we have performed DFT calculations on a reduced active site model for the reactants and products of the catalytic reaction. The reactants (i.e. Cpd I + H₂O₂) are found to spontaneously initiate the reaction: hydrogen

peroxide transfers one proton to the distal His and a hydrogen atom to Cpd I, yielding a Cpd II-like species and a superoxide anion radical. Afterwards, proton transfer from the distal His to the ferryl oxygen and electron transfer from superoxide to the iron render the products (i.e. Por-Fe^{III} + H₂O + O₂). Therefore, *our results predict the H[•] / H⁺+ET mechanism to be the route of the catalatic reaction*. Moreover, it is shown that *oxygen is released in a triplet state, irrespective of the global spin state of the products*. These results will be confirmed in Chapter VII by CP QM/MM metadynamics simulations.

In summary, the conclusions of this chapter are the following:

- The commonly assumed association of the H⁺ / H⁻ scheme with the generation of singlet oxygen is not justified.
- Taking into account the spin state of all the species involved in the catalatic reaction (and not only H₂O₂), any of the two previously proposed mechanisms (H⁺ / H⁻ or H[•] / H[•]) can generate both singlet and triplet oxygen.
- A H[•] / H⁺ + ET mechanism, leading to either triplet or singlet oxygen as a reaction product, is also compatible with the conservation of the total spin. Indeed, our calculations predict that this mechanism is the route of the catalatic reaction.
- The reduction of Cpd I by H₂O₂ is initiated by proton transfer to the distal His and hydrogen atom transfer to Cpd I, yielding a Cpd II-like species and superoxide (O₂⁻).
- Subsequent proton transfer from the distal His to the ferryl oxygen and electron transfer from superoxide to the iron, possibly in a concerted fashion, lead to the products.
- Regardless of the global spin state of the products, molecular oxygen is released in a triplet state.

CHAPTER VII

THE MOLECULAR MECHANISM OF THE CATALASE REACTION

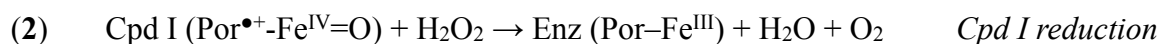
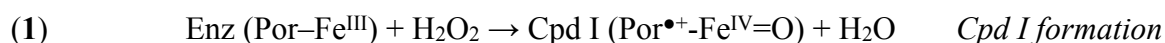
M. Alfonso-Prieto, X. Biarnés,
P. Vidossich and C. Rovira.

The molecular mechanism of the catalase reaction

J. Am. Chem. Soc. **2009**, 131 (33), pp 11751–11761

1. INTRODUCTION

The catalase reaction, the decomposition of hydrogen peroxide into water and oxygen, consists of two steps:



Several heme enzymes (e.g. catalases, peroxidases, catalase-peroxidases and myoglobin) are able to form Cpd I (reaction **1**), but only catalases can perform reaction **2** with high efficiency. Hence, the term “catalase reaction” or “catalatic reaction” is often used to refer to Cpd I reduction by H₂O₂.

Cpd I formation (reaction **1**) has been studied in the group for *Horse radish* peroxidase (Derat, 2007). As predicted by Poulos and Kraut (Poulos & Kraut, 1980), we found that the distal His acts as acid-base catalyst, and, in addition, we showed that a water molecule is essential for the reaction to proceed with a low barrier (Derat, 2007). It is expected that the same mechanism is operative in catalases, although without the participation of water, because the catalase active site is not solvent exposed (Jones & Dunford, 2005).

Cpd I reduction in catalase was first studied by Fita and Rossmann (Fita & Rossmann, 1985). On the basis of the crystal structure of native bovine catalase, they proposed that the two hydrogens of H₂O₂ are sequentially transferred to the oxoferryl unit of Cpd I, with the distal His playing an active role in the reaction. Nevertheless, the precise mechanism how the two protons and two electrons of H₂O₂ are transferred to Cpd I was not discussed. Recently, the group of Watanabe, by means of a detailed kinetic study, was able to disentangle the rate constants of Cpd I formation and reduction for *Micrococcus lysodeikticus* catalase (MLC) and a series of Mb mutants (Kato, 2004; Watanabe, 2007). Two different kinetic behaviors were observed in H₂O and D₂O for reaction **2**, which were interpreted as two different mechanisms. Namely, it was proposed that the reduction of Cpd I by H₂O₂ in native catalase, as well as in the F43H/H64L Mb mutant, involves the transfer of a hydride ion from H₂O₂ to Cpd I and the transfer of a proton mediated by the distal His (Figure 1a, hereafter named as the *His-mediated* mechanism). This mechanism thus follows the Fita-Rossmann model (Fita & Rossmann, 1985), with the distal His acting as an acid-base catalyst. Besides, for certain Mb mutants lacking a distal residue that could act as acid-base catalyst (H64X; X being Ala, Ser and Asp, and L29H/H64L), an alternative mechanism was proposed (Kato, 2004; Watanabe, 2005), in which two hydrogen atoms of H₂O₂ are directly transferred to the oxoferryl group (the *direct* mechanism, see Figure 1b).

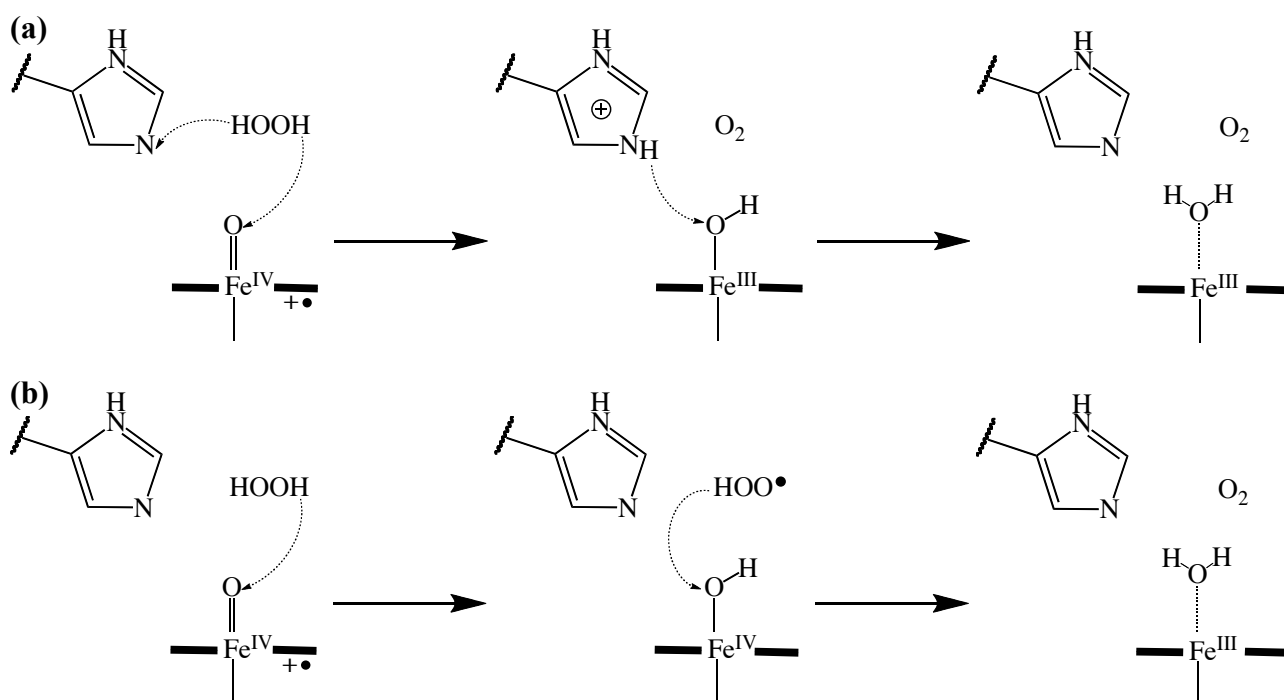


Figure 1. Proposed mechanisms of Cpd I reduction by H₂O₂ (reaction 2). **(a)** The His-mediated mechanism. **(b)** The direct mechanism

Cpd I reduction by H₂O₂ in catalase has been preliminary studied in Chapter VI to address the problem of the spin state of the released molecular oxygen. It was found that the reaction is compatible with the His-mediated (Fita-Rossmann) mechanism and that it involves the formation of a Cpd II-like intermediate (Por-Fe^{IV}-OH). Here we explicitly model the mechanism of Cpd I reduction by H₂O₂ (reaction 2) using CP QM/MM molecular dynamics, in combination with the metadynamics approach (see Chapter II) in order to reconstruct the free energy landscape of the reaction as a function of two reaction coordinates.

The calculations have been performed on the two catalases studied throughout this thesis: *Helicobacter pylori* catalase (HPC) and *Penicillium vitale* catalase (PVC), whose structure was shown in Chapter III, Figure 1. This allows to test the influence of the type of heme and the different protein environment on the molecular mechanism. Besides, we have investigated the role of the distal His in Cpd I reduction by using a catalase mutant lacking this histidine.

2. RESULTS AND DISCUSSION

2.1. Reactants (Cpd I : H₂O₂ complex)

As initial guess for the orientation of hydrogen peroxide in the active site of catalase Cpd I, we used the conformation proposed by Fita and Rossmann (Fita & Rossmann, 1985), in which hydrogen peroxide forms hydrogen bonds with the distal His and Asn residues, as well as with the oxoferryl unit. These initial structures of the HPC and PVC Cpd I : H₂O₂ complexes were optimized in the quartet state as described in Appendix D, section 1.

In the optimized geometries (Figure 2), the H₂O₂ molecule accommodates into the distal pocket maintaining the initial hydrogen bond pattern for both catalases. As can be seen in Table 1, the hydrogen bonds formed with the distal His ($H_b-N_{\epsilon,His} = 1.64 / 1.66 \text{ \AA}$, HPC and PVC, respectively) and the oxoferryl oxygen ($O-H_a = 1.56 / 1.72 \text{ \AA}$) are rather short, whereas the one formed with the NH₂ group of the distal Asn residue is presumably weaker ($O_b-H_{\delta,Asn} = 2.26 / 2.28 \text{ \AA}$).

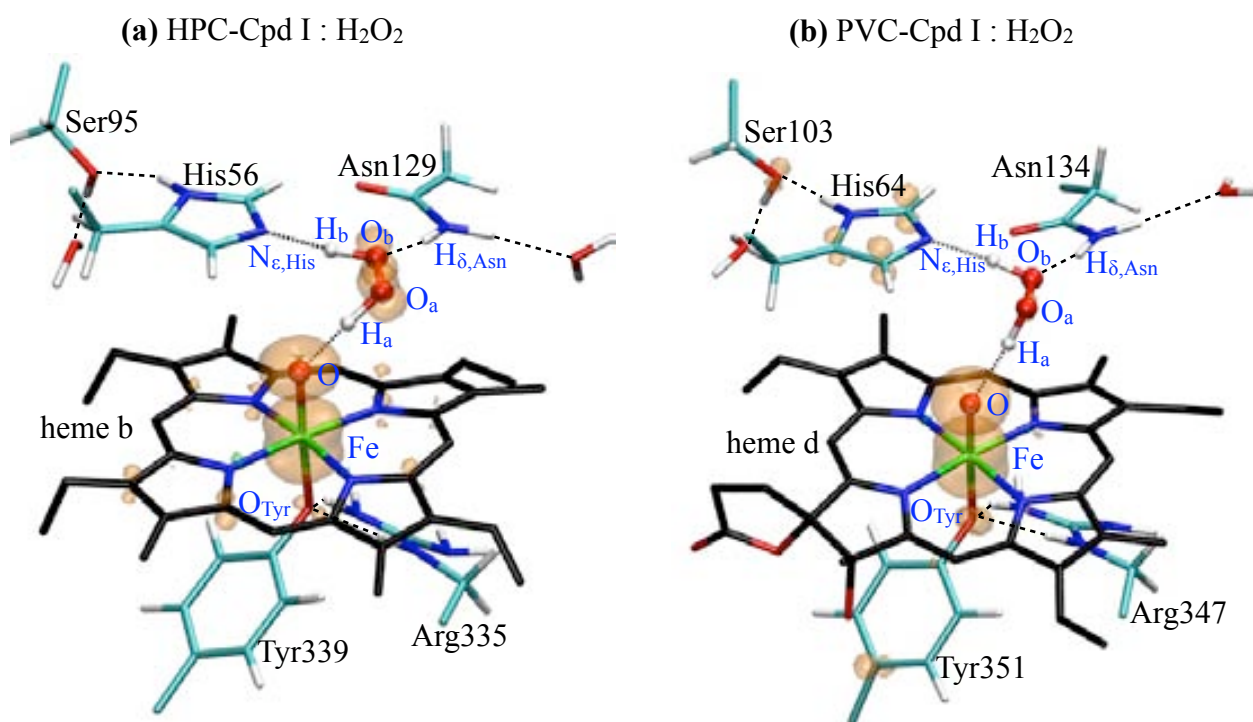


Figure 2. Optimized structures of the reactants (i.e. the Cpd I : H₂O₂ complex). Only the QM atoms are shown. Spin isodensity surfaces at 0.007 e \AA^{-3} are also plotted in orange.

Table 1. Main distances^a defining the optimized structure of the Cpd I : H₂O₂ complexes and the Cpd II-like intermediates^b of HPC and PVC.

distance (Å)	HPC		PVC	
	Cpd I : H ₂ O ₂	Cpd II-like ^b	Cpd I : H ₂ O ₂	Cpd II-like
Fe-O	1.70	1.76	1.69	1.76
Fe-O _{Tyr}	2.07	2.02	2.08	2.00
O-H _a	1.56	0.99	1.72	1.00
O _a -H _a	1.04	1.86	1.01	1.72
O _a -O _b	1.47	1.31	1.51	1.27
O _b -H _b	1.05	1.08	1.03	1.69
H _b -N _{ε,His}	1.64	1.51	1.66	1.05
O _b -H _{δ,Asn}	2.26	2.47	2.28	2.69

^a For atom names see Figures 2 and 3.

^b A representative snapshot of the CP QM/MM MD simulation (i.e. the Cpd II-like intermediate) was optimized using the same computational setup as for the reactants (see Appendix D, section 1).

To explore other possible orientations of the H₂O₂ molecule, 2 ps CP QM/MM molecular dynamics simulation were performed (see Appendix D, section 1). For both catalases, hydrogen peroxide was found to be not stable and spontaneously evolved to a Cpd II-like intermediate.

For HPC (Figure 3a), transfer of one hydrogen atom (H_a) from H₂O₂ to the oxoferryl unit was observed, resulting in a complex between a hydroxoferryl Cpd II-like species and a peroxy radical (HOO[•]). The peroxy radical is characterized by a reduction of the O_a-O_b distance (1.31 Å compared to 1.47 Å in the Cpd I : H₂O₂ complex, see Table 1), and a spin density distribution on the O_a-O_b moiety originating from one unpaired electron in a π orbital (see Figure 3a). HOO[•] is hydrogen bonded to the distal His (His-N_ε⋯H_b-O_bO_a = 1.51 Å) and to the hydroxoferryl unit (HOO_a⋯H_aO-Fe = 1.86 Å), keeping the weak hydrogen bond with the distal Asn (2.47 Å, Table 1). Upon transfer of H_a, the iron-oxygen distance increases from 1.70 Å to 1.76 Å (Table 1), as expected for a change from a double Fe=O to a single Fe-OH bond, and the unpaired spin density observed on the porphyrin in the reactants disappears, indicating that the porphyrin cation radical has been reduced. Thus, the spin density distribution of the heme (Figure 3a) resembles that of catalase Cpd II: a triplet state with two unpaired electrons on the hydroxoferryl unit.

For PVC (Figure 3b), the CP QM/MM MD simulation led to slightly different results. As in HPC, H_a is transferred, as a hydrogen atom, from hydrogen peroxide to the oxoferryl unit. However, the second hydrogen of H₂O₂ (H_b) was also transferred, as a proton, to the distal His. Therefore, the resulting state is a Cpd II-like species and a superoxide ion, with the distal His protonated (Cpd II···O₂⁻···HisH⁺, see Figure 3b). The superoxide is characterized by a reduction of the O_a-O_b distance (1.27 Å with respect to 1.51 Å in the Cpd I : H₂O₂ complex, see Table 1), and a spin density distribution (Figure 3b) originating from one unpaired electron in a π orbital of the O_a-O_b moiety. O₂⁻ is hydrogen bonded to the protonated distal His (His-N_e-H_b···O_bO_a = 1.69 Å) and to the hydroxoferryl unit (O_bO_a···H_aO-Fe = 1.72 Å), keeping the weak hydrogen bond with the distal Asn (2.69 Å, see Table 1). As for the heme, the hydroxoferryl group (Fe-OH) shows a longer iron-oxygen distance (1.76 Å) compared to the oxoferryl (Fe=O) Cpd I (1.69 Å, see Table 1), and a spin density distribution (Figure 3b) compatible to a Cpd II-like species.

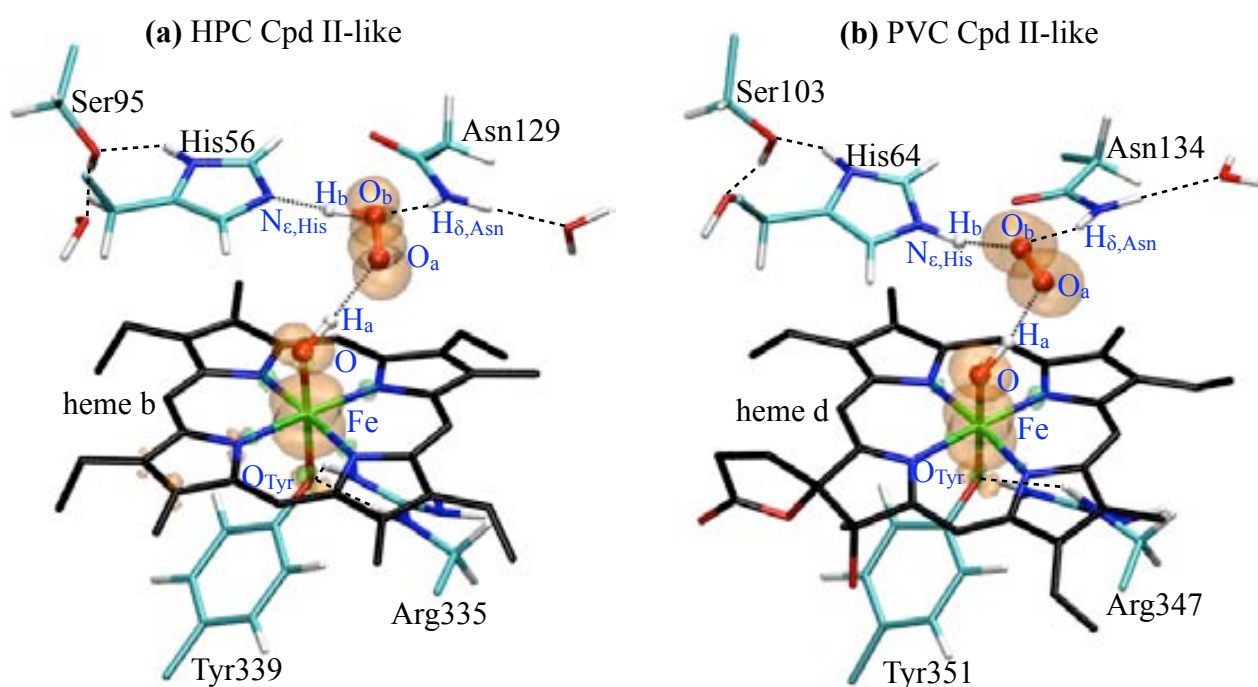


Figure 3. Representative snapshot of the molecular dynamics of the reactants at 300 K, showing the Cpd II-like intermediate formed. Only the QM atoms are displayed. Spin isodensity surfaces at $0.007 \text{ e } \text{Å}^{-3}$ are also plotted in orange.

In both cases (HPC and PVC) to reach the products state it is still necessary that the second hydrogen atom of hydrogen peroxide (H_b) "travels" to the hydroxoferryl oxygen.

2.2. Metadynamics simulations and reaction free energy landscapes

Starting from the Cpd II-like configurations of HPC and PVC (Figures 3a and 3b, respectively), which formed spontaneously during the initial room temperature equilibrium MD simulations, we performed metadynamics simulations to study the mechanism and energetics of the reaction. The simulations were performed in the quartet state, which is the ground state of the reactants. Analysis of the spin state energies along the reaction (see Appendix D, section 5) shows that this is a valid approximation. The computational details, as well as the evolution of the system during the metadynamics simulations are also described in Appendix D (sections 3 and 4, respectively). Here we recall the collective variables used and report the free energy landscapes that were reconstructed from the simulations.

The collective variables used in the metadynamics simulation were taken as a combination of coordination indices of the covalent bonds being formed / broken. Specifically, the first collective variable was taken as the coordination number between the two oxygen atoms of the H₂O₂ molecule and their two hydrogens, $CV_1 = N_{coord}(O_a, O_b; H_a, H_b)$ (i.e. A = O_a, O_b; B = H_a, H_b in Formula 1 of Appendix D). An interesting feature of CV₁ is that it does not dictate which hydrogen is bonded to which oxygen during the simulation (i.e. H_b-O_b, H_a-O_a, H_b-O_a or H_a-O_b), but each hydrogen is allowed to coordinate to any oxygen (i.e. the two hydrogen atoms and the two oxygen atoms of H₂O₂ are treated in an equivalent way). The second collective variable was taken as the coordination number between the oxoferryl oxygen and the two peroxide hydrogens $CV_2 = N_{coord}(O; H_a, H_b)$ (i.e. A = O; B = H_a, H_b in Formula 1). The values of these two collective variables in the different states along the reaction (Figure 4) are different enough to ensure that the two states will appear in different regions of the free energy surface, a necessary condition for a suitable characterization of the reaction path in a metadynamics simulation (Lai, 2005; Ensing, 2005 & 2006). It is important to note that this choice of the collective variables does not force nor restrict that any of the two peroxide hydrogens binds to the distal His during the reaction.

To better understand the free energy landscapes, let us note the physical meaning of the two collective variables (Figure 4). The first one [$CV_1 = N_{coord}(O_a, O_b; H_a, H_b)$] gives an idea of the degree of detachment of the two hydrogens (H_a, H_b) from the two oxygens (O_a, O_b) of hydrogen peroxide. At the beginning of the simulation (i.e. the Cpd II-like intermediate), in HPC (Figure 3a) only one hydrogen is coordinated to a peroxide oxygen (O_b-H_b), thus $CV_1 \approx 0.5$ (see Formula 1 in Appendix D; note that, because $N_A = 2$, a factor $\frac{1}{2}$ applies). By contrast, in PVC (Figure 3b) none

of the two hydrogen atoms of H_2O_2 is covalently bonded to the peroxide oxygens. Nevertheless, CV_1 is not zero, because they are hydrogen-bonded (i.e. $\text{HisN}_\epsilon\text{-H}_b\cdots\text{O}_b$ and $\text{FeO-H}_a\cdots\text{O}_a$). At the end of the simulation (i.e. native enzyme + H_2O + O_2), $\text{CV}_1 \approx 0$ in both catalases because none of the peroxide hydrogens is bonded to either O_a or O_b . The second collective variable [$\text{CV}_2 = N_{\text{coord}}(\text{O}; \text{H}_a, \text{H}_b)$] indicates the degree of formation of the product water molecule. At the beginning of the simulation (Figures 3a and 3b), one hydrogen atom is already coordinated to the ferryl oxygen (O-H_a) in both catalases, thus $\text{CV}_2 \approx 1.0$ (see Formula 1 in Appendix D; note that in this case $N_A = 1$, thus no prefactor applies in the formula). At the end of the simulation, the two peroxide hydrogens (H_a and H_b) are bonded to O , thus $\text{CV}_2 \approx 2$.

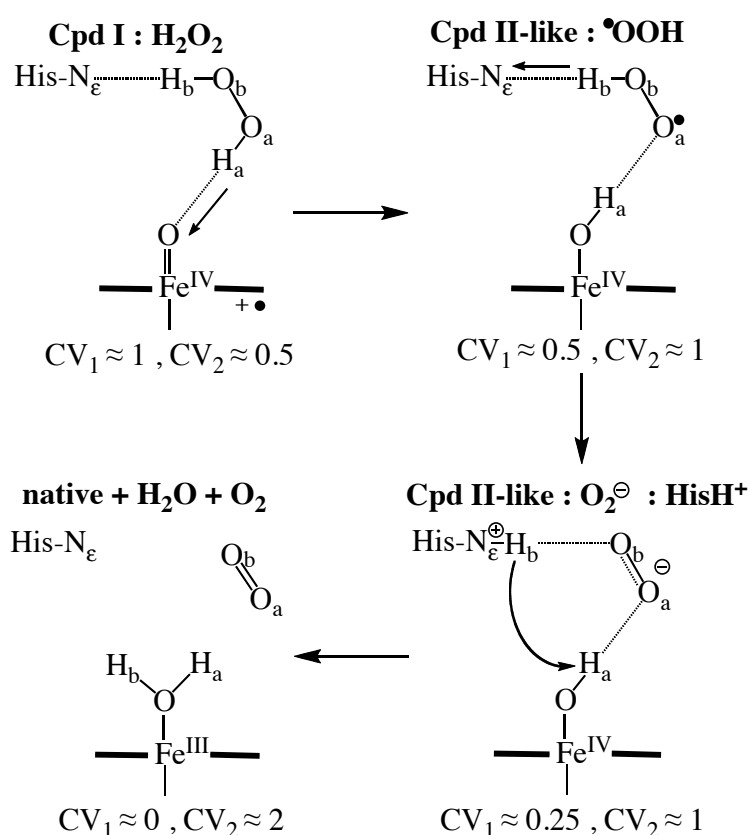


Figure 4. Evolution of the collective variables [$\text{CV}_1 = N_{\text{coord}}(\text{O}_a, \text{O}_b; \text{H}_a, \text{H}_b)$ and $\text{CV}_2 = N_{\text{coord}}(\text{O}; \text{H}_a, \text{H}_b)$] used in the metadynamics simulations of Cpd I reduction by H_2O_2 .

• HPC

The free energy surface (FES) reconstructed from the metadynamics simulation of HPC is shown as a contour plot in Figure 5. Two competing pathways joining the Cpd II-like : $\bullet\text{OOH}$ complex and products valleys appear clearly differentiated (pathways **A** and **B**). Each pathway contains several local minima of different well depth, separated by transition states.

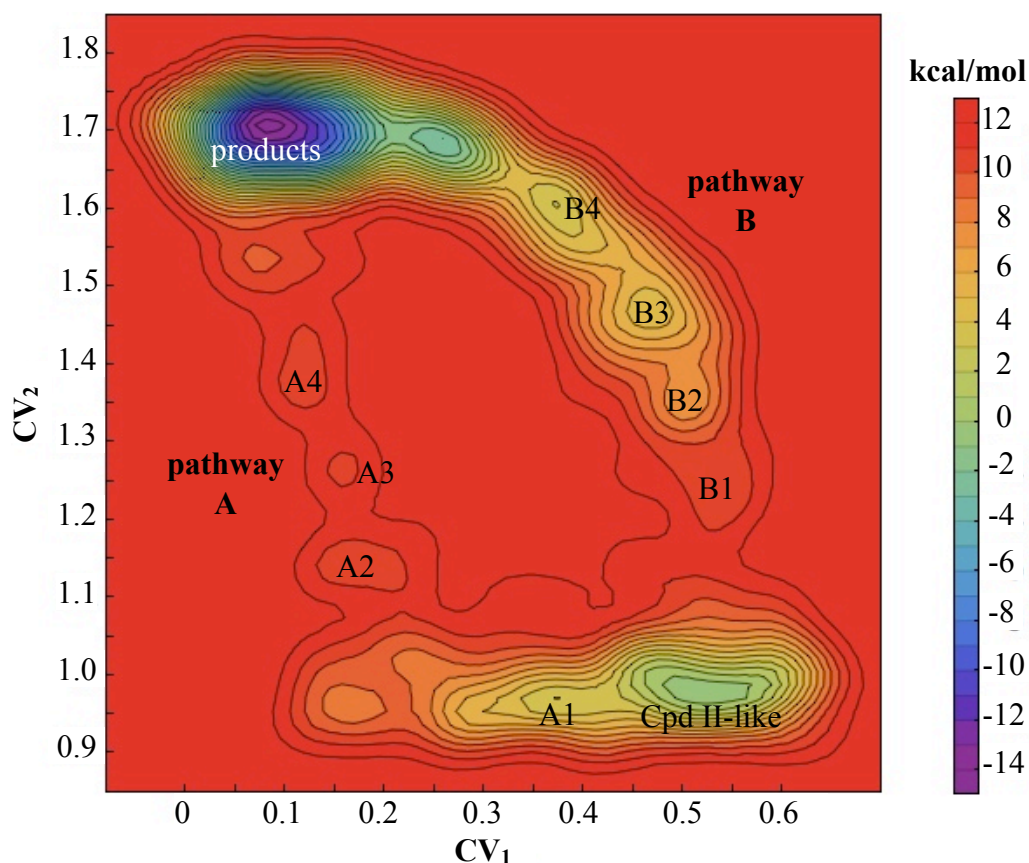


Figure 5. Free energy landscape reconstructed from the metadynamics simulation of HPC. Contour lines are plotted at 1 kcal/mol.

Pathway A

The atomic and spin reorganization along pathway **A** in HPC is shown in Figure 6. Starting from the {Cpd II-like : $\cdot\text{OOH}$, HisH⁺} configuration, proton transfer (PT) from the peroxy radical to the distal His yields the {Cpd II-like : O₂⁻, HisH⁺} configuration (basin A1 in Figures 5 and 6). Afterwards, the distal His rotates such that it breaks the hydrogen bond with the superoxide anion (A2, Figures 5 and 6). At the same time, the hydroxoferryl group rotates around the Fe-O bond, breaking the hydrogen bond with O₂⁻, and positioning one oxygen lone pair in a suitable orientation to interact with the histidine proton (A3, Figures 5 and 6). A4 differs from A3 in the degree of rotation of the distal His around the C_β-C_γ bond and the absence of hydrogen bond between the hydroxoferryl hydrogen and superoxide. In the products state (Figures 5 and 6), because H_b has been transferred to the hydroxoferryl oxygen, the Fe-O distance has increased (from 1.83 ± 0.06 Å in A4 to 2.08 ± 0.07 Å in the products, see Table 2) and a water molecule has been formed. The decrease of the O_a-O_b distance (from 1.33 ± 0.02 Å in A1 to 1.25 ± 0.02 Å in the products), together with the change of the spin density distribution (Figure 6 and Table 2), signals the change from O₂⁻

to O₂. Interestingly, the distal Asn changes conformation gradually (from the Cpd II-like configuration to the products), facilitating the release of the product oxygen towards the main channel.

Therefore, from an electronic point of view, *pathway A consists of proton transfer from HOO• to His, electron transfer from O₂⁻ to reduce Fe(IV) to Fe(III) and proton transfer from the distal HisH⁺ to Fe–OH.*

As can be seen in Figure 5, proton transfer to the distal His (Cpd II-like → A1) has a small barrier of 4 kcal/mol. Structures A2, A3 and A4 are at similar energies, 8 kcal/mol over A1. Thus, the transition state along this pathway corresponds to all the process through A2, A3 and A4, i.e. rupture of the hydrogen bond between the superoxide and the distal HisH⁺, rotation of the latter to form a hydrogen bond with the hydroxoferryl, and transfer of H_b towards it. The highest states along this sequence of events are 9 kcal/mol over A1 and 12 kcal/mol over the initial Cpd II-like.

Table 2. Distances^a and number of unpaired electrons^b of relevant fragments for stationary points along pathway A of HPC.

structure	distance (Å)		number of unpaired electrons			
	O–H _b	O _a –O _b	Fe=O	O _a –O _b	Porph	Tyr
Cpd I : H₂O₂	(3.19)	(1.47)	2.15	0.23	0.52	0.06
Cpd II-like	(3.68) 3.45 ± 0.23	(1.34) 1.35 ± 0.03	(1.87)	(0.99)	(0.10)	(0.02)
A1	3.51 ± 0.13	1.33 ± 0.02	1.83	1.05	0.03	0.07
A2	2.41 ± 0.10	1.29 ± 0.02	1.65	1.45	0.01	0.07
A3	2.01 ± 0.06	1.28 ± 0.01	1.56	1.54	0.02	0.06
A4	1.73 ± 0.02	1.27 ± 0.02	1.52	1.65	0.01	0.10
Products	(1.02) 1.01 ± 0.04	(1.25) 1.26 ± 0.02	1.12	1.77	0.02	0.06

^a Distances are given as averages along the metadynamics simulation, except for values in parentheses, that refer to optimized structures. The Cpd I : H₂O₂ complex, the Cpd II-like species and the products were optimized using the computational setup described in Appendix D, section 1. Geometry optimization of the A1-A4 configurations was not attempted since their basins are very shallow.

^b The number of unpaired electrons was obtained by integration of the spin density of either representative snapshots along the path or optimized structures (values in parentheses) using Bader's Atoms-In-Molecules theory (Bader, 1990).

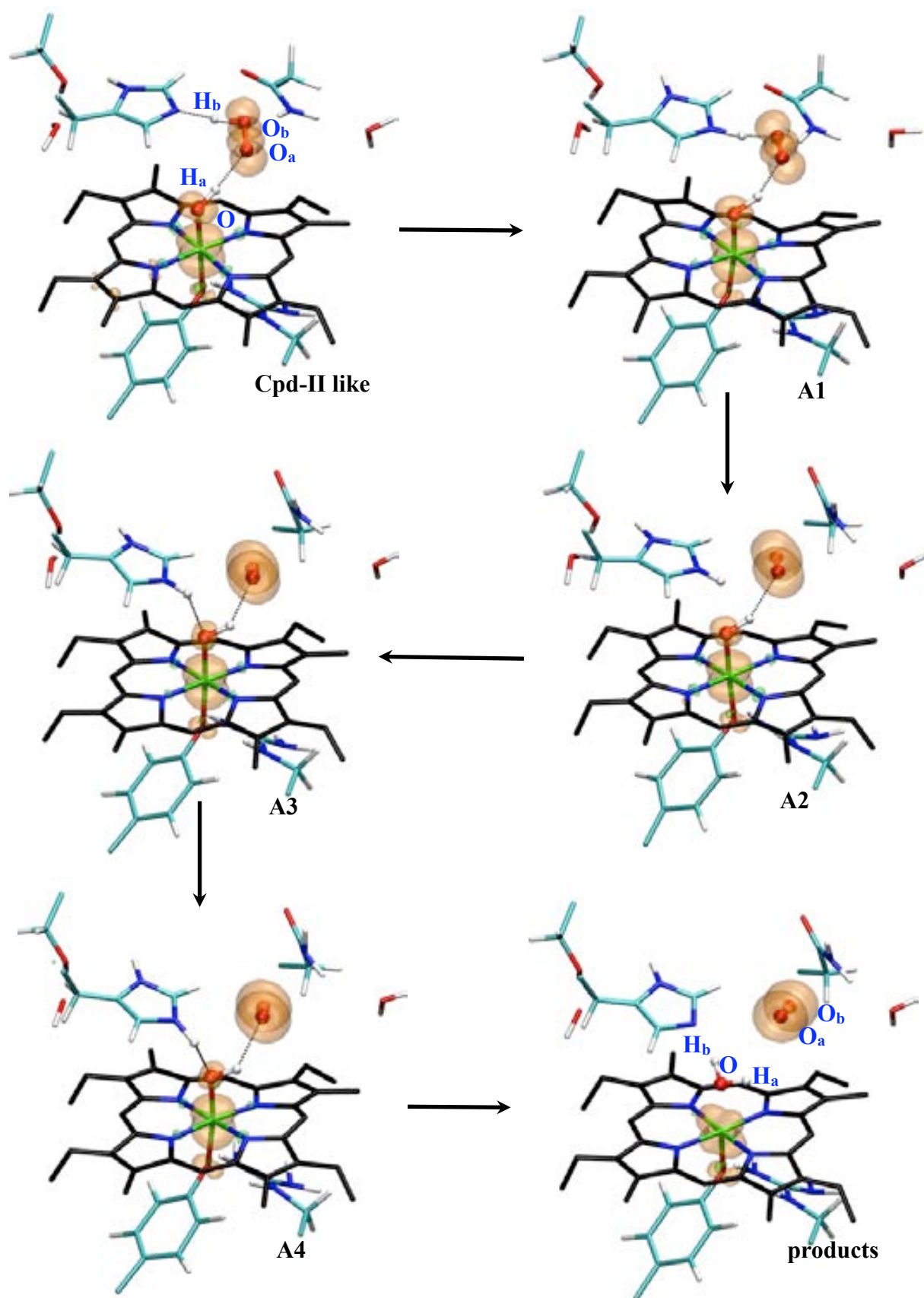


Figure 6. Atomic rearrangement along reaction pathway A in HPC. Only the QM atoms are displayed. Spin isodensity surfaces at $0.007 e \text{ \AA}^{-3}$ are plotted in orange.

Pathway B

Representative structures corresponding to pathway **B** in HPC are shown in Figure 7. Along this path, the hydroxoferryl unit first rotates around the Fe-O bond, breaking the hydrogen bond with O_a (B1). Afterwards, the peroxy radical flips orientation, with H_b changing hydrogen bond partner from the distal His to the hydroxoferryl oxygen (B2). The distal His, not involved in any hydrogen bond interaction, moves upwards (B1 → B2) to facilitate the rotation of the peroxy radical. Structures B2, B3 and B4 mainly differ for the O \cdots H_b distance (see Table 3) and the degree of rotation of the hydroxoferryl unit (Figure 7). Finally, transfer of H_b to the hydroxoferryl oxygen leads to the product water and oxygen molecules. The change in the O_a-O_b distance (Table 3) from B4 (1.33 ± 0.03 Å) to the products (1.25 ± 0.02 Å), together with the changes in spin density distribution (Table 3 and Figure 7), evidences that H_b transfers as a hydrogen atom. Once the oxygen molecule forms, the distal Asn rotates to facilitate its escape towards the main channel, as it was also observed for pathway **A**. This illustrates the interplay of the His and Asn active site residues in the catalytic mechanism and underlines the importance of taking into account their dynamics on the modeling of the reaction.

Therefore, from an electronic point of view, *pathway B consists in a hydrogen atom transfer from the peroxy radical to the hydroxoferryl unit.*

As can be seen in Figure 5, the highest barrier that the system needs to overcome along pathway **B** is in going from the Cpd II-like intermediate to the B1 basin (12 kcal/mol)¹, corresponding to the rupture of the hydrogen bond between the hydroferryl and the peroxide radical. From B1 onward, the energetic profile is downhill, with each intermediate lower in energy than the preceding one.

¹ The influence of the exchange-correlation functional in this barrier is investigated in Appendix D, section 7.

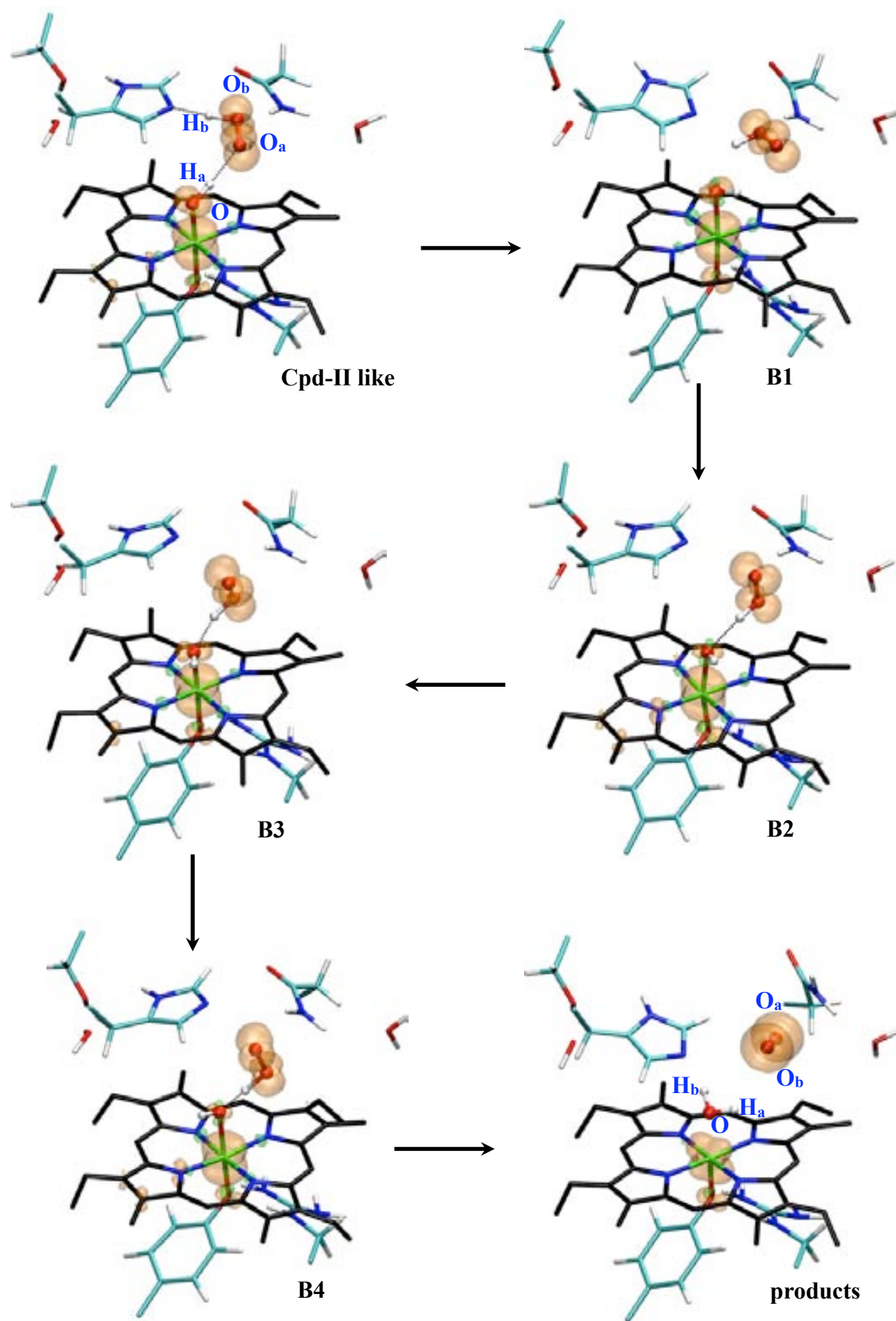


Figure 7. Atomic rearrangement along reaction pathway **B** in HPC. Only the QM atoms are displayed. Spin isodensity surfaces at $0.007 \text{ e } \text{\AA}^{-3}$ are plotted in orange.

Table 3. Distances^a and number of unpaired electrons^b of relevant fragments for stationary points along pathway **B** of HPC.

structure	distance (Å)		number of unpaired electrons			
	O-H _b	O _a -O _b	Fe=O	O _a -O _b	Porph	Tyr
Cpd I : H₂O₂	(3.19)	(1.47)	(2.15)	(0.23)	(0.52)	(0.06)
Cpd II-like	(3.68) 3.45 ± 0.23	(1.34) 1.35 ± 0.03	(1.87)	(0.99)	(0.10)	(0.02)
B1	2.08 ± 0.08	1.34 ± 0.02	1.83	0.98	0.08	0.09
B2	1.79 ± 0.04	1.32 ± 0.00	1.72	1.00	0.22	0.03
B3	1.53 ± 0.05	1.33 ± 0.03	1.79	1.01	0.12	0.04
B4	1.29 ± 0.05	1.33 ± 0.03	1.66	1.07	0.22	0.01
Products	(1.02) 1.01 ± 0.04	(1.25) 1.26 ± 0.02	(1.12)	(1.77)	(0.02)	(0.06)

^a Distances are given as averages along the metadynamics simulation, except for values in parentheses, that refer to optimized structures. The Cpd I : H₂O₂ complex, the Cpd II-like species and the products were optimized using the computational setup described in Appendix D, section 1. Geometry optimization of the B1-B4 configurations was not attempted since their basins are very shallow.

^b The number of unpaired electrons was obtained by integration of the spin density of either representative snapshots along the path or optimized structures (values in parentheses) using Bader's Atoms-In-Molecules theory (Bader, 1990).

• PVC

The reconstructed FES obtained from the metadynamics simulation of PVC is shown in Figure 8. Here, a unique pathway joining the {Cpd II-like : O₂⁻, HisH⁺} configuration with the products valleys is found (hereafter **A**).

Representative structures along this pathway are shown in Figure 9. Consistent with the finding that the PVC-Cpd I : H₂O₂ complex evolved spontaneously towards the {Cpd II-like : O₂⁻, HisH⁺} configuration during the room temperature CP QM/MM MD simulation (Figure 3b), the FES shows only one minimum corresponding to this state ($CV_1 \approx 0.22$, Figure 8) and there is no minimum corresponding to {Cpd II-like : •OOH, His} ($CV_1 \approx 0.5$). From the {Cpd II-like : O₂⁻, HisH⁺} complex, the single pathway in PVC involves the same intermediates as pathway **A** in HPC. First, the distal His rotates around the C_β-C_γ bond (A2, Figure 9), then the hydroxoferryl group also rotates around the Fe-O bond (A3 and A4, Figure 9), and finally proton transfer from the distal His to the hydroxoferryl oxygen forms the products (Figure 9). The change in the O_a-O_b distance (Table

4) from the Cpd II-like ($1.29 \pm 0.01 \text{ \AA}$) to the products ($1.24 \pm 0.01 \text{ \AA}$), together with the changes in spin density distribution (Table 4 and Figure 9), signals the change from O_2^- to O_2 . Therefore, electronically, *pathway A* consists of an electron transfer from O_2^- to reduce Fe(IV) to Fe(III) , followed by a proton transfer from the distal His to Fe-OH , similar to HPC.

The energy barrier along pathway **A** is similar to the one found in HPC for the corresponding steps (8 kcal/mol), with the highest energy state found in going from A2 to A3. However, considering that, in HPC, H_b has first to be transferred to the distal His requiring 4 kcal/mol, path **A** results 4 kcal/mol lower in free energy in PVC than in HPC. The fact that pathway **B** is not sampled in the metadynamics simulation of PVC could be due to the fact that it is higher in energy compared with pathway **A**. However, the absence of the minimum corresponding to the {Cpd II-like : $\cdot\text{OOH}$, His} configuration (as shown in Figure 3b the $\cdot\text{OOH}$ is not stable in PVC) is probably the reason of the disappearance of pathway **B** in PVC.

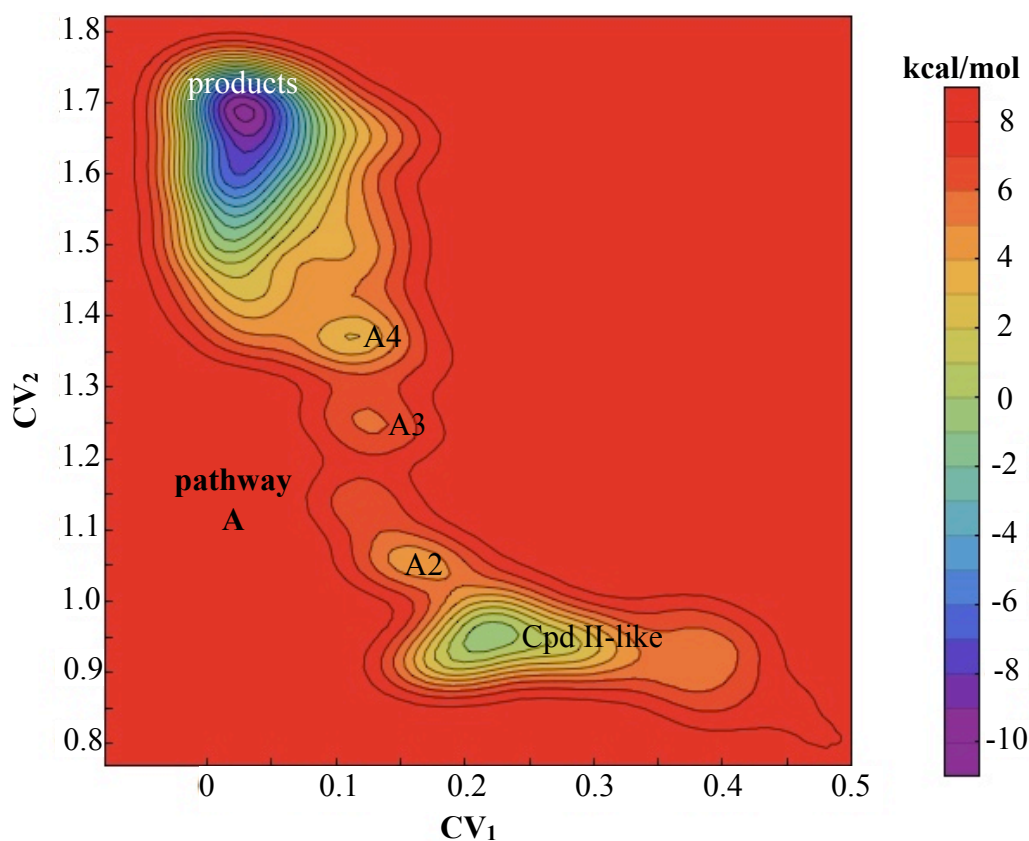


Figure 8. Free energy landscape reconstructed from the metadynamics simulation of PVC. Contour lines are plotted at 1 kcal/mol.

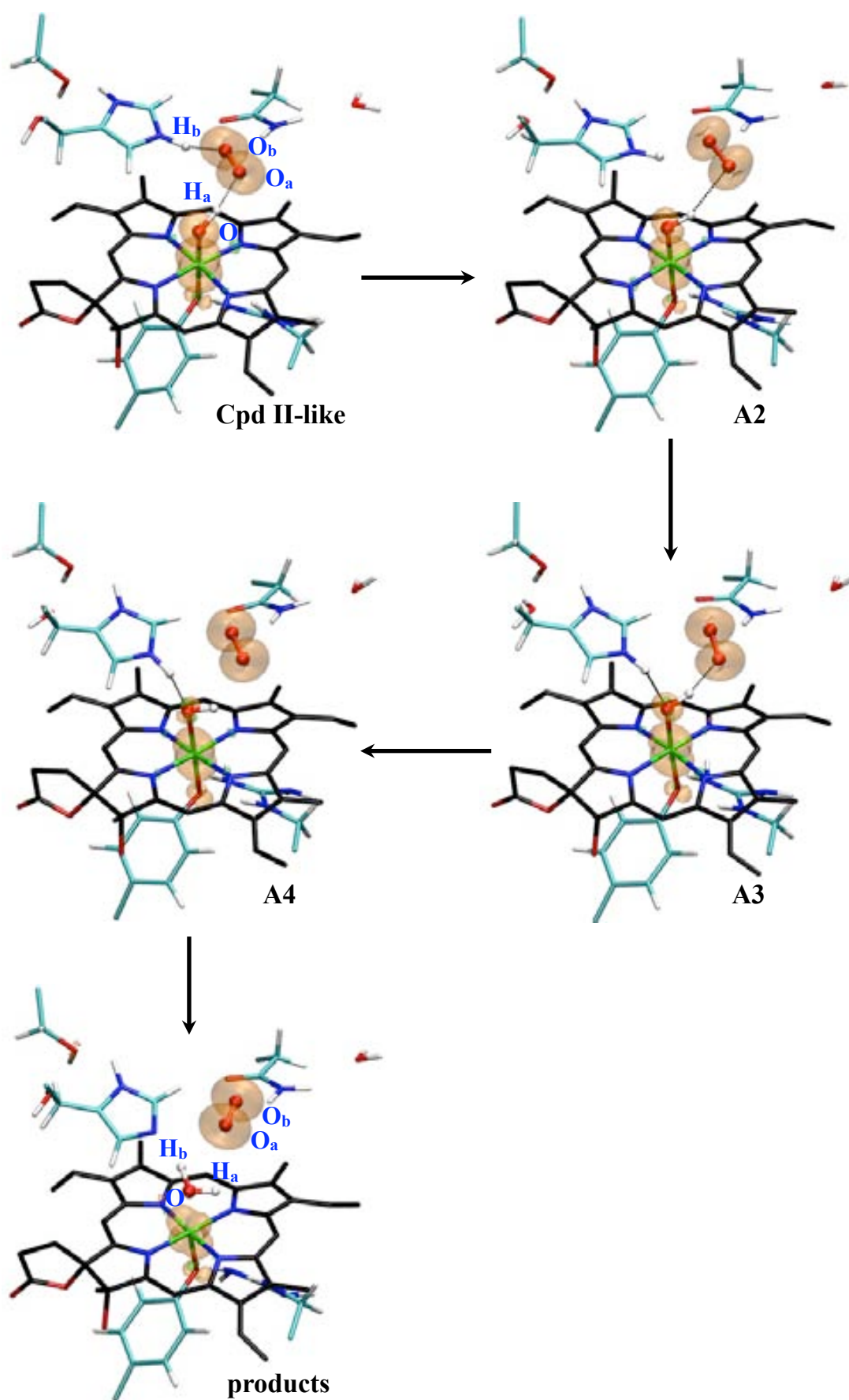


Figure 9. Atomic rearrangement along reaction pathway A in PVC. Only the QM atoms are displayed. Spin isodensity surfaces at $0.007 e \text{ \AA}^{-3}$ are plotted in orange.

Table 4. Distances^a and number of unpaired electrons^b of relevant fragments for stationary points along pathway **A** of PVC. Spin-up electrons are indicated by [↑] and spin-down electrons by [↓].

structure	distance (Å)		number of unpaired electrons			
	O-H _b	O _a -O _b	Fe=O	O _a -O _b	Porph	Tyr
Cpd I : H₂O₂	(3.63)	(1.51)	(2.28) [↑]	(0.04) [↑]	(0.13 + 0.21) [↑] ^c	(0.18) [↑]
Cpd II-like	3.85 ± 0.21	1.29 ± 0.01	1.68 [↑]	1.32 [↑]	0.06 [↑]	0.04 [↑]
A2	2.93 ± 0.05	1.28 ± 0.02	1.45 [↑]	1.56 [↑]	0.06 [↓]	0.02 [↑]
A3	2.02 ± 0.04	1.26 ± 0.01	1.37 [↑]	1.62 [↑]	0.07 [↓]	0.05 [↑]
A4	1.74 ± 0.03	1.26 ± 0.02	1.25 [↑]	1.70 [↑]	0.05 [↓]	0.08 [↑]
Products	1.13 ± 0.05	1.24 ± 0.01	1.03 [↑]	1.91 [↑]	0.01 [↓]	0.02 [↑]

^a Distances are given as averages along the metadynamics simulation, except for values in parentheses that refer to the optimized structure of the PVC-Cpd I : H₂O₂ complex.

^b The number of unpaired electrons was obtained by integration of the spin density of either representative snapshots along the path or optimized structures (values in parentheses) using Bader's Atoms-In-Molecules theory (Bader, 1990).

^c The radical is shared between the porphyrin (0.13 e⁻) and the distal His (0.21 e⁻) (Figure 2b).

2.3. Spin state analysis

As described previously, the metadynamics simulations were constrained to the quartet spin state, which is the ground state of both Cpd I (de Visser, 2006) and the Cpd I : H₂O₂ complex (see Appendix D, Table 1). To investigate the validity of this single surface approximation, we optimized the structure of the main reaction intermediates of HPC (the Cpd I : H₂O₂ complex, the Cpd II-like configuration and the products) in different spin states (doublet, quartet, sextet and octuplet). For the shallow minima along the **A** and **B** reaction pathways (A1-A4 and B1-B4), no geometry optimization was attempted, and only vertical energy gaps among spin states were computed. The results of these calculations are given in Appendix D, section 5.

The quartet was found to be the ground state of all the reaction intermediates (Appendix D, Table 1), indicating that the quartet free energy surface is representative of the process investigated. Nevertheless, the ground state of the products was found to be the sextet state ($S_{tot}=5/2$), and therefore spin crossing from quartet to sextet probably affects only the final step of the reaction (A4 → products and B4 → products).

2.4. Mechanism of Cpd I reduction by H₂O₂

• Comparison HPC-PVC

Our calculations show that the Cpd I : H₂O₂ complex, both in HPC and PVC, evolves spontaneously at room temperature to a Cpd II-like species (Figure 3), in which formally a hydrogen atom transfer has occurred (i.e. proton transfer to the ferryl oxygen and electron transfer to the porphyrin). HPC and PVC differ in that in PVC the second proton of hydrogen peroxide is transferred too (to the distal His, forming HisH⁺···O₂⁻, Figure 3b), whereas it is not in HPC (His···HOO•, Figure 3a). This difference may be understood considering that the intrinsic pK_a of a histidine (6.5, but proposed to be 5.0 in peroxidase Cpd I (Jones & Dunford, 2006)) and that of HO₂• (4.8 (Hoare, 1985)) are similar, and thus slight changes may stabilize any of the two states (O₂⁻···HisH⁺ or •OOH···His). HPC and PVC differ in the nature of the prosthetic group and in the protein sequence (see Chapter IV, Figure 1). HPC contains heme b, whereas PVC has heme d, in which one of the propionates has formed a lactone with the porphyrin ring, resulting in a reduced overall charge (carboxylate to ester) of the active site and a 2-electron less porphyrin π system (one of the porphyrin double bonds is missing with respect to heme b). It could be argued that the different charge distribution between the two types of heme favours one state over the other (O₂⁻···HisH⁺ or •OOH···His). However, the gas phase calculations on the heme b-Cpd I···H₂O₂ complex in Chapter VI also converged to the O₂⁻···HisH⁺ configuration. This excludes the type of heme as the responsible for the different Cpd II-like species formed in HPC and PVC, and points to the protein environment as a determinant factor. HPC and PVC belong to different clades of the catalase family and only share 47 % / 64 % sequence identity / similarity (70% / 77 % considering residues within 10 Å from the Fe atom)². Attempts to calculate the pK_a of the distal His in Cpd I and II for the two proteins by solution of the Poisson-Boltzmann equation (data not shown) did not reproduce the above findings, possibly due to the limitations of the method used. Thus, we conclude that the protein frame is responsible for the stabilization of either O₂⁻···HisH⁺ or •OOH···His forms, although we could not identify the residues responsible of such effect.

Starting from the Cpd II-like intermediate, metadynamics simulations were used to investigate how the reaction proceeds to the products. Two general collective variables (or reaction coordinates, see Figure 4) that characterize the nuclear reorganization along the reaction, without any preconceived assumption on the involvement of active site residue, were used to drive the

² Analysis excluding the variable N-terminal end and the flavodoxin-like C-terminal domain, following reference (Díaz, 2009).

reaction and reconstruct the free energy surface (FES). We found that HPC and PVC display a similar reaction pathway (A^{HPC} in Figure 6 and A^{PVC} in Figure 9), in which the distal His acts as an acid-base catalyst. The free energy along this pathway **A** shows a different profile in the two proteins (Figure 5 and Figure 8), because, as explained above, the initial states are different ($\text{O}_2^- \cdots \text{HisH}^+$ in PVC, or $^{\bullet}\text{OOH} \cdots \text{His}$ in HPC), and thus in HPC it is required that the proton is firstly transferred to the His, with a barrier of 4 kcal/mol. Once the $\text{O}_2^- \cdots \text{HisH}^+$ state is reached, the highest energy barriers are similar in the two proteins (9 kcal/mol in HPC and 8 kcal/mol in PVC, see Figure 10) and correspond to the conformational change of the HisH^+ leading to the formation of a hydrogen bond with the hydroxoferryl. Subsequently, the HisH^+ proton and one electron from O_2^- transfer to the hydroxoferryl unit, yielding the products.

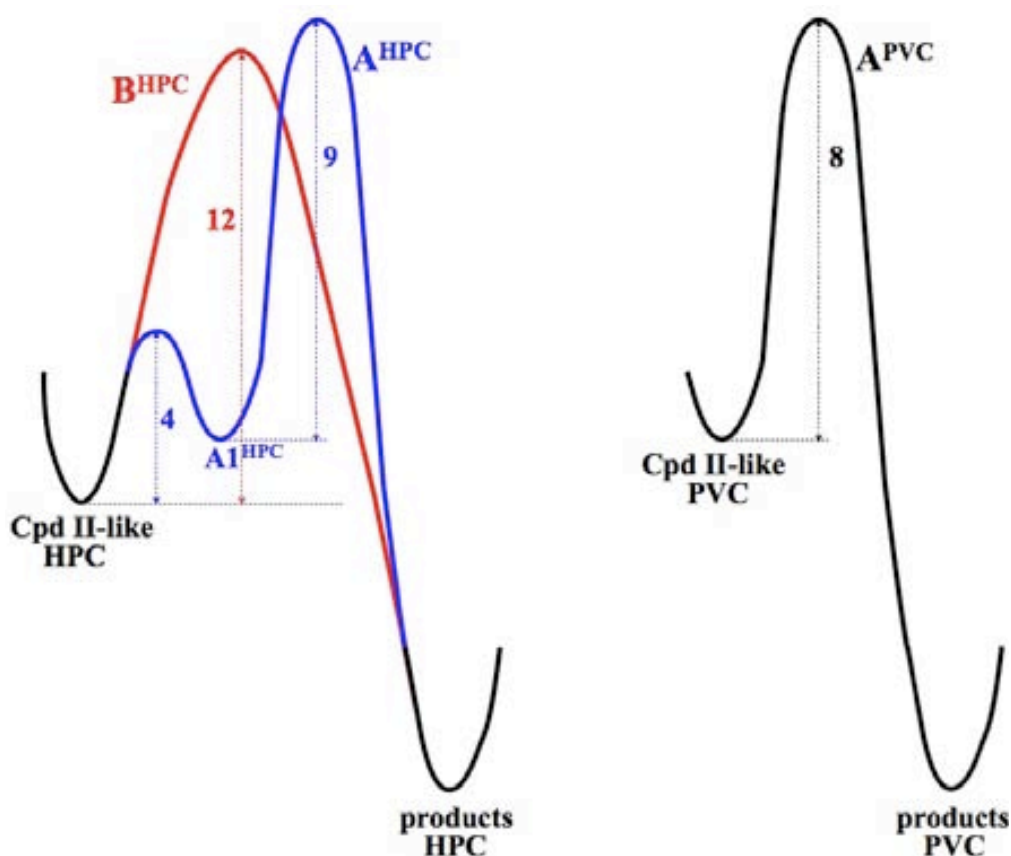


Figure 10. Comparison of the pathways found from the Cpd II-like intermediate to the products in HPC and PVC. Note that the configuration of both $A1^{\text{HPC}}$ and $\text{Cpd II-like}^{\text{PVC}}$ is $\{\text{Por-Fe}^{\text{IV}}\text{-OH} : \text{O}_2^-, \text{HisH}^+\}$.

In HPC a further pathway was observed (B^{HPC} , Figures 5 and 7), not involving residues of the active site. Mechanism **B** consists in the flip of the peroxy radical, with a barrier of 12 kcal/mol

(Figure 5), and the subsequent transfer of a hydrogen atom (H^\bullet , Figure 7 and Table 3). Because the two pathways found in HPC (A^{HPC} and B^{HPC}) have similar barriers (13 and 12 kcal/mol, respectively, see Figure 10), they are competitive.

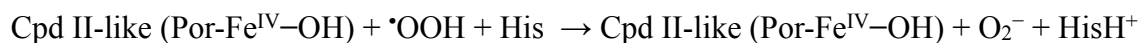
Another interesting feature of the mechanism is the rotation of the distal Asn side chain towards the main channel (Figure 6), facilitating the escape of the oxygen molecule released in the reaction and supporting the previously proposed role of this residue in ligand entry/escape (Rovira, 2005 & 2006). This could explain why the protein is engineered such that there is no hydrogen-bonding interaction towards the carbonyl oxygen atom of the distal Asn. Such interactions would restrain its conformational flexibility and Asn would not be efficient for catalysis.

- *Comparison to previously proposed mechanisms*

We have found that Cpd I reduction by H_2O_2 in catalases starts with a hydrogen atom transfer to form of a Cpd II-like species:



Afterwards, two different routes are possible. In pathway **A**, the distal His mediates a proton transfer to the hydroxoferryl, coupled to an electron transfer:



Alternatively, in pathway **B**, the peroxy radical reorients in the distal pocket and transfers a second hydrogen atom:



Overall, *the catalytic reaction may take place by two different mechanisms, either a hydrogen atom transfer plus a (concerted but nonsynchronous) electron and proton transfer ($H^\bullet / ET+H^+$), or a double hydrogen atom transfer (H^\bullet/H^\bullet).*

The $H^\bullet / ET + H^+$ mechanism (pathway A) is similar to the His-mediated (Fita-Rossmann) mechanism (Figure 1a), in which the distal His acts as an acid-base catalyst delivering a proton to the ferryl oxygen (Fita & Rossmann, 1985). It has been commonly assumed (Jones & Perkins, 1967; Jones & Suggett, 1968; Dounce, 1983; Kato, 2004; Watanabe, 2007) that the remaining proton plus 2 electrons of hydrogen peroxide are transferred directly to the oxoferryl heme as a hydride ion. By contrast, we have found that the two electrons are transferred separately, one as a hydrogen atom and the other one coupled to the His-mediated proton transfer. This is in line with

recent studies on heme enzymes showing that high valent Fe=O species easily abstract hydrogen atoms or give proton coupled electron transfer (PCET) (Derat, 2006c; Shaik, 2008; Jeong, 2008; Wang, 2009). Thus, it should not be regarded as surprising that catalase Cpd I undertakes similar elementary steps.

The H^\bullet / H^\bullet mechanism (pathway B) is essentially the direct mechanism (Figure 1b), proposed by Kato et al. for certain myoglobin mutants (Kato, 2004; Watanabe, 2007). Because it does not involve the distal His, it is tempting to suggest that this mechanism is operative when this histidine cannot act as acid-base catalyst, e.g. at low pH conditions or in His mutants.

2.5. Influence of the distal His in Cpd I reduction

Pathways A^{HPC} and A^{PVC} (Figures 6 and 9) point to the role of the distal histidine as an acid-base catalyst, facilitating the transfer of a proton to the hydroxoferryl moiety. Site directed mutation of the distal His in catalases suppresses the ability to form Cpd I, thus making the experimental proof of the involvement of His also in Cpd I reduction impossible. On the contrary, the role of His can be easily proved by molecular modeling. With this aim, we performed a CP QM/MM simulation of the HPC-Cpd I : H₂O₂ complex in the absence of the distal His side chain. This was accomplished by including His56 in the MM region and zeroing the charges and van der Waals parameters of its side chain (i.e. we generated an *in silico* His56Gly mutant).

Starting from the same initial structure of the HPC-Cpd I : H₂O₂ complex as for the wild type enzyme (Figure 2a), CP QM/MM MD simulations of the His56Gly mutant show that the transfer of one hydrogen atom from H₂O₂ to the Fe=O unit is not spontaneous, different from wild-type HPC. Therefore, we studied the formation of the Cpd II-like species by computing the potential energy profile along the O_a···H_a coordinate (Figure 11). It turned out that the first part of reaction 2, from the Cpd I : H₂O₂ complex to the Cpd II-like species, has a barrier of 8 kcal/mol in the His56Gly mutant, compared to the barrierless process found in wild-type HPC. Results from gas phase calculations on model systems (Appendix D, section 6) show that the barrier for the hydrogen atom transfer increases with increasing donor - acceptor distance. Therefore, the energy barrier for the transfer of H_a increases in the His56Gly mutant because the O-O_a distance (2.68 Å) is longer than in the wild-type HPC (2.60 Å), due to the loss of the hydrogen bond with the distal His. This indicates that *the hydrogen-bond network at the distal site plays a key role in positioning the peroxide such that the reaction can proceed with a low barrier.*

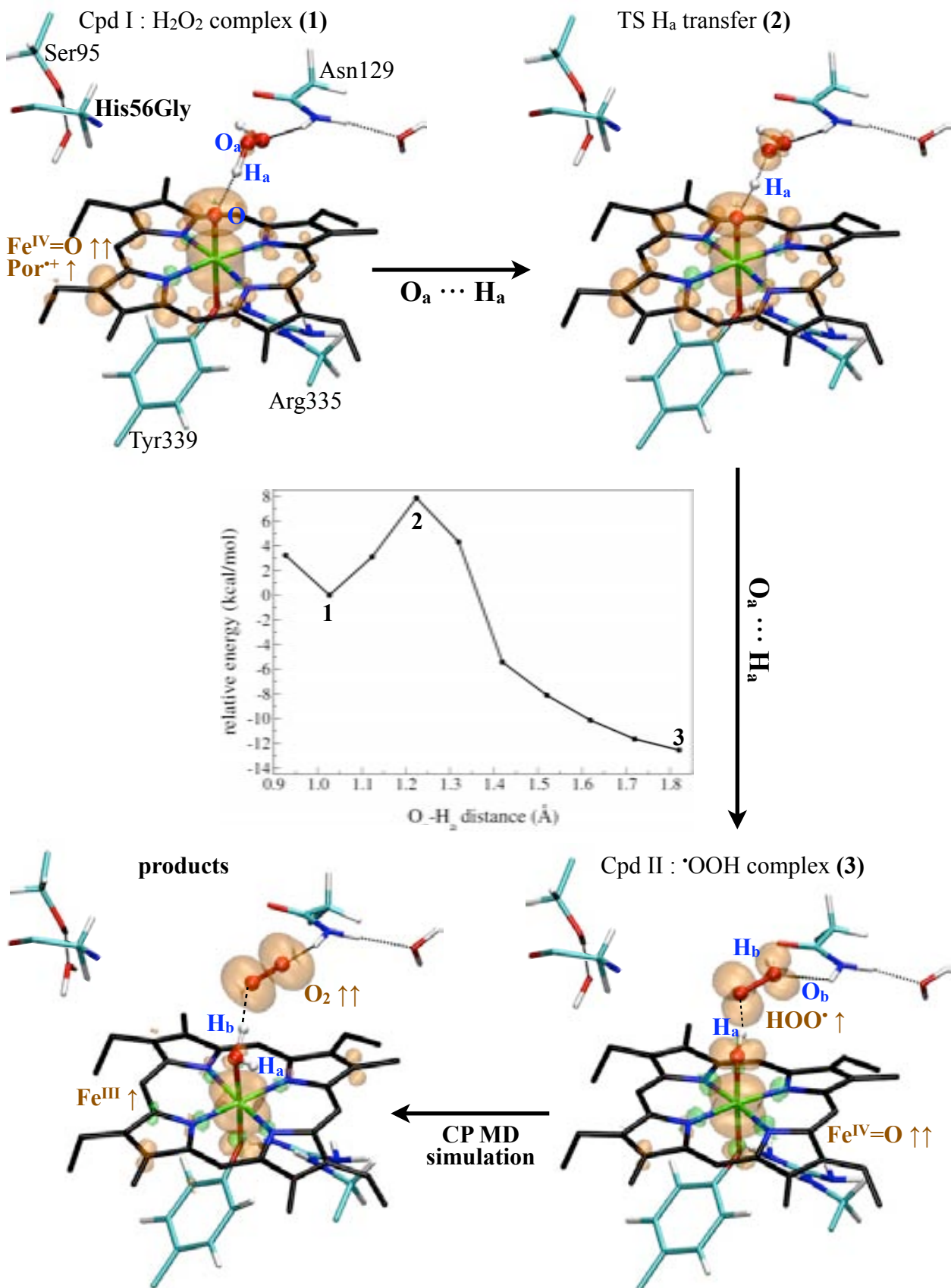


Figure 11. The catalytic reaction in the His56Gly *in silico* mutant of HPC. 1, 2 and 3 represent three points along the stretching of the O_a-H_a distance. The energy profile for this reaction coordinate is also shown. Spin isodensity surfaces at 0.004 e Å⁻³ are plotted in orange.

The second part of reaction **2**, from the Cpd II : $\cdot\text{OOH}$ complex to the products, was also found to be different from the wild-type enzyme. Starting from the same initial structure of the Cpd II-like species as for the wild type enzyme (Figure 3a), a CP QM/MM MD simulation at room temperature of the His56Gly mutant shows that the peroxy radical spontaneously transfers a hydrogen atom to the Cpd II-like heme via pathway **B** (Figure 11). The same situation has been observed in a non-heme catalase mimic (Sicking, 2007).

Therefore, *the shape of the free energy landscape of the $\text{H}^{\bullet}/\text{H}^{\bullet}$ mechanism is drastically affected by the absence of the distal His (i.e. the His56Gly mutant of HPC)*. The barrier of the initial hydrogen atom transfer increases compared to the wild-type enzyme. By contrast, the barrier for the second H^{\bullet} transfer decreases with respect to the wild-type HPC. The calculations support that, in the absence of the distal His, the catalase reaction takes place via pathway **B**. This is also the most likely scenario for the myoglobin mutants H64A, H64S, H64D and L29H/H64L (Kato, 2004; Watanabe, 2007) (see below).

2.6. Comparison of the computed mechanisms with experimental data

It is interesting to relate the computed mechanism with the results of previous experimental investigations of Kato et al. In their study (Kato, 2004; Watanabe, 2007), the kinetic isotope effect (KIE) on the catalase reaction was measured for MLC and Mb mutants (Figure 12). MLC belongs to the same clade classification as HPC, sharing 45 % / 66 % sequence identity/similarity with HPC, and their active sites are identical (Figure 12a). It is thus expected that they share a common mechanism. The myoglobin mutants were designed to probe the role of distal site residues in heme catalysis. Specifically, all the investigated mutants lack Mb His64 (Figure 12b) which was shown to inhibit Cpd I formation. F43H/H64L (Figure 12c) and L29H/H64L (Figure 12d) were designed to investigate how the location of the distal His affects the catalase activity, whereas H64A, H64S and H64D probed the effect of accessible volume and polarity of the distal pocket. Two different kinetic behaviors were observed in H_2O and D_2O for reaction **1**. Small KIE (< 4) were measured for MLC and the F43H/H64L mutant of Mb, whereas a large KIE (10-29) were observed for L29H/H64L, H64D, H64A and H64S Mb mutants.

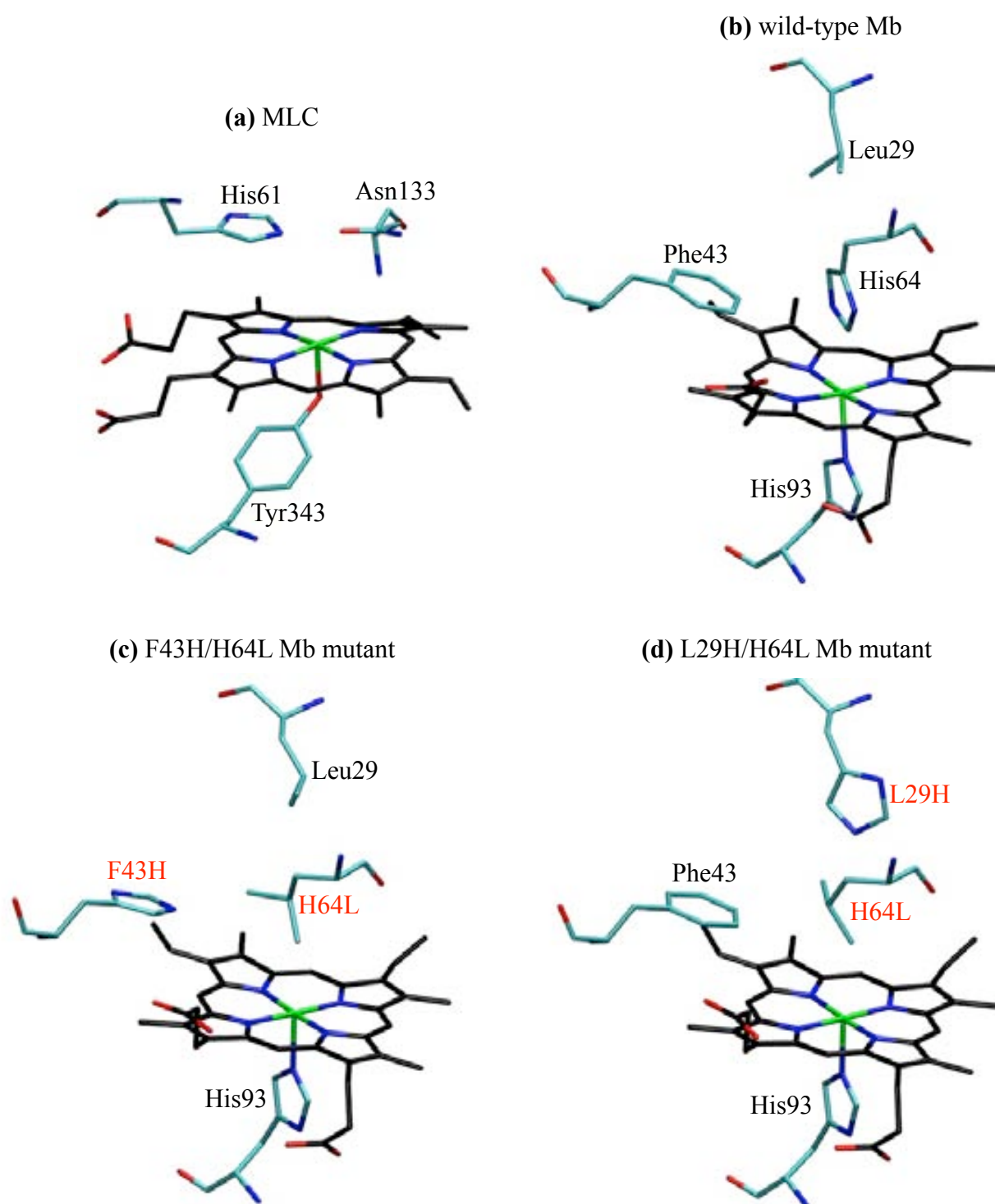


Figure 12. Comparison of the active sites of (a) catalase (MLC) (Murshudov, 2002), (b) wild-type myoglobin (Hubbard, 1990) and (c)-(d) Mb mutants (Matsui, 1999). The corresponding PDB entries are 1GWE, 2MM1, 1OFK and 1OFJ, respectively.

The free energy landscape of the catalase reaction (Figures 5 and 8) shows that the most relevant barrier does not correspond to any hydrogen transfer in neither of the two pathways (A and B), but to changes of the hydrogen bond pattern (see section 2.2.). Since small KIE (< 5) is

commonly found when the rate determining step does not involve H/D exchange (Bishop & Davidson, 1995), our result is in line with the experimental findings for MLC and the F43H/H64L mutant of Mb. However, a disparity is noted, in that Kato et al. assumed that the His-mediated mechanism follows an *ionic* mechanism, with the transfer of a proton (through the distal His) and a hydride ion from H₂O₂ to the heme-Cpd I. In contrast, here we have shown that the His-mediated pathway (Figures 6 and 9), together with the initial hydrogen atom transfer from H₂O₂ to the oxoferryl (Figure 3), consists, from an electronic point of view, in a hydrogen atom transfer plus an electron and proton transfer (H[•] / ET+H⁺).

As mentioned above, the study of Kato *et al.* also reported large KIE (10-29) for L29H/H64L, H64D, H64A and H64S Mb mutants, which were ascribed to tunneling effects. In our calculations on catalase, tunneling will likely be at work for the acid-base steps along pathway **A** and the hydrogen transfer process along pathway **B**. However, its effect on the rate of reaction would be likely hidden by the conformational change of the distal His and the hydroxoferryl group, which give higher free energy barriers than the former proton / hydrogen atom transfer events (section 2.2.). By contrast, for the His56Gly mutant of HPC we have shown that the initial hydrogen atom transfer becomes rate-limiting (section 2.5.), and thus a large KIE would be observed. In the His56Gly mutant of HPC, as well as in the L29H/H64L, H64D, H64A and H64S Mb mutants, the mutation increases the size of the distal cavity, and thus H₂O₂ does not attain short interactions with the oxoferryl unit. As a consequence, the barrier of the first step increases (see Appendix D, section 6), resulting in a large KIE. Therefore, the initial hydrogen atom transfer, which becomes rate-limiting upon increasing the size of the distal cavity, is likely to be the reason for the large isotope effects found experimentally in certain Mb mutants.

3. SUMMARY AND CONCLUSIONS

Even though the catalase reaction has been known since 1940s (Nicholls, 2001), the mechanism of Cpd I reduction by H_2O_2 (reaction 2) in catalase has yet to be clarified. In particular it is not known how the two protons and two electrons of hydrogen peroxide are transferred to Cpd I and whether the released oxygen molecule is a singlet or a triplet. In Chapter VI, we have seen that the mode of electron and proton transfer does not determine the spin state of the released oxygen, and we also predicted that the reaction probably involves two one-electron transfers, in contrast to the common assumption that the two electrons are transferred in a single elementary step.

To verify these predictions, here we explicitly modelled the mechanism of the catalatic reaction by means of QM/MM Car-Parrinello molecular dynamics simulations (Car & Parrinello, 1985) in combination with the recently developed metadynamics technique (Laio & Parrinello, 2002; Iannuzzi, 2003) to enhance the sampling of the reactive space and reconstruct the free energy surface. Calculations were performed in both *Helicobacter pylori* catalase (HPC) and *Penicillium vitale* catalase (PVC) in order to probe the influence of the different type of heme (heme b *versus* heme d) and the different protein environment on the reaction mechanism.

Our calculations show that the Cpd I : H_2O_2 complex spontaneously evolves to Cpd II-like species through a hydrogen atom transfer. To complete the reaction, two mechanisms may be operative: a His-mediated or a direct mechanism. The His-mediated mechanism (Fita & Rossman, 1985) involves the distal His as an acid-base catalyst, mediating the transfer of a proton associated with an electron transfer (i.e. pathway **A**). By contrast, in the direct mechanism a hydrogen atom transfer occurs (pathway **B**). Overall, we found that *the catalatic reaction may take place by two different mechanisms, either a $\text{H}^\bullet / \text{ET} + \text{H}^+$ or a $\text{H}^\bullet / \text{H}^\bullet$ mechanism*, and that, independently of the mechanism, the reaction proceeds by two one-electron transfers, rather than one two-electron transfer, as has long been the lore. Our results also confirm that *the oxygen molecule released by catalase is in the triplet state*.

Besides, we have investigated the role of the distal His in Cpd I reduction by using a catalase mutant lacking this residue. Our calculations show that *the hydrogen-bond network at the distal site plays a key role in positioning the peroxide such that the reaction can proceed with a low barrier*, and explain the results of kinetic isotope measurements on catalase and Mb mutants. Therefore, in line with recent investigations (Poulos, 1996; Matsui, 1999), we suggest that Cpd I reactivity depends on the shape and nature of the distal pocket.

In summary, the conclusions of this chapter are the following:

- The catalatic reaction in monofunctional catalases proceeds by two steps.
- First, the Cpd I : H₂O₂ complex spontaneously evolves to a Cpd II-like species through a hydrogen atom transfer.
- Second, either the distal His mediates the transfer of a proton (associated with an electron transfer, i.e. the His-mediated mechanism) or a hydrogen atom transfer (i.e. the direct mechanism) occurs.
- Independently of the pathway, the reaction does not involve the simultaneous transfer of two electrons, as it was previously assumed.
- The oxygen molecule released by catalase is in the triplet state.
- The hydrogen-bonding network in the distal pocket is essential for the reaction to proceed with low barriers.

CHAPTER VIII

SUMMARY AND CONCLUSIONS

In the present thesis Quantum Mechanics (QM) and hybrid Quantum Mechanics / Molecular Mechanics (QM/MM) simulations have been used to study the catalase intermediates, Compound I (Cpd I), Compound II (Cpd II) and Compound I* (Cpd I*). First, gas phase calculations (Chapter III) have been performed to investigate the intrinsic properties of the aforementioned intermediates and to elucidate the effect of the type of heme (heme b or heme d) on these properties. In a further step, QM/MM simulations (Chapter IV) have helped to assign the structure and electronic configuration of oxidized *Helicobacter pylori* catalase (HPC) and *Penicillium vitale* catalase (PVC), in combination with structural and spectroscopic data.

In order to explain why HPC and PVC show different oxidized intermediates (Cpd I* and Cpd I, respectively), the free energies of electron transfer and proton transfer have been computed in Chapter V by using QM/MM calculations and CP QM/MM metadynamics simulations. The results obtained have rationalized the different propensity of HPC and PVC for reduction and protonation. Besides, a plausible candidate for the protein radical site in HPC has been proposed (Tyr351) and its feasibility has been tested using QM/MM.

In addition, the mechanism of the catalase reaction (i.e. Cpd I reduction by H₂O₂) has been studied. The arguments commonly used to predict the spin state of the released molecular oxygen have been reevaluated, and this analysis has been complemented by QM calculations on models of the reactants and products of the reaction (Chapter VI). The complete mechanism of the catalase reaction has been modelled in Chapter VII for both HPC and PVC, by means of CP QM/MM metadynamics simulations. These simulations have disentangled how the two protons and two electrons of hydrogen peroxide are transferred to Cpd I and have highlighted the key role of the distal residues in the reaction, providing clues for the reaction to proceed with low barriers.

The conclusions obtained in the present thesis are the following:

- The structure of catalase intermediates (Cpds I and II) is similar to other hemeproteins and is hardly affected by the heme modification. In contrast, the electronic configuration of catalase Cpd I (i.e. the symmetry and the distribution of the porphyrin cation radical) depends on the type of heme.
- Oxidized PVC bears an oxoferryl porphyrin cation radical ($\text{Por}^{+\bullet}\text{-Fe}^{\text{IV}}=\text{O}$), i.e. a canonical Cpd I. On the contrary, oxidized HPC contains a hydroxoferryl neutral porphyrin with a protein radical ($\text{Por-Fe}^{\text{IV}}\text{-OH, aa}^{\bullet}$), i.e. Cpd I*.
- Catalase Cpds II and I* are protonated (i.e. $\text{Por-Fe}^{\text{IV}}\text{-OH}$)
- The reduction potential of Cpd I in HPC and PVC is very similar, but the number of possible electron donors near the heme is larger for HPC than PVC. Therefore, electron transfer (ET) from a protein residue to the heme is more likely for HPC.
- Upon ET, the distal His transfers a proton to the oxoferryl group of the heme, stabilizing Cpd I* formation in both catalases. However, proton transfer (PT) stabilizes more HPC Cpd I* than PVC.
- Overall, we propose that Cpd I* is not observed in PVC because of (i) the lower accessibility to reductants and (ii) the lower stabilization by protonation.
- Tyr351 is a plausible protein radical site for HPC Cpd I*.

- The commonly assumed association of the H^+ / H^- mechanism with the generation of singlet oxygen in the catalase reaction is not justified. Taking into account the spin state of all the species involved (and not only hydrogen peroxide) any of the two previously proposed mechanisms (H^+ / H^- or H^\bullet / H^\bullet) can generate either singlet or triplet oxygen.
- The catalase reaction starts with a spontaneous hydrogen atom transfer from H_2O_2 to Cpd I, forming a Cpd II-like species and a peroxy radical. To complete the reaction, two mechanisms are operative, depending on the involvement of the distal His in the reaction: a His-mediated (Fita-Rossmann) mechanism or a direct mechanism.
- Independently of the mechanism, the catalase reaction consists of two one-electron transfers, rather than a single two-electron transfer, as has long been the lore.
- The molecular oxygen released by catalase is a triplet.
- The hydrogen-bond network at the distal site plays a key role in positioning the peroxide such that the reaction can proceed with a low barrier. This explains why myoglobin and peroxidases perform the catalase reaction at much lower pace.

**PUBLICATIONS
AND PRESENTATIONS IN CONGRESSES**

PUBLICATIONS

The present thesis has given rise to the following publications:

- Rovira, C.; Alfonso-Prieto, M.; Biarnés, X.; Carpena, X.; Fita, I. & Loewen, P.C. (2006) A first principles study of the binding of formic acid in catalase complementing high resolution X-ray structures. *Chem. Phys.* 323(1): 129-137.
- Alfonso-Prieto, M.; Borovik, A.; Carpena, X.; Murshudov, G.; Melik-Adamyanyan, W.; Fita, I.; Rovira, C. & Loewen P.C. (2007) The structures and electronic configuration of Compound I intermediates of *Helicobacter pylori* and *Penicillium vitale* catalases determined by X-ray crystallography and QM/MM density functional theory calculations. *J. Am. Chem. Soc.* 129(14): 4193-5205.
- Alfonso-Prieto, M.; Vidossich, P.; Rodríguez-Forteza, A.; Carpena, X.; Fita, I.; Loewen, P.C. & Rovira C. (2008) Electronic state of the molecular oxygen released by catalase. *J. Phys. Chem. A.* 112(50): 12842-12848.
- Alfonso-Prieto, M.; Biarnés, X.; Vidossich, P. & Rovira C. (2009) The molecular mechanism of the catalase reaction. *J. Am. Chem. Soc.* 131 (33): 11751–11761.
- Alfonso-Prieto, M.; Blumberger, J.; Rovira, C.; Kohlmeyer, A. & Klein, M.L. (in preparation) Electron transfer and ferryl protonation in catalases.
- Alfonso-Prieto, M. & Rovira, C. (in preparation) Density functional study of the factors influencing the electronic structure of catalase intermediates.

Besides, the work done during the PhD training has given rise to other publications not presented in this thesis:

- Vidossich, P.; Alfonso-Prieto, M.; Carpena, X.; Loewen, P.C.; Fita, I & Rovira C. (2007) Versatility of the electronic structure of Compound I in catalase-peroxidases. *J. Am. Chem. Soc.* 129 (44): 13436-13446.
- Derat, E.; Shaik, S.; Rovira, C.; Vidossich, P. & Alfonso-Prieto, M. (2007) The effect of a water molecule on the mechanism of formation of Compound 0 in *Horseradish* peroxidase. *J. Am. Chem. Soc.* 129(20): 6346-6347.
- Nygaard, T.P.; Peters, G.H.; Jensen, M.; Rovira, C. & Alfonso-Prieto M. (2009) Ab initio molecular dynamics study of substrate recognition in *E.coli* ammonia channel AmtB. *Biophys. J.* (under revision).
- Addington, T.; Calisto, B.; Alfonso-Prieto, M.; Rovira, C.; Fita, I. & Planas A. (2009) Unpredicted loop rearrangement while attempting to reengineer β -glucanase towards xyloglucan endotransglycosylase-like substrate specificity. *PEDS: Protein Engineering; Design and Selection* (under revision).
- Valle-Delgado, J. J.; Alfonso-Prieto, M.; de Groot, N. S.; Ventura, S.; Samitier, J.; Rovira, C.; & Fernández-Busquets (2009) Modulation of A β ₄₂ fibrillogenesis by glycosaminoglycan structure. *Nature Chem. Bio.* (submitted)
- Vidossich, P.; Fiorin, G.; Alfonso-Prieto, M.; Derat, E.; Shaik, S. & Rovira, C. (2009) On the role of water in peroxidase catalysis: a theoretical investigation of HRP Compound I formation. *J. Phys. Chem. B* (submitted)
- Alfonso-Prieto, M.; Biarnés, X.; Kumar, M.; Rovira, C. & Kozłowski PM. (in preparation) The reductive cleavage mechanism of Co-C bond in cobalamin-dependent methionine synthase.

PRESENTATIONS IN CONGRESSES

The work of this thesis has been presented in the following congresses:

- Alfonso-Prieto, M.; Fita, I.; Loewen, P.C. & Rovira C. (2005) **Poster presentation**: The structure of Compound I intermediate of *Helicobacter pylori* catalase. Experimental and computational study. FEBS Advanced Course “Theoretical Modeling of ligand binding and enzyme catalysis”. University of Tromso (Norway).
- Alfonso-Prieto, M.; Borovik, A.; Carpena, X.; Murshudov, G.; Melik-Adamyanyan, W.; Fita, I.; Rovira, C. & Loewen P.C. (2006) **Invited talk**: First-principles MD simulations of the reaction intermediates of heme catalases. Electronic consequences of heme modifications. 1st CMM “Users meet Developers” Workshop on QM/MM Simulations. Center for Molecular Modeling; University of Pennsylvania (Philadelphia; USA).
- Alfonso-Prieto, M.; Borovik, A.; Carpena, X.; Murshudov, G.; Melik-Adamyanyan, W.; Fita, I.; Rovira, C. & Loewen P.C. (2006) **Invited seminar**: First-principles MD simulations of the reaction intermediates of heme catalases. Electronic consequences of heme modifications. Department of Chemistry; New York University (USA).
- Alfonso-Prieto, M.; Borovik, A.; Carpena, X.; Murshudov, G.; Melik-Adamyanyan, W.; Fita, I.; Rovira, C. & Loewen P.C. (2007) **Poster presentation**: Electronic consequences of heme modifications in the reaction intermediates of heme catalases. CECAM Workshop “Progress in ab initio modelling of biomolecules: towards computational spectroscopy”. Physics Department; University of Rome (Italy).
- Alfonso-Prieto, M.; Vidossich, P.; Derat, E.; Shaik, S. & Rovira, C. (2007) **Oral communication**: QM/MM modeling of the enzymatic reaction of peroxidases. Effect of a water molecule. XXIII Meeting of the Theoretical Chemistry Network of Catalonia. Universitat Rovira i Virgili (Tarragona; Spain).
- Alfonso-Prieto, M.; Vidossich, P.; Derat, E.; Shaik, S. & Rovira C. (2007) **Invited seminar**: The effect of a water molecule in the enzymatic mechanism of peroxidases. A DFT QM/MM investigation. Institut de Recerca Biomèdica (Barcelona; Spain).
- Alfonso-Prieto, M.; Borovik, A.; Carpena, X.; Murshudov, G.; Melik-Adamyanyan, W.; Fita, I.; Rovira, C. & Loewen P.C. (2008) **Poster presentation**: Electronic consequences of heme modifications in the reaction intermediates of heme catalases. CECAM Workshop “Understanding Molecular simulations”. University of Amsterdam (The Netherlands).

- Alfonso-Prieto, M.; Biarnés, X.; Vidossich, P. & Rovira, C. (2008) **Poster presentation**: The molecular mechanism of Compound I reduction in heme catalases. A QM/MM metadynamics investigation. CPMD 2008 - Conference on Modeling and Computation of Structure and Dynamics of Condensed Phase Systems. International Centre for Theoretical Physics (Trieste; Italy).
- Alfonso-Prieto, M.; Biarnés, X.; Vidossich, P. & Rovira, C. (2009) **Poster presentation**: The molecular mechanism of Compound I reduction in heme catalases. A QM/MM metadynamics investigation. Theoretical Chemistry: Modeling reactivity from gas phase to biomolecules and solids. Celebrating 25 years of the Theoretical Chemistry Network of Catalonia. Universitat de Barcelona (Barcelona; Spain).

Additional information for Chapter IV

M. Alfonso-Prieto, A. Borovik, X. Carpena,
G. Murshudov, W. Melik-Adamyanyan, I. Fita, C. Rovira, and P. C. Loewen.

The structures and electronic configuration of Compound I intermediates
of *Helicobacter pylori* and *Penicillium vitale* catalases
determined by X-ray crystallography and QM/MM Density Functional Theory calculations.

J. Am. Chem. Soc. **2007**, 129 (14), pp 4193–4205

1. CLASSICAL MOLECULAR DYNAMICS SIMULATIONS

Starting structures

Before starting the CP QM/MM simulations, the two catalase structures (Alfonso-Prieto, 2007) were equilibrated by a force-field based MD simulation. For HPC, the full tetrameric protein was used (PDB entry: 2IQF), whereas for PVC (PDB entry: 2IUJ) the C-terminal flavodoxin-like domain was omitted in each of the four subunits for computational economy. For HP11 (another large subunit, *heme d*-containing catalase), a likewise truncated variant was found to have nearly identical properties to the complete protein (Chelikani, 2005).

Conventional (pH = 7) protonation states were chosen for all residues. The protonation state of the histidine residues took into account their hydrogen bond environment, and all aspartates and glutamates were taken as deprotonated to carboxylate anion, except when there was a close contact between two acidic residues. The proximal tyrosines (339 in HPC and 351 in PVC) were taken as deprotonated. Four sodium ions per subunit of HPC and seven per subunit of PVC were added to achieve neutrality of the protein structure. The system was enveloped in a box of equilibrated TIP3P water molecules with volume $104 \text{ \AA} \times 119 \text{ \AA} \times 121 \text{ \AA}$ for HPC and $120 \text{ \AA} \times 119 \text{ \AA} \times 144 \text{ \AA}$ for PVC. The total size of the system is 128,856 / 178,558 atoms, respectively, (31,856 / 32,443 protein and heme atoms + 97,000 / 146,115 water and counterion atoms).

Simulation details

For protein residues, the Cornell et al. force-field (Cornell, 1995), as implemented in the AMBER 7.0 program (Pearlman, 1995), was employed. For *heme b* in HPC, the parameters of Banci et al. (Banci, 1997) were used, and for the *cis*-hydroxy- γ -spirolactone *heme d* in PVC the parameters from GAFF (Wang, 2004 & 2006) in the AMBER package were used. A renormalization of the charges is needed to reproduce the formal oxidation states of the iron atom (+4) and the ligands (-1 and -2 for the porphyrin in Cpd I and II, respectively; -2 for the axial oxygen atom of the oxoferryl unit; and -1 for the OH ligand). For oxidized *heme b*, the charges reported previously for a *heme b* based Cpd I were used (Collins, 1991; Harris, 1995). In the case of *heme d*, the charges were obtained from a CPMD gas-phase calculation of the prosthetic group and the proximal tyrosinate and arginine.

The system was equilibrated in several steps. First, all water molecules and counterions were relaxed with a gradient minimizer, and then the protein was also minimized. Because of the

enormous size of the tetrameric protein (~2000 and ~2800 residues, respectively), only the first subunit was allowed to move, and the other three were fixed. Next, the solvent was equilibrated for 40 / 80 ps at 150 K (protein constrained), and again the first subunit was equilibrated at the same temperature for another 40 / 80 ps. Once the whole system was at 150 K, it was equilibrated at 300 K for 280 / 233 ps, also coupling a bath to achieve the desired temperature. The simulation was continued for about one nanosecond at constant pressure, allowing the cell volume to evolve until equilibration. The structure after MD simulation did not change significantly with respect to the initial X-ray structure.

2. CP QM/MM CALCULATIONS

Models

Once the system was equilibrated, CP QM/MM simulations (Laio, 2002a,b) were initiated. For computational reasons, the calculations were performed on a reduced model consisting of all residues within ~ 20 Å from the heme iron. This corresponds to a sizable protein fragment (4141 and 4986 atoms, in HPC and PVC, respectively) and it is expected to account for all the relevant heme-protein interactions affecting the electronic structure at the active center.

Figure 1 shows the QM/MM partition used in the calculation, which included the iron-porphyrin with its methyl and vinyl groups and the *cis*-hydroxy- γ -spirolactone in *heme d*, the phenolate side chain of the proximal Tyr339/351 (HPC / PVC residue numbering), and the methylguanidinium side chain of Arg335/347, which is hydrogen bonded to the phenolate oxygen atom of Tyr339/351. Previous work demonstrated that both Tyr339/351 and Arg335/347 influence significantly the structure and ligand properties of the heme (Rovira, 2003). On the distal side of the heme, the catalytic residues (Asn129/137 and His56/64, modeled by methylimidazole and ethylamide, respectively) (Nicholls, 2001), the water molecule coordinated by histidine and asparagine, and the side chain of Ser95/103, which interacts with its N δ -H of His56/64, were included. Two additional conserved water molecules hydrogen bonded to the distal residues Asn129/137 and Ser95/103 were also incorporated. The rest of the system was treated with the AMBER force field (Pearlman, 1995). The QM-MM interface is modeled by the use of a link atom pseudopotential (von Lilienfeld, 2005) that saturates the QM region. Seven link atoms were used, located at Asn129/137, His56/64, Ser95/103, Tyr339/351, Arg335/347, and the two *heme b* or the one *heme d* propionates (Figure 1).

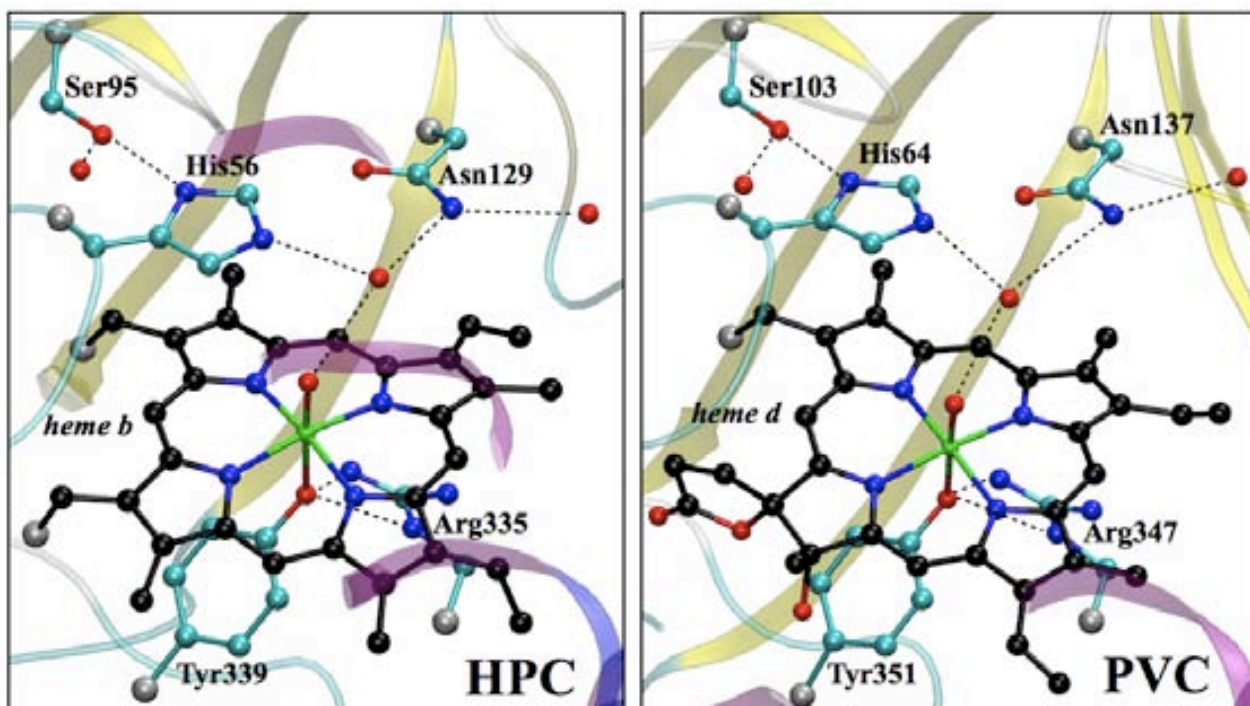


Figure 1. QM-MM partition used in the calculations. The QM region is shown in ball and stick representation. Hydrogen atoms are omitted for clarity, and the link atoms are coloured in silver.

Six different configurations for the heme-ligand bonds were considered (Figure 2). First, the canonical configuration of Cpd I (i.e. $\text{Por}^{\bullet+}\text{-Fe}^{\text{IV}}=\text{O}$), as described in previous studies (Green, 2001; Rydberg, 2004; de Visser, 2006), was examined (**Ia**). Then, taking into account the crystal structures of oxidized HPC and PVC were solved at a slightly acidic pH (5.6 and 5.2, respectively), a proton was added to the active site. Two different protonated forms were considered. Configuration **Ib** bears a proton on the distal histidine $\{\text{Por}^{\bullet+}\text{-Fe}^{\text{IV}}=\text{O}, \text{His-H}^+\}$, as the pKa of this residue is estimated to be 5.0 in *Horse radish* peroxidase (HRP) (Jones & Dunford, 2006). Alternatively, **Ic** explores the possibility of a proton transfer from the distal His to the ferryl oxygen, yielding a hydroxoferryl Cpd I (i.e. $\{\text{Por}^{\bullet+}\text{-Fe}^{\text{IV}}\text{-OH}^+\}$). Afterwards, one-electron reduced forms of Cpd I were considered. They are useful models of Cpd II (i.e. $\{\text{Por}\text{-Fe}^{\text{IV}}\text{-OH}\}$) as well as Cpd I* (i.e. $\{\text{Por}\text{-Fe}^{\text{IV}}\text{-OH}, \text{aa}^{\bullet+}\}$), because both species are isoelectronic on the active site region. A larger QM region for Cpd I*, covering all protein residues (aa= Tyr or Trp) close to the heme where the radical can migrate, is beyond our computational capabilities. Similarly to Cpd I, three different protonation states were considered for Cpd II / Cpd I* (Figure 2): non-protonated (**IIa**, $\text{Por}\text{-Fe}^{\text{IV}}=\text{O}$) and bearing a proton either on the distal His (**IIb**, $\{\text{Por}\text{-Fe}^{\text{IV}}=\text{O}, \text{His-H}^+\}$) or on the ferryl oxygen (**IIc**, $\text{Por}\text{-Fe}^{\text{IV}}\text{-OH}$).

Ia	Ib	Ic
His $\begin{array}{c} \text{O} \\ \\ \text{Fe}^{\text{IV}} \end{array}$	HisH ⁺ $\begin{array}{c} \text{O} \\ \\ \text{Fe}^{\text{IV}} \end{array}$	His $\begin{array}{c} \text{OH}^+ \\ \\ \text{Fe}^{\text{IV}} \end{array}$
charge=+1; M=4	charge=+2; M=4	charge=+2; M=4
IIa	IIb	IIc
His $\begin{array}{c} \text{O} \\ \\ \text{Fe}^{\text{IV}} \end{array}$	HisH ⁺ $\begin{array}{c} \text{O} \\ \\ \text{Fe}^{\text{IV}} \end{array}$	His $\begin{array}{c} \text{OH} \\ \\ \text{Fe}^{\text{IV}} \end{array}$
charge= 0; M=3	charge=+1; M=3	charge=+1; M=3

Figure 2. Oxidized intermediates considered in the QM/MM calculations.

Simulation details

Hybrid CP QM/MM optimizations were performed for each of the six isomers. The method developed by Laio, VandeVondele, and Röthlisberger (Laio, 2002a) combining the first principles molecular dynamics method of Car and Parrinello (CPMD) (Car & Parrinello, 1985) with a force-field molecular dynamics methodology (hereafter CP QM/MM MD) was used. Bonded and van der Waals interactions between the QM and the MM region are treated with the standard AMBER force field. Long-range electrostatic interactions between MM atoms have been described with P3M implementation (Hünenberger, 2000) using a $64 \times 64 \times 64$ mesh. The details of the QM calculation are the same as for the gas phase models described on Chapter III. The QM system was enclosed in an isolated supercell of size $15.341 \times 21.160 \times 20.102 \text{ \AA}^3$ (HPC) / $22.483 \times 18.780 \times 18.515 \text{ \AA}^3$ (PVC). For the iron, besides the eight valence electrons pseudopotential (supplemented with NLCC (Louie, 1982)) used in the previous studies of the group (see for instance, Rovira 2005 & 2006), we tested a 16 valence electrons pseudopotential on HPC-**Ia** (oxoferryl Cpd I), **Ic** and **II** (hydroxoferryl Cpd I or Cpd II, respectively) models. Only slight changes in the Fe-O and Fe-O_{Tyr} distances were found (± 0.02 and $\pm 0.04 \text{ \AA}$, respectively). Therefore, we used the eight valence electrons pseudopotential with NLCC for all the systems studied.

Structural optimizations of all the intermediates (Figure 2) were performed by means of molecular dynamics with annealing of the atomic velocities, until the maximum component of the nuclear gradient was lower than 5×10^{-4} au. Short CP QM/MM MD simulations (~ 1 ps) for the A6

oxoferryl Cpd I forms (PVC-**Ia** and HPC-**Ia**) were performed to analyze the changes in the spatial distribution of the spin density owing to the thermal motion. A time step of 0.12 fs and a fictitious electronic mass of the CP Lagrangian of 700 au were used.

Additional information for Chapter V

1. COMPUTATIONAL DETAILS

1.1. Classical molecular dynamics simulations of the ET to Cpd I

Starting structures

Sampling of the vertical energy gap over the relevant ET timescale (ns) is crucial to obtain converged results for the parameters of the ET (Blumberger, 2008). Therefore, we performed a ~20 nanosecond classical molecular dynamics (MD) simulations on the oxidized (O) and reduced (R) states of HPC and PVC. The starting X-ray structures correspond to PDB entries 2IQF and 2IUF, respectively, and include the four subunits of catalase. This computational setup is the same as in Chapter IV, except for PVC. Instead of a truncated form of PVC used in Chapter IV (i.e. lacking the additional C-terminal domain in each of the four subunits), the complete tetrameric protein is used, because the redox potential depends not only on the cofactor but also on the protein and surrounding solvent (Blumberger, 2008).

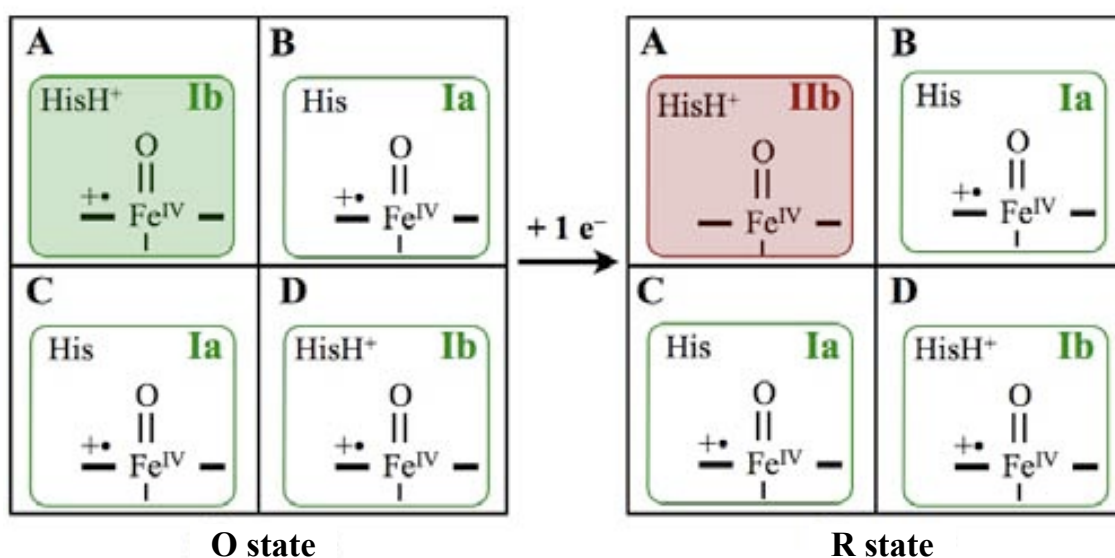


Figure 1. Schematic representation of the oxidation and protonation states of the active site in each of the four catalase subunits (A-D), as employed in the classical molecular dynamics of the O and R states of HPC and PVC. The oxidation state of the heme is denoted as **I** and **II** (Cpd I or Cpd II, respectively). The protonation state of the distal His is indicated as **a** and **b** (neutral or protonated His, respectively).

Figure 1 shows the oxidation and protonation states of the active site in each of the four catalase subunits. In the O state, all the hemes were considered to be in the Cpd I configuration, whereas in the R state only one out of the four hemes was reduced to Cpd II. In both oxidation states the oxoferryl group was taken as deprotonated, assuming that protonation of the oxoferryl in

the R state occurs following ET. The distal His was taken as protonated in protein subunits **A** and **C**, and neutral in **B** and **D**. After ET, HisH⁺ is expected to transfer the proton to the oxoferryl Cpd II through the pocket water. Therefore, in the O state the active site of subunits **A** and **C** is equivalent to the QM/MM model **Ib** in Chapter IV, whereas for subunits **B** and **D** it mimics the QM/MM model **Ia** (see Figure 1). In the R state, only the active site in subunit **A** gets reduced, and thus it becomes equivalent to the QM/MM model **IIb** (see Figure 1), while the active sites of the other subunits remain unaltered (**B-D** in Figure 1).

Conventional (pH = 7) protonation states were chosen for all residues. The protonation state of the histidine residues took into account their hydrogen bond environment, and all aspartates and glutamates were taken as deprotonated to carboxylate anion, except when there was a close contact between two acidic residues. The proximal tyrosines (339 in HPC and 351 in PVC) were taken as deprotonated. 3,5 sodium ions per subunit of HPC and 9 per subunit of PVC were added to achieve neutrality of the protein structure. The system was enveloped in a box of equilibrated TIP3P water molecules with volume 110,1 Å × 123,3 Å × 129,6 Å for HPC and 128,9 Å × 125,7 Å × 167,6 Å for PVC. The total size of the system is 155,541 / 244,608 atoms, respectively (31,858 / 42,238 protein and heme atoms + 123,683 / 202,370 water and counterion atoms).

Simulation details

The parameters employed for protein residues, the heme b in HPC and the heme d of PVC were the same as in the classical MD in Chapter IV. Only the parameters describing the interaction between Fe and its ligands were slightly modified. The same force constants as in Banci et al. (Banci, 1997) were used, except for the Fe=O bond, whose force constant was re-estimated from a short QM/MM molecular dynamics simulation for model **Ib** (Chapter IV, section 2.1.). The equilibrium bond and angle values were also substituted for those obtained in the QM/MM geometry optimizations of model **Ib** (Chapter IV, section 2.1.). Besides, the RESP charges of the heme cofactor, the proximal Tyr and Arg, the protonated distal His and the pocket water were reparametrized. Using the CPMD QM/MM optimized geometries **Ib** and **IIb** (Chapter IV, section 2.1.), a simplified model was built, comprising the porphyrin without substituents (except the *cis*-hydroxy- γ -spirolactone in heme d), the proximal Tyr and Arg (modelled as phenolate and methylguanidium), a water molecule and the distal His (replaced by a methylimidazolium). The valences were saturated with hydrogen atoms, whose position was optimized within the Gaussian program (Frisch, 2004) using BP86/6-31G*, whereas the rest of the structure was kept at the CPMD

QM/MM geometry. ESP charges were obtained using BP86/6-31⁺⁺G^{**} and the final RESP charges were fitted using the Antechamber program (Wang, 2006) in the AMBER package (Pearlman, 1995). Overall, the parameters of the O and the R states are identical, except for the RESP charges of the active site in subunit A (i.e. modeling Cpd I in the O state and Cpd II in the R state).

The solvated O state was equilibrated in several steps. First, all water molecules and counterions were relaxed with a gradient minimizer, and then the protein was also minimized. Next, the solvent was equilibrated for 400 / 600 ps (HPC or PVC, respectively) at 150 K (protein constrained), and afterwards the protein was equilibrated at the same temperature for another 200 / 200 ps. Once the whole system was at 150 K, it was equilibrated at 300 K for 1.0 / 2.5 ns, also coupling a bath to achieve the desired temperature. The simulation was continued for about 20 nanoseconds at constant pressure. The first 10 ns were used to equilibrate the system and the cell volume and the last 10 ns were taken for calculation of configurational averages (see section 1.2.). The MD simulation of the R state was started using as initial geometry a snapshot of the O state after 2 ns of equilibration in the NPT ensemble. After equilibration for 10 ns, the following 10 ns were also taken for calculation of configurational averages (see section 1.2.). During both runs, the center of mass of each subunit was constrained to the initial value with a harmonic force of $k=5$ kcal/mol in order to avoid rotation of the entire protein complex, which brings protein atoms close to the boundary of the cubic unit cell. Analysis of the trajectories was carried out using standard tools of AMBER (Pearlman, 1995) and VMD (Humphrey, 1996).

1.2. QM/MM calculations of the ET to Cpd I

Ensemble of configurations

To calculate the relative free energy of ET to Cpd I (reaction 5 in Chapter V), 21 snapshots were extracted from the last 10 ns of the classical MD simulations (section 1.1.) of each oxidation state (O and R), i.e. 42 snapshots were obtained for each protein (HPC and PVC).

Model

The QM region used in the QM/MM calculations is shown in Figure 2. It includes the heme (with all the substituents except for the propionates), the proximal Tyr⁻ and Arg⁺ (Tyr339/351 and Arg335/347, according to HPC / PVC numbering), the distal HisH⁺ (His56/64) and the pocket water (Figure 2). Although this QM region is smaller than the one used in Chapter IV, we found that it is

enough to converge the vertical ionization energies (see section 4). This QM region is contained in a cubic box of dimensions $16.88 \times 20.00 \times 18.83 \text{ \AA}^3$ for HPC or $20.90 \times 19.73 \times 20.79 \text{ \AA}^3$ for PVC.

The QM-MM boundary was saturated with “dummy” hydrogen atoms (located at His56/64, Tyr339/351, Arg335/347 and the two heme b or the one heme d propionates) (see Chapter II, section 2.2.). Eventhough the structure of the model is hardly affected by the choice of the boundary atom approach, the vertical ionization energies using monovalent pseudopotentials display larger deviations with respect to all-QM calculations (Blumberger, 2008).

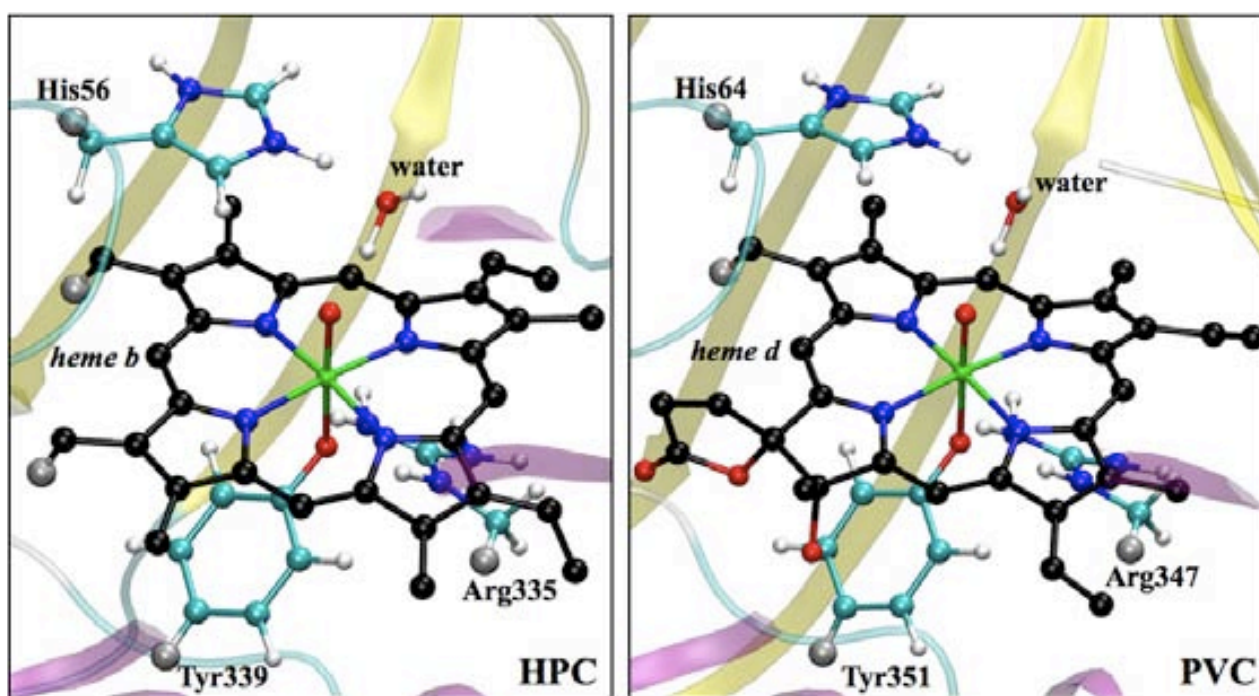


Figure 2. QM-MM partition used in the calculation of the vertical ionization energies of Cpd I and Cpd II in HPC and PVC. The QM region is shown in ball and stick representation and the link atoms are coloured in silver. The hydrogen atoms of the heme group are omitted for clarity.

Computational details

The details of the DFT calculation are the same as described in Appendix A (section 2), except that the iron pseudopotential was changed to a sixteen valence electrons (semicore) pseudopotential and the PW kinetic energy cutoff was increased up to 90 Ry. Tests performed in porphyrin-based systems showed that the geometry is hardly affected by the iron pseudopotential employed, while the change in the vertical ionization energies is larger (Blumberger, 2006 & 2008).

The cutoff radii for handling the electrostatic interactions between the QM and MM regions (Laio, 2002a) was set to $r_{\text{NN}} = r_{\text{MIX}} = 5.3 \text{ \AA}$ and $r_{\text{RESP}} = 132.3 \text{ \AA}$. We found these cutoff radii are a reasonable compromise between accuracy and computational cost (see section 4). This means that for the MM atoms within 5.3 \AA of any QM atom, the electrostatic interaction energy is calculated from the electrons + nuclei density on the QM subsystem and the point charges of the MM atoms. All other MM atoms interact with the D-RESP charges assigned to the QM atoms (i.e. no MM atom was coupled via a multipole expansion). Long-range electrostatic interactions between MM atoms have been described with P3M implementation (Hünenberger, 2000) using a $256 \times 256 \times 256$ mesh.

Calculation of the free energy of ET to Cpd I ($\Delta G^{\text{Cpd I, ET}}$)

Table 1 shows the equations used to calculate the redox energies associated to the ET to Cpd I (see also equations 35a,b, 39-40 in Chapter II).

Table 1. Equations used to calculate the redox energies associated to ET to Cpd I.

$\langle \text{EA} \rangle = \langle E_{\text{Cpd I}}(\mathbf{R}_{\text{Cpd I}}) - E_{\text{Cpd II}}(\mathbf{R}_{\text{Cpd I}}) \rangle$	$\Delta A = [\langle \text{IP} \rangle + \langle \text{EA} \rangle] / 2$
$\langle \text{IP} \rangle = \langle E_{\text{Cpd I}}(\mathbf{R}_{\text{Cpd II}}) - E_{\text{Cpd II}}(\mathbf{R}_{\text{Cpd II}}) \rangle$	$\lambda = [\langle \text{IP} \rangle - \langle \text{EA} \rangle] / 2$
$\langle \Delta E \rangle = \langle E_{\text{Cpd II}}(\mathbf{R}_{\text{Cpd II}}) - E_{\text{Cpd I}}(\mathbf{R}_{\text{Cpd I}}) \rangle$	

$E_{\text{M}}(\mathbf{R}_{\text{M}})$, $\text{M} = \text{Cpd I, Cpd II}$, is the ground state QM/MM potential energy in the oxidized or the reduced state and \mathbf{R}_{M} denotes the ion configuration. The brackets $\langle \dots \rangle$ indicate the thermal average at 300K. IP and EA are the ionization potential and the electron affinity, respectively, and ΔE is the adiabatic energy of reduction. The free energy or driving force of ET (ΔA) and the reorganization free energy (λ) are calculated under the linear response approximation (see Chapter II, section 4.3.).

To compare the two catalases the difference in the free energy of ET to Cpd I ($\Delta \Delta G^{\text{ET}}$) is computed as:

$$\Delta \Delta G^{\text{ET}} \approx \Delta \Delta A = [\Delta A^{\text{HPC}} - \Delta A^{\text{PVC}}] \quad (\text{eq. 1})$$

Besides, the influence of the different parts of the system was probed by decomposing the total values into the *inner-sphere* (i.e. heme and first-shell residues) and the *outer-sphere* (i.e. protein and solvent) contributions:

$$\Delta \Delta G^{\text{ET}} \approx \Delta \Delta A = [\Delta \Delta A^{\text{i}} + \Delta \Delta A^{\text{o}}] \quad (\text{eq. 2})$$

where $\Delta \Delta A^{\text{i}} = \Delta \Delta A_{\text{QM}}$ and $\Delta \Delta A^{\text{o}} = (\Delta \Delta A_{\text{MM}} + \Delta \Delta A_{\text{QM-MM}})$ (see Chapter II, section 4.4.).

1.3. Metadynamics simulations of the PT to Cpd I*

Computational details

$\Delta G^{\text{Cpd I}^*,\text{PT}}$, the free energy of the water-mediated proton transfer from the distal His to the oxoferryl Cpd II (reaction 6 in Chapter V), was computed by means of CP QM/MM metadynamics simulations (Laio & Parrinello, 2002, Iannuzzi, 2003). Two reaction coordinates (or collective variables) were chosen (Figure 3). The first one, $CV_1 = N_{\text{coord}}(\text{O}_w\text{-H}_1) - N_{\text{coord}}(\text{O}\text{-H}_1)$, is the difference between the coordination numbers of the water oxygen and the oxoferryl with respect to the H₁ water proton (see Chapter II, equation 20), and measures the degree of proton transfer from the pocket water to the ferryl oxygen. The second one, $CV_2 = N_{\text{coord}}(\text{O}_w\text{-H}_2) - N_{\text{coord}}(\text{N}_\epsilon\text{-H}_2)$, is the difference between the coordination numbers of the N_ε atom of the distal His and the water oxygen with respect to the H₂ water proton (see Chapter II, equation 20), and gives an idea of the deprotonation of the distal His.

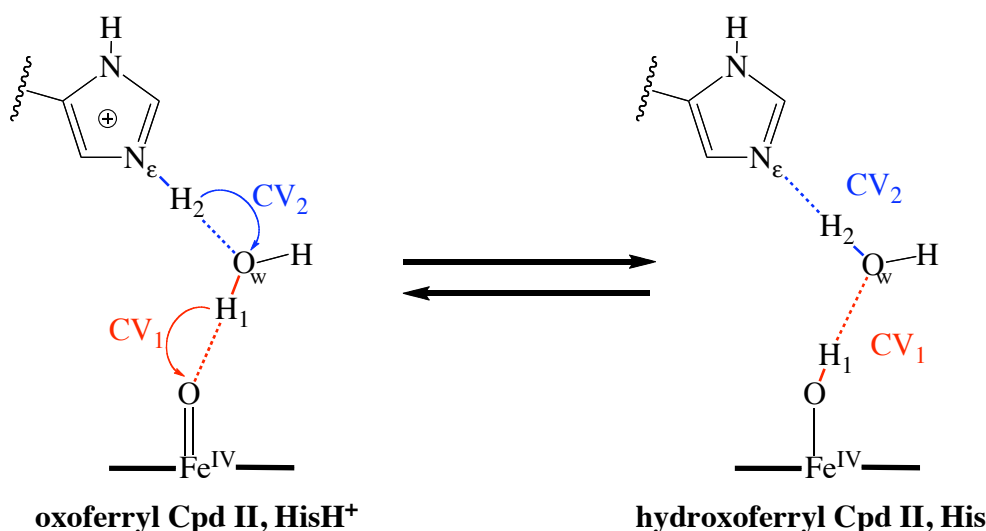


Figure 3. Collective variables used to model the water-mediated proton transfer from the protonated distal His to the oxoferryl.

The values of the threshold distance (d_{cut}) and the exponents (p and q) of the coordination numbers (see Chapter II, equation 20) are given in Table 2. The values for the mass of the fictitious particle (M) and the force constant (k) coupling it to the real system, as well as the height (w) and the width (δs) of the Gaussian history-dependent potential (see Chapter II, section 3) are also shown in Table 2. A new Gaussian-like potential was added every 150 MD steps (i.e. 18 ps).

Table 2. Parameters of the coordination numbers (d_{cut} , p and q) used as collective variables (CV_1 and CV_2), the harmonic potential coupling the fictitious particles to them (M and k) and the Gaussian history-dependent potential (w and δs).

HPC	d_{cut} (Å)	p	q	M (a.u.)	k (a.u.)	w (kcal/mol)	δs
CV_1	0.8	6	15	30	6	1	0.02
CV_2	1.8	3	18	3	3	1	0.05
PVC	d_{cut} (Å)	p	q	M (a.u.)	k (a.u.)	w (kcal/mol)	δs
CV_1	1.0	3	9	1	6	0.5	0.07
CV_2	1.0	6	12	1	6	0.5	0.07

Starting structures

To study the PT from the distal His to the oxoferryl (reaction **6** in Chapter V), the simulation should in principle start from the {oxoferryl Cpd II, HisH⁺} configuration on the left side of Figure 3. However, for HPC (heme b-containing catalase), this configuration is not stable and the PT occurred spontaneously during geometry optimization (see Chapter IV, section 2.1.), yielding the {hydroxoferryl Cpd II, neutral His} configuration on the right side of Figure 3. Hence, the PT in HPC was studied in the *reverse* direction (i.e. from hydroxoferryl Cpd II to oxoferryl Cpd II). For PVC (heme d-containing catalase), the PT was studied in the *forward* direction (i.e. from oxoferryl Cpd II to hydroxoferryl Cpd II), as the {oxoferryl Cpd II, HisH⁺} configuration is a stable minimum (see Chapter IV, section 2.1.).

Initial equilibration

Starting from the optimized geometries of HPC-**IIc** and PVC-**IIb**, CP QM/MM molecular dynamics at room temperature were performed in order to equilibrate the system (~ 1.7 ps for HPC and ~ 2.7 ps for PVC). The following parameters were used: $\delta t = 0.12$ fs (time step), $\mu_e = 700$ au (fictitious electronic mass of the CP Lagrangian), $\nu = 650$ cm⁻¹ (frequency of the Nosé-Hoover thermostat).

Metadynamics simulations

After equilibration, metadynamics simulations were initiated. To completely explore the free energy landscape, it was necessary to add ~ 230 / ~ 150 Gaussians for HPC / PVC, respectively. In

terms of simulation time, this corresponds to $\sim 3.5 \times 10^4 / \sim 2.3 \times 10^4$ MD steps ($\sim 4.1 / \sim 2.7$ ps). The metadynamics simulations were stopped once recrossing to the initial state was observed.

1.4. Classical molecular dynamics simulations of the ET from Tyr to Cpd I in HPC

Starting structures

Classical MD simulations were performed for the RO and OR states of HPC (see Chapter II, section 4.4.). The RO state correspond to {Tyr, Cpd I} configuration, i.e. reduced Tyr and oxidized heme, whereas the OR state is a {Tyr⁺, Cpd II} configuration, i.e. oxidized Tyr and reduced heme (Figure 4).

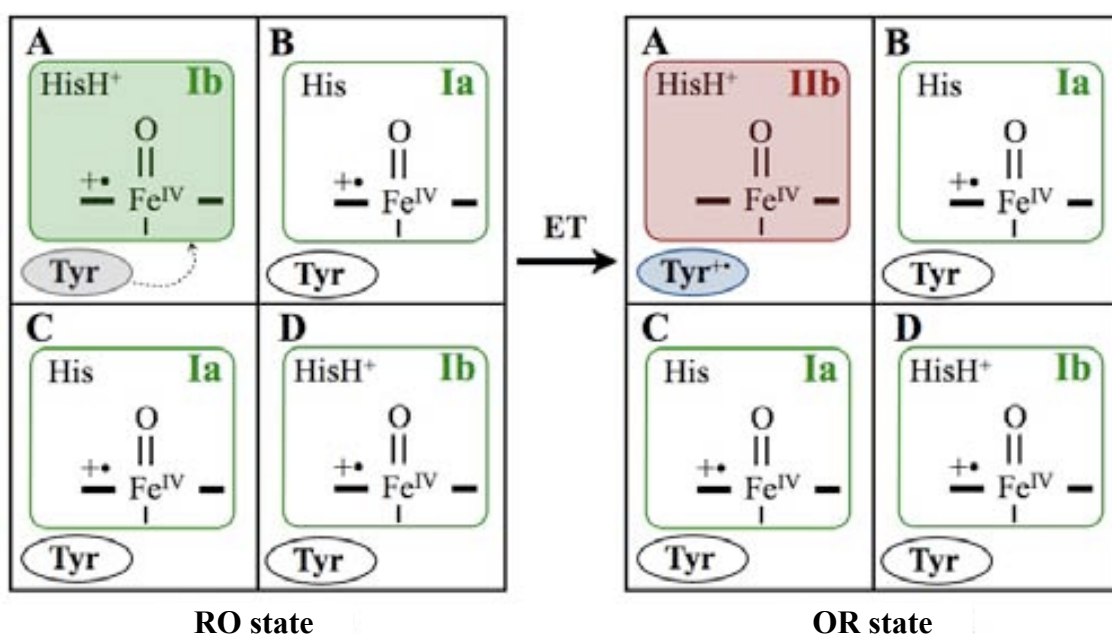


Figure 4. Schematic representation of the oxidation and protonation states of the active site and the Tyr in each of the four catalase subunits (A-D), as employed in the classical molecular dynamics of the {Tyr, Cpd I} (RO) and {Tyr⁺, Cpd II} (OR) states of HPC. The oxidation state of the heme is denoted as I or II (Cpd I or Cpd II, respectively). The protonation state of the distal His is indicated as **a** and **b** (neutral or protonated His, respectively). The reduced form of tyrosine is **Tyr**, whereas **Tyr⁺** is the oxidized form.

The RO state (i.e. {Tyr, Cpd I}) coincides with the O state in section 1.1.. The starting structure for the OR state (i.e. {Tyr⁺, Cpd II}) was taken as a snapshot of the R state in section 1.1. (i.e. {Tyr, Cpd II}), after 2 ns of equilibration in the NPT ensemble. Tyr was then converted into

Tyr^{•+} by changing the point charges of this residue, generating the starting structure of the {Tyr^{•+}, Cpd II} state .

Simulation details

The bonding and van der Waals parameters of the Tyr cation radical were taken to be the same as for the neutral Tyr in AMBER version 99 (Cheatham, 1999), whereas the RESP charges were reparametrized. The ESP charges (at BP86/6-31^{++G**} level) were obtained with the Gaussian program (Frisch, 2004), using the CPMD gas phase optimized geometries of isolated Tyr^{•+} (see section 3.1.). The RESP charges were then fitted with the Antechamber program (Wang, 2006) in the AMBER package (Pearlman, 1995). Overall, the parameters of the RO and the OR states are identical, except for the RESP charges of the Tyr and the heme active site (i.e. the heme, the proximal Tyr and Arg, the pocket water and the distal His) in subunit A (Figure 4).

The system was equilibrated for 10 ns in the NPT ensemble. Afterwards, the simulation was continued by 10 ns more to obtain an ensemble of configurations (see section 1.5.).

1.5. QM/MM calculations of the ET from Tyr to Cpd I in HPC

Ensemble of configurations

To calculate the free energy of ET from Tyr to Cpd I in HPC (reaction **15**), 21 snapshots were extracted from the last 10 ns of the classical MD simulations of each oxidation state (RO and OR), i.e. 42 snapshots in total.

Model

The QM region used is shown in Figure 5. It comprises Tyr351 (modeled as methylphenolate), His 343 (methylimidazole), Glu1516 (acetate), Arg344 (methylguanidinium) and two water molecules hydrogen-bonded to them, and it is contained in a cubic box of dimensions $14.28 \times 17.46 \times 18.78 \text{ \AA}^3$. The charge of the QM system is 0 for neutral Tyr and +1 for the cation radical, and the multiplicity is a singlet and a doublet, respectively. The rest of computational details (PW cutoff, QM-MM boundary, cutoff radii for QM-MM electrostatic interactions) are the same as in section 1.2..

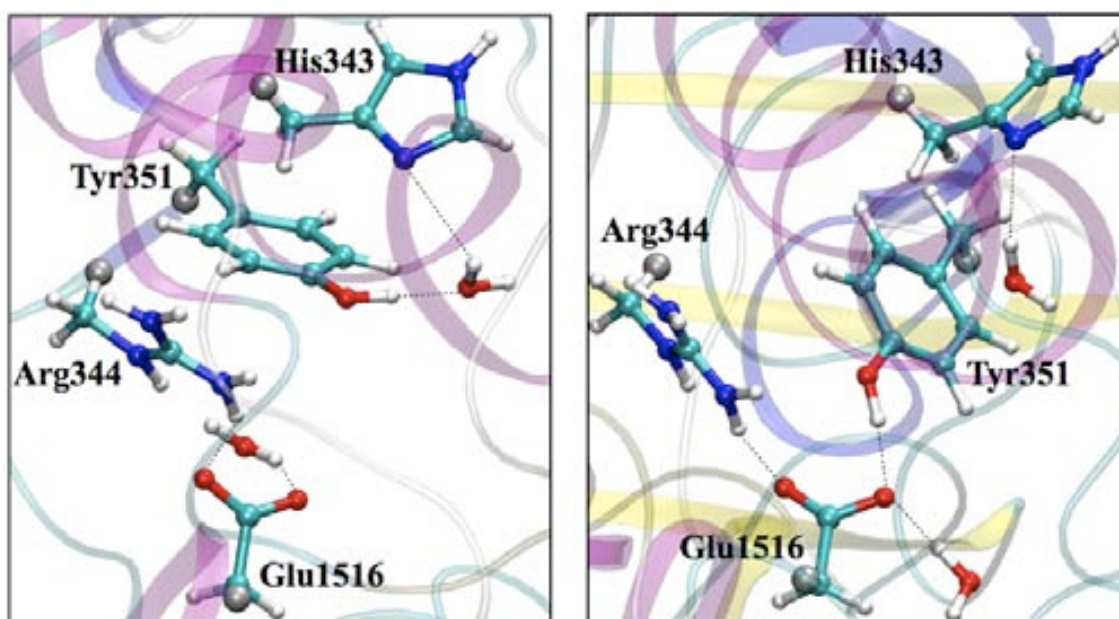


Figure 5. QM-MM partition used in the calculation of the vertical ionization energies of Tyr. The QM region is displayed in ball and stick representation and the link atoms are coloured in silver. Two representative configurations of the His-conf (*left*) and Glu-conf (*right*) conformations are shown (see Chapter V, section 3.6.).

Calculation of the free energy of ET from Tyr351 to Cpd I ($\Delta G^{\text{Tyr/Cpd I, ET}}$)

As explained in Chapter II (section 4.4.), ET from Tyr351 to Cpd I can be decomposed into two separate processes:



If the MD is carried out in the RO state (i.e. {Tyr, Cpd I}), the vertical ET energy (ΔE) is calculated as:

$$\Delta E_{\text{Tyr, Cpd I}} = \text{IP (Tyr)} - \text{EA (Cpd I)} \quad (\text{eq. 3})$$

whereas in the OR state (i.e. {Tyr^{*+}, Cpd II}), it is:

$$\Delta E_{\text{Tyr}^{*+}, \text{Cpd II}} = \text{EA (Tyr}^{*+}) - \text{IP (Cpd II)} \quad (\text{eq. 4})$$

The residue that gets ionized (the heme or Tyr) is treated at the QM level, whereas the other redox partner (Tyr or the heme, respectively), the protein and the solvent are described by MM (see Chapter IV, section 4.4.). The calculation of the EA of Cpd I and the IP of Cpd II was performed as described in section 1.2. (Table 1). The IP of Tyr and the EA of Tyr^{*+} were calculated in an analogous way as:

$$\text{IP}_{\text{Tyr}} = (\Delta E_0)_{\text{Tyr}} = E_{\text{Tyr}^{*+}}(\text{R}_{\text{Tyr}}) - E_{\text{Tyr}}(\text{R}_{\text{Tyr}}) \quad (\text{eq. 5})$$

$$\text{EA}_{\text{Tyr}^{*+}} = (\Delta E_0)_{\text{Tyr}^{*+}} = E_{\text{Tyr}^{*+}}(\text{R}_{\text{Tyr}^{*+}}) - E_{\text{Tyr}}(\text{R}_{\text{Tyr}^{*+}}) \quad (\text{eq. 6})$$

Then, the driving force and the reorganization free energy are calculated applying the linear response (LR) approximation:

$$\Delta A = (\langle \Delta E \rangle_{\text{Tyr, Cpd I}} + \langle \Delta E \rangle_{\text{Tyr}^{\bullet+}, \text{Cpd II}}) / 2 \quad (\text{eq. 7})$$

$$\lambda = (\langle \Delta E \rangle_{\text{Tyr, Cpd I}} - \langle \Delta E \rangle_{\text{Tyr}^{\bullet+}, \text{Cpd II}}) / 2 \quad (\text{eq. 8})$$

1.6. QM/MM optimizations of the tyrosyl cation radical

Models

To investigate the protonation state of the tyrosyl cation radical, two snapshots containing Tyr351 in the oxidized state were extracted from the {Tyr^{•+}, Cpd II} classical MD, one corresponding to the His-conformation and the other to the Glu-conformation (see Chapter V, Figure 15). QM/MM optimizations of the tyrosyl radical were performed both without constraints and fixing the O_{Tyr}-H_{Tyr} distance. For comparison, a snapshot containing Tyr351 in the reduced state was also extracted from the {Tyr, Cpd I} classical MD.

Computational details

The computational details are the same as in section 1.5., except that the PW cutoff was reduced to 70 Ry, which is accurate for structural properties. In the reduced state (i.e. neutral tyrosine) and the His-conformation of the oxidized state (i.e. tyrosyl radical), the QM region was reduced to His343, Tyr351 and the water molecule hydrogen-bonded to them, as Glu1516 and Arg344 are far enough to be well described by the forcefield. For the Glu-conformation of the oxidized state, the complete QM region shown in Figure 5 is used.

Calculation of the inner-sphere redox energies

Table 3 shows the equations used to calculate the inner-sphere redox energies of tyrosine (see also equations 28-32 in Chapter II). B denotes the base hydrogen-bonded to Tyr, either His or Glu (see Figure 5). Tyr (B) is the reduced state (tyrosine), whereas Tyr^{•+} (B) and Tyr[•] (+HB) represent the oxidized state, either a tyrosyl cation radical (*plus* a deprotonated base) or a tyrosyl neutral radical (*plus* a protonated base). E_M (R_M), M = reduced or oxidized Tyr, is the ground state QM potential energy, and thus the redox energies should be regarded as inner-sphere (i.e. they only include the contribution of the tyrosine and first-shell ligands). R_M denotes the ion configuration, i.e. the optimized structure of Tyr (B), Tyr^{•+} (B) or Tyr[•] (+HB). IP and EA are the ionization potential and the electron affinity, ΔE is the adiabatic energy of reduction, and λ is the reorganization energy.

Table 3. Equations used to calculate the redox energies of tyrosine / tyrosyl neutral radical or tyrosine / tyrosyl cation radical. B = His or Glu hydrogen-bonded to Tyr (see Figure 5).

Tyr (B) / Tyr[•] (+HB)^a	Tyr (B) / Tyr^{•+} (B)^b
$EA^i_{\text{Tyr}^{\bullet}(\text{+HB})} = E_{\text{Tyr}^{\bullet}(\text{+HB})}(\text{R}_{\text{Tyr}^{\bullet}}) - E_{\text{Tyr}(\text{B})}(\text{R}_{\text{Tyr}^{\bullet}(\text{+HB})})$	$EA^i_{\text{Tyr}^{\bullet+}(\text{B})} = E_{\text{Tyr}^{\bullet+}(\text{B})}(\text{R}_{\text{Tyr}^{\bullet+}(\text{B})}) - E_{\text{Tyr}(\text{B})}(\text{R}_{\text{Tyr}^{\bullet+}(\text{B})})$
$IP^i_{\text{Tyr}(\text{B})} = E_{\text{Tyr}^{\bullet+}(\text{B})}(\text{R}_{\text{Tyr}(\text{B})}) - E_{\text{Tyr}(\text{B})}(\text{R}_{\text{Tyr}(\text{B})})$	$IP^i_{\text{Tyr}(\text{B})} = E_{\text{Tyr}^{\bullet+}(\text{B})}(\text{R}_{\text{Tyr}(\text{B})}) - E_{\text{Tyr}(\text{B})}(\text{R}_{\text{Tyr}(\text{B})})$
$\Delta E^i = E_{\text{Tyr}^{\bullet}(\text{+HB})}(\text{R}_{\text{Tyr}^{\bullet}(\text{+HB})}) - E_{\text{Tyr}(\text{B})}(\text{R}_{\text{Tyr}(\text{B})})$	$\Delta E^i = E_{\text{Tyr}^{\bullet+}(\text{B})}(\text{R}_{\text{Tyr}^{\bullet+}(\text{B})}) - E_{\text{Tyr}(\text{B})}(\text{R}_{\text{Tyr}(\text{B})})$
$\lambda^i = (IP^i_{\text{Tyr}(\text{B})} - EA^i_{\text{Tyr}^{\bullet}(\text{+HB})}) / 2$	$\lambda^i = (IP^i_{\text{Tyr}(\text{B})} - EA^i_{\text{Tyr}^{\bullet+}(\text{B})}) / 2$

^a QM/MM optimized structures without constraints. ^b QM/MM optimized structures fixing the O_{Tyr}-H_{Tyr} distance.

2. PRELIMINARY CALCULATIONS ON CPD I REDUCTION

2.1. Gas phase vertical ionization energies of Cpd I and Cpd II

Before computing the Cpd I reduction potential of HPC and PVC, we probed the intrinsic redox properties of the heme b and heme d cofactors, i.e. without the influence of the protein environment.

• Computational details

Models

The electron affinity of Cpd I (EA) and the ionization potential of Cpd II¹ (IP) were calculated for the optimized gas phase models **1-4** described in Chapter III.

Simulation details

The computational details are the same as in Chapter III, except that the iron pseudopotential was changed to a sixteen valence electrons (semicore) pseudopotential and the PW kinetic energy cutoff was increased up to 90 Ry. As mentioned in section 1.1., the geometry is hardly affected by the iron pseudopotential employed, while the change in the vertical ionization energies is larger (Blumberger, 2006 & 2008).

Calculation of the gas phase redox energies

Table 4 shows the equations used to calculate the gas phase redox energies of Cpd I and Cpd II (see also equations 28-32 in Chapter II). $E_M(\text{R}_M)$, $M=\text{Cpd I, Cpd II}$, is the ground state potential

¹ Cpd II is used as a model of Cpd I* because both Compounds are isoelectronic in the heme active site.

energy in the oxidized or the reduced state and R_M denotes the ion configuration (i.e. the optimized structure of Cpd I or Cpd II). IP and EA are the ionization potential and the electron affinity, ΔE is the adiabatic energy of reduction and λ is the reorganization energy.

Table 4. Equations used to calculate the redox energies of Cpd I and Cpd II.

$EA = E_{\text{Cpd I}}(R_{\text{Cpd I}}) - E_{\text{Cpd II}}(R_{\text{Cpd I}})$	$\Delta E = E_{\text{Cpd II}}(R_{\text{Cpd II}}) - E_{\text{Cpd I}}(R_{\text{Cpd I}})$
$IP = E_{\text{Cpd I}}(R_{\text{Cpd II}}) - E_{\text{Cpd II}}(R_{\text{Cpd II}})$	$\lambda = (\lambda_R + \lambda_O) / 2 = (IP - EA) / 2$

• Results and discussion

Table 5 shows the redox energies of Cpd I and Cpd II for both heme groups. For all the models considered (see Chapter III, Figure 2), the electron affinities of both cofactors are rather similar, in agreement with the saturation across the C_β atoms of pyrrole III in heme d not destroying the aromatic character of the macrocycle (Timkovich & Bondoc, 1990). Therefore, the reduction potentials of heme b and heme d are expected to be similar as well.

Table 5. Gas phase redox energies (in eV) of Cpd I and Cpd II for heme b / heme d.

	model 1 ^a	model 2 ^b	model 3 ^c	model 4 ^d (Fe=O)	model 4 ^d (Fe-OH)
IP	7.00 / 6.85	6.52 / 6.45	6.17 / 6.30	8.16 / 8.06	8.45 / 8.34
EA	6.95 / 6.66	6.47 / 6.34	5.73 / 5.89	7.82 / 7.81	7.82 / 7.81
ΔE	6.98 / 6.77	6.51 / 6.41	5.93 / 6.04	7.80 / 7.84	8.26 / 8.16
λ	0.02 / 0.09	0.02 / 0.05	0.22 / 0.21	0.17 / 0.12	0.32 / 0.26

^a Heme cofactor without substituents except the *cis*-hydroxy- γ -spirolactone modification of heme d.

^b Heme cofactor with substituents.

^c Model 1 with the proximal Tyr and Arg residues.

^d Gas phase model equivalent to the QM region used in the QM/MM calculations (see Figure 2).

For gas phase model 1, the porphyrin cation radical (i.e. heme b Cpd I) has a higher EA than the chlorin (i.e. heme d Cpd I), indicating that heme b is easier to reduce than heme d. The macrocycle substituents (model 2) reduce the EA, most likely because the methyl and vinyl groups and the propionic sidechains are electron donating groups, and thus they stabilize the positive charge on the oxidized macrocycle (He, 1996). The addition of the proximal Tyr and Arg (model 3) further reduces the EA, because the negative charge of the proximal ligand stabilizes the high-valent iron (i.e. the *push* effect, see for instance (Wang & deVisser, 2007)). The decrease in the EA is

larger for heme b than for heme d, and thus heme d becomes easier to reduce than heme b. The last model (model **4**) is equivalent to the QM region used in the QM/MM calculations (see Figure 2), and shows the largest EA values, suggesting that hydrogen-bonding to the distal residues favours reduction of Cpd I into Cpd II or Cpd I*. The electron affinity of both hemes is almost identical, and thus *the propensity for reduction of Cpd I is expected to be almost identical for heme b and heme d.*

The IP of both hemes are also rather similar for all the models considered, and thus *the propensity of Cpd II for oxidation is expected to be almost identical for heme b and heme d.* In parallel to the EA, stabilization of the macrocycle cation radical upon inclusion of the pyrrole substituents (model **2**) and the proximal Tyr and Arg (model **3**) decrease the IP, whereas incorporation of the distal residues (HisH⁺ and the pocket water) in model **4** disfavours oxidation of Cpd II (or Cpd I*) back to Cpd I.

Interestingly, the hydroxoferryl (i.e. Fe–OH) form of Cpd II model **4** is more stable than the oxoferryl (i.e. Fe=O) by 10.7 / 7.4 kcal/mol (HPC / PVC, respectively). Hence, *protonation of the oxoferryl upon ET is expected to increase significantly the exothermicity of Cpd I reduction.* Besides, proton transfer from His to the oxoferryl increases the IP by ~300 meV, i.e. the neutral hydroxoferryl Cpd II is harder to oxidize than the negatively charged oxoferryl Cpd II. Therefore, *protonation of the oxoferryl group most likely hinders the oxidation of Cpd II (or Cpd I*) back to Cpd I.*

Regarding the reorganization energies, models **1** and **2** show similar values (~ 10-90 meV) to those calculated (50-98 meV) (Sigfridsson, 2001) or measured experimentally (120-140 meV) for ZnP (Amashukeli, 2004), taking into account DFT calculations are known to underestimate them. The inclusion of the proximal Tyr and Arg (model **3** and **4**) increases the reorganization energies, due to a significant shortening of the hydrogen bonds between the proximal Tyr⁻ and Arg⁺ upon reduction. In Cpd I the tyrosinate bears some radical character (Green, 2001; Rydberg, 2004; de Visser, 2006; Alfonso-Prieto, 2007), thus weakening the hydrogen-bonds with the Arg. By contrast, upon reduction, this partial radical character is quenched, and thus the Tyr-Arg salt bridges strengthen.

In model **4**, proton transfer to the oxoferryl further increases λ , as expected for a PCET (i.e. oxoferryl Cpd I \rightarrow hydroxoferryl Cpd II) compared to a pure ET (oxoferryl Cpd I \rightarrow oxoferryl Cpd II). Whereas the iron-axial ligand distances remain almost identical upon ET (see Chapter IV), concomitant protonation of the oxoferryl lengthens the Fe-O distance and shortens the Fe-O_{Tyr} bond (Rovira, 2005; Alfonso-Prieto, 2007).

2.2. QM/MM vertical ionization energies of Cpd I and Cpd II

Several studies have demonstrated that oxo-iron hemes are chameleonic species very sensitive to changes in the local environment (deVisser, 2003 & 2006; De Biase, 2007). They have a manifold of close-lying molecular orbitals, whose relative ordering and possible mixing is easily modified, thus changing the molecular orbital where the electron is inserted or removed from (see Chapter III). Therefore, we decided to investigate the effect of the closest protein environment of HPC and PVC (i.e. residues within 20 Å of the heme iron) on the redox properties of the heme b and heme d cofactors, respectively.

• *Computational details*

Models

Calculation of the vertical ionization energies were performed using the optimized structures of the QM/MM models **Ib** (oxidized state) and **Iib** and **Iic** (reduced states)² described in Chapter IV. As shown in Figure 6, Cpd I bears an oxoferryl group (**Ib**), whereas Cpd II can contain either an oxoferryl (**Iib**) or a hydroxoferryl (**Iic**) moiety. Therefore, two different processes may occur: a simple ET (oxoferryl Cpd I \rightarrow oxoferryl Cpd II) or a PCET (oxoferryl Cpd I \rightarrow hydroxoferryl Cpd II).

The QM region and the QM-MM interface used are the same as in section 1.1.. The MM region only comprises the residues within 20 Å of the iron heme, whereas in section 1.1. it includes the complete tetrameric protein with solvent and counterions.

² Cpd II have the same heme electronic configuration as Cpd I*.

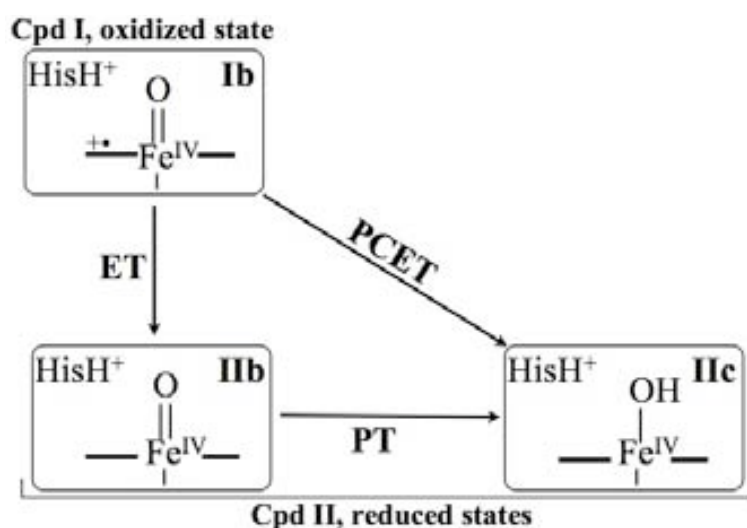


Figure 6. Possible stationary states during Cpd I reduction.

Computational details

The DFT and molecular mechanics details are the same as in section 1.1.. Only the cutoff radii for handling the electrostatic interactions between the QM and MM regions (Laio, 2002a) was changed. r_{NN} , r_{MIX} and r_{ESP} were set to 30 Å, such that for all the MM atoms the electrostatic QM-MM interaction energy is calculated from the electrons + nuclei density on the QM subsystem and the point charges of the MM atoms (see Chapter II, section 2.3.).

Calculation of the QM/MM redox energies

Table 6 shows the equations used to calculate the QM/MM redox energies of Cpd I and Cpd II (see also equations 28-32 in Chapter II). $E_{\text{M}}(\text{R}_{\text{M}})$, $\text{M}=\text{Cpd I, Cpd II}$, is the ground state QM potential energy in the oxidized or the reduced state. Because it only includes the contribution of the heme and the first-shell ligands (Figure 2), the redox energies should be regarded as inner-sphere. R_{M} denotes the ion configuration (i.e. the optimized structure of Cpd I or Cpd II). IP and EA are the ionization potential and the electron affinity, respectively. ΔE is the adiabatic energy of reduction and λ is the reorganization energy.

Table 6. Equations used to calculate the redox energies of Cpd I and Cpd II.

$EA^i = E_{\text{Cpd I}}(\text{R}_{\text{Cpd I}}) - E_{\text{Cpd II}}(\text{R}_{\text{Cpd I}})$	$\Delta E^i = E_{\text{Cpd II}}(\text{R}_{\text{Cpd II}}) - E_{\text{Cpd I}}(\text{R}_{\text{Cpd I}})$
$IP^i = E_{\text{Cpd I}}(\text{R}_{\text{Cpd II}}) - E_{\text{Cpd II}}(\text{R}_{\text{Cpd II}})$	$\lambda^i = (IP^i - EA^i) / 2$

• Results and discussion

Table 7 shows the redox energies obtained for HPC and PVC. The electron affinity (EA) of Cpd I is 0.14 eV (HPC) or 0.18 eV (PVC) lower than the corresponding gas phase model 4 (Table 5), due to the polarization of the QM electronic density by the MM point charges. Nevertheless, the EA difference between heme b-containing HPC and heme d-containing PVC (30 meV) is again small, as between gas phase heme b and heme d (10 meV for model 4). Although heme d has one less double bond compared to heme b, the aromatic character of the macrocycle is maintained (Timkovich & Bondoc, 1990), and thus the stability of the heme d cation radical is not very different from the heme b cation radical. Therefore, both the gas phase and the QM/MM results indicate that the Cpd I reduction potentials of HPC and PVC are most likely similar³.

Table 7. Inner-sphere redox energies (in eV) of oxoferryl Cpd I and oxoferryl Cpd II for HPC and PVC. IP^i and EA^i are the ionization potential and the electron affinity, and λ^i is the reorganization energy (see Table 6). The values in parentheses correspond to the PCET process (oxoferryl Cpd I \rightarrow hydroxoferryl Cpd II).

	HPC	PVC	(HPC – PVC)
IP^i	8.15 (8.69)	8.08 (8.53)	0.07 (0.04)
EA^i	7.96	7.99	0.03
λ^i	0.09 (0.37)	0.05 (0.27)	0.04 (0.10)

The difference in the IP of Cpd II between the two catalases (70 meV) is of the same order as between gas phase models of heme b and heme d (100 meV for Fe=O model 4). The IP of the hydroxoferryl Cpd II is again larger than for the oxoferryl form. Therefore, both gas phase and QM/MM results indicate that protonation of the oxoferryl Cpd II hinders the oxidation back to Cpd I.

The reorganization free energies for the ET between the oxoferryl forms of Cpd I and Cpd II are ~94 and ~45 meV for HPC and PVC⁴, respectively, similar to those calculated for model

³ The differences with the average inner-sphere ionization energies at 300 K (see Chapter V-Table 2) may be explained by (i) the possible error in the IP and EA calculations at the optimized structures, owing to the model only including the residues within 20 Å of the heme iron, (ii) temperature effects and (iii) the possible error introduced in the calculation of the average IP and EA at 300 K by sampling the dynamics with a force field.

⁴ The reorganization energy of heme d (PVC) at the optimized structures is lower than the average λ^i calculated at 300 K. This is because the hydroxyl group of the cofactor is in the same conformation in the oxidized and reduced optimized structures, whereas during the dynamics of the oxidized state it is observed to fluctuate between two conformations (see Chapter V, Figure 4).

porphyrins, such as FeP(im)₂ (85 meV) (Sigfridsson, 2001) or ZnP (50-98 meV) (Amashukeli, 2004). This is consistent (Jensen & Ryde, 2001) with the small changes in the iron-ligand distances upon ET (see Chapter IV-Tables 2 and 3). By contrast, λ is larger for the oxoferryl Cpd I \rightarrow hydroxoferryl Cpd II process, as expected for a PCET (see Figure 4), because protonation of the oxoferryl lengthens the Fe-O distance and shortens the Fe-O_{Tyr} bond (Rovira, 2005; Alfonso-Prieto, 2007).

In summary, the almost identical EA values suggest that *the propensity of PVC (heme d) Cpd I to be reduced to Cpd II or Cpd I* is similar to HPC (heme b)*. Besides, the larger IP values for the hydroxoferryl Cpd II compared to the oxoferryl Cpd II indicate that *protonation of the oxoferryl Cpd II or Cpd I* hinders its oxidation back to Cpd I*.

2.3. Protonation of the Fe=O group and the distal His

Before computing the free energy of PT from the distal His to the oxoferryl Cpd II⁵, it is useful to analyze separately the protonation energies of the proton donor (the distal His) and the proton acceptor (Fe=O), and whether the heme oxidation state affects them.

• Computational details

Models

As shown in Figure 7, calculation of the protonation energies of the Fe=O group, protE(Fe=O), and the distal His, protE(His), were performed using the QM/MM models **Ia**, **Ib**, **Ic**, **IIa**, **IIb** and **IIc** described in Chapter IV.

Simulation details

All the calculations were performed as explained in Appendix A (section 2).

Calculation of the protonation energies (protE)

Protonation energies (protE) of the Fe=O group and the distal His in each oxidation state were calculated as:

$$\begin{aligned} \text{protE}(\text{His}^{\text{Cpd I}}) &= E(\mathbf{Ib}) - E(\mathbf{Ia}) \quad , \quad \text{protE}(\text{His}^{\text{Cpd II}}) = E(\mathbf{IIb}) - E(\mathbf{IIa}) \\ \text{protE}(\text{FeO}^{\text{Cpd I}}) &= E(\mathbf{Ic}) - E(\mathbf{Ia}) \quad , \quad \text{protE}(\text{FeO}^{\text{Cpd II}}) = E(\mathbf{II}) - E(\mathbf{IIa}) \end{aligned}$$

⁵ The heme electronic configuration and the protonation state of oxoferryl (Fe=O) are the same in Cpd II and Cpd I*.

where E is the ground state QM potential energy at the QM/MM optimized structure of each configuration. The change in the protonation energies upon reduction from Cpd I to Cpd II was computed as:

$$\Delta\text{protE}(\text{His}) = \text{protE}(\text{His}^{\text{Cpd II}}) - \text{protE}(\text{His}^{\text{Cpd I}})$$

$$\Delta\text{protE}(\text{FeO}) = \text{protE}(\text{FeO}^{\text{Cpd II}}) - \text{protE}(\text{FeO}^{\text{Cpd I}})$$

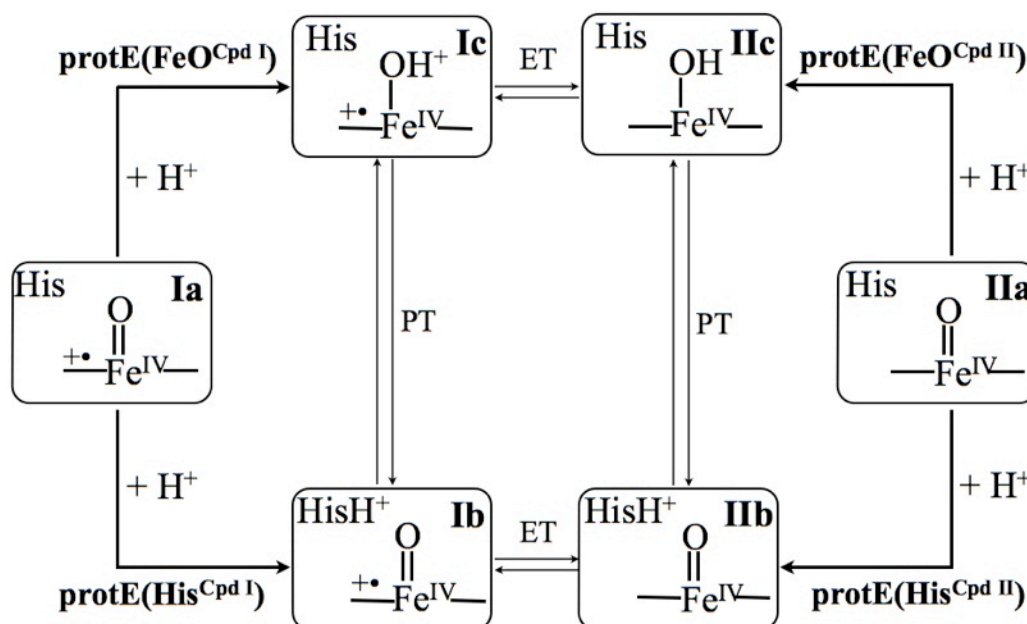


Figure 7. Relationship between the different protonation states of Cpd I and Cpd II. Protonation energies (protE) are calculated for the addition of a proton either on the heme oxoferryl moiety ($\text{Fe}=\text{O} + \text{H}^+ \rightarrow \text{Fe}-\text{OH}$) or the distal His ($\text{His} + \text{H}^+ \rightarrow \text{HisH}^+$).

• Results and discussion

The protonation energies obtained for the oxidized (Cpd I) and reduced (Cpd II) states are shown in Table 8 (protE(FeO)) and 9 (protE(His)).

Table 8. Protonation energies (in kcal/mol) of the $\text{Fe}=\text{O}$ group in the oxidized (Cpd I) and reduced (Cpd II) states.

catalase	protE ($\text{FeO}^{\text{Cpd I}}$)	protE ($\text{FeO}^{\text{Cpd II}}$)	$\Delta\text{protE}(\text{FeO})^c$
HPC (<i>heme b</i>)	-244.86	-317.70	-72.84
PVC (<i>heme d</i>)	-218.22	-269.11	-50.89

The heme oxoferryl group is found to be more prone to protonation in Cpd II than in Cpd I ($\Delta\text{protE}(\text{FeO}) < 0$). This is in agreement with the fact that Cpd II of several hemeproteins is basic (see section 1), and may be explained in terms of charge balance, i.e. in case electron transfer is accompanied by protonation, Cpd II maintains the same charge as Cpd I (Nilsson, 2004; Green, 2004 & 2006; Silaghi-Dumitrescu, 2007). Therefore, it is very likely that either ET occurs previous to PT (ET+PT) or they are concerted (PCET), as assumed in Chapter V, section 2.1..

Table 9. Protonation energies (in kcal/mol) of the distal His in the oxidized (Cpd I) and reduced (Cpd II) states.

catalase	protE (His^{Cpd I})^a	protE (His^{Cpd II})^b	$\Delta\text{protE (His)}$^c
HPC (heme b)	-262.65	-327.77	-65.12
PVC (heme d)	-239.42	-294.45	-55.03

Likewise, reduction from Cpd I to Cpd II increases the basicity of the distal His ($\Delta\text{protE}(\text{His}) < 0$). This is in agreement with the pKa values observed experimentally for the distal His of HRP (5.0 for Cpd I and 8.6 for Cpd II) (Jones and Dunford, 2006). This pKa shift was explained in terms of an electron density circuit (EDC) model (Jones and Dunford, 2005 & 2006), which might be applied to catalases as well. Because one electron is added to the porphyrin ring, reduction from Cpd I to Cpd II increases the heme electron density. In turn, this strengthens the hydrogen-bonding network connecting one of the heme propionates and the distal His (heme-COO⁻...Wat...Ser...HisH⁺; see Chapter I, Figure 7), thus stabilizing the protonated His in the Cpd II state.

Comparing HPC and PVC, the protonation energy of the distal His is lower in HPC than in PVC for both oxidation states (Cpd I and Cpd II). This may have an orbital explanation. In PVC Cpd I the half-filled occupied porphyrin orbital is the a_{1u} orbital, which has nodes on the pyrrole carbon atoms, and thus can mix with the π orbitals of the distal His stacked above pyrrole III (see Chapter IV, Figure 9). As a consequence, the electron density of the distal His decreases, making it less prone to protonation. Therefore, at the same pH, the percentage of protonated distal His is expected to be lower in PVC Cpd I than in HPC. Assuming Cpd I* formation starts from a Cpd I configuration with a protonated distal His (see Chapter V, section 2.1.), our results suggest that a lower pH is required to trigger Cpd I* reduction in PVC compared to HPC.

It can also be observed that the protonation energy of the oxoferryl Cpd II is lower in HPC than in PVC. This is in agreement with PT from the distal His to the oxoferryl group being spontaneous for HPC Cpd II, but not for PVC (see Chapter IV-section 2.1.). Again, this may have an orbital explanation. During ET to HPC Cpd I, an electron is inserted into the a_{2u} porphyrin orbital. Because this orbital mixes with the π system of the proximal phenolate ligand, the electron density increases on the Fe-Tyr bond, and, in turn, on the Fe-O bond due to the push-pull effect (Wang & deVisser, 2007). This results in a more negatively charged oxo group, and thus a larger proton affinity.

In summary, our calculations predict that *reduction from Cpd I to Cpd II or Cpd I* increases the pKa of both the oxoferryl group and the distal His*. This reinforces our previous assumption that in Cpd I reduction either ET precedes PT (ET+PT) or both transfers are concerted (PCET). PCET is very likely to occur for HPC, as the PT from the distal His to the oxoferryl Cpd II was found to be spontaneous (Chapter IV, section 2.1.). By contrast, this is not the case for PVC, since (i) the percentage of protonated distal His in the Cpd I state is lower, and (ii) the oxoferryl Cpd II is less basic.

3. PRELIMINARY CALCULATIONS ON TYROSINE OXIDATION

Calculations on gas phase models of tyrosine were performed in order to get a first insight into (i) the protonation state of the tyrosyl cation radical and (ii) the intrinsic redox properties of Tyr.

• *Computational details*

Models

Figure 8 show the three gas phase models studied. Model **1** represents an isolated Tyr (modeled as methylphenol), whereas models **2** and **3** correspond to a hydrogen-bonded Tyr. In model **2** Tyr is hydrogen-bonded to a His (methylimidazole) through a water molecule. By contrast, in model **3** Tyr is hydrogen-bonded to a Glu-Arg salt bridge (modeled as acetate and methylguanidinium, respectively). Therefore, models **2** and **3** are equivalent to the His- and Glu-conformations observed in HPC (see Chapter V, Figure 15), respectively.

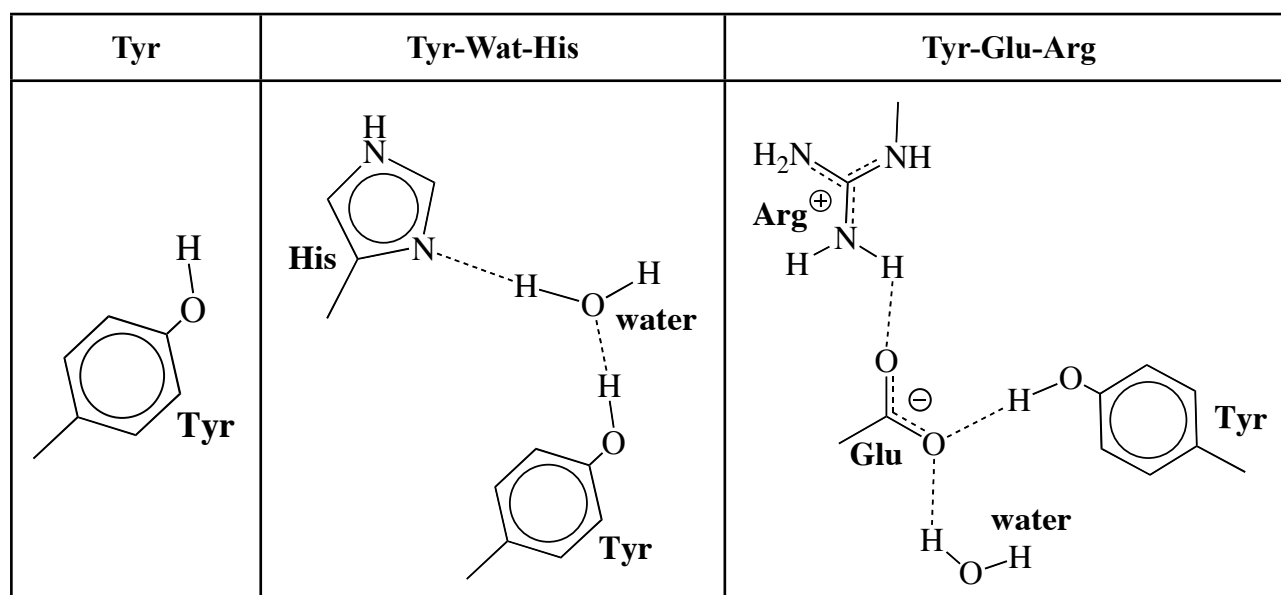


Figure 8. Gas phase models of an isolated Tyr (Tyr) and a hydrogen-bonded Tyr (His-Wat-Tyr or Arg-Glu-Tyr).

Geometry optimizations

For all the models, the reduced state (Tyr) is a closed-shell singlet with charge 0. In the oxidized state (Tyr⁺), the charge increases up to +1 and the multiplicity is a doublet. The geometry optimizations of the gas phase models were carried out as already described in Chapter III. The methylic carbon atoms of Tyr, His, Glu and Arg were fixed to mimic the sterix constraints imposed by the protein. Optimizations of models **2** and **3** in the oxidized state were carried out both without constraints and fixing the O_{Tyr}-H distance.

Calculation of the gas phase redox energies

The redox energies of the gas phase Tyr models were calculated applying the equations in Table 10 (see also equations 28-32 in Chapter II). E_M , $M=\text{Tyr, Tyr}^+$, is the ground state potential energy in the reduced or the oxidized state and R_M denotes the ion configuration (i.e. the optimized structure of Tyr or Tyr⁺). The vertical ionization energies are represented by IP (ionization potential) and EA (electron affinity), ΔE is the adiabatic energy of oxidation and λ is the reorganization energy. As explained in section 1.5., in these calculations the PW cutoff was increased up to 90 Ry (compared to the 70 Ry of the geometry optimizations).

Table 10. Equations used to calculate the redox energies of the gas phase Tyr models.

$EA = E_{\text{Tyr}^{\bullet+}}(\text{R}_{\text{Tyr}^{\bullet+}}) - E_{\text{Tyr}}(\text{R}_{\text{Tyr}^{\bullet+}})$	$\Delta E = E_{\text{Tyr}^{\bullet+}}(\text{R}_{\text{Tyr}^{\bullet+}}) - E_{\text{Tyr}}(\text{R}_{\text{Tyr}})$
$IP = E_{\text{Tyr}^{\bullet+}}(\text{R}_{\text{Tyr}}) - E_{\text{Tyr}}(\text{R}_{\text{Tyr}})$	$\lambda = (IP - EA) / 2$

- *Optimized structures*

Table 11 shows the main structural parameters describing the gas phase Tyr models in both oxidation states.

Table 11. Main distances (in Å) describing the gas phase Tyr models (shown in Figure 8) in the reduced (neutral tyrosine) and oxidized (tyrosyl radical) states.

model	Tyr		Tyr-Wat-His		Tyr-Glu-Arg	
	reduced	oxidized	reduced	oxidized	reduced	oxidized
$\text{C}_{\text{meta,Tyr}}-\text{C}_{\text{para,Tyr}}$	1.40	1.42-1.43	1.40-1.41	1.42	1.40	1.42-1.43
$\text{C}_{\text{orto,Tyr}}-\text{C}_{\text{meta,Tyr}}$	1.39-1.40	1.37	1.39-1.40	1.37	1.39-1.40	1.37
$\text{C}_{\text{ipso,Tyr}}-\text{C}_{\text{orto,Tyr}}$	1.40	1.42-1.43	1.40-1.41	1.45	1.40	1.45
$\text{C}_{\text{ipso,Tyr}}-\text{O}_{\text{Tyr}}$	1.38	1.33	1.37	1.28	1.38	1.29
$\text{O}_{\text{Tyr}}-\text{H}_{\text{Tyr}}$	0.95	0.99	1.01	1.65	1.05	1.62
$\text{H}_{\text{Tyr}}-\text{O}_{\text{Wat}}$	–	–	1.72	1.03	–	–
$\text{O}_{\text{Wat}}-\text{H}_{\text{Wat}}$	–	–	1.02	1.53	–	–
$\text{H}_{\text{Wat}}-\text{N}_{\delta,\text{His}}$	–	–	1.77	1.11	–	–
$\text{H}_{\text{Tyr}}-\text{O}_{\epsilon 1,\text{Glu}}$	–	–	–	–	1.58	1.04

In the reduced state (Tyr, Figure 9a), hydrogen-bonding hardly modifies the structure of tyrosine, except that it polarizes the $\text{O}_{\text{Tyr}}-\text{H}_{\text{Tyr}}$ bond, which lengthens by 0.06 / 0.10 Å (Tyr-Wat-His model or Tyr-Glu-Arg model, respectively).

By contrast, in the oxidized state ($\text{Tyr}^{\bullet+}$) hydrogen bonding results in a spontaneous deprotonation of the tyrosyl cation radical, as already reported (Kanamori, 2005; Sjödin, 2006, Markle, 2008; Zhang, 2008). In the Tyr-Wat-His model (Figure 9b) the water molecule mediates a PT between $\text{Tyr}^{\bullet+}$ and His, i.e. a neutral tyrosyl radical (Tyr^{\bullet}) and an imidazolium cation (HisH^+) are

formed. This is in agreement with the pKa of Tyr^{•+} (ca. -2) being lower than that of His (ca. 6). Likewise, in the Tyr-Glu-Arg model (Figure 9c) Tyr^{•+} transfers the proton to Glu, yielding Tyr[•] and a neutral carboxylic acid (GluH). This is again consistent with the pKa of Tyr^{•+} and Glu (ca. -2 and 4, respectively). Regardless of the proton acceptor, Tyr[•] shows a quinone-type geometry, as indicated by the shorter C_{ipso,Tyr}-O_{Tyr} distance (1.28-1.29 Å for Tyr[•] compared to 1.37-1.38 Å for Tyr, see Table 10). This is also consistent with the unpaired spin density being only delocalized over the tyrosyl radical (Figure 9).

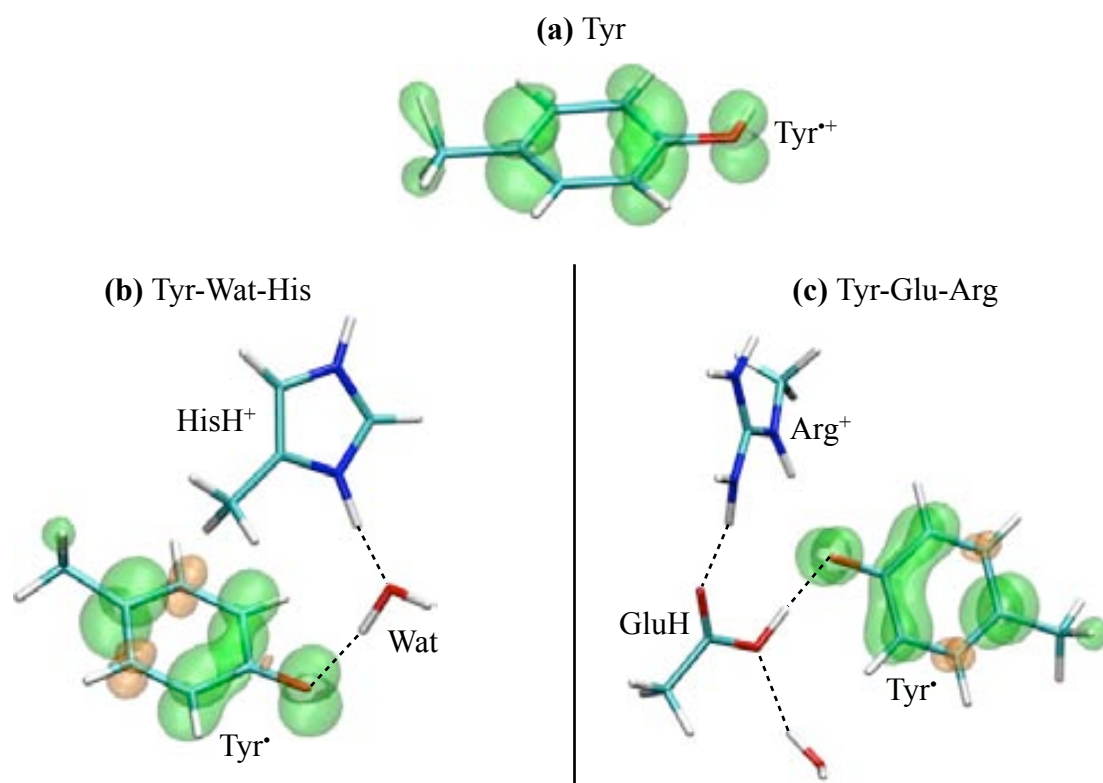


Figure 9. Spin density distributions of the gas phase models of tyrosine in the oxidized state (tyrosyl radical). (a) Tyr, (b) Tyr-Wat-His, and (c) Tyr-Glu-Arg. Spin isodensity surfaces are plotted at $0.004 e \text{ \AA}^{-3}$.

Therefore, *in case Tyr is already hydrogen-bonded to a nearby base (such as His or Glu), oxidation of tyrosine is accompanied by a spontaneous proton transfer, resulting in a neutral tyrosyl radical.* In other words, *oxidation of a hydrogen-bonded Tyr is a PCET process, as previously suggested (Fecenko, 2006; Sjödin, 2006; Irebo, 2008).*

• Redox properties

The redox energies associated to Tyr oxidation (Table 12) are calculated using equations in Table 10. For isolated Tyr, oxidation of Tyr is a pure ET (i.e. $\text{Tyr} \rightarrow \text{Tyr}^{++} + e^-$), whereas for the hydrogen-bonded models the process is a PCET (i.e. $\text{Tyr} + \text{B} \rightarrow \text{Tyr}^{++} + \text{BH}^+ + e^-$, where B = His or Glu).

In the reduced state (i.e. Tyr), hydrogen bonding lowers the IP by 0.8 / 0.94 eV (Tyr-Wat-His or Tyr-Glu-Arg models, respectively). The same effect has been previously observed for Photosystem II models (i.e. Tyr \cdots His) (O'Malley, 1998; Blomberg, 1998; Wang & Eriksson, 2001) and a Tyr \cdots Glu model (Zhang, 2008). This suggests that *hydrogen-bonding favours oxidation of Tyr*.

In the oxidized state (i.e. radical Tyr), the EA of the neutral tyrosyl radical is lower than that of the tyrosyl cation radical, indicating that *PT hinders the back reduction of the radical*. The reorganization energy of Tyr \cdot is larger than for Tyr $^{++}$, as expected for a PCET compared to a simple ET.

Table 12. Redox energies of tyrosine oxidation^a. IP and EA are the ionization potential and the electron affinity, respectively, ΔE is the adiabatic energy of oxidation and λ is the reorganization energy (see Table 10). All the values are in eV.

model	IP	EA	ΔE	λ
isolated Tyr	7.96	7.51	7.63	0.22
Tyr-Wat-His	7.16	5.33	6.57	0.92
Tyr-Glu-Arg	7.02	5.35	6.16	0.84

^aFor isolated Tyr, oxidation of Tyr is a pure ET (i.e. $\text{Tyr} \rightarrow \text{Tyr}^{++} + e^-$), whereas for the hydrogen-bonded models the process is a PCET (i.e. $\text{Tyr} + \text{B} \rightarrow \text{Tyr}^{++} + \text{BH}^+ + e^-$, where B = His or Glu).

• Comparison ET versus PCET

As seen above, oxidation of isolated Tyr is a simple ET (i.e. a tyrosyl cation radical is formed), whereas for the hydrogen-bonded models it is a PCET (i.e. it yields a neutral tyrosyl radical). In order to study just the ET part of the oxidation reaction, the Tyr-Wat-His and Tyr-Glu-Arg models were reoptimized fixing the $\text{O}_{\text{Tyr}}\text{-H}_{\text{Tyr}}$ distance to preclude deprotonation of the tyrosyl

cation radical. Tyr^{•+} turns out to be less stable than Tyr[•] by 8.9 kcal/mol (Tyr-Wat-His model) or 15.2 kcal/mol (Tyr-Glu-Arg model). Hence, *the spontaneous PT coupled to the oxidation of Tyr increases the exothermicity of tyrosyl radical formation.*

Table 13. Main distances (in Å) describing the neutral and cationic tyrosyl radicals for the gas phase models of Tyr.

model	Tyr	Tyr-Wat-His		Tyr-Glu-Arg	
tyrosyl radical	Tyr ^{•+}	Tyr ^{•+}	Tyr [•]	Tyr ^{•+}	Tyr [•]
C _{meta,Tyr} -C _{para,Tyr}	1.42-1.43	1.42-1.43	1.42	1.42	1.42-1.43
C _{orto,Tyr} -C _{meta,Tyr}	1.37	1.37	1.37	1.38	1.37
C _{ipso,Tyr} -C _{orto,Tyr}	1.42-1.43	1.43	1.45	1.43	1.45
C _{ipso,Tyr} -O _{Tyr}	1.33	1.32	1.28	1.33	1.29
O _{Tyr} -H _{Tyr}	0.99	0.98	1.65	0.96	1.62
H _{Tyr} -O _{Wat}	–	1.61	1.03	–	–
O _{Wat} -H _{Wat}	–	1.03	1.53	–	–
H _{Wat} -N _{δ,His}	–	1.75	1.11	–	–
H _{Tyr} -O _{ε1,Glu}	–	–	–	1.60	1.04

Table 13 compare the structures of the neutral and cationic tyrosyl radicals. They are rather similar except for C_{ipso,Tyr}-O_{Tyr} distance (1.32-1.33 Å for Tyr^{•+} compared to 1.29-1.28 Å for Tyr[•]). This slight shortening of the C_{ipso,Tyr}-O_{Tyr} bond corresponds to a change from a single (i.e. C–OH) to a double (i.e. C=O) bond.

The redox energies for a hydrogen-bonded Tyr^{•+} (i.e. a pure ET, as for isolated Tyr) are shown in Table 14. Hydrogen bonding without deprotonation still decreases the EA of the tyrosyl cation radical. However, the decrease in the EA (by 0.75 eV for the Tyr-Wat-His model and by 1.14 eV for the Tyr-Glu-Arg model) is less than for the neutral tyrosyl radical (2.18 and 2.16 eV, respectively). Most likely the positive charge of the protonated tyrosyl radical (Tyr^{•+}) explains the larger EA compared to the deprotonated radical (Tyr[•]). By contrast, the reorganization energy of the hydrogen-bonded Tyr^{•+} is similar to isolated Tyr and lower than for Tyr[•] (Table 9), because the only process taking place is an ET.

Table 14. Redox energies of the Tyr / Tyr⁺ redox pair ^a. IP and EA are the ionization potential and the electron affinity, ΔE is the adiabatic energy of oxidation, λ_R and λ_O are the reorganization energies of reduction and oxidation, respectively, and λ is the reorganization energy (see Table 10). All the values are in eV.

model	IP	EA	ΔE	λ
isolated Tyr	7.96	7.51	7.63	0.22
Tyr-Wat-His	7.16	6.76	6.95	0.20
Tyr-Glu-Arg	7.02	6.37	6.82	0.33

^aFor all models only the ET process is considered (i.e. Tyr \rightarrow Tyr⁺ + e⁻).

Therefore, *hydrogen bonding (i) favours oxidation of Tyr and (ii) hinders back reduction of the tyrosyl cation radical*. Additionally, *deprotonation by a nearby base (e.g. His or Glu) stabilizes the tyrosyl radical and further disfavours its back reduction*.

4. CONVERGENCE OF THE IONIZATION ENERGIES OF THE HEME

• Size of the QM region

The convergence of the ionization energies of the heme was investigated using the models shown in Figure 10.

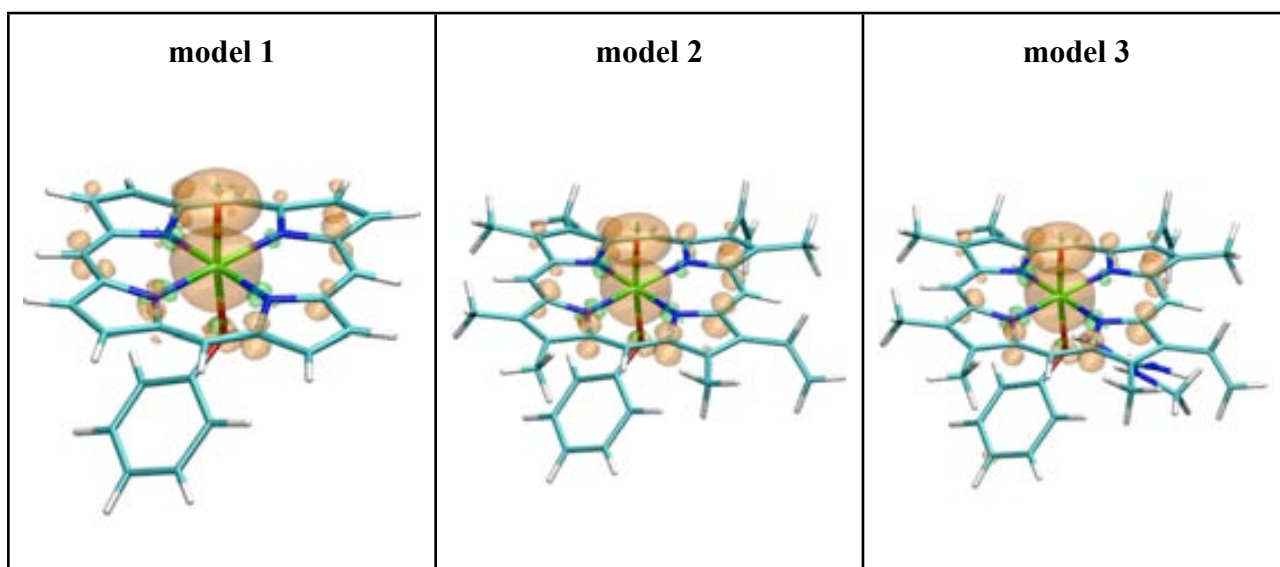


Figure 10. Models used to test the convergence of the ionization energies of the heme with the size of the QM region. Only the QM atoms are displayed. Spin isodensity surfaces (at 0.004 e Å⁻³) corresponding to the oxidized state (i.e. Cpd I) are also shown.

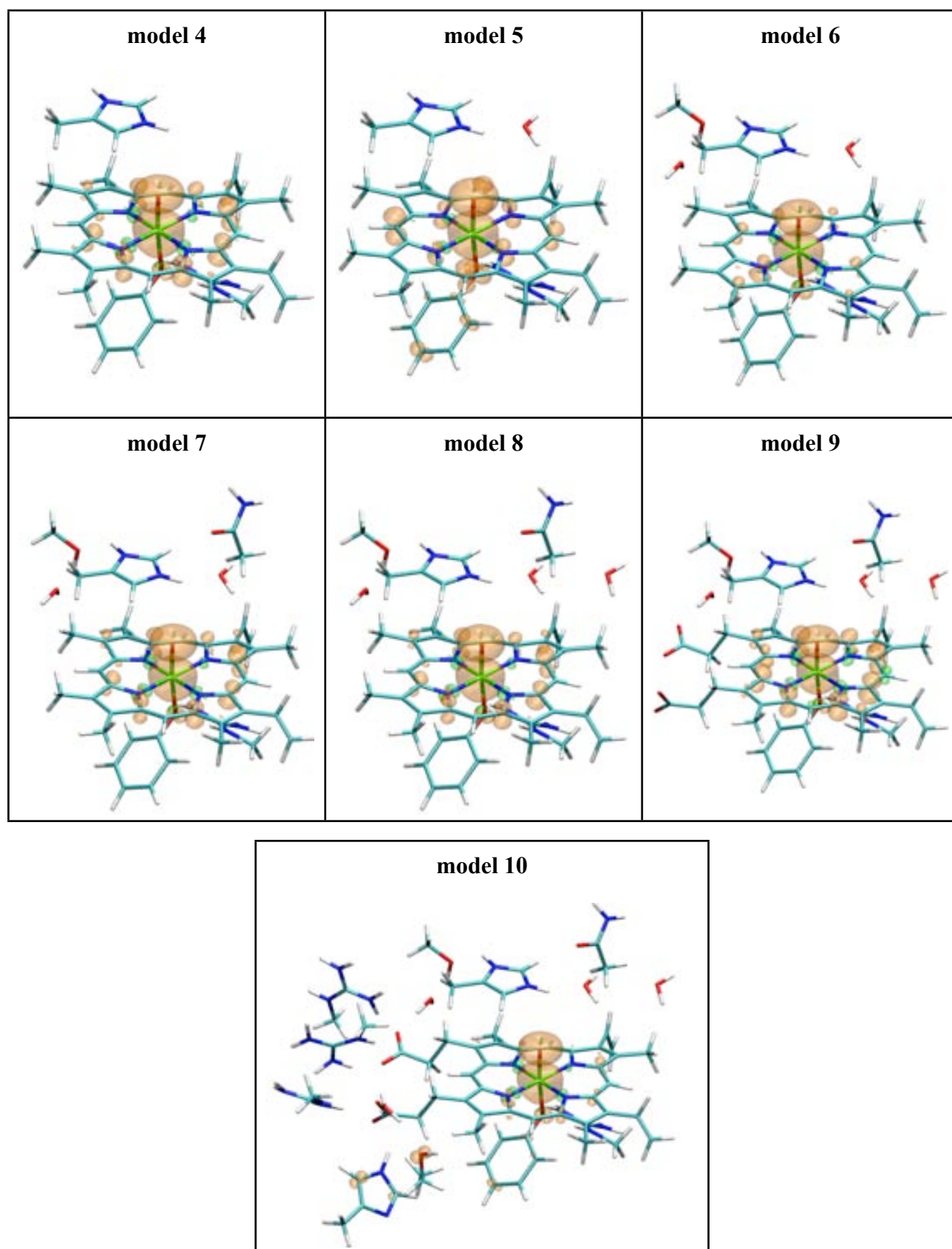


Figure 10 (cont.). Models used to test the convergence of the ionization energies of the heme with the size of the QM region. Only the QM atoms are displayed. Spin isodensity surfaces (at $0.004 \text{ e } \text{\AA}^{-3}$) corresponding to the oxidized state (i.e. Cpd I) are also shown.

All the models correspond to the same atomic configuration, obtained from a snapshot of the oxidized state of HPC (see section 1.1.). The only difference is whether some residues are treated as QM or MM. Model **1** includes the oxoferryl porphyrin with all the substituents replaced by dummy hydrogen atoms and the proximal Tyr. The heme substituents are added in model **2**: the methyl and vinyl groups and the propionate sidechains, which are saturated with dummy hydrogen atoms at C α to -CH $_3$. Model **3** incorporates the proximal Arg hydrogen-bonded to the phenolate ligand (methylguanidinium), whereas models **4** and **5** incorporates the essential histidine (methylimidazole) and the pocket water. Models **6**, **7** and **8** add the other distal residues: the serine hydrogen-bonded to His (methanol) and the water molecule connecting Ser and one of the propionates of the heme, the asparagine (acetamide) and another water molecule hydrogen-bonded to it. In model **9** the propionate sidechains, which were represented as -CH $_3$ in the previous models, are completed (i.e. -CH $_2$ -COO $^-$). Finally, model **10** adds all the residues hydrogen-bonded to propionates.

Table 15. Dependence of the ionization energy of the heme (i.e. the EA of HPC Cpd I) on the number of QM atoms (see Figure 11). All the energies are given in eV.

model	# QM atoms	IE	IE _{QM}	IE _{QM-MM}	IE _{MM}
1	50	-7.08	3.56	-9.25	-1.55
2	76	4.35	3.44	-0.96	1.66
3	89	4.63	5.49	-1.61	0.82
4	102	5.17	7.75	-3.13	0.68
5	105	5.17	7.77	-3.23	0.74
6	114	5.17	7.80	-3.61	1.03
7	123	4.90	7.64	-3.50	0.98
8	126	5.17	7.62	-3.83	1.25
9	136	4.63	3.84	-0.60	1.17
10	202	4.90	8.73	-5.50	1.71

Table 15 shows the ionization energies of the heme (i.e. the EA of HPC Cpd I) calculated as explained in section 1.2. The deviation between the model used in the calculations (model **5**) and the largest model is 0.27 eV (IE). Albeit large, this is of the same order of magnitude expected for

the fluctuations of the ionization energies (Blumberger, 2008). The change in IE_{QM} (0.96 eV) is even larger. Nevertheless, it should be noted that the outer-sphere contribution $\{(QM-MM)+MM\}$ of -1.3 eV almost counteracts it. Besides, models **5** and **10** show different spin density distributions (Figure 10): whereas in model **5** the radical is delocalized over the porphyrin (i.e. $Porph^{\bullet+}-Fe^{IV}=O$), for model **10** it is mainly concentrated in the oxoferryl moiety (i.e. $Porph-Fe^V=O$). Because the electron is inserted in a different orbital, the electron affinity changes. However, catalase Cpd I has been shown to bear an oxoferryl porphyrin cation radical (Benecky, 1993), as displayed by model **5**. Therefore, we decided to take model **5** for the calculation of the ionization energies of the heme.

• Cutoff radius of the QM-MM interactions

The variation of the ionization energies of the heme (i.e. the EA of HPC Cpd I using model **5**) with the cutoff radius (r_{NN}) is shown in Table 16. r_{MIX} is taken equal to r_{NN} , and $r_{RESP} \rightarrow \infty$ (practically 132.3 Å), such that for the MM atoms within “ r_{NN} ” Å of any QM atom, the electrostatic QM-MM interaction energy is calculated from the electrons + nuclei density on the QM subsystem and the point charges of the MM atoms. All other MM atoms interact with the D-RESP charges assigned to the QM atoms (i.e. no MM atom was coupled via a multipole expansion). Since the difference in the energy gap compared to $r_{NN} \rightarrow \infty$ is very small, we considered $r_{NN}=5.3$ Å as a reasonable compromise between accuracy and computational cost.

Table 16. Dependence of the ionization energy of the heme (i.e. the EA of HPC Cpd I using model **5**) on the cutoff radius of the QM-MM interactions. All the energies are given in eV.

r_{NN} (Å)	IE	IE_{QM}	IE_{QM-MM}	IE_{MM}
5.3	5.442	7.837	-3.226	0.735
10.6	5.442	7.836	-3.228	0.735
15.9	5.442	7.835	-3.226	0.735
21.2	5.442	7.835	-3.226	0.735
26.5	5.442	7.835	-3.227	0.735
529	5.442	7.839	-3.226	0.735
79.4	5.442	7.839	-3.226	0.735
105.8	5.442	7.839	-3.226	0.735
132.3	5.442	7.839	-3.226	0.735

• **Sampling of gap energies**

Table 17 shows the variation of the ionization energies of the heme (i.e. the EA of HPC Cpd I using model 5) with the sampling density (i.e. the time interval for extracting the ensemble of configurations from the MD simulation). It can be seen that the energy gap and the width of the fluctuations are rather converged for a sampling density of 0.5 ns.

Table 17. Dependence of the ionization energy of the heme (i.e. the EA of HPC Cpd I using model 5) on the sampling of gap energies. All the energies are given in eV.

sampling density (ns)	number of configurations	IE	IE _{QM}	IE _{QM-MM}	IE _{MM}
2	6	5.31 ± 0.38	7.81 ± 0.13	-3.28 ± 0.24	0.79 ± 0.04
1	11	5.42 ± 0.33	7.86 ± 0.12	-3.23 ± 0.20	0.81 ± 0.09
0.5	21	5.48 ± 0.30	7.89 ± 0.12	-3.23 ± 0.20	0.81 ± 0.09

5. OUTER-SPHERE ENERGIES FOR THE ET TO CPD I

Table 18. Outer-sphere energies (protein and solvent) for the ET to Cpd I decomposed into QM-MM and MM contributions. $\langle \Delta E \rangle$ is the average adiabatic energy of reduction and $\langle IP \rangle$ and $\langle EA \rangle$ are the ionization potential and the electron affinity, respectively, ΔA is the driving force and λ is the reorganization free energy. See Chapter II, equations 46-48.

	QM-MM (heme b-HPC)	MM (HPC)	QM-MM (heme d-PVC)	MM (PVC)
$\langle \Delta E \rangle$ (eV) ^a	4.54 ± 0.79	-7.32 ± 14.63	5.25 ± 0.69	-3.34 ± 18.21
$\langle IP \rangle$ (eV) ^b	-1.48 ± 0.18	0.73 ± 0.06	-2.04 ± 0.14	0.97 ± 0.24
$\langle EA \rangle$ (eV) ^b	-3.23 ± 0.20	0.81 ± 0.09	-3.02 ± 0.28	0.71 ± 0.22
λ (meV) ^c	2.36 ± 0.27 ^d	-0.77 ± 0.11 ^e	2.53 ± 0.31 ^d	-0.84 ± 0.32 ^e
ΔA (eV) ^c	0.87 ± 0.27 ^f	-0.04 ± 0.11 ^g	0.49 ± 0.31 ^f	0.13 ± 0.32 ^g

$$^a \langle \Delta E^{(QM-MM)} \rangle = \langle E^{(QM-MM)}_{Cpd II}(R_{Cpd II}) - E^{(QM-MM)}_{Cpd I}(R_{Cpd I}) \rangle, \langle \Delta E^{MM} \rangle = \langle E^{MM}_{Cpd II}(R_{Cpd II}) - E^{MM}_{Cpd I}(R_{Cpd I}) \rangle$$

$$^b \langle EA^{(QM-MM)} \rangle = \langle E^{(QM-MM)}_{Cpd I}(R_{Cpd I}) - E^{(QM-MM)}_{Cpd II}(R_{Cpd II}) \rangle, \langle EA^{MM} \rangle = \langle E^{MM}_{Cpd I}(R_{Cpd I}) - E^{MM}_{Cpd II}(R_{Cpd II}) \rangle$$

$$\langle IP^{(QM-MM)} \rangle = \langle E^{(QM-MM)}_{Cpd I}(R_{Cpd II}) - E^{(QM-MM)}_{Cpd II}(R_{Cpd II}) \rangle, \langle IP^{MM} \rangle = \langle E^{MM}_{Cpd I}(R_{Cpd II}) - E^{MM}_{Cpd II}(R_{Cpd II}) \rangle$$

$$^c \Delta A^{(QM-MM)} = [\langle IP^{(QM-MM)} \rangle + \langle EA^{(QM-MM)} \rangle] / 2, \Delta A^{MM} = [\langle IP^{MM} \rangle + \langle EA^{MM} \rangle] / 2$$

$$\langle \lambda^{(QM-MM)} \rangle = [\langle IP^{(QM-MM)} \rangle - \langle EA^{(QM-MM)} \rangle] / 2, \langle \lambda^{MM} \rangle = [\langle IP^{MM} \rangle - \langle EA^{MM} \rangle] / 2$$

$$^d \sigma_{\lambda^{(QM-MM)}} = \sqrt{(\sigma_{IP^{(QM-MM)}}^2 + \sigma_{EA^{(QM-MM)}}^2)} \quad ^d \sigma_{\lambda^{MM}} = \sqrt{(\sigma_{IP^{MM}}^2 + \sigma_{EA^{MM}}^2)}$$

$$^f \sigma_{\Delta A^{(QM-MM)}} = \sqrt{(\sigma_{IP^{(QM-MM)}}^2 + \sigma_{EA^{(QM-MM)}}^2)} \quad ^g \sigma_{\Delta A^{MM}} = \sqrt{(\sigma_{IP^{MM}}^2 + \sigma_{EA^{MM}}^2)}$$

6. COMPARISON TO CYTOCHROME C

The same methodology we have used to study the Cpd I / Cpd II ET in catalase has been applied to Fe^{II} / Fe^{III} ET in cytochrome c (cyt c). Cyt c has been extensively used as a model system in both experimental and computational studies of electron transfer in proteins. Therefore, it would be interesting to compare the results we have obtained with those for cyt c (Blumberger, 2008).

The standard deviation of the inner-sphere vertical ionization energies is wider for catalase (~0.10 eV, see Chapter V, Table 2) than for cyt c (~0.07 eV) (Blumberger, 2008). In cyt c, this standard deviation is due to the protein thermal fluctuations through the polarization of the QM electron density. In catalases, besides this effect, the QM region fluctuations further broaden the IP or EA distributions. Whereas ionization in cyt c occurs from a localized Fe d-orbital, the orbital involved in ionization in catalases is mainly porphyrin-based, but it has also contributions from the iron and the proximal Tyr as well. The QM region fluctuations modulate the contributions of these different moieties to the orbital where ionization takes place, as can be seen in Table 19. The fluctuations of the EAⁱ of heme d (0.31 eV, see Chapter V, Table 2) are much larger than those of the heme d IPⁱ or the vertical ionization energies of heme b. This is probably due to the conformational change of the *cis*-hydroxy- γ -spirolactone modification present in heme d, as explained in Chapter V (section 3.1.).

Table 19. Change in the number of unpaired electrons on relevant fragments upon ET to catalase Cpd I in HPC and PVC. The larger the change in the number of unpaired electrons, the larger the contribution of the corresponding moiety to the orbital where ionization occurs.

Δunpaired electrons (%) ^a		HPC	PVC
Fe=O		35.8 \pm 11.2	16.3 \pm 12.6
Porph	a_{2u}	40.6 \pm 20.9	5.5 \pm 12.9
	a_{1u}	8.2 \pm 21.9	50.6 \pm 20.8
Tyr		15.4 \pm 8.5	27.5 \pm 13.4

$$^a \Delta \text{unpaired electrons}_i = \frac{\left(\text{unpaired electrons}^{\text{Cpd I plus 1 electron}} - \text{unpaired electrons}^{\text{Cpd I}} \right) \times 100}{\sum_{i=1}^n \Delta \text{unpaired electrons}_i}$$

7. FURTHER ANALYSIS OF THE REDOX-ACTIVE RESIDUES

Table 20. Decomposition of the total number of electron-donating aminoacids in HPC and PVC into the different types of electron donors (Tyr, Trp, Cys, Met and His residues). The analysis was performed on the crystal structures of oxidized HPC and PVC (PDB entries: 2IUJ and 2IQF) (Alfonso-Prieto, 2007).

distance ^a (Å)	# redox-active residues ^b	Tyr	Trp	Cys	Met	His
7	6 / 5	1 / 1	0 / 0	0 / 0	2 / 1	3 / 3
14	28 / 21	12 / 4	6 / 3	1 / 0	3 / 3	6 / 11
20	64 / 40	34 / 7	12 / 7	1 / 0	5 / 6	12 / 20
whole protein	256 / 160	100 / 44	44 / 32	8 / 0	32 / 20	72 / 64

^a Sphere of 7 Å, 14 Å, 20 Å or ∞ Å (whole protein) around the heme.

^b Number of Tyr + Trp + Cys + Met + His residues within this sphere for HPC / PVC. Oxidized methionines (16 for HPC and 20 for PVC) are excluded, as they cannot longer act as electron donors.

8. CONVERGENCE OF THE IONIZATION ENERGIES OF TYR351

• Size of the QM region

The convergence of the ionization energies of Tyr351 was investigated using the 5 different models shown in Figure 11. All the models correspond to the same atomic configuration, obtained from a snapshot of the RO {Cpd I, Tyr} state (see section 1.4.). The only difference is whether some residues are treated as QM or MM.

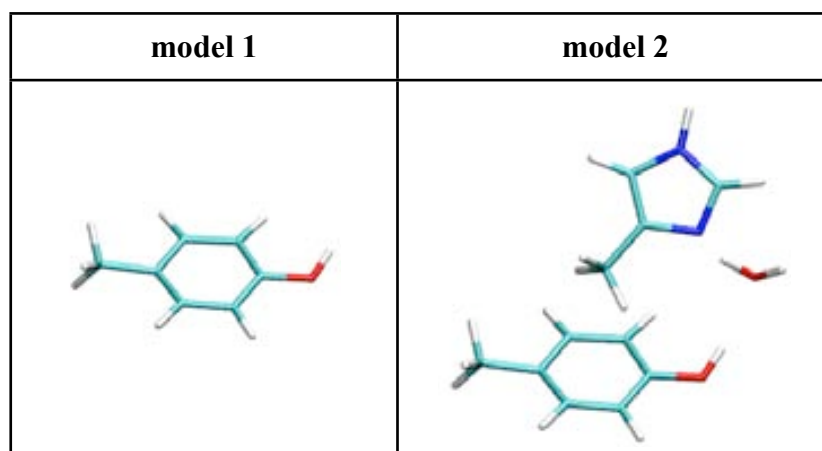


Figure 11. Models used to test the convergence of the ionization energies of Tyr351 with the size of the QM region. Only the QM atoms are displayed.

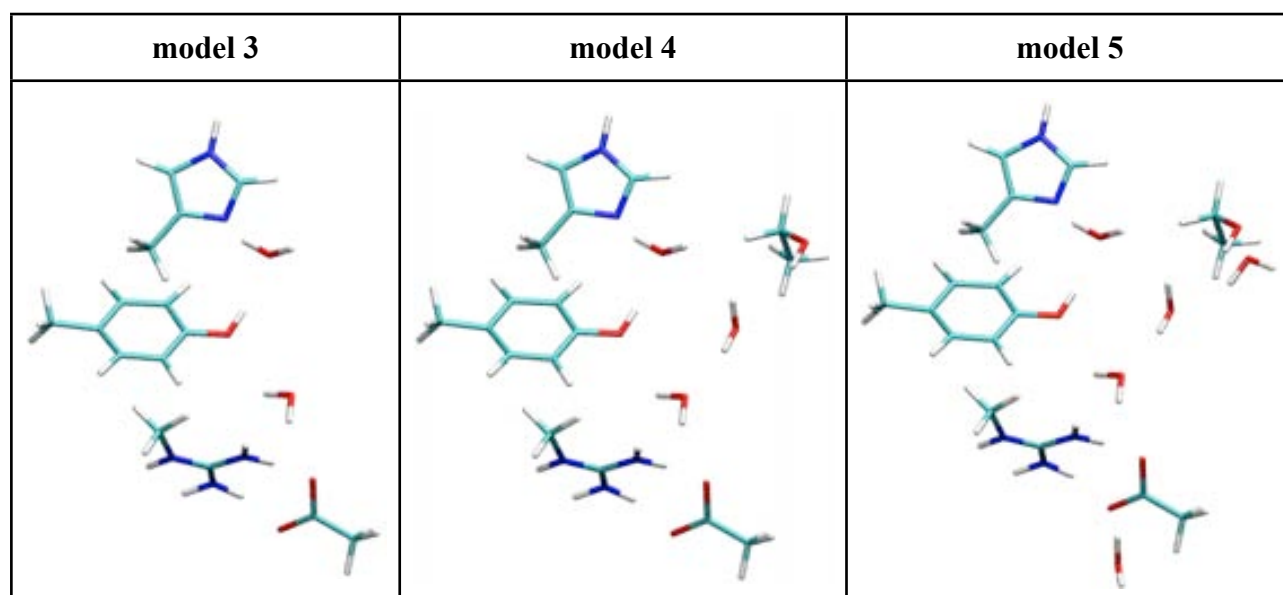


Figure 11 (cont.). Models used to test the convergence of the ionization energies of Tyr351 with the size of the QM region.

Model **1** includes only the Tyr351 (modeled as *p*-methyl-phenol), whereas model **2** incorporates the first-shell residues hydrogen-bonded to it in the His-conformation (see Chapter V, Figure 15): a bridging water molecule and His343 (2-methyl-imidazole). Model **3** includes the first-shell environment of Tyr351 in the Glu-conformation (see Chapter V, Figure 15): Glu1516 (acetate), a water molecule and Arg344 (methyl-guanidinium). Model **4** adds second-shell residues: Thr316 (ethanol) and a water molecule connecting Thr316 to Glu1516 through hydrogen bonds. Finally, model **5** incorporates two additional water molecules hydrogen-bonded to Glu1516 and Thr316.

Table 21. Dependence of the ionization energy of Tyr351 (i.e. the IP of neutral tyrosine in the {Tyr, Cpd I} state) on the number of QM atoms (see Figure 12). All the energies are given in eV.

model	# QM atoms	IE	IE _{QM}	IE _{QM-MM}	IE _{MM}
1	16	8.44	7.79	0.03	0.60
2	31	7.59	7.19	-0.20	0.57
3	54	7.40	6.77	-0.01	0.63
4	66	7.08	6.75	-0.18	0.60
5	72	7.35	6.84	-0.21	0.63

Table 21 shows the ionization energies of Tyr351 (i.e. the IP of neutral tyrosine in the {Tyr, Cpd I} state) calculated as explained in section 1.5. The deviation between the model used in the calculations (model 3) and the largest model is only 0.05 eV (IE). Therefore, we chose model 3 to calculate the ionization energies of Tyr351.

• Cutoff radii of the QM-MM interactions

The variation of the ionization energies of Tyr351 (i.e. the IP of neutral tyrosine using model 3) with the cutoff radius (r_{NN}) is shown in Table 22. r_{MIX} is taken equal to r_{NN} , and $r_{\text{RESP}} \rightarrow \infty$ (practically 132.3 Å). Since the difference in the energy gap compared to $r_{\text{NN}} \rightarrow \infty$ is very small, we considered $r_{\text{NN}}=5.3$ Å as a reasonable compromise between accuracy and computational cost.

Table 22. Dependence of the ionization energy of Tyr351 (i.e. the IP of neutral tyrosine using model 3) on the cutoff radius of the QM-MM interactions. All the energies are given in eV.

r_{NN} (Å)	IE	IE _{QM}	IE _{QM-MM}	IE _{MM}
5.3	7.401	6.766	-0.010	0.626
26.5	7.374	6.764	-0.013	0.626
529	7.402	6.764	-0.013	0.626
79.4	7.402	6.764	-0.012	0.626
105.8	7.402	6.764	-0.012	0.626
132.3	7.402	6.764	-0.012	0.626

• Sampling of gap energies

Table 23 shows the variation of the ionization energies of Tyr351 (i.e. the IP of neutral tyrosine using model 3) with the sampling density (i.e. the time interval for extracting the ensemble of configurations from the MD simulation). It can be seen that the energy gap and the width of the fluctuations are rather converged for a sampling density of 0.5 ns.

Table 23. Dependence of the ionization energy of Tyr351 (i.e. the IP of neutral tyrosine using model 3) on the sampling of gap energies. All the energies are given in eV.

sampling density (ns)	number of configurations	IE	IE _{QM}	IE _{QM-MM}	IE _{MM}
2	6	7.57 ± 0.38	6.85 ± 0.24	0.19 ± 0.27	0.54 ± 0.09
1	11	7.43 ± 0.35	6.76 ± 0.26	0.18 ± 0.30	0.48 ± 0.10
0.5	21	7.43 ± 0.31	6.70 ± 0.21	0.25 ± 0.31	0.48 ± 0.10

9. CONTRIBUTIONS TO THE ET FROM TYR 351 TO CPD I

As done for the “electrochemical” reduction of Cpd I (see Chapter V, section 3.1.), we have investigated the influence of the different parts of the system on the ET from Tyr351 to HPC Cpd I. The total driving force and reorganization free energy have been decomposed into the inner-sphere (i.e. heme, tyrosine and first-shell environment) and outer-sphere (i.e. rest of the protein and solvent) contributions (see equations 46-48 in Chapter II).

• *Inner-sphere*

Tables 24 and 25 show the inner-sphere contribution to the ET. The EAⁱ of Cpd I is substantially higher than the IPⁱ of the Tyr (see Table 24) and thus the vertical ET energy (ΔE^i in Table 24) is highly exothermic. Likewise, the driving force (ΔA^i in Table 25) predicts a thermodynamically favoured ET. The inner-sphere reorganization energies (λ^i in Table 25) are much lower than the total values (Chapter V, Table 9), and thus fluctuations of the first-shell hydrogen-bonding network are not the major source of the large λ observed.

• *Outer-sphere*

Tables 26 and 27 show the outer-sphere (i.e. protein and solvent) contribution to the ET. The high exothermicity of the inner-sphere contribution is compensated by the outer-sphere contribution, resulting in a small total driving force, as expected for a biological ET (Reece, 2006). As can be seen in Table 27, the outer-sphere reorganization energy is the responsible for the unusually large λ . Therefore, size effects are most likely responsible for this overestimation of the reorganization energy. In particular, decomposition of the outer-sphere energies into the QM-MM and MM contributions (Tables 28-29) shows that the main source is the QM-MM part.

Table 24. Inner-sphere contribution (i.e. heme, Tyr and first-shell residues) to the average vertical energy gaps ($\langle \text{IP}^i \rangle$ and $\langle \text{EA}^i \rangle$) and vertical ET energies ($\langle \Delta \text{E}^i \rangle$) for the ET from Tyr351 to Cpd I. His-conf and Glu-conf refer to the two conformations of the Tyr^{•+} observed in the classical MD (see Chapter V, Figure 15). All the energies are in eV.

{Tyr, Cpd I} state ^a		{Tyr ^{•+} , Cpd II} state ^b		
$\langle \text{IP}^i \rangle_{\text{Tyr}}$	6.70 ± 0.21	$\langle \text{IP}^i \rangle_{\text{Cpd II}}$		7.95 ± 0.17
$\langle \text{EA}^i \rangle_{\text{Cpd I}}$	7.89 ± 0.12	$\langle \text{EA}^i \rangle_{\text{Tyr}^{\bullet+}}$	His-conf	6.28 ± 0.20
			Glu-conf	6.48 ± 0.09
$\langle \Delta \text{E}^i \rangle_{\text{Tyr, Cpd I}}$	-1.18 ± 0.24^c	$\langle \Delta \text{E}^i \rangle_{\text{Tyr}^{\bullet+}, \text{Cpd II}}$	His-conf	-1.67 ± 0.27^c
			Glu-conf	-1.47 ± 0.19^c

$$^a \langle \text{IP}^i \rangle_{\text{Tyr}} = \langle \text{E}^{\text{QM}}_{\text{Tyr}^{\bullet+}}(\text{R}_{\text{Tyr}}) - \text{E}^{\text{QM}}_{\text{Tyr}}(\text{R}_{\text{Tyr}}) \rangle, \langle \text{EA}^i_{\text{Cpd I}} \rangle = \langle \text{E}^{\text{QM}}_{\text{Cpd I}}(\text{R}_{\text{Cpd I}}) - \text{E}^{\text{QM}}_{\text{Cpd II}}(\text{R}_{\text{Cpd I}}) \rangle$$

$$\langle \Delta \text{E}^i_{\text{Tyr, Cpd I}} \rangle = \langle \text{IP}^i_{\text{Tyr}} \rangle - \langle \text{EA}^i_{\text{Cpd I}} \rangle$$

$$^b \langle \text{IP}^i \rangle_{\text{Cpd II}} = \langle \text{E}^{\text{QM}}_{\text{Cpd I}}(\text{R}_{\text{Cpd II}}) - \text{E}^{\text{QM}}_{\text{Cpd II}}(\text{R}_{\text{Cpd II}}) \rangle, \langle \text{EA}^i_{\text{Tyr}^{\bullet+}} \rangle = \langle \text{E}^{\text{QM}}_{\text{Tyr}^{\bullet+}}(\text{R}_{\text{Tyr}^{\bullet+}}) - \text{E}^{\text{QM}}_{\text{Tyr}}(\text{R}_{\text{Tyr}^{\bullet+}}) \rangle$$

$$\langle \Delta \text{E}^i_{\text{Tyr}^{\bullet+}, \text{Cpd II}} \rangle = \langle \text{EA}^i_{\text{Tyr}^{\bullet+}} \rangle - \langle \text{IP}^i_{\text{Cpd II}} \rangle$$

$$^c \sigma_{\Delta \text{E}^i} = \sqrt{(\sigma_{\text{IP}^i}^2 + \sigma_{\text{EA}^i}^2)}$$

Table 25. Inner-sphere contribution (i.e. heme, Tyr and first-shell residues) to the average driving force ^a ($\langle \Delta \text{A}^i \rangle$) and reorganization free energy ^b (λ^i) for the ET from Tyr351 to Cpd I. His-conf and Glu-conf refer to the two conformations of the Tyr^{•+} observed in the classical MD (Chapter V, Figure 15). All the energies are in eV.

	His-conf	Glu-conf
ΔA^i	-1.43 ± 0.25^c	-1.33 ± 0.22^c
λ^i	0.25 ± 0.25^c	0.14 ± 0.22^c

$$^a \Delta \text{A}^i = (\langle \Delta \text{E}^{\text{QM}} \rangle_{\text{Tyr, Cpd I}} + \langle \Delta \text{E}^{\text{QM}} \rangle_{\text{Tyr}^{\bullet+}, \text{Cpd II}}) / 2$$

$$^b \lambda^i = (\langle \Delta \text{E}^{\text{QM}} \rangle_{\text{Tyr, Cpd I}} - \langle \Delta \text{E}^{\text{QM}} \rangle_{\text{Tyr}^{\bullet+}, \text{Cpd II}}) / 2$$

$$^c \sigma_{\Delta \text{A}^i} = \sigma_{\lambda^i} = \sqrt{(\sigma_{\Delta \text{E}^i}^2(\text{Tyr, Cpd I}) + \sigma_{\Delta \text{E}^i}^2(\text{Tyr}^{\bullet+}, \text{Cpd II})) / 2}$$

Table 26. Outer-sphere contribution (i.e. protein and solvent) to the average vertical energy gaps ($\langle \text{IP}^0 \rangle$ and $\langle \text{EA}^0 \rangle$) and vertical ET energies ($\langle \Delta E^0 \rangle$) for the ET from Tyr351 to Cpd I. His-conf and Glu-conf refer to the two conformations of the Tyr^{•+} observed in the classical MD (Chapter V, Figure 15). All the energies are in eV.

{Tyr, Cpd I} state ^a		{Tyr ^{•+} , Cpd II} state ^b		
$\langle \text{IP}^0 \rangle_{\text{Tyr}}$	0.73 ± 0.32	$\langle \text{IP}^0 \rangle_{\text{Cpd II}}$	-0.71 ± 0.37	
$\langle \text{EA}^0 \rangle_{\text{Cpd I}}$	-2.43 ± 0.22	$\langle \text{EA}^0 \rangle_{\text{Tyr}^{\bullet+}}$	His-conf	-1.46 ± 0.29
			Glu-conf	-2.07 ± 0.40
$\langle \Delta E^0 \rangle_{\text{Tyr, Cpd I}}$	3.16 ± 0.39	$\langle \Delta E^0 \rangle_{\text{Tyr}^{\bullet+}, \text{Cpd II}}$	His-conf	-0.75 ± 0.47
			Glu-conf	-1.36 ± 0.55

$$^a \langle \text{IP}^0 \rangle_{\text{Tyr}} = \langle \text{IP}^{\text{(QM-MM)}} \rangle_{\text{Tyr}} + \langle \text{IP}^{\text{MM}} \rangle_{\text{Tyr}}, \langle \text{EA}^0 \rangle_{\text{Cpd I}} = \langle \text{EA}^{\text{(QM-MM)}} \rangle_{\text{Cpd I}} + \langle \text{EA}^{\text{MM}} \rangle_{\text{Cpd I}}$$

$$\langle \Delta E^0_{\text{Tyr, Cpd I}} \rangle = \langle \text{IP}^0_{\text{Tyr}} \rangle - \langle \text{EA}^0_{\text{Cpd I}} \rangle$$

$$^b \langle \text{IP}^0 \rangle_{\text{Cpd II}} = \langle \text{IP}^{\text{(QM-MM)}} \rangle_{\text{Cpd II}} + \langle \text{IP}^{\text{MM}} \rangle_{\text{Cpd II}}, \langle \text{EA}^0 \rangle_{\text{Tyr}^{\bullet+}} = \langle \text{EA}^{\text{(QM-MM)}} \rangle_{\text{Tyr}^{\bullet+}} + \langle \text{EA}^{\text{MM}} \rangle_{\text{Tyr}^{\bullet+}}$$

$$\langle \Delta E^0_{\text{Tyr}^{\bullet+}, \text{Cpd II}} \rangle = \langle \text{EA}^0_{\text{Tyr}^{\bullet+}} \rangle - \langle \text{IP}^0_{\text{Cpd II}} \rangle$$

$$^c \sigma_{\Delta E^0} = \sqrt{(\sigma_{\text{IP}^0}^2 + \sigma_{\text{EA}^0}^2)}$$

Table 27. Outer-sphere contribution (i.e. protein and solvent) to the average driving force ^a ($\langle \Delta A^0 \rangle$) and reorganization free energy ^b (λ^0) for the ET from Tyr351 to Cpd I. His-conf and Glu-conf refer to the two conformations of the Tyr^{•+} observed in the classical MD (Chapter V, Figure 15). All the energies are in eV.

	His-conf	Glu-conf
ΔA^0	1.20 ± 0.43	0.90 ± 0.45
λ^0	1.95 ± 0.43	2.26 ± 0.45

$$^a \Delta A^0 = \Delta A^{\text{(QM-MM)}} + \Delta A^{\text{MM}}$$

$$^b \lambda^0 = \lambda^{\text{(QM-MM)}} + \lambda^{\text{MM}}$$

$$^c \sigma_{\Delta A^0} = \sigma_{\lambda^0} = \sqrt{(\sigma_{\Delta E^0}^2(\text{Tyr, Cpd I}) + \sigma_{\Delta E^0}^2(\text{Tyr}^{\bullet+}, \text{Cpd II})) / 2}$$

Table 28. Decomposition of the outer-sphere (i.e. protein and solvent) energies into the QM-MM and MM contributions. $\langle \text{IP} \rangle$ and $\langle \text{EA} \rangle$ are the average vertical energy gaps and $\langle \Delta E \rangle$ the vertical ET energies for the ET from Tyr351 to Cpd I. His-conf and Glu-conf refer to the two conformations of the Tyr^{•+} observed in the classical MD (Chapter V, Figure 15). All the energies are in eV.

{Tyr, Cpd I} state ^a			{Tyr ^{•+} , Cpd II} state ^b			
outer-sphere	QM-MM	MM	outer-sphere	QM-MM	MM	
$\langle \text{IP} \rangle_{\text{Tyr}}$	0.25±0.31	0.48±0.10	$\langle \text{IP} \rangle_{\text{Cpd II}}$	-1.14±0.24	0.43±0.28	
$\langle \text{EA} \rangle_{\text{Cpd I}}$	-3.23±0.20	0.81±0.09	$\langle \text{EA} \rangle_{\text{Tyr}^{\bullet+}}$	His-conf	-2.31±0.27	0.85±0.09
				Glu-conf	-2.95±0.39	0.88±0.11
$\langle \Delta E \rangle_{\text{Tyr,Cpd I}}$	3.48±0.37	-0.32±0.13	$\langle \Delta E \rangle_{\text{Tyr}^{\bullet+},\text{Cpd II}}$	His-conf	-1.18±0.36	0.43±0.29
				Glu-conf	-1.81±0.46	0.45±0.30

$$^a \langle \text{IP}^{\text{QM-MM}} \rangle_{\text{Tyr}} = \langle E^{\text{QM-MM}}_{\text{Tyr}^{\bullet+}}(\mathbf{R}_{\text{Tyr}}) - E^{\text{QM-MM}}_{\text{Tyr}}(\mathbf{R}_{\text{Tyr}}) \rangle, \langle \text{IP}^{\text{MM}} \rangle_{\text{Tyr}} = \langle E^{\text{MM}}_{\text{Tyr}^{\bullet+}}(\mathbf{R}_{\text{Tyr}}) - E^{\text{MM}}_{\text{Tyr}}(\mathbf{R}_{\text{Tyr}}) \rangle$$

$$\langle \text{EA}^{\text{QM-MM}} \rangle_{\text{Cpd I}} = \langle E^{\text{QM-MM}}_{\text{Cpd I}}(\mathbf{R}_{\text{Cpd I}}) - E^{\text{QM-MM}}_{\text{Cpd II}}(\mathbf{R}_{\text{Cpd I}}) \rangle, \langle \text{EA}^{\text{MM}} \rangle_{\text{Cpd I}} = \langle E^{\text{MM}}_{\text{Cpd I}}(\mathbf{R}_{\text{Cpd I}}) - E^{\text{MM}}_{\text{Cpd II}}(\mathbf{R}_{\text{Cpd I}}) \rangle$$

$$\langle \Delta E^{\text{QM-MM}} \rangle_{\text{Tyr,Cpd I}} = \langle \text{IP}^{\text{QM-MM}} \rangle_{\text{Tyr}} - \langle \text{EA}^{\text{QM-MM}} \rangle_{\text{Cpd I}} \rangle, \langle \Delta E^{\text{MM}} \rangle_{\text{Tyr,Cpd I}} = \langle \text{IP}^{\text{MM}} \rangle_{\text{Tyr}} - \langle \text{EA}^{\text{MM}} \rangle_{\text{Cpd I}} \rangle$$

$$^b \langle \text{IP}^{\text{QM-MM}} \rangle_{\text{Cpd II}} = \langle E^{\text{QM-MM}}_{\text{Cpd I}}(\mathbf{R}_{\text{Cpd II}}) - E^{\text{QM-MM}}_{\text{Cpd II}}(\mathbf{R}_{\text{Cpd II}}) \rangle, \langle \text{IP}^{\text{MM}} \rangle_{\text{Cpd II}} = \langle E^{\text{MM}}_{\text{Cpd I}}(\mathbf{R}_{\text{Cpd II}}) - E^{\text{MM}}_{\text{Cpd II}}(\mathbf{R}_{\text{Cpd II}}) \rangle$$

$$\langle \text{EA}^{\text{QM-MM}} \rangle_{\text{Tyr}^{\bullet+}} = \langle E^{\text{QM-MM}}_{\text{Tyr}^{\bullet+}}(\mathbf{R}_{\text{Tyr}^{\bullet+}}) - E^{\text{QM-MM}+\text{MM}}_{\text{Tyr}}(\mathbf{R}_{\text{Tyr}^{\bullet+}}) \rangle, \langle \text{EA}^{\text{MM}} \rangle_{\text{Tyr}^{\bullet+}} = \langle E^{\text{MM}}_{\text{Tyr}^{\bullet+}}(\mathbf{R}_{\text{Tyr}^{\bullet+}}) - E^{\text{MM}}_{\text{Tyr}}(\mathbf{R}_{\text{Tyr}^{\bullet+}}) \rangle$$

$$\langle \Delta E^{\text{QM-MM}} \rangle_{\text{Tyr}^{\bullet+},\text{Cpd II}} = \langle \text{EA}^{\text{QM-MM}} \rangle_{\text{Tyr}^{\bullet+}} - \langle \text{IP}^{\text{QM-MM}} \rangle_{\text{Cpd II}} \rangle, \langle \Delta E^{\text{MM}} \rangle_{\text{Tyr}^{\bullet+},\text{Cpd II}} = \langle \text{EA}^{\text{MM}} \rangle_{\text{Tyr}^{\bullet+}} - \langle \text{IP}^{\text{MM}} \rangle_{\text{Cpd II}} \rangle$$

$$^c \sigma_{\Delta E^{\text{QM-MM}}} = \sqrt{(\sigma_{\text{IP}^{\text{QM-MM}}}^2 + \sigma_{\text{EA}^{\text{QM-MM}}}^2)} \quad , \quad \sigma_{\Delta E^{\text{MM}}} = \sqrt{(\sigma_{\text{IP}^{\text{MM}}}^2 + \sigma_{\text{EA}^{\text{MM}}}^2)}$$

Table 29. Decomposition of the outer-sphere (i.e. protein and solvent) energies into the QM-MM and MM contributions. $\langle \Delta A \rangle$ is the average driving force ^a and λ the reorganization free energy ^b for the ET from Tyr351 to Cpd I. His-conf and Glu-conf refer to the two conformations of the Tyr^{•+} observed in the classical MD (Chapter V, Figure 15). All the energies are in eV.

outer-sphere	His-conf		Glu-conf	
	QM-MM	MM	QM-MM	MM
ΔA	1.15 ± 0.37	0.05 ± 0.22	0.83 ± 0.42	0.06 ± 0.23
λ	2.33 ± 0.37	-0.38 ± 0.22	2.65 ± 0.42	-0.39 ± 0.23

$$^a \Delta A^{\text{QM-MM}} = [(\langle \Delta E^{\text{QM-MM}} \rangle_{\text{Tyr,Cpd I}} + \langle \Delta E^{\text{QM-MM}} \rangle_{\text{Tyr}^{\bullet+},\text{Cpd II}}) / 2], \Delta A^{\text{MM}} = [(\langle \Delta E^{\text{MM}} \rangle_{\text{Tyr,Cpd I}} + \langle \Delta E^{\text{MM}} \rangle_{\text{Tyr}^{\bullet+},\text{Cpd II}}) / 2]$$

$$^b \lambda^{\text{QM-MM}} = [(\langle \Delta E^{\text{QM-MM}} \rangle_{\text{Tyr,Cpd I}} - \langle \Delta E^{\text{QM-MM}} \rangle_{\text{Tyr}^{\bullet+},\text{Cpd II}}) / 2], \lambda^{\text{MM}} = [(\langle \Delta E^{\text{MM}} \rangle_{\text{Tyr,Cpd I}} - \langle \Delta E^{\text{MM}} \rangle_{\text{Tyr}^{\bullet+},\text{Cpd II}}) / 2]$$

$$^c \sigma_{\Delta A^{\text{QM-MM}}} = \sigma_{\lambda^{\text{QM-MM}}} = \sqrt{(\sigma_{\Delta E^{\text{QM-MM}}(\text{Tyr,Cpd I})}^2 + \sigma_{\Delta E^{\text{QM-MM}}(\text{Tyr}^{\bullet+},\text{Cpd II})}^2) / 2}$$

$$\sigma_{\Delta A^{\text{MM}}} = \sigma_{\lambda^{\text{MM}}} = \sqrt{(\sigma_{\Delta E^{\text{MM}}(\text{Tyr,Cpd I})}^2 + \sigma_{\Delta E^{\text{MM}}(\text{Tyr}^{\bullet+},\text{Cpd II})}^2) / 2}$$

10. COMPARISON OF THE QM/MM OPTIMIZED STRUCTURES OF THE NEUTRAL AND CATIONIC TYROSYL RADICALS

Upon ET, the initially formed tyrosyl cation radical is spontaneously deprotonated by the hydrogen-bonded base, either His343 or Glu1516 (see Chapter V, section 3.7.). In order to study the consequences of this PT, the QM/MM geometry optimizations of the tyrosyl radical in both the His- and Glu-conformations (see section 1.6.) have been repeated fixing the $O_{\text{Tyr}}\text{-}H_{\text{Tyr}}$ distance to preclude deprotonation. It is found that the neutral tyrosyl radical is more stable by 22.8 kcal/mol (His-conformation) or 21.4 kcal/mol (Glu-conformation) compared to the tyrosyl cation radical. Therefore, PT is expected to increase the exothermicity of the ET from Tyr351 to HPC Cpd I.

Table 30 compares the QM/MM optimized structures for neutral and cationic tyrosyl radicals. They are very similar, except for the $C_{\text{ipso,Tyr}}\text{-}O_{\text{Tyr}}$ distance (1.33-1.32 Å for Tyr^{•+} compared to 1.28 Å for Tyr[•]), as for gas phase models (Table 13). This slight shortening of the $C_{\text{ipso,Tyr}}\text{-}O_{\text{Tyr}}$ bond corresponds to a change from a single (i.e. C–OH) to a double (i.e. C=O) bond.

Table 30. Main distances (in Å) describing the QM/MM optimized structures of neutral and cationic tyrosyl radicals.

tyrosyl radical	His-conformation		Glu-conformation	
	Tyr ^{•+}	Tyr [•]	Tyr ^{•+}	Tyr [•]
$C_{\text{meta,Tyr}}\text{-}C_{\text{para,Tyr}}$	1.42	1.42	1.42-1.43	1.42-1.43
$C_{\text{orto,Tyr}}\text{-}C_{\text{meta,Tyr}}$	1.38	1.37-1.38	1.37	1.37
$C_{\text{ipso,Tyr}}\text{-}C_{\text{orto,Tyr}}$	1.42	1.45	1.42-1.43	1.44-1.45
$C_{\text{ipso,Tyr}}\text{-}O_{\text{Tyr}}$	1.33	1.28	1.32	1.28
$O_{\text{Tyr}}\text{-}H_{\text{Tyr}}$	0.96	1.63	0.96	1.51
$H_{\text{Tyr}}\text{-}O_{\text{Wat}}$	1.71	1.02	–	–
$H_{\text{Wat}}\text{-}N_{\delta,\text{His}}$	3.33	1.10	–	–
$H_{\text{Tyr}}\text{-}O_{\epsilon 1,\text{Glu}}$	–	–	1.68	1.06

Additional information for Chapter VI

M. Alfonso-Prieto, P. Vidossich, A. Rodríguez-Fortea,
X. Carpena, I. Fita, C. Rovira, and P. C. Loewen.

Electronic state of molecular oxygen released by catalase

J. Phys. Chem. A **2008**, 112 (50), pp 12842–12848

1. COMPUTATIONAL DETAILS

1.1. Gas phase model

The calculations of the reactants and products of the catalytic reaction were performed using a reduced model of the catalase active site, shown in Figure 1.

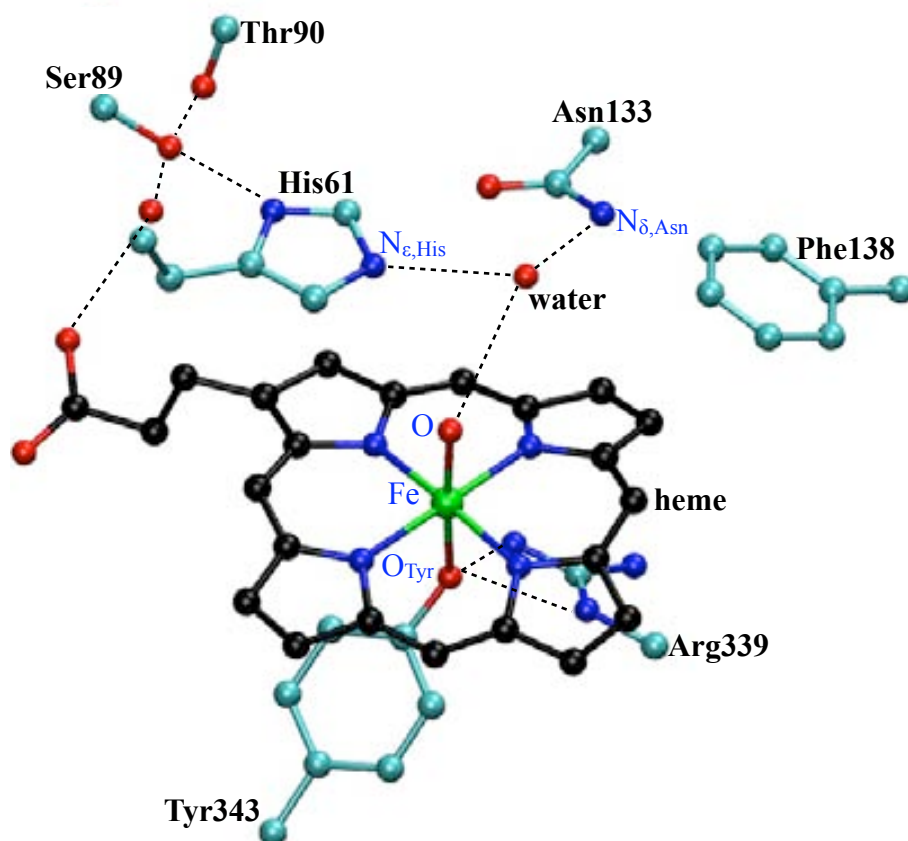


Figure 1. Model of the catalase active site used in the calculations. The residue numbering corresponds to *Micrococcus luteus* catalase (MLC, PDB entry 1GWF) (Murshudov, 2002). The hydrogen atoms are omitted for clarity.

The initial structure was taken from the work of Rovira on catalase Cpd II (Rovira, 2005). Essential residues for the catalase reaction (Loewen, 1993; Zámocky & Koller, 1999; Nicholls, 2001), as well as second shell ligands were included in the model. Specifically, we included the axial Tyr343 residue (replaced by a phenolate anion) and the proximal Arg339 residue (replaced by a methylguanidinium cation) that interacts with the tyrosine oxygen atom (residue numbering corresponding to *Micrococcus lysodeikticus* catalase, MLC). Previous work demonstrated that both residues influence significantly the structure and ligand properties of the heme (Rovira, 2003). The distal side chains of Asn133 and His61 were modeled as ethylamide and methylimidazole, respectively. The Phe138 side chain was also included because it was found to be necessary to keep

the H₂O₂ substrate in the distal pocket. To better describe the acid/base character of the distal histidine, the residues interacting with its N_δ-H were also taken into account (Ser89 side chain, replaced by methanol and Thr90 backbone, replaced by formaldehyde). The heme was modeled with an iron porphyrin plus the propionic acid side chain that interacts with Ser89 through a bridging water molecule. The propionate was taken a protonated to mimic the effect of the two positively charged Arg residues hydrogen-bonded to it in the protein.

1.2. Starting structures

The reactants of the catalytic reaction (i.e. Cpd I + H₂O₂) were modeled by replacing the water molecule in Figure 1 by hydrogen peroxide, as proposed by Fita and Rossmann (Fita & Rossmann, 1985) (see Chapter VI, Figure 10). To obtain the products (i.e. native enzyme + H₂O + O₂) we took the optimized structure of the intermediate species (i.e. Cpd II-like + O₂⁻) and moved the histidine proton to the hydroxoferryl unit.

The total charge of the system is +1. The reactants were optimized in the doublet and quartet states, because the ground state of catalase Cpd I is known to be a quartet, with a doublet state very close in energy (de Visser, 2006). The sextet and octet states were not considered, because they are expected to be high-energy configurations for Cpd I (see section 3.1.). For the products, all the possible spin states (quartet, doublet, sextet and octet) were considered.

1.3. Geometry optimizations

The simulations details are the same as explained in Chapter II, except for the size of the isolated supercell (here 20.5 × 19 × 19 Å³). The structure was optimized by keeping the terminal atoms of the distal and proximal residues fixed to mimic the steric restraints imposed by the protein environment.

2. ANALYSIS OF THE REACTIVE OXYGEN SPECIES POSSIBLY INVOLVED IN THE CATALATIC REACTION ¹

Table 1. Comparison between gas phase optimized structures (CPMD / BP86 level) and experimental data (Herzberg, 1950; Abrahams, 1951; Huber, 1972; Gubelman & Willimas, 1983; Linstrom & Mallard, 2005) of the reactive oxygen species possibly involved in the catalatic reaction.

model	O-O distance (Å)	
	calculated	experimental
H_2O_2 ($S=0$)	1.51	1.49
$\text{HOO}\cdot$ ($S=1/2$)	1.34	1.35
O_2^- ($S=1/2$)	1.31	1.30
O_2 ($S=1$)	1.23	1.21

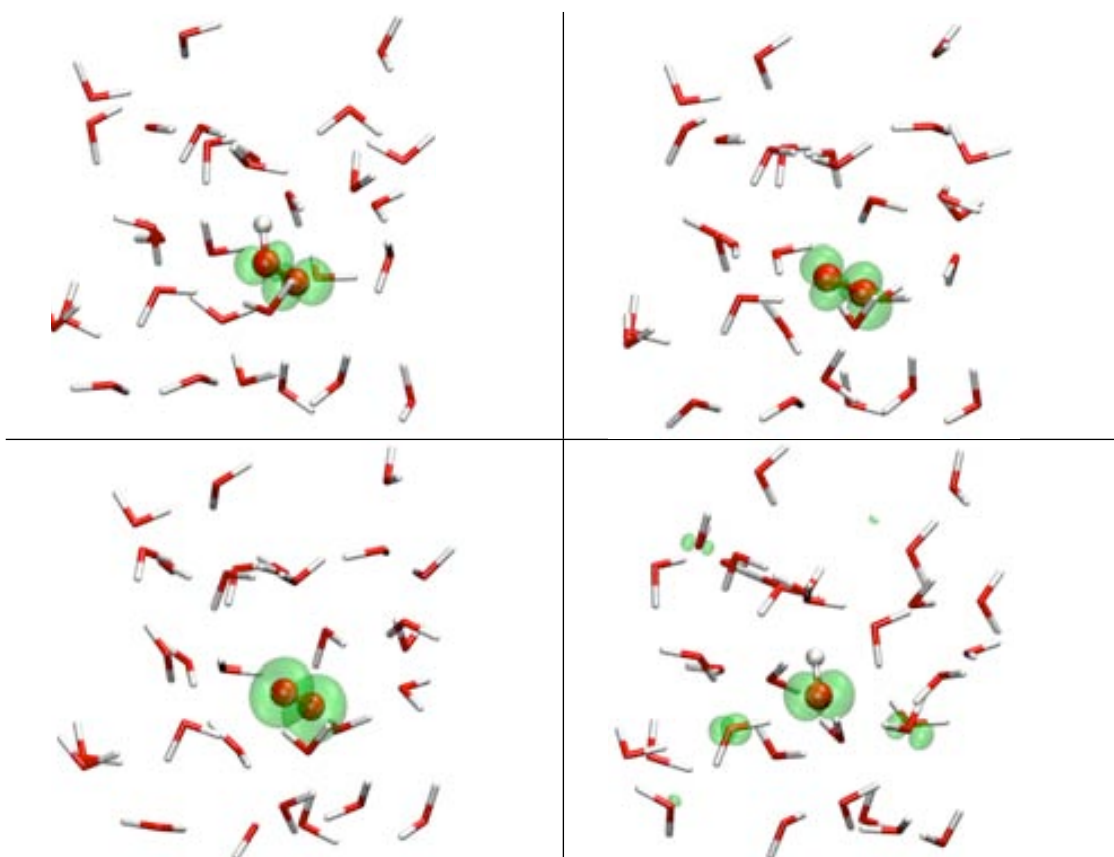


Figure 2. Snapshots from Car-Parrinello molecular dynamics of aqueous $\text{HO}_2\cdot$ ($S=1/2$), O_2^- ($S=1/2$), O_2 ($S=1$) and $\text{HO}\cdot$ ($S=1/2$). Spin isodensity surfaces at $0.01 \text{ e } \text{Å}^{-3}$ are plotted in green.

¹ These calculations were done by Dr. Pietro Vidossich in our group.

To assess the accuracy of the Becke-Perdew functional in describing reactive oxygen species (ROS), we compared optimized gas phase geometries to experimental data of H_2O_2 ($S=0$), HO_2^\bullet ($S=1/2$), O_2^- ($S=1/2$) and O_2 ($S=1$), which show a good agreement (Table 1). We also computed the spin density of the ROS with unpaired electrons ($S \neq 0$) in a box of water molecules² (see Figure 2). It turned out that the integrated spin densities are 0.97 (HO_2^\bullet), 0.97 (O_2^-) and 1.95 (O_2). Therefore, the Becke-Perdew calculations of the peroxy radical, superoxide and dioxygen do not suffer of the severe spin delocalization as it occurs, for example, for the hydroxyl radical (HO^\bullet , $S=1/2$) (VandeVondele & Sprik, 2005), for which the integrated spin density is 0.69.

3. ORBITAL ANALYSIS

To complement the analysis of the spin state, we analyze here the orbitals involved in the catalytic reaction (i.e. the heme and dioxygen orbitals).

3.1. Heme orbitals

- *Orbital occupancy in Cpd I*

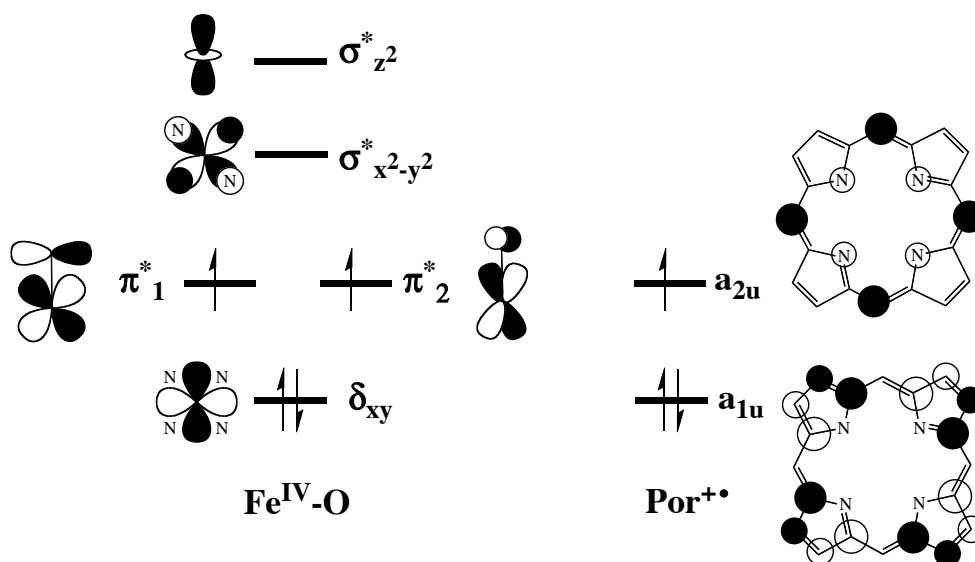


Figure 3. High-lying occupied and low-lying virtual orbitals of catalase Cpd I (adapted from (de Visser, 2003)). The π_1^* and π_2^* Fe-O orbitals result from the combination of the iron d_{xz} and d_{yz} orbitals with the p_x and p_y orbitals of the oxygen atom. The orbital occupancy corresponds to the ground state of catalase Cpd I (de Visser, 2006): a quartet A_{2u} oxoferryl porphyrin cation radical.

² Each species was solvated inside a box of 31 water molecules. The following parameters were used in the Car-Parrinello molecular dynamics: BP86 exchange-correlation functional, $\mu_e = 5$ a.u., $\delta t = 0.12$ fs.

Figure 3 shows the high-lying occupied and low-lying virtual orbitals of catalase Cpd I: five metal 3d orbitals, which split into the usual t_{2g} - e_g set of orbitals (left side) and two high-lying heme orbitals, a_{1u} and a_{2u} (right side). In the Cpd I oxidation state, this set of orbitals is occupied by nine electrons; the occupancy shown in Figure 3 corresponds to the ground state of catalase Cpd I (de Visser, 2006): $(\delta_{xy})^2 (\pi^*)^2 (a_{1u})^2 (a_{2u})^1$.

quartet ($S_{heme} = 3/2$)	doublet ($S_{heme} = 1$)
$\sigma_{z^2}^*$ $\sigma_{x^2-y^2}^*$ π_1^* \uparrow \uparrow π_2^* \uparrow a_{2u} $\uparrow\downarrow$ δ_{xy} $\uparrow\downarrow$ a_{1u} Fe^{IV}=O Por^{+•}	$\sigma_{z^2}^*$ $\sigma_{x^2-y^2}^*$ π_1^* \uparrow \uparrow π_2^* \downarrow a_{2u} $\uparrow\downarrow$ δ_{xy} $\uparrow\downarrow$ a_{1u} Fe^{IV}=O Por^{+•}
sextet ($S_{heme} = 5/2$)	octet ($S_{heme} = 7/2$)
$\sigma_{z^2}^*$ \uparrow $\sigma_{x^2-y^2}^*$ π_1^* \uparrow \uparrow π_2^* \uparrow a_{2u} \uparrow δ_{xy} $\uparrow\downarrow$ a_{1u} Fe^{IV}=O Por^{+•}	\uparrow $\sigma_{z^2}^*$ \uparrow $\sigma_{x^2-y^2}^*$ π_1^* \uparrow \uparrow π_2^* \uparrow a_{2u} \uparrow δ_{xy} \uparrow a_{1u} Fe^{III}=O Por²⁺

Figure 4. Orbital occupancy in the quartet, doublet, sextet and octet states of catalase Cpd I.

The orbital occupancy in other possible spin states of catalase Cpd I is depicted in Figure 4. In the doublet state, the occupancy is the same as in the quartet, but the unpaired spin on the porphyrin cation radical is antiparallel to the two unpaired spins on the Fe-O unit. The coupling between the π_{FeO}^* and $a_{2u, Por}$ orbitals is probably small, as the quartet and doublet states are very close in energy (Rydberg, 2004; de Visser, 2006). In the sextet state, one iron electron has been promoted from the δ to the $\sigma_{x^2-y^2}^*$ orbital. Additionally, in the octet state, one porphyrin electron has also been promoted to the $\sigma_{z^2}^*$ orbital. Because the oxo group is a strong field ligand, these excited spin states are higher-in-energy configurations than the quartet and doublet (de Visser, 2006).

- *Orbital occupancy in Cpd II*

Cpd II results from one-electron reduction of Cpd I. Depending on which orbital from Cpd I “receives” the transferred electron, two different electromers are possible. It could be either that this electron couples with the unpaired porphyrin electron (i.e. Por-Fe^{IV}-OH) or that it couples with one of the unpaired electrons of the oxoferryl unit (i.e. Por⁺-Fe^{III}-OH) (Derat, 2006a). The orbital occupancy of these two electromers of catalase Cpd II in all the possible spin states is shown in Figure 5.

For both electromers the ground state of Cpd II is a triplet (Filatov, 1999; Derat, 2006a), and the singlet is very close in energy, because it only differs in the coupling between the two unpaired electrons (ferromagnetic in the triplet and antiferromagnetic in the singlet). Electron excitations from the π^* and δ orbitals to the σ_{xy}^* and $\sigma_{z^2}^*$ orbitals result in higher spin configurations (quintuplet and septuplet) which are higher in energy (Filatov, 1999).

Cpd II, Por-Fe ^{IV} -OH electromer		
triplet ($S_{heme} = 1$)	singlet ($S_{heme} = 0$)	quintuplet ($S_{heme} = 2$)

Figure 5. (a) Orbital occupancy in the triplet, singlet and quintuplet states of catalase Cpd II, Por-Fe^{IV}-OH electromer.

Cpd II, Por ⁺⁺ -Fe ^{III} -OH electromer			
triplet ($S_{heme} = 1$)		singlet ($S_{heme} = 0$)	
$\sigma_{z^2}^*$ $\sigma_{x^2-y^2}^*$		$\sigma_{z^2}^*$ $\sigma_{x^2-y^2}^*$	
π_1^*	π_2^*	π_1^*	π_2^*
a_{2u}	a_{1u}	a_{2u}	a_{1u}
δ_{xy} Fe ^{III} -OH	δ_{xy} Por ^{+•}	δ_{xy} Fe ^{III} -OH	δ_{xy} Por ^{+•}
quintuplet ($S_{heme} = 2$)		septuplet ($S_{heme} = 3$)	
$\sigma_{z^2}^*$ $\sigma_{x^2-y^2}^*$		$\sigma_{z^2}^*$ $\sigma_{x^2-y^2}^*$	
π_1^*	π_2^*	π_1^*	π_2^*
a_{2u}	a_{1u}	a_{2u}	a_{1u}
δ_{xy} Fe ^{III} -OH	δ_{xy} Por ^{+•}	δ_{xy} Fe ^{III} -OH	δ_{xy} Por ^{+•}

Figure 5 (cont). (b) Orbital occupancy in the triplet, singlet, quintuplet and septuplet states of catalase Cpd II, Por⁺⁺-Fe^{III}-OH electromer.

• *Orbital occupancy in Por-Fe^{III}*

Figure 6 shows the occupancy of the iron d orbitals in a Fe^{III}-porphyrin. This represents the alkaline and the aqua forms of catalase (i.e. Por-Fe^{III}-OH⁻ and Por-Fe^{III}-OH₂, respectively), in which the iron atom is hexacoordinated, as well as the native enzyme (i.e. Por-Fe^{III}), in which the iron atom is pentacoordinated.

In these iron (III) porphyrin complexes, the ground spin state depends on the energy gap between the t_{2g} and e_g orbitals. Because the hydroxo group is a strong field ligand (Evans & Reed, 2000), the ground state of Por-Fe^{III}-OH⁻ is expected to be a doublet. Indeed, spectroscopic studies have shown that the alkaline form of horse erythrocyte catalase (Yshida, 1970), as well as that of other hemeproteins (Sono & Dawson, 1982; Yonetani & Anni, 1987; Sitter, 1988), bears a low spin Fe^{III}. DFT calculations of Rydberg and coworkers also found (Rydberg, 2004) that the ground state of catalase Por-Fe^{III}-OH⁻ is a doublet. By contrast, water is a weaker field ligand than the hydroxyl

group (Evans and Reed, 2000), and hence the ground state of catalase Por-Fe^{III}-OH₂ is found to be a quartet (i.e. an intermediate spin Fe^{III}) with a very close in energy doublet state (Rydberg, 2004).

Different from these hexacoordinated complexes, the energy gap between the t_{2g} and e_g orbitals in the pentacoordinated Por-Fe^{III} complex is expected to be smaller, and thus the ground state of catalase Por-Fe^{III} is found to be a sextet (Rydberg, 2004). This is also in agreement with native catalase being a high spin Fe^{III} (Sharma, 1989).

doublet ($S_{heme} = 1/2$) low spin Fe ^{III}	quartet ($S_{heme} = 3/2$) intermediate spin Fe ^{III}	quintuplet ($S_{heme} = 5/2$) high spin Fe ^{III}
$\sigma^*_{z^2} (d_{z^2})$ — — $\sigma^*_{x^2-y^2} (d_{x^2-y^2})$	$\sigma^*_{z^2} (d_{z^2})$ — ↑ — $\sigma^*_{x^2-y^2} (d_{x^2-y^2})$	$\sigma^*_{z^2} (d_{z^2})$ ↑ ↑ — $\sigma^*_{x^2-y^2} (d_{x^2-y^2})$
$\pi^*_1 (d\pi_1)$ ↑↑ — ↑ — $\pi^*_2 (d\pi_2)$ ↑↑ — $\delta_{xy} (d_{xy})$	$\pi^*_1 (d\pi_1)$ ↑ — ↑ — $\pi^*_2 (d\pi_2)$ ↑↑ — $\delta_{xy} (d_{xy})$	$\pi^*_1 (d\pi_1)$ ↑ — ↑ — $\pi^*_2 (d\pi_2)$ ↑ — $\delta_{xy} (d_{xy})$

Figure 6. Orbital occupancy in the doublet, quartet and sextet states of the alkaline, aqua and native forms of catalase. The iron orbitals are named δ , π^* and σ^* in the hexacoordinated complexes (i.e. Por-Fe^{III}-OH⁻ and Por-Fe^{III}-OH₂), and d and d_π in the pentacoordinated complex (i.e. Por-Fe^{III}).

3.2. Dioxygen orbitals

Figure 7 shows the molecular orbitals of dioxygen, which result from the combination of the 2p orbitals of the two oxygen atoms. The different reactive oxygen species just differ in the occupancy of the 2π_g^{*} orbitals. Hydrogen peroxide (H₂O₂) shows two doubly occupied 2π_g^{*} orbitals. Abstraction of one electron (from one 2π_g^{*} orbital) results in a peroxy radical (HOO[•]) or a superoxide anion radical (O₂⁻) with one doubly occupied and one half-filled 2π_g^{*} orbitals. As a consequence, one-electron oxidation is accompanied by an increase in the bond order from 1 to 1.5 (i.e. the O-O distance decreases from ~ 1.5 to ~ 1.3 Å, as can be seen in Table 1). On the contrary, a two-electron oxidation of H₂O₂ or one-electron oxidation of HOO[•] and O₂⁻ leads to molecular oxygen, in which the bond order increases to 2 and thus the O-O distance is the shortest (1.23 Å, see Table 1).

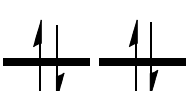
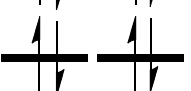

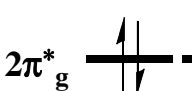
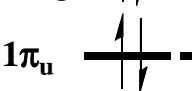
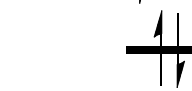
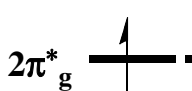
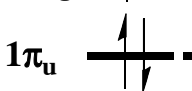

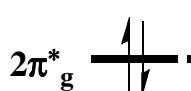
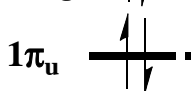

H_2O_2 ($S_{OO} = 0$)	$\text{HOO}^\bullet, \text{O}_2^{\bullet-}$ ($S_{OO} = 1/2$)	O_2 ($S_{OO} = 1$)	O_2 ($S_{OO} = 0$)
$4\sigma_u^*$ ——— $2\pi_g^*$  $1\pi_u$  $3\sigma_g$ 	$4\sigma_u^*$ ——— $2\pi_g^*$  $1\pi_u$  $3\sigma_g$ 	$4\sigma_u^*$ ——— $2\pi_g^*$  $1\pi_u$  $3\sigma_g$ 	$4\sigma_u^*$ ——— $2\pi_g^*$  $1\pi_u$  $3\sigma_g$ 

Figure 7. Orbital occupancy in the reactive oxygen species possibly involved in the catalytic reaction.

4. EFFECT OF THE PROTONATION STATE OF THE PROPIONIC SIDE CHAIN

In the reduced model of the catalase active site used in the calculations, the propionate side chain of the heme cofactor was taken as protonated (Figure 1). This *propionic* model mimics the salt bridges of this propionate with two positively charged Arg residues present in the protein environment. In order to assess the effect of the protonation state of the propionic heme side chain, we also performed additional calculations with a non-protonated carboxylate (i.e. *propionate* model).

These additional calculations showed that the electronic structure of neither the intermediate species (Figure 8) nor the products (Figure 9) is affected by the protonation state of the propionic heme side chain. The tiny unpaired spin density observed on the carboxylate oxygen atoms is expected to be an artifact of the propionate model. As already found by Shaik *et al.* in cytochrome P450, when the protein residues screening the negative charge of the propionates are included, this spin density disappears (see for instance: Derat, 2005). Instead of adding the two Arg residues hydrogen-bonded to the propionate side chain in catalase, we have chosen to protonate the carboxylate (i.e. the propionic model) for computational economy.

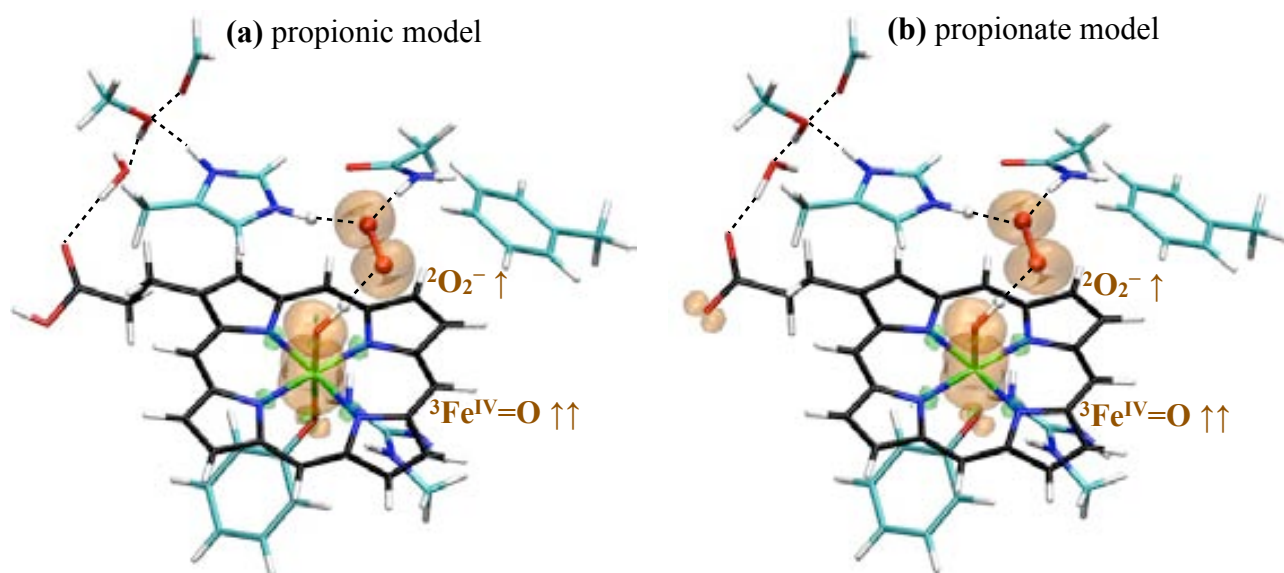


Figure 8. Comparison of the spin density distributions of the propionate and propionic models for the intermediate species (i.e. Cpd II-like + O_2^-) in the quartet state. Spin isodensity surfaces at $0.004 \text{ e } \text{\AA}^{-3}$ are plotted in orange (spin-up) and green (spin-down). The atoms of H_2O_2 are represented in ball and stick.

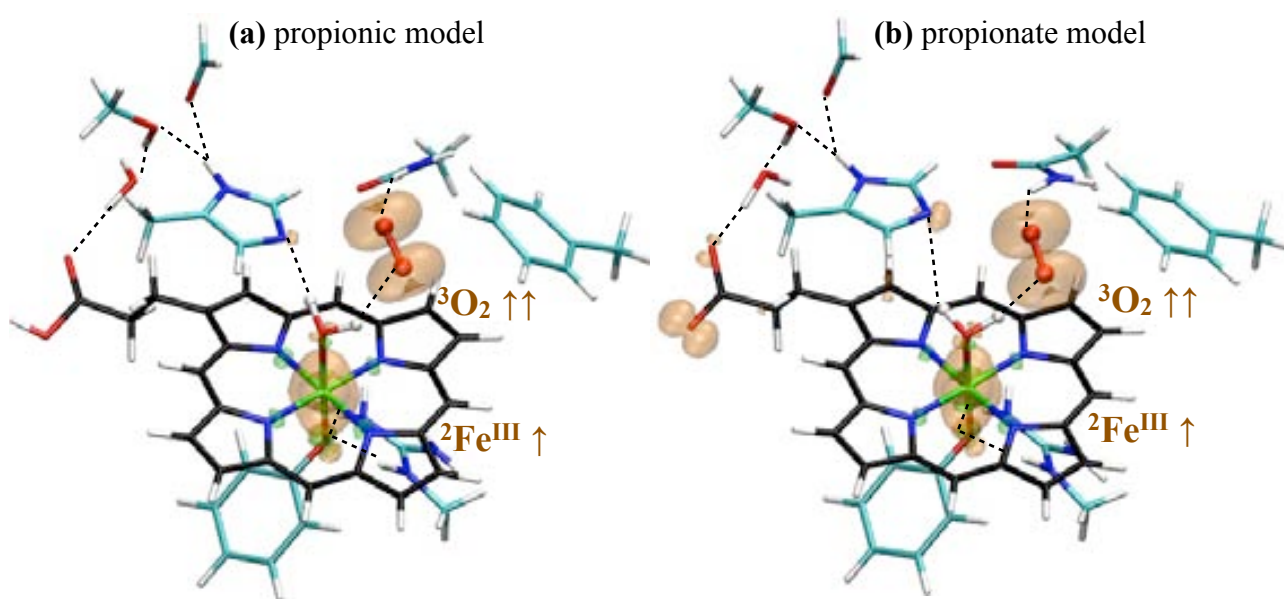


Figure 9. Comparison of the spin density distributions of the propionate and propionic models for the products (i.e. Por- Fe^{III} + H_2O + O_2) of the catalytic reaction in the quartet state. Spin isodensity surfaces at $0.004 \text{ e } \text{\AA}^{-3}$ are plotted in orange (spin-up) and green (spin-down). The atoms of H_2O_2 are represented in ball and stick representation.

5. INFLUENCE OF THE EXCHANGE-CORRELATION FUNCTIONAL

In order to assess the possible effect of the self-interaction error (SIE), we also performed additional single-point calculations with the B3LYP functional (Becke, 1988; Lee, 1988; Becke, 1993) and the same PW basis set (Todorova, 2006), because the inclusion of a Hartree-Fock (HF) exchange part decreases the SIE (Lundberg & Siegbahn, 2005).

As can be seen Table 2 and Figures 10-11, single-point calculations with B3LYP yield the same electronic distributions as BP86 for the reactants (i.e. Cpd II-like + superoxide, Figure 10) and the product (doublet Fe^{III} + triplet oxygen, Figure 11). Although this result does not exclude completely the SIE, because catalase is experimentally found to form Cpd II and Cpd II-like intermediates (see Chapter I, section 3.3.), it is reasonable to think that the catalytic reaction can also take place through such intermediate.

Table 2. Comparison of the BP86 and B3LYP number of unpaired electrons on relevant fragments^a of the intermediate species (i.e. Cpd II-like + O₂⁻) and the products (i.e. Por-Fe^{III} + H₂O + O₂) of the catalytic reaction. The spin density distributions obtained using the BP86 and B3LYP functionals (Figures 10 and 11) were integrated using Bader's Atoms-In-Molecules theory (Bader, 1990).

number of unpaired electrons	intermediate		products	
	BP86	B3LYP	BP86	B3LYP
Fe	1.45 [↑]	1.69 [↑]	1.06 [↑]	1.01 [↑]
O	0.26 [↑]	0.19 [↑]	0.02 [↑]	0.01 [↑]
FeO	1.71 [↑]	1.88 [↑]	1.08 [↑]	1.02 [↑]
O _{Tyr}	0.03 [↑]	0.02 [↑]	0.02 [↑]	0.01 [↑]
O _a -O _b	1.28 [↑]	1.18 [↑]	1.89 [↑]	1.96 [↑]
N _{Por}	0.05 [↓]	0.05 [↓]	0.02 [↓]	0.03 [↓]

^a For atom names see Chapter VI, Figures 9, 10 and 12.

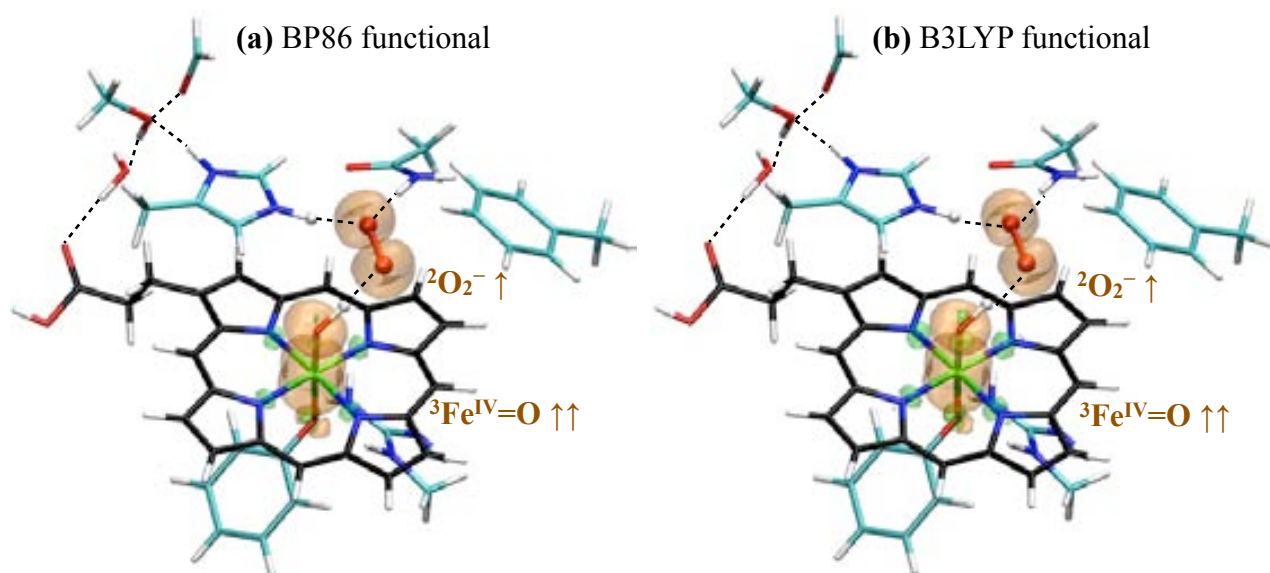


Figure 10. Comparison of the BP86 and B3LYP spin density distributions of the intermediate species (i.e. Cpd II-like + O_2^-) of the catalytic reaction in the quartet state. Spin isodensity surfaces at $0.004 \text{ e } \text{\AA}^{-3}$ are plotted in orange (spin-up) and green (spin-down). The atoms of H_2O_2 are represented in ball and stick representation.

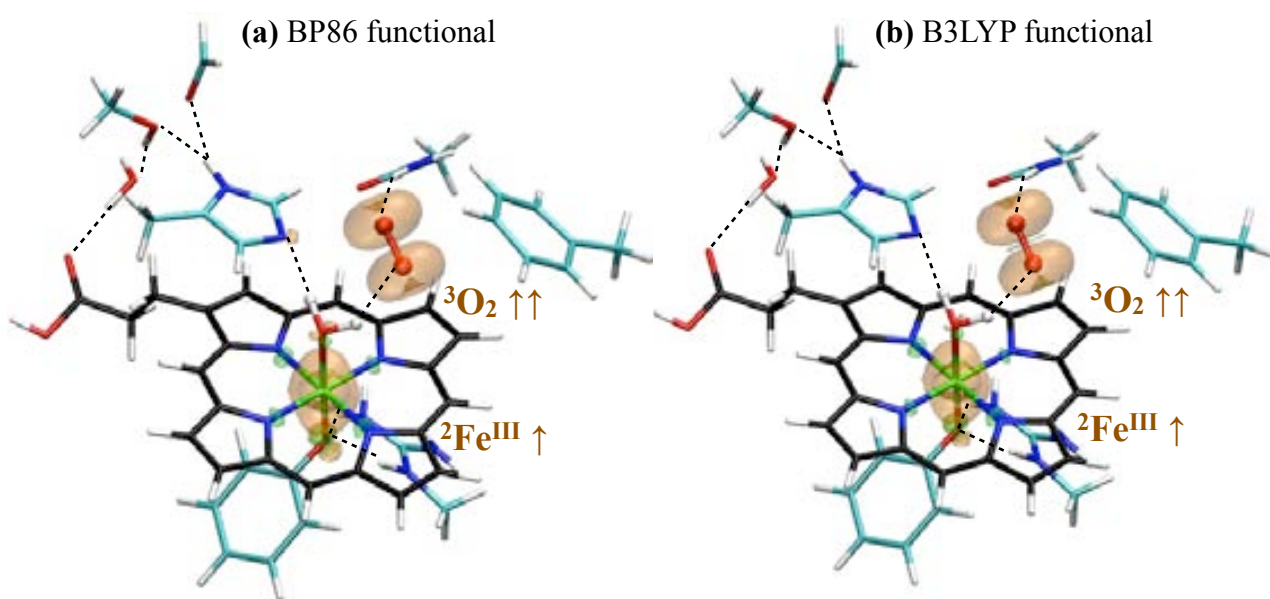


Figure 11. Comparison of the BP86 and B3LYP spin density distributions of the products (i.e. Por- Fe^{III} + H_2O + O_2) of the catalytic reaction in the quartet state. Spin isodensity surfaces at $0.004 \text{ e } \text{\AA}^{-3}$ are plotted in orange (spin-up) and green (spin-down). The atoms of H_2O_2 are represented in ball and stick.

Additional information for Chapter VII

M. Alfonso-Prieto, X. Biarnés,
P. Vidossich and C. Rovira.

The molecular mechanism of the catalase reaction

J. Am. Chem. Soc. **2009**, 131 (33), pp 11751–11761

1. COMPUTATIONAL DETAILS OF THE QM/MM SIMULATIONS

Starting structures

The initial structures of HPC-Cpd I and PVC-Cpd I for the QM/MM simulations were taken from Chapter IV (configuration **Ia**). To model the Cpd I : H₂O₂ complex, the pocket water was replaced by the H₂O₂ molecule, which was accommodated into the active site as proposed by Fita and Rossmann (Fita & Rossmann, 1985) (Figure 1).

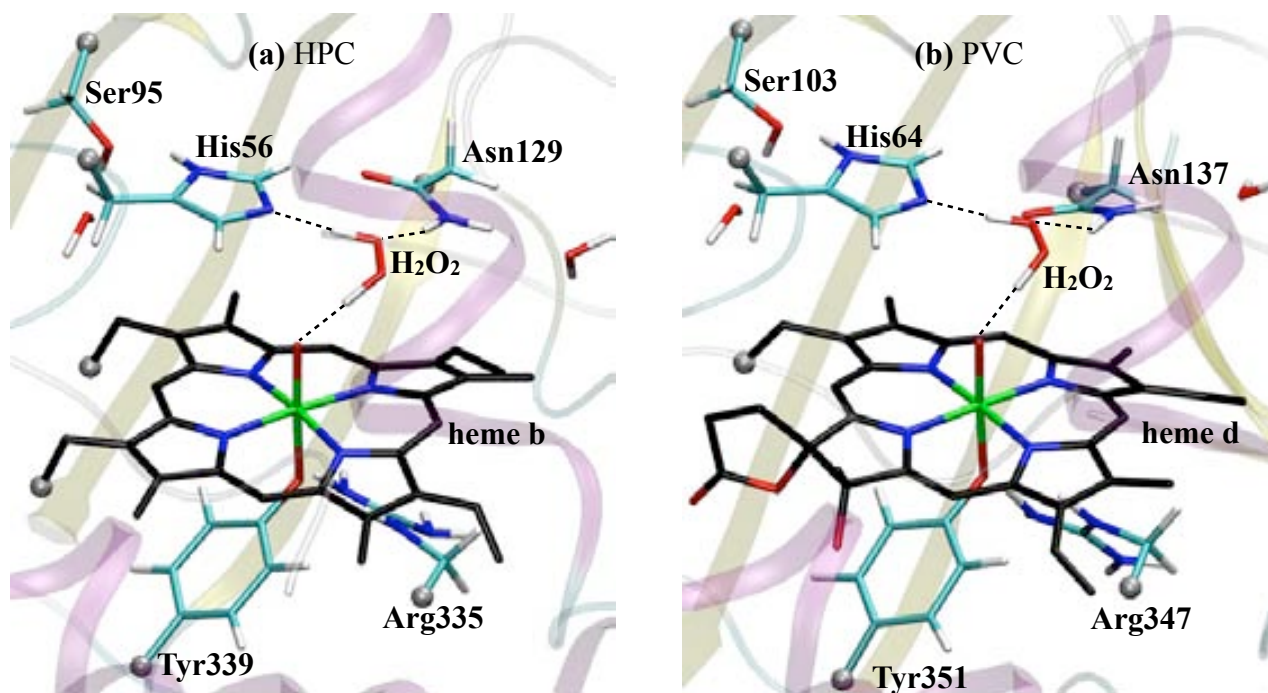


Figure 1. QM-MM partition used in the calculations. The heme cofactor is shown in black and the corresponding hydrogen atoms are omitted for clarity. The link atoms are displayed as grey balls.

Structure optimizations

Figure 1 shows the QM region used in the calculations. Except for the presence of the hydrogen peroxide molecule, the simulation details are the same as for configuration **Ia** in Chapter IV.

Molecular dynamics simulations

CP QM/MM simulations at an average temperature of 300 K were performed (~ 2ps) in order to equilibrate the system before starting the metadynamics simulations. A timestep of 0.12 fs and a fictitious electronic mass of the CP Lagrangian of 700 au were used.

2. REACTION PATHWAY USING A SINGLE GEOMETRIC VARIABLE

To get a first glimpse into the reaction mechanism, we initially considered a single geometric variable. The simulation was performed for HPC, starting from configuration (**1**) in Figure 2b (i.e. a Cpd II-like species and a peroxy radical), since the reactants evolved spontaneously to this species in an AIMD simulation (see Chapter VII, section 2.1.). The reaction coordinate (rc) was taken as the difference of the distances between the bonds that need to be formed ($O-H_b$) and broken (O_b-H_b) [i.e. $\xi = d(O-H_b) - d(O_b-H_b)$]. A constrained optimization was performed for different values of ξ (using steps of 0.5 Å from 2.5 to -2.5). In each optimization, the value of ξ is fixed and the remaining degrees of freedom are optimized. It is important to point out that the chosen rc does not require that H_b binds to the distal His during the reaction.

The resulting reaction pathway is shown in Figure 2, along with the potential energy profile. In the first part of the reaction, H_b transfers as a proton from O_b to the distal His (**1** \rightarrow **2** in Figure 2b), resulting in a superoxide anion (O_2^-), as can be seen from the spin density distribution shown in Figure 3. Subsequently, O_2^- rotates and H_b transfers to O_a , restoring the peroxy radical (**3**). Once the proton is in O_a , it is closer to the hydroxoferryl moiety than it was before. In the next step, the peroxy radical rotates around the O_a-O_b bond and the hydrogen bond between H_b and the distal His breaks. At the same time, the Fe-OH unit rotates around the Fe-O bond, orienting properly the lone pair of the ferryl oxygen to form a new hydrogen bond with H_b (**4**). Finally, H_b transfers to the hydroxoferryl unit, forming one water and one oxygen molecule (**5**). The final transfer of H_b takes place in the form of one hydrogen atom, as indicated by the changes in spin density distribution (see Figure 3), decreasing the oxidation state of the iron atom from Fe^{IV} to Fe^{III} and forming oxygen.

Therefore, according to this simulation, the role of the distal His is just to exchange the proton between the two oxygen atoms. In other words, it holds the proton while the O_2^- rotates and adopts a configuration suitable for the transfer of H_b to the FeOH unit. Formally, the whole reaction can be described as a double hydrogen atom transfer (H_a^\bullet and H_b^\bullet). This is somehow different from the *His-mediated* (Fita-Rossmann) mechanism (see Chapter VII, Figure 1a), in which the His acts as an acid-base residue delivering one proton to the Fe-OH unit. It is also different from the *direct* mechanism proposed for certain Mb mutants, in which the two hydrogen atoms transfer directly from H_2O_2 to the oxoferryl unit (Chapter VII, Figure 1b). However, the computed pathway exhibits features of the two previously proposed mechanisms. It starts with His acting as acid/base catalyst

(as in the His-mediated mechanism) but it ends up with a direct hydrogen atom transfer from the peroxy radical to the ferryl oxygen (as in the direct mechanism).

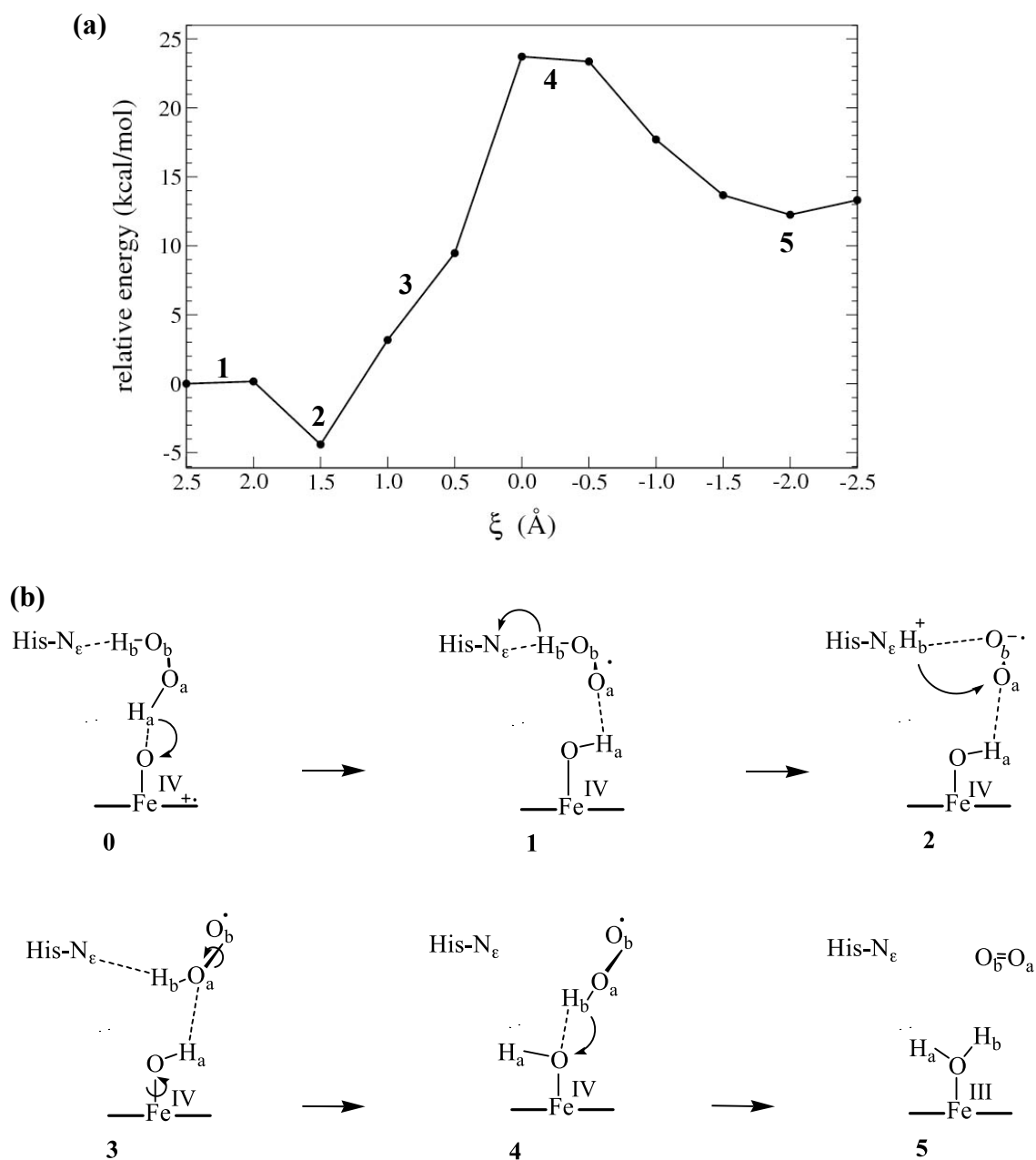


Figure 2. (a) Energy profile obtained from the constrained structure optimizations using one reaction coordinate in HPC. (b) Schematic representation of the reaction pathway.

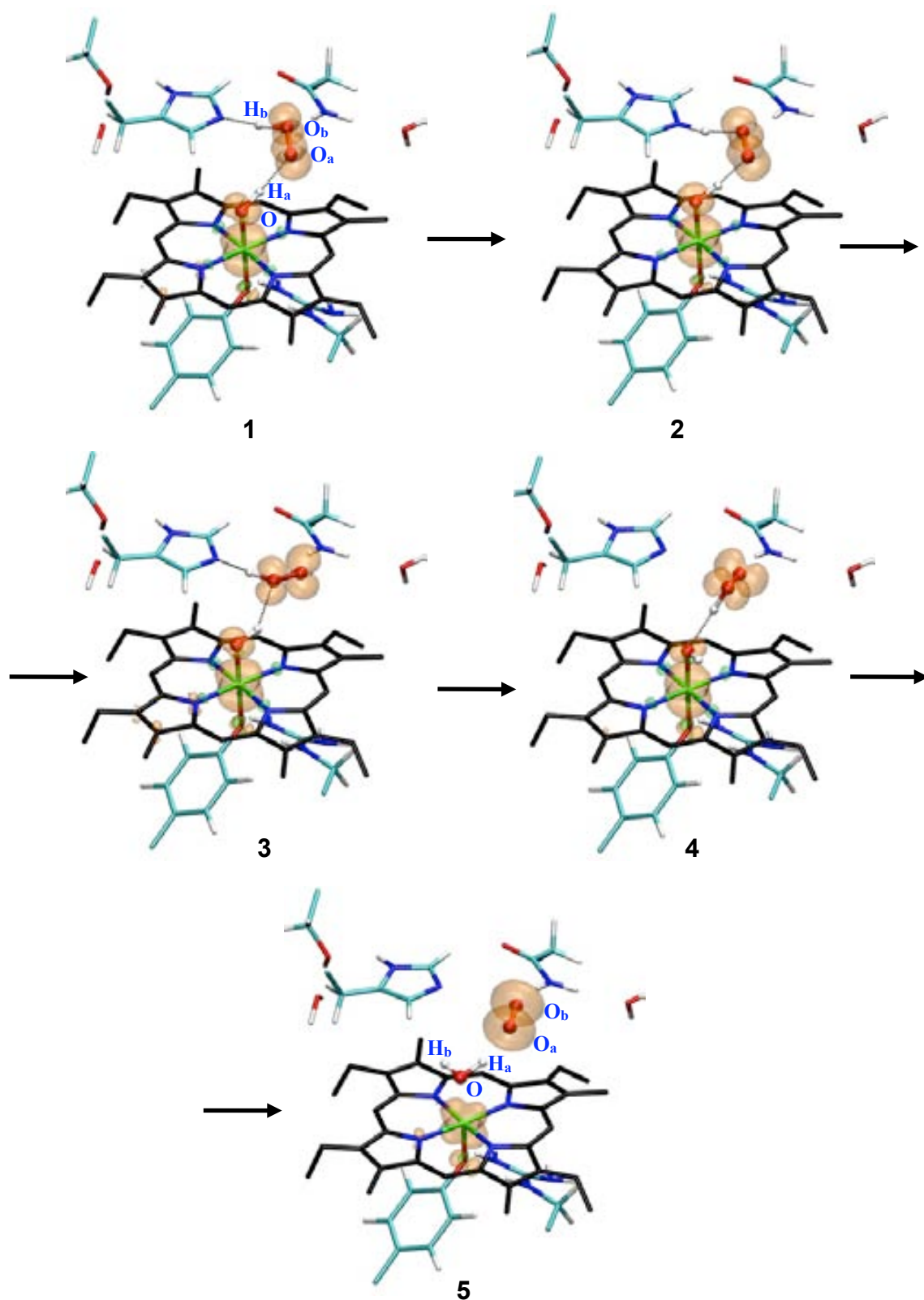


Figure 3. Spin density distribution of some of the constrained optimized structures along the reaction pathway in HPC using one reaction coordinate. Only the QM atoms are shown. Spin isodensity surfaces at $0.007 \text{ e } \text{\AA}^{-3}$ are plotted in orange (α spin) and green (β spin).

Even though the previous mechanism could be conceivable, several aspects made us think that either the reaction coordinate used is not sufficient to describe the reaction pathway and / or temperature effects are important. First of all, it is surprising that the reaction turns out to be endothermic (by 11 kcal/mol, see Figure 2a), while the catalase reaction is known to be highly exothermic (Nielson & Kiesow, 1972). Secondly, the fact that the distal His acts merely to help transferring H_a from O_a to O_b, instead of transferring H_a directly to the Fe-OH unit, could be due to the limited flexibility of the distal His in the optimization of the structure (i.e. the dynamics of the active site could be important to describe the reaction). Thirdly, the energy barrier (≈ 24 kcal/mol) is anomalously high and very different from the experimental measurements. The rate constant of $1.20 \pm 1.98 \times 10^7 \text{ M}^{-1} \text{ s}^{-1}$ measured for MLC in reference (Kato, 2004) corresponds to a pseudo first-order rate constant of $2.16\text{-}19.2 \times 10^4 \text{ s}^{-1}$ (at $[\text{H}_2\text{O}_2] = 1.8\text{-}16 \times 10^{-3} \text{ M}$) and thus to an activation free energy of 14 kcal/mol.

3. COMPUTATIONAL DETAILS OF THE METADYNAMICS SIMULATIONS

The collective variables used in the metadynamics simulations are a combination of coordination numbers of the covalent bonds being formed / broken. We adopt the definition of coordination number of a species A with a species B, $N_{\text{coord}}(A,B)$, as in reference (Iannuzzi, 2003 & Boero, 2004):

$$N_{\text{coord}}(A,B) = \sum_{i=1}^{N_A} \frac{1}{N_A} \left[\sum_{i=1}^{N_B} \frac{1 - (r_{ij} / d_{AB})^p}{1 - (r_{ij} / d_{AB})^{(p+q)}} \right] \quad \text{Formula 1}$$

where N_A and N_B are the number of atoms of species A and B, respectively, r_{ij} are the interatomic distances, d_{AB} is a threshold distance for bonding and p and q are exponents which determine the steepness of the decay of N_{coord} with respect to r_{ij} . This definition has been previously used in several studies of chemical and biochemical reactions using the metadynamics approach (Iannuzzi, 2003; Boero, 2004). The following values of d_{AB} , p and q were taken for the simulations: $d_{AB,1} = 1 \text{ \AA}$, $p_1 = 12$, $q_1 = 3$ and $d_{AB,2} = 1.8 \text{ \AA}$, $p_2 = 3$, $q_2 = 3$, where the subindexes 1 and 2 refer to CV₁ and CV₂, respectively.

Values of 3 (m_1) and 30 (m_2) a.m.u for the mass of the fictitious particle and 3 (k_1) and 30 (k_2) a.u. for the force constant were used in the MTD simulations. The height of the Gaussian terms was set at 1 kcal·mol⁻¹, which ensures sufficient accuracy for the reconstruction of the free energy

surface (Laio, 2005; Ensing, 2005 & 2006). The width of the Gaussian terms was set at 0.03 according to the oscillations of the selected collective variables observed in a free dynamics. A new Gaussian-like potential was added every 150 MD steps.

In order to explore completely the free energy landscape it was necessary to add 349 / 306 Gaussians for HPC / PVC. In terms of simulation time this corresponds to 5.3×10^4 / 4.2×10^4 MD steps (6.4 / 5.1 ps). Additional calculations working selectively in one of the two pathways found for HPC were done to probe the convergence of the FES. It turned out that the height of the energy barrier changed within one kcal/mol, which corresponds to the resolution of the hills being used. In the case of PVC, the back reaction (from products to reactants) occurred while the product oxygen molecule was escaping towards the main channel. All our attempts to avoid it, by using either constraints or walls in the metadynamics simulation, did not succeed. Therefore the free energy landscape (see Chapter VII, Figure 8) has been represented using only the forward reaction.

The ground state of catalase Cpd I is a quartet ($S = 3/2$), which also turned out to be the ground state of the Cpd I : H₂O₂ complex. For products, either quartet or octuplet are expected as ground states based on the spin state of the isolated fragments (triplet dioxygen triplet; sextet Fe^{III}) and depending on whether unpaired spins couple ferro- or antiferromagnetically. Thus we decided to run the metadynamics on the quartet state and investigate this single surface approximation a posteriori, computing the relative energies among different spin states (doublet, quartet, sextet and octuplet) for the main reaction intermediates (see section 5).

4. SYSTEM EVOLUTION DURING THE METADYNAMICS TRAJECTORY

The metadynamics simulation started from the Cpd II-like configuration formed spontaneously during the initial room temperature equilibrium CP QM/MM MD simulations of HPC (Chapter VII, Figure 3a) and PVC (Chapter VII, Figure 3b).

• HPC

After the spontaneous transfer of H_a from the H₂O₂ molecule to Cpd I (Chapter VII, section 2.1.), this hydrogen atom remains covalently bonded to the ferryl oxygen all the time ($O-H_a = 1.00 \pm 0.04$ Å, Figure 4). Thus, H_b is the only hydrogen atom of the substrate that rearranges along the metadynamics simulation, as can be seen in the changes of the O_b-H_b distance in Figure 5. During the first ≈ 3.6 ps of the metadynamics simulation, H_b travels back and forth between the peroxy radical and the distal His (note the concerted change in the O_b-H_b and N_{ε,His}-H_b distance in Figure

5). H_b , being either covalently bound to O_b or to the N_ϵ of His, is far from the ferryl oxygen. Thus the $O-H_b$ distance is maximum (between 3 and 4 Å), and its oscillations are due to the transitions of H_b between the distal His and the peroxy radical (Figure 5). At ≈ 3.7 ps, there is an abrupt decrease of the $O-H_b$ distance (Figure 4), corresponding to the peroxy radical flipping over and the breakage of the hydrogen bond with the distal His. This is accompanied by an increase in the $N_{\epsilon,His}-H_b$ distance (Figure 5), resulting in the direct transfer of H_b from the peroxy radical to the ferryl oxygen, generating the products of the reaction ($CV_1 \approx 0$ and $CV_2 \approx 2$, see Figure 6). The shortening of the O_a-O_b bond length and the increase in the Fe-O distance (Figure 7) are also indicative of the formation of oxygen and water. The spin densities correspond to a triplet oxygen and a doublet Fe^{III} for the products of the reaction (see Chapter VII, Figure 7) indicating that H_b transfers to the hydroxoferryl unit as a hydrogen atom. Overall, the system reaches the product state via the *direct* mechanism (Figure 1b), in which the peroxy radical rotates and allows H_b to be transferred directly to the hydroxoferryl unit, without passing through the distal His¹.

In a metadynamics simulation, once the product of the reaction is reached, the reaction is expected to return to the reactants state via the same path (recrossing), unless there are alternative reaction paths (Boero, 2004), in which case a new area of the free energy surface is explored. This was found to be the case here. Once the products state is reached (at ≈ 4 ps, as can be seen from the value of CV_2 in Figure 6), H_b tries to go back to O_b repeatedly (note the changes on the O_b-H_b distance between ≈ 4.2 ps and ≈ 6.6 ps in Figure 5). However, after these unsuccessful recrossing attempts, the system finally returns to the products state ($O-H_a$ and $O-H_b$ distances are very similar after ≈ 6.6 ps, Figure 4) and remains there for ≈ 1 ps. Then the system starts to explore another pathway. As seen in Figure 4, at ≈ 7.7 ps there is a sudden increase of the $O-H_b$ distance up to ≈ 4 Å, due to the transfer of H_b to the distal His (note the concerted change in the $O-H_b$ and $N_{\epsilon,His}-H_b$ distances in Figure 5). Next, H_b jumps from the distal His to O_b (O_b-H_b distance returns to the same value as at the start of the metadynamics simulation, Figure 5), forming again the initial Cpd II-like species and completing one reaction cycle. Although observed in reverse sense, this is precisely the His-mediated mechanism (Chapter VII, Figure 1a), in which the distal His acts as an acid-base residue to mediate the transfer of H_b from the peroxy radical to the hydroxoferryl. Therefore, the metadynamics simulation for HPC shows that there are two different reaction pathways between the Cpd II-like configuration and the products.

¹ Even though in the metadynamics simulation we observed first the transfer of H_b to the distal His (because it has a smaller barrier, ~ 4 kcal/mol, see Chapter VII, section 2.2), once we added enough gaussians, the system was able to overcome a higher barrier (~ 12 kcal/mol, see Chapter VII, section 2.2) and explore a different region of the free energy surface, which corresponds to the direct pathway from the Cpd II-like intermediate to the products.

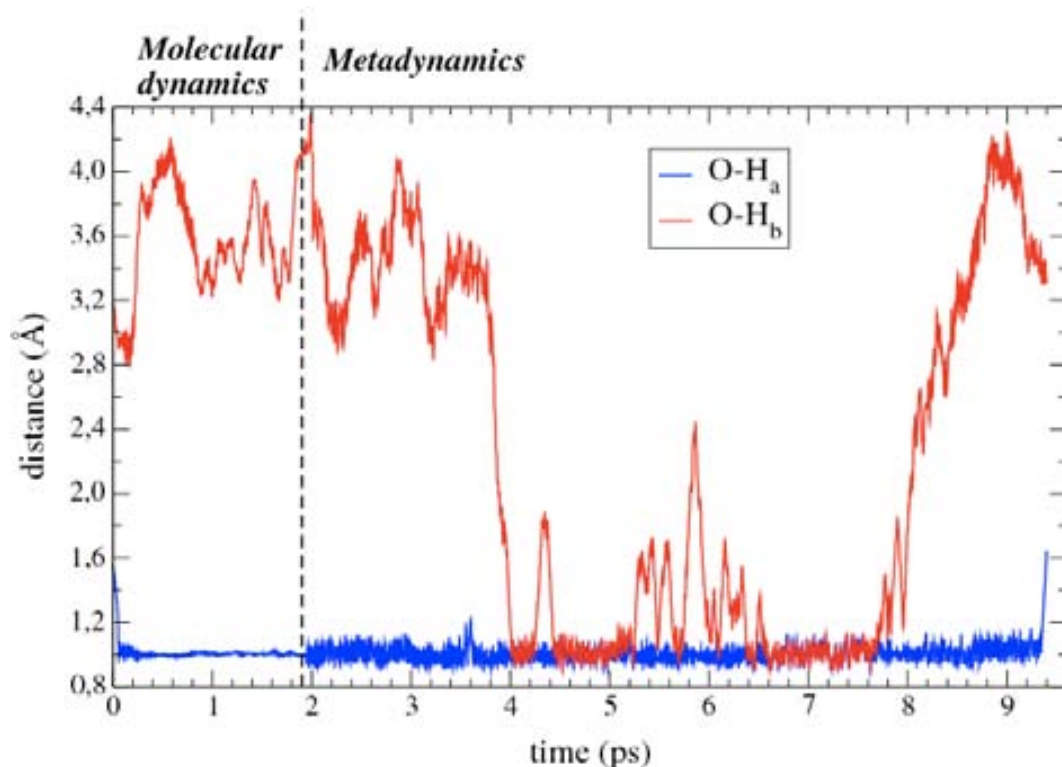


Figure 4. Time evolution of the $O-H_a$ and $O-H_b$ distances (see atom labeling in Chapter VII, Figure 3a) during one reaction cycle for HPC (≈ 9 ps). The results of the initial AIMD simulation (the first ≈ 1.9 ps), leading to the Cpd II-like : peroxy radical configuration, have been added to the metadynamics simulation (last ≈ 7 ps) in order to cover the entire reaction mechanism.

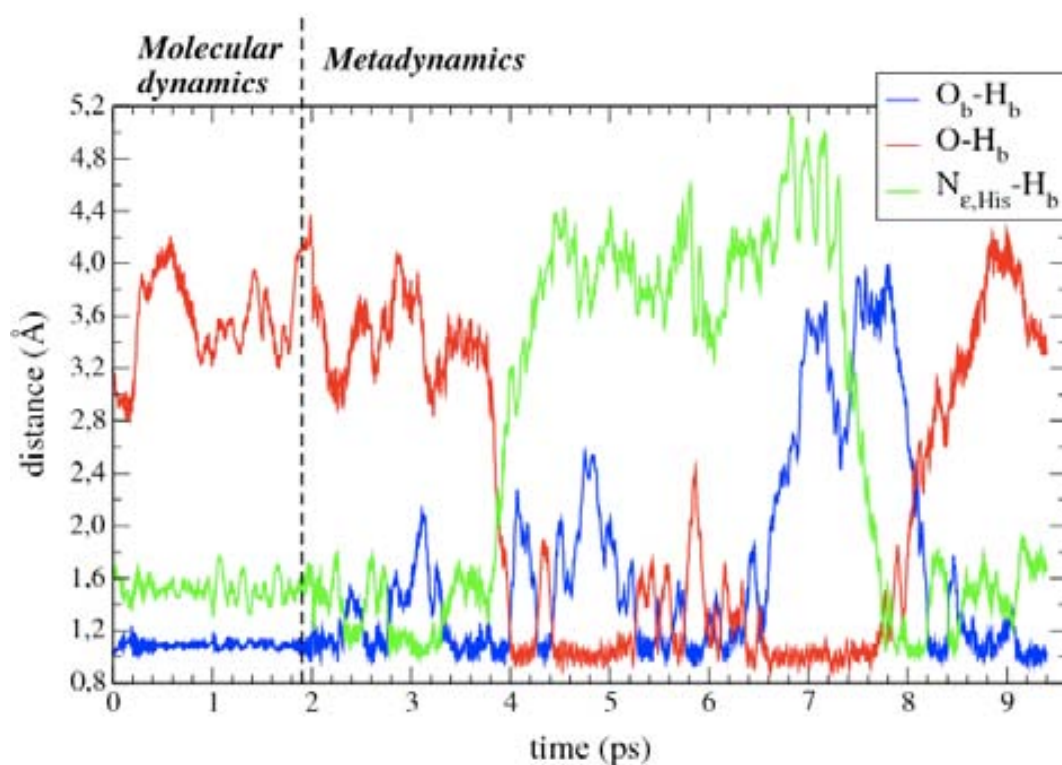


Figure 5. Time evolution of the O_b-H_b , $O-H_b$ and $N_{\epsilon,His}-H_b$ distances (see atom labeling in Chapter VII, Figure 3a) during one reaction cycle for HPC (≈ 9 ps).

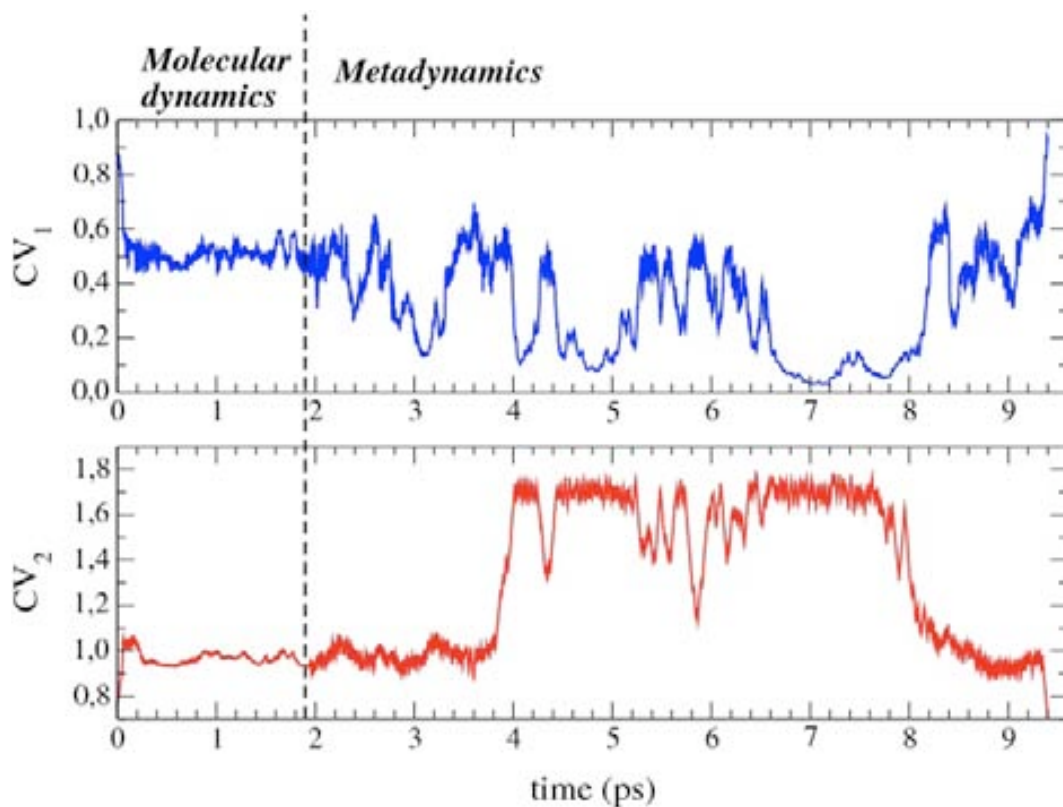


Figure 6. Time evolution of the coordination numbers (used as collective variables in the metadynamics simulation, see section 3) during one reaction cycle for HPC (≈ 9 ps).

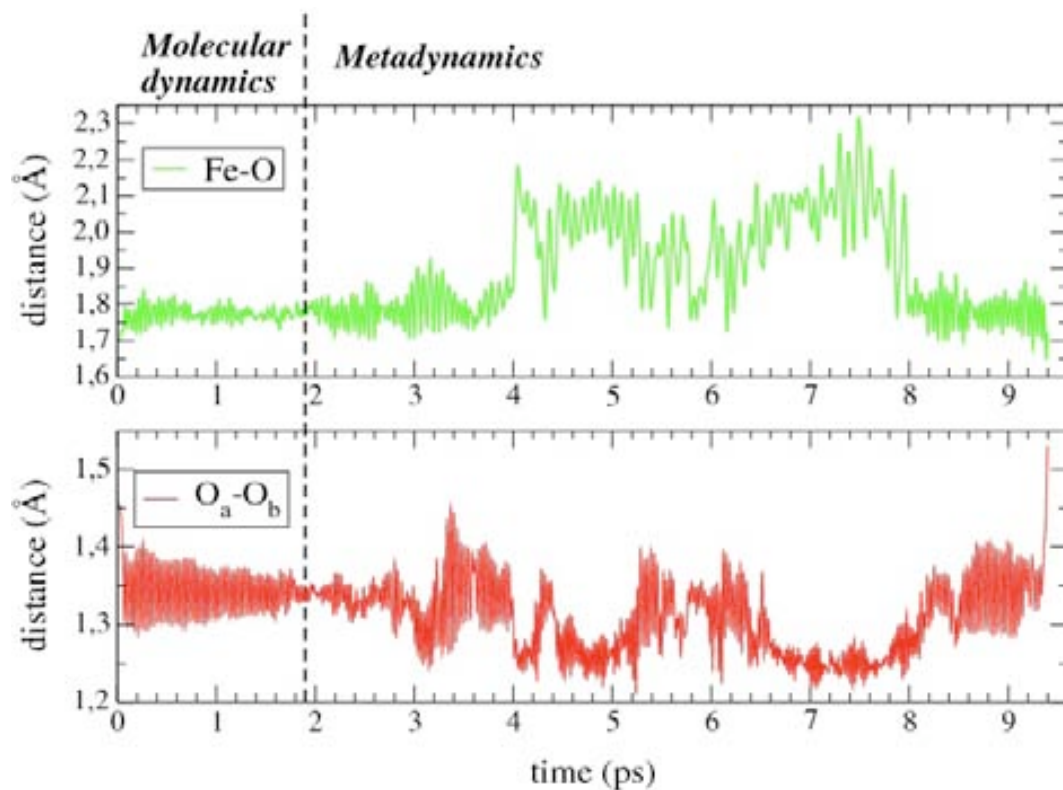


Figure 7. Time evolution of the Fe-O and the O_a-O_b distances (see atom labeling in Chapter VII, Figure 3a) during one reaction cycle for HPC (≈ 9 ps).

• *PVC*

The simulation for PVC (Chapter VII, Figures 8-9) gave qualitatively different results. As in HPC, H_a remains covalently bonded to the oxoferryl ($O-H_a = 1.00 \pm 0.05 \text{ \AA}$, Figure 8) during the metadynamics simulation. At $\approx 2.8 \text{ ps}$, the distal His rotates and H_b transfers to the hydroxoferryl oxygen (note the concerted change in the $O-H_b$ and $N_{e,His}-H_b$ distances in Figure 9), forming the product water ($CV_2 \sim 1.8$, Figure 10). Analysis of the structures (Figure 11) and the spin densities (Chapter VII, Figure 9) shows that the proton transfer of H_b from the distal His to the oxoferryl is accompanied by an electron transfer from the superoxide anion to the Fe^{IV} , yielding an oxygen molecule and an iron(III). Therefore, the system evolves from the Cpd II-like configuration to the products state following the His-mediated mechanism (Chapter VII, Figure 1a).

During the next $\approx 2.5 \text{ ps}$, the distal His maintains the hydrogen bond with the water molecule, such that H_b can go back and forth between the distal His and the ferryl oxygen ($H_b - N_{e,His}$ and H_b-O in Figure 9). After exploring the products state, at $\approx 5.6 \text{ ps}$ the system returns to the reactant state (CV_2 decreases in Figure 10) via the same His-mediated pathway and no alternative pathways are sampled. As can be seen in Figure 9, at $\approx 5.6 \text{ ps}$ the $O-H_b$ distance increases and the $N_{e,His}-H_b$ distance shortens to a covalent bond, indicating that H_b has been transferred back from the ferryl oxygen to the distal His and thus the initial Cpd II-like configuration has been recovered. However, the $O-H_b$ and O_b-H_b distances in the last $\approx 1 \text{ ps}$ of the metadynamics simulation are longer than at the beginning (see Figures 9 and 10). This is due to the escape of the oxygen molecule from the pocket. The absence of the direct mechanism for PVC is probably due to the disappearance of the minimum involving the peroxy radical, as discussed in Chapter VII, section 2.2.

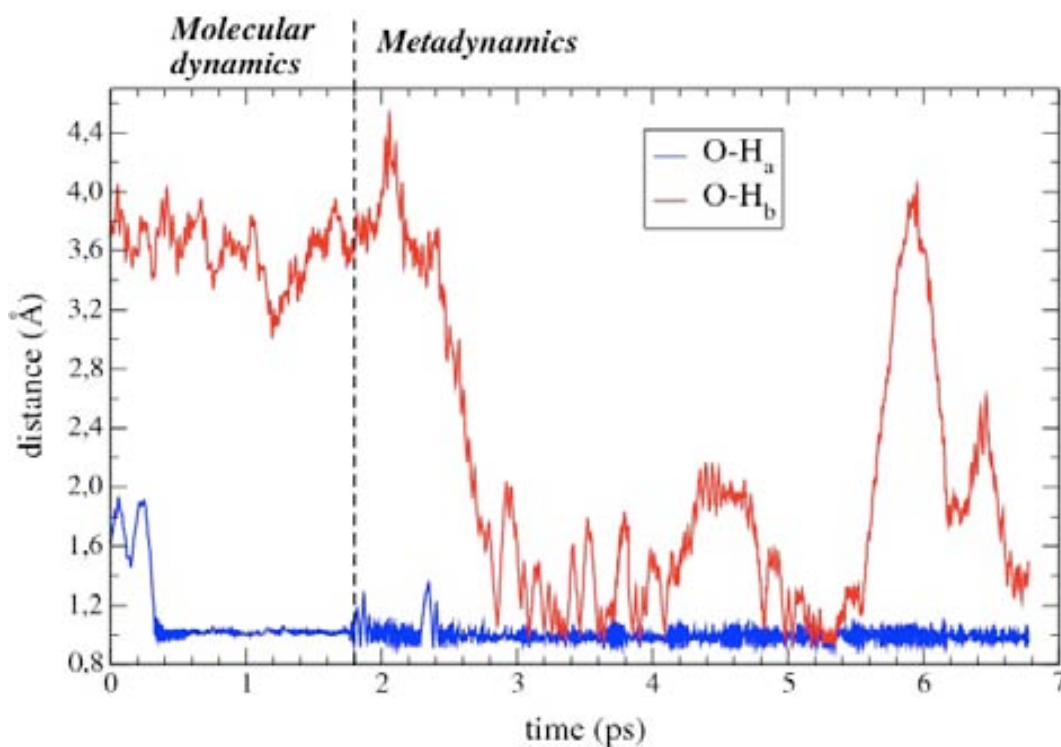


Figure 8. Time evolution of the O-H_a and O-H_b distances (see atom labeling in Chapter VII, Figure 3b) during one reaction cycle for PVC (≈ 7 ps). The results of the initial AIMD simulation (the first ≈ 1.8 ps), leading to the Cpd II-like : superoxide anion, HisH⁺ configuration, have been added to the metadynamics simulation (last ≈ 5 ps) in order to cover the entire reaction mechanism.

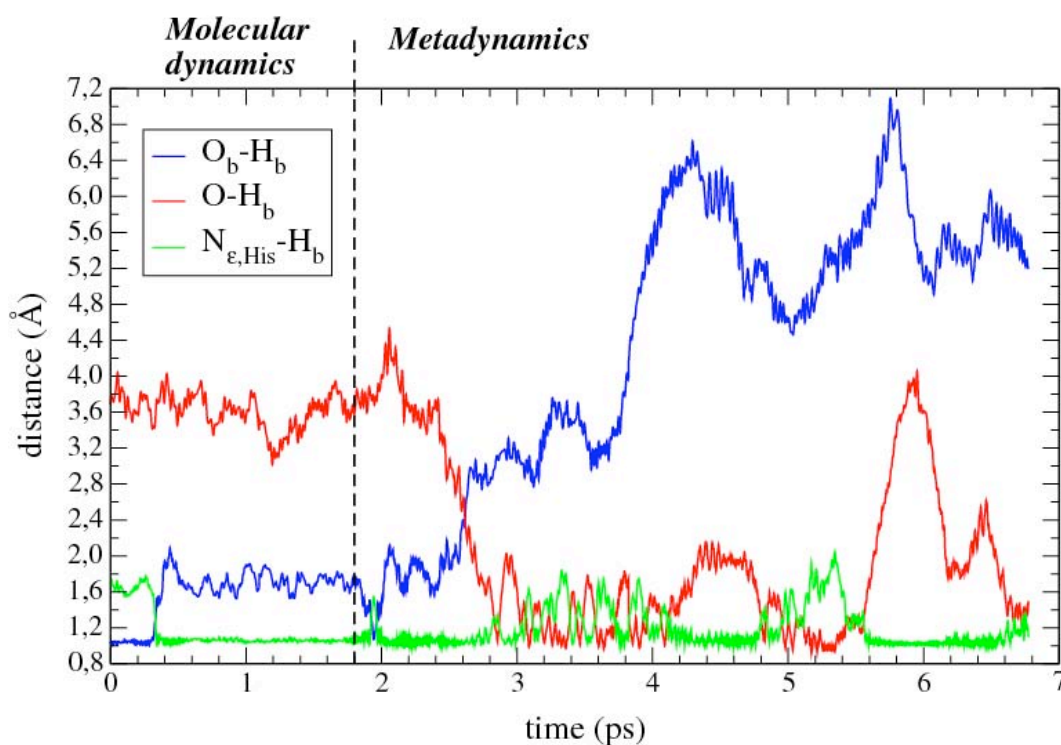


Figure 9. Time evolution of the O_b-H_b, O-H_b and N_{ε,His}-H_b distances (see atom labeling in Chapter VII, Figure 3b) during one reaction cycle for PVC (≈ 7 ps).

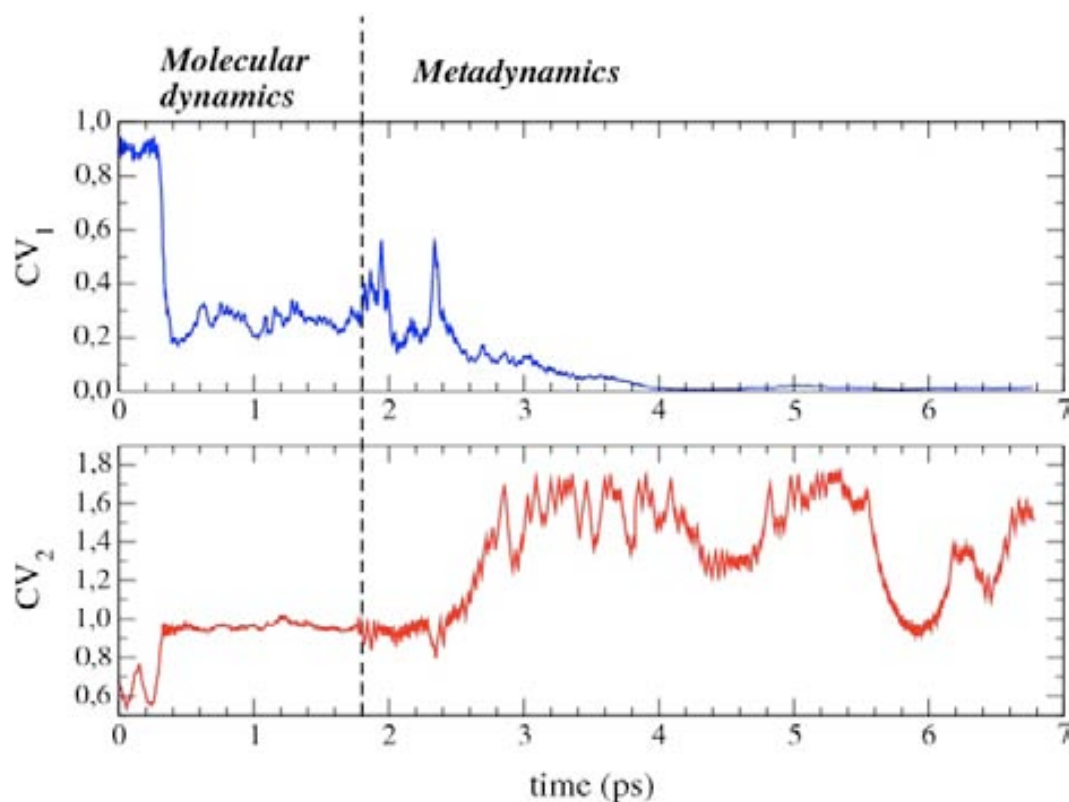


Figure 10. Time evolution of the coordination numbers (used as collective variables in the metadynamics simulation, see section 3) during one reaction cycle for PVC (≈ 7 ps).

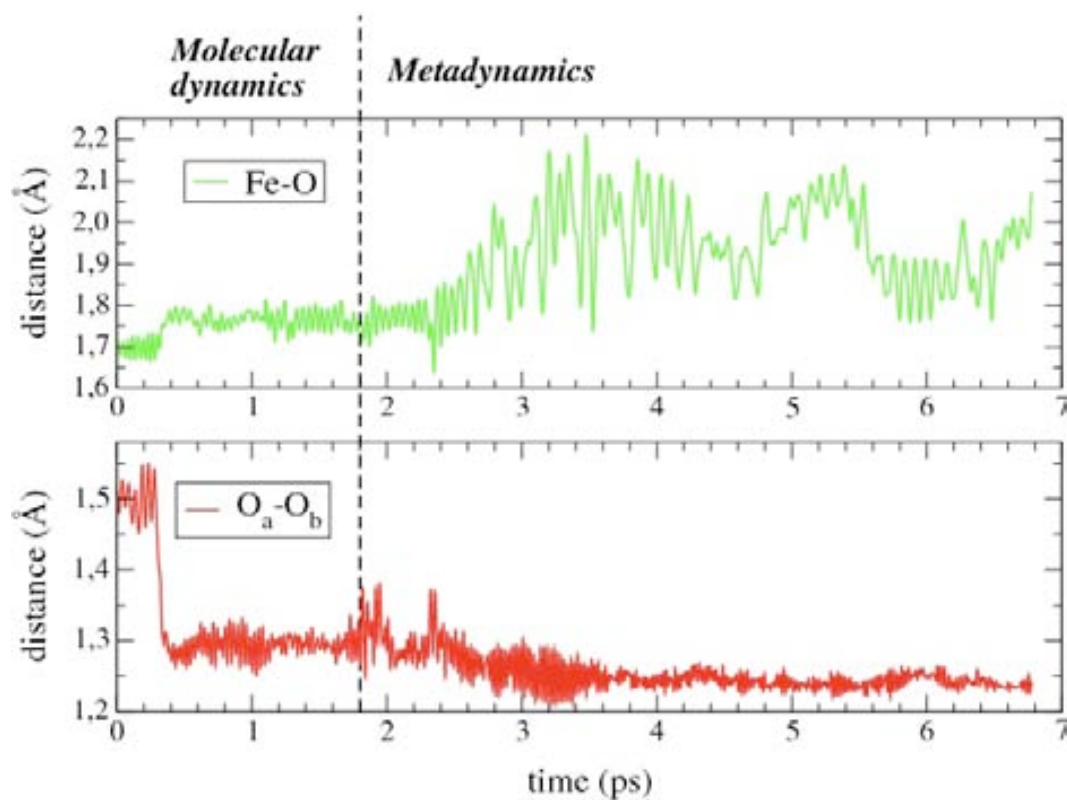


Figure 11. Time evolution of the Fe-O and the O_a-O_b distances (see atom labeling in Chapter VII, Figure 3b) during one reaction cycle for PVC (≈ 7 ps).

5. SPIN STATE ANALYSIS

5.1. Distribution of unpaired electrons

Table 1. Number of unpaired electrons^a of relevant fragments in each spin state along the reaction pathways found for HPC (**A**^{HPC} and **B**^{HPC}). Spin-down electrons are indicated in italics. M= multiplicity = $(2 S_{tot} + 1)$, **I** = Cpd I : H₂O₂ complex, **II** = Cpd II-like configuration and **P** = products.

M	Fe=O				O _a -O _b				Porph ^b				Tyr ^c			
	2	4	6	8	2	4	6	8	2	4	6	8	2	4	6	8
I	1.70	2.15	3.66	<i>−^d</i>	<i>0.05</i>	0.23	0.02	<i>−^d</i>	<i>0.48</i>	0.52	1.23	<i>−^d</i>	<i>0.14</i>	0.06	0.05	<i>−^d</i>
II	1.86	1.87	3.47	4.39	<i>0.98</i>	0.99	1.00	0.99	0.08	0.10	0.57	0.90	0.02	0.02	<i>0.06</i>	0.68
A1	1.84	1.83	3.35	3.94	<i>0.95</i>	1.05	1.02	1.22	0.04	0.03	0.55	1.27	0.07	0.07	0.05	0.20
A2	1.84	1.65	3.22	3.91	<i>1.31</i>	1.45	1.45	1.64	0.05	0.01	0.50	0.86	0.07	0.07	0.01	0.11
A3	1.86	1.56	2.79	3.90	<i>1.42</i>	1.54	1.71	1.74	0.08	0.02	0.42	0.84	0.07	0.06	0.03	0.11
A4	<i>0.89</i>	1.52	3.07	3.96	1.71	1.65	1.65	1.84	0.09	0.01	0.40	0.66	0.01	0.10	0.01	0.18
B1	1.84	1.83	3.33	4.25	<i>0.98</i>	0.98	0.98	0.99	0.05	0.08	0.62	1.48	0.09	0.09	0.03	0.21
B2	1.72	1.72	3.30	4.24	<i>1.00</i>	1.00	1.00	1.03	0.22	0.22	0.68	1.38	0.02	0.03	0.01	0.29
B3	1.80	1.79	3.34	4.26	<i>0.98</i>	1.01	1.01	1.08	0.13	0.12	0.63	1.36	0.04	0.04	0.02	0.25
B4	1.83	1.66	3.36	4.20	<i>1.08</i>	1.07	0.90	1.29	0.19	0.22	0.76	1.21	0.03	0.01	0.05	0.25
P	<i>0.96</i>	1.12	2.60	4.09	1.88	1.77	1.96	1.95	0.08	0.02	0.19	0.70	<i>0.02</i>	0.06	0.21	0.22

^a The spin density was integrated using Bader's Atoms-In-Molecules theory (Bader, 1990). The values correspond to a single-point calculation on a selected snapshot of the metadynamics simulation (see Chapter VII, Figures 5-7), except for values in parentheses that refer to optimized structures (Cpd I : H₂O₂ complex, Cpd II-like configuration and products).

^b Previous studies have shown that charge transfer between the high-lying porphyrin orbitals and the iron orbitals may occur (Derat, 2006a; Shaik, 2004)

^c Similarly, the π system of the axial tyrosinate ligand can mix with the a_{2u} porphyrin orbital (Green, 2001; de Visser, 2006).

^d The Cpd I : H₂O₂ complex in the octuplet state evolved spontaneously to the Cpd II-like configuration during geometry optimization.

- Quartet and doublet surfaces

The electronic structure in both quartet and doublet surfaces is the same, except for the ferro- (quartet) or antiferromagnetic (doublet) coupling (Figure 12). The Cpd I : H₂O₂ complex already has some unpaired spin density on the O_a-O_b moiety and less than one unpaired electron over the porphyrin cation radical (Table 1), indicating certain Cpd II-like character. In the Cpd II : •OOH complex the spin density on the porphyrin disappears and there is one unpaired electron on

the O_a-O_b moiety, consistent with the transfer of a hydrogen atom. The A1–A4 intermediates also have ≈ 2 unpaired electrons on the Fe–OH unit and ≈ 1 on the O_a-O_b moiety (Table 1), indicating that a proton has been transferred to the distal His. Nevertheless, along pathway A the number of unpaired electrons on the the Fe–OH unit progressively decreases, concomitant with an increase on the O_a-O_b moiety (Table 1). Therefore, although the electronic configuration of the A1–A4 intermediates can be mainly described as {Porph-Fe^{IV}-OH, O₂⁻} (i.e. *ferryl* electromer), there is also some contribution of the {Porph-Fe^{III}-OH, O₂} configuration (i.e. *ferric* electromer), suggesting a multiconfigurational character (Figure 13). This resembles the multiconfigurational character found in correlated ab initio calculations for the hydroxo P450 intermediate, either {Porph-Fe^{IV}-OH, R^{*}} or {Porph⁺-Fe^{III}-OH, R^{*}}, where R is the substrate (Altun, 2008). Since the electronic configuration of the ferric electromer resembles that of the products, its contribution increases from A1 to A4, as indicated by the change in the number of unpaired electrons on the Fe–OH unit and the O_a-O_b moiety (Table 1) and the decrease in the O_a-O_b distance (Chapter VII, Table 2). By contrast, in pathway **B**, the change on the number of unpaired electrons occur in the last step, from B4 to the products, consistent with a hydrogen atom transfer. In the products, there is one unpaired electron on the iron and two on the oxygen molecule, i.e. a low spin Fe^{III} and a triplet O₂ are formed.

	Cpd I : H₂O₂	Cpd II-like	A1	Products
doublet	His HOOH O ↑↑ —Fe ^{IV} ₊₊ ↓	His ↓·OOH OH ↑↑ —Fe ^{IV} —	HisH ⁺ ↓O ₂ ⁻ OH ↑↑ —Fe ^{IV} —	His O ₂ ↑↑ HOH ↓ —Fe ^{III} —
quartet	His HOOH O ↑↑ —Fe ^{IV} ₊₊ ↑	His ↑·OOH OH ↑↑ —Fe ^{IV} —	HisH ⁺ ↑O ₂ ⁻ OH ↑↑ —Fe ^{IV} —	His O ₂ ↑↑ HOH ↑ —Fe ^{III} —

Figure 12. Interpretation of the spin densities given in Table 1 for the doublet and the quartet surfaces. The electronic structures of the A2-A4 configurations are the same as for A1 (see Chapter VII, Figure 6), and thus they are not shown. Likewise, the electronic structures of the B1-B4 configurations are the same as for the Cpd II-like (see Chapter VII, Figure 7).

	A1 {ferryl}	A1 {ferric}
doublet	$\text{HisH}^+ \quad \downarrow \text{O}_2^-$ OH $\uparrow\uparrow $ $-\text{Fe}^{\text{IV}}-$	$\text{HisH}^+ \quad \downarrow\downarrow \text{O}_2$ OH $\uparrow $ $-\text{Fe}^{\text{III}}-$
quartet	$\text{HisH}^+ \quad \uparrow \text{O}_2^-$ OH $\uparrow\uparrow $ $-\text{Fe}^{\text{IV}}-$	$\text{HisH}^+ \quad \uparrow\uparrow \text{O}_2$ OH $\uparrow $ $-\text{Fe}^{\text{III}}-$

Figure 13. Alternative electronic structures for the A1 intermediate in the doublet and quartet surfaces.

- *Sextet surface*

The sextet surface (Figure 14) is similar to the doublet and quartet (Figure 12), except that the iron ion is locally in a higher spin state, due to the promotion of one of the electron from the doubly occupied δ iron orbital to the virtual σ^* iron orbital (see Appendix C, section 3). The now half-filled δ iron orbital is close in energy to the high-lying orbitals of the porphyrin, allowing charge transfer from the porphyrin to the iron. As a consequence, the porphyrin shows unpaired spin density, as can be seen in Table 1. Hence, the Cpd II-like (and the B1-B4 intermediates) can be described by two possible electromers (Figure 15): a *ferryl* iron with a neutral porphyrin (Porph- $\text{Fe}^{\text{IV}}-\text{OH}$), as for the doublet and quartet states, or a *ferric* iron with a porphyrin cation radical (Porph $^{+\cdot}-\text{Fe}^{\text{III}}-\text{OH}$), as found for HRP Cpd II (Derat, 2006a). Likewise, the A1-A4 intermediates have a multiconfigurational character (Figure 15), with the contribution of the ferryl electromer progressively increasing as the reaction proceeds (Table 1). In the products, the oxygen molecule is in a triplet state, as in the quartet and doublet surfaces, and the iron is locally a quartet (i.e. an intermediate spin Fe^{III}).

	Cpd I : H ₂ O ₂	Cpd II-like	A1	Products
sextet	His HOOH O †††† —Fe ^{IV} — ₊₊ †	His †•OOH OH †††† —Fe ^{IV} —	HisH ⁺ †O ₂ ⁻ OH †††† —Fe ^{IV} —	His O ₂ †† HOH ††† —Fe ^{III} —

Figure 14. Interpretation of the spin densities given in Table 1 for the sextet surface. The electronic structures of the A2-A4 configurations are the same as for A1 (see Chapter VII, Figure 6), and thus they are not shown. Likewise, the electronic structures of the B1-B4 configurations are the same as for the Cpd II-like (see Chapter VII, Figure 7).

	Cpd II-like {ferryl}	Cpd II-like {ferric}
sextet	His †•OOH OH †††† —Fe ^{IV} —	His †•OOH OH †††† —Fe ^{III} — ₊₊ †
	A1 {ferryl}	A1 {ferric}
	HisH ⁺ †O ₂ ⁻ OH †††† —Fe ^{IV} —	HisH ⁺ ††O ₂ OH †††† —Fe ^{III} —

Figure 15. Alternative electronic structures for the Cpd II-like and A1 intermediates in the sextet surface.

- *Octuplet surface*

The octuplet surface is slightly different from the lower spin states. First, the Cpd I : H₂O₂ complex evolved spontaneously to the Cpd II-like configuration during geometry optimization, most likely because a (+2) porphyrin cation radical is not stable. The only possible electromer for the Cpd II-like intermediate (Figure 16) corresponds to a ferric ion plus a porphyrin cation radical (Porph^{+•}-Fe^{III}-OH), instead of the Porph-Fe^{IV}-OH observed for the other spin states. The A1 intermediate has two possible electronic configurations (Figure 17): a *superoxide* configuration {Porph^{+•}-Fe^{III}-OH, O₂⁻}, and an *oxygen* configuration, {Porph-Fe^{III}-OH, O₂}. The superoxide configuration resembles the reactants (as the ferryl species for the other spin states), whereas the oxygen electromer is more similar to the products (as the ferric species for the lower spin states). Then, the weight of {Porph-Fe^{III}-OH, O₂} configuration is expected to increase on going from the A1 to A4 intermediates, as can be seen by the gradual decrease in the number of unpaired electrons on porphyrin (Table 1). Similar to the lower spin states, the products contain a triplet oxygen molecule, and only the local spin state of the ferric differs (i.e. a high spin Fe^{III}). The spin density on the porphyrin does not reach zero in the products, most likely due to charge transfer from the high-lying porphyrin orbitals to the half-filled δ iron orbital (see Appendix C, section 3).

	Cpd I : H ₂ O ₂	Cpd II-like	A1	Products
octuplet	 His HOOH O ↑↑↑↑↑ —Fe^{III}₂₊↑↑ 	His ↑OOH OH ↑↑↑↑↑ —Fe ^{III} _{+•} ↑	HisH ⁺ ↑O ₂ ⁻ OH ↑↑↑↑↑ —Fe ^{III} _{+•} ↑	His O ₂ ↑↑ HOH ↑↑↑↑↑ —Fe ^{III} —

Figure 16. Interpretation of the spin densities given in Table 1 for the octuplet surface. The Cpd I : H₂O₂ complex evolved spontaneously to the Cpd II-like configuration during geometry optimization. The electronic structures of the A2-A4 configurations are the same as for A1 (see Chapter VII, Figure 6), and thus they are not shown. Likewise, the electronic structures of the B1-B4 configurations are the same as for the Cpd II-like (see Chapter VII, Figure 7).

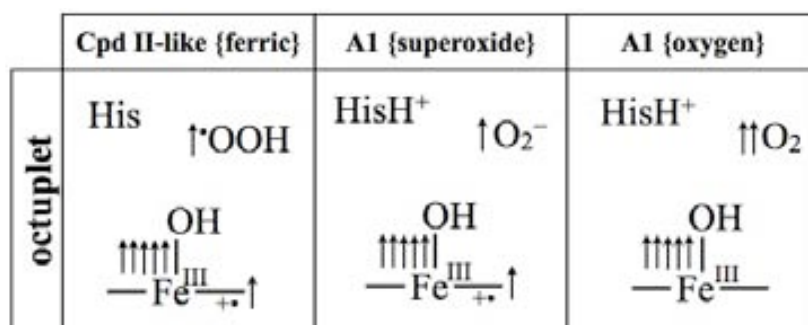


Figure 17. Alternative electronic structures for the A1 intermediate (compared to the Cpd II-like) in the octuplet surface.

5.2. Spin state energies

Table 2. Potential energies relative to the quartet state (in kcal/mol) for selected snapshots from the metadynamics simulation of HPC (see Chapter VII-Figures 5-7)^a. Spin contamination^b in the quartet state is also given.

	doublet	quartet	sextet	octet	spin contamination
Cpd I : H₂O₂	0.63 (5.65)	0	25.10 (15.06)	66.52 (-) ^c	3.8%
Cpd II-like	1.08 (0.63)	0	36.94 (21.96)	60.11 (28.24)	6.5%
A1	0.63	0	26.98	60.86	5.3%
A2	3.14	0	21.34	37.02	11.6%
A3	3.14	0	20.08	40.16	11.1%
A4	4.39	0	25.73	37.65	14.0%
B1	0.63	0	23.85	45.18	6.6%
B2	0.00	0	29.49	47.06	7.8%
B3	0.63	0	26.36	52.71	7.1%
B4	0.63	0	25.10	38.28	7.7%
products	1.44 (7.25)	0	11.42 (-9.56)	8.35 (4.21)	5.8%

^a The values correspond to single-point calculations, except those in parentheses, that refer to energy differences after geometry optimization (Cpd I : H₂O₂ complex, Cpd II-like configuration and products).

^b The relative error in the expectation value of the spin operator, [$\langle \hat{S}^2 \rangle - S(S + 1)$] / [$S(S + 1)$] × 100 (Wang, 1995; Cohen, 2007)

^c The Cpd I : H₂O₂ complex evolved spontaneously to the Cpd II-like configuration, and thus, the energy difference could not be calculated.

• *Quartet and doublet spin states*

As can be seen in Table 2, the quartet state is found to be the ground spin state for all the reaction intermediates, except for the products (see below). The amount of spin contamination, computed according to Wang *et al.* (Wang, 1995), turns out to be small ($< 10\%$ for optimized geometries and $< 15\%$ for single point calculations, Table 2). The doublet state is very close in energy (Table 2), and thus it is reasonable that at room temperature both states may coexist in equilibrium. Since quartet and doublet only differ in the sign of the unpaired spin density (Table 1) it is expected that the mechanism of the catalytic reaction (Chapter VII, Figures 6 and 7) will be the same on both surfaces.

This is also shown in Figure 18 and Table 3. The optimized structures of the Cpd I : H₂O₂ complex, the Cpd II-like configuration and the products in these two spin states are nearly identical (Table 3), as also found for the gas phase models in Chapter VI. This in line with the electronic configuration in both spin states being the same, except for the coupling of the unpaired spins, antiferromagnetic in the quartet and ferromagnetic in the doublet (Figure 18). As a consequence, no significant difference is expected between the doublet and the quartet reaction surfaces, as already reported for a non-heme catalase mimic (Sicking, 2007). Therefore, *the quartet free energy surface is representative of the process investigated.*

Table 3. Main distances^a (quartet / doublet) defining the optimized structures of the Cpd I : H₂O₂ complex, the Cpd II-like configuration and the products^b in the quartet and doublet states.

distance (Å)	Cpd I : H ₂ O ₂	Cpd II-like	products
Fe-O	1.70 / 1.70	1.76 / 1.77	2.07 / 1.08
Fe-O _{Tyr}	2.07 / 2.04	2.02 / 2.01	1.86 / 1.93
O-H _a	1.56 / 1.48	0.99 / 1.00	0.98 / 0.98
O-H _b	3.19 / 3.08	3.68 / 3.67	1.02 / 1.02
O _a -H _a	1.04 / 1.06	1.86 / 1.95	2.84 (2.93 ^c) / 2.78 (3.04 ^c)
O _a -O _b	1.47 / 1.46	1.31 / 1.34	1.25 / 1.24
O _b -H _b	1.05 / 1.05	1.08 / 1.11	3.62 / 3.59
H _b -N _{ε,His}	1.64 / 1.61	1.51 / 1.48	1.70 / 1.84
O _b -H _{δ,Asn}	2.26 / 2.19	2.47 / 2.50	3.16 / 3.41

^a For atom names see Figures 2 and 3.

^b The computational details of the geometry optimizations are described in Appendix D, section 1. ^c O_a-H_b distance.

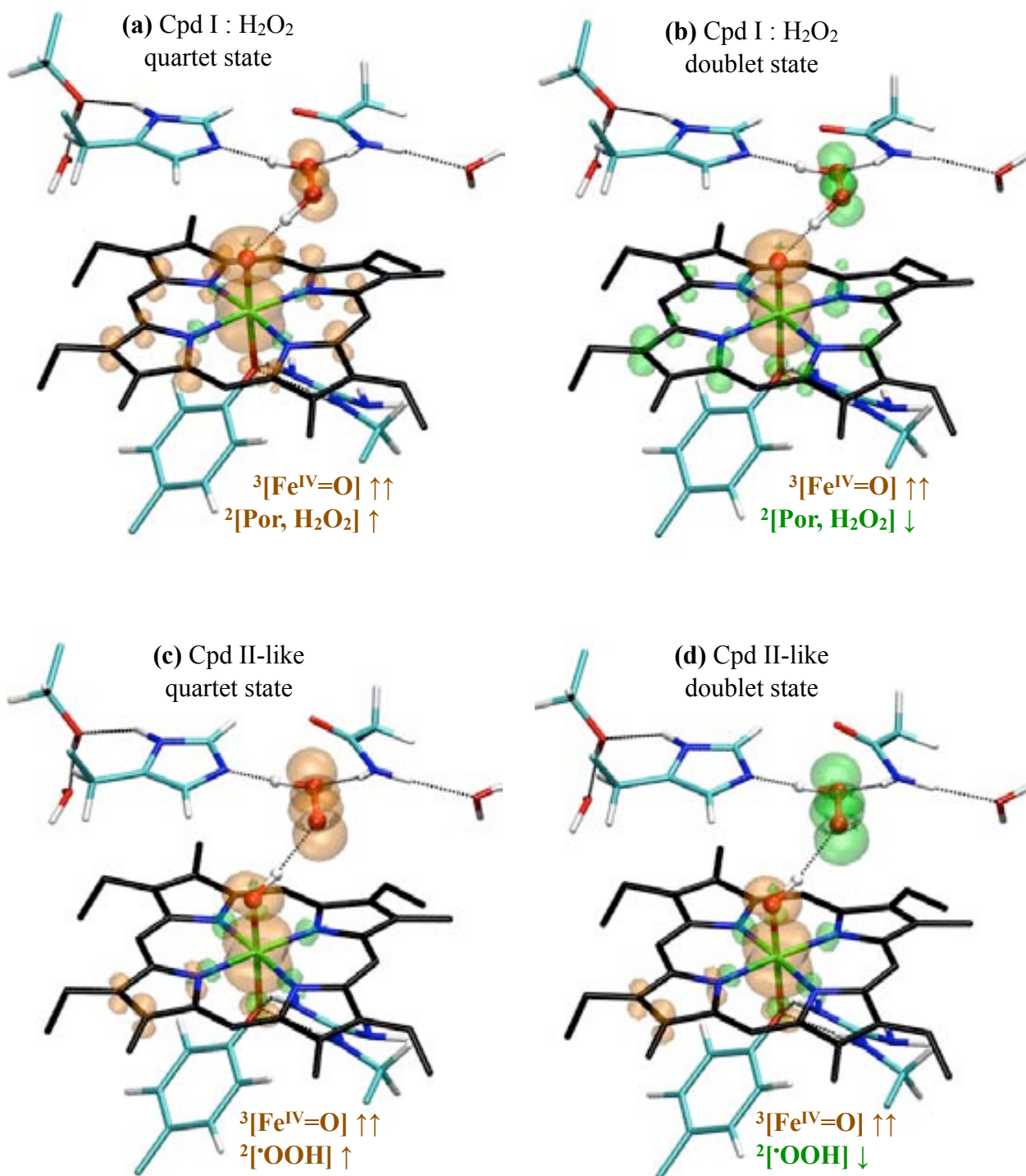


Figure 18. Optimized structures of the Cpd I : H₂O₂ complex (a, b) and the Cpd II-like configuration (c, d) in the quartet and doublet states, respectively. Only the QM atoms are shown. Spin isodensity surfaces at 0.004 e Å⁻³ are plotted in orange (spin-up unpaired electrons) and green (spin-down).

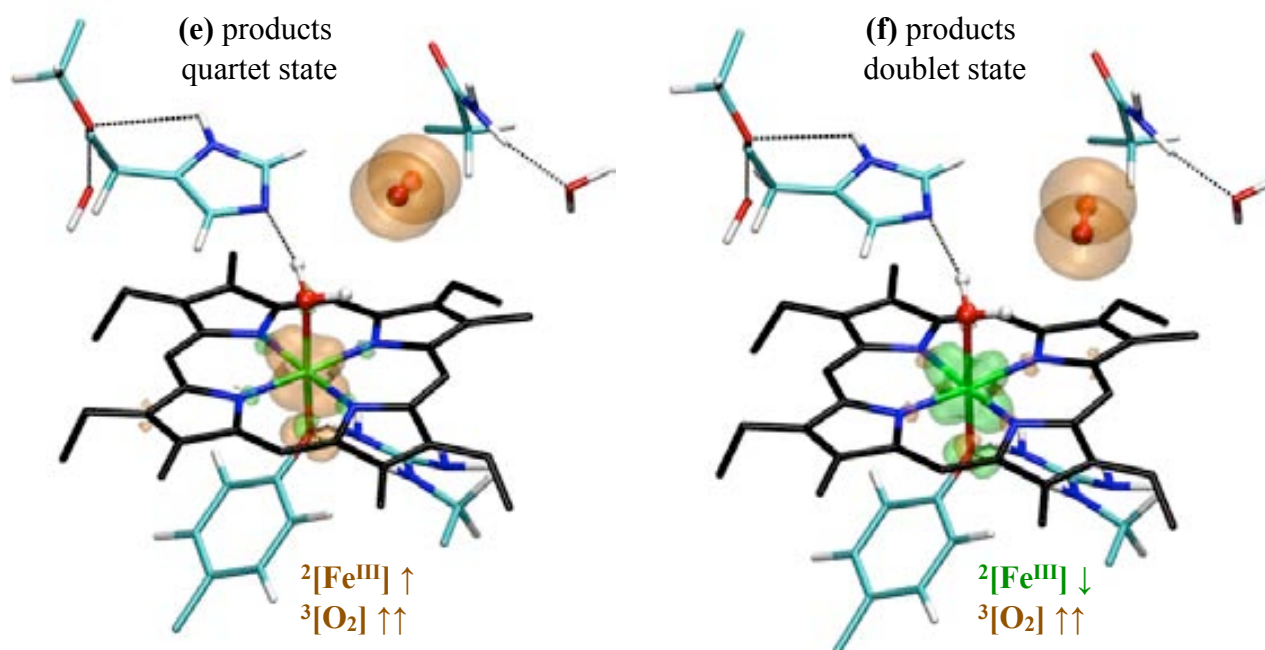


Figure 18 (cont.). Optimized structures of the products (**e, f**) in the quartet and doublet states. Only the QM atoms are shown. Spin isodensity surfaces at $0.004 \text{ e } \text{\AA}^{-3}$ are plotted in orange (spin-up unpaired electrons) and green (spin-down).

- *Sextet spin state*

Although it is higher in energy than the quartet along the reaction (Table 2), *the sextet state becomes the ground state of the products upon geometry optimization.* Certainly, geometry relaxation would also bring configurations A1-A4 and B1-B4 closer to the sextet surface. However, we expect such stabilization to be smaller in those configurations than in the products for the following reason. The products correspond to a configuration in which Fe(IV) has been reduced to Fe(III) and the axial hydroxyl has been protonated (to form H_2O). These two conditions, which should result in either a $S_{\text{heme}} = 3/2$ 6-coordinated Fe or a $S_{\text{heme}} = 5/2$ 5-coordinated Fe (as experimentally observed for the resting enzyme), are not given simultaneously in any of the above configurations (A1-A4 and B1-B4).

Along pathway **A**, although the electron transfer starts early in the path (from A1 to A2), the proton passes to the ferryl oxygen (Fe–OH) only in the last step, from A4 to products. Thus, the A1-A4 intermediates (section 5.1.) are either Por-Fe^{IV}–OH with a triplet ground state ($S_{\text{heme}} = 1$) (Filatov, 1999; Rydberg, 2004; Derat, 2006b), or Por-Fe^{III}–OH with a doublet ground state ($S_{\text{heme}} = 1/2$) (Yshida, 1970; Rydberg, 2004). By contrast, a sextet global state ($S_{\text{heme}} = 5/2$) requires either a

quintuplet Por-Fe^{IV}-OH ($S_{heme} = 2$) with a doublet superoxide ($S_{OO} = 1/2$), or a quartet Por-Fe^{III}-OH ($S_{heme} = 3/2$) with a triplet oxygen ($S_{OO} = 1$). Therefore, even upon geometry relaxation of A1-A4, the sextet state is expected to be still higher in energy than the quartet.

Similarly, along pathway **B**, the hydrogen atom is transferred in the last step, from B4 to the products. Thus, the B1-B4 intermediates (section 5.1.) contain Por-Fe^{IV}-OH, whose ground state is a triplet ($S_{heme} = 1$) (Filatov, 1999; Rydberg, 2004; Derat, 2006b). By contrast, a sextet state requires a quintuplet Por-Fe^{IV}-OH ($S_{heme} = 2$) with a doublet peroxy radical ($S_{OO} = 1/2$). Therefore, even upon geometry relaxation of B1-B4, the sextet state is expected to be still higher in energy than the quartet.

In summary, because the sextet state is a high-energy configuration for A1-A4 and B1-B4, we infer that *spin crossing from quartet to sextet would affect only the final step of the reaction* (A4 → products or B4 → products).

- *Octet spin state*

The octet state lies rather high in energy along the two paths (Table 2), and it is still higher than the quartet after geometry relaxation (Cpd II-like and products configurations). Thus it is unlikely that it participates in the reaction.

5.3. Structure and spin state of the products (Enz + H₂O + O₂)

The optimized structures of the products in each spin state are shown in Figure 19 and Table 4 lists the main distances. For all spin states, the O_a-O_b distance along with the spin density distribution are consistent with the formation of an oxygen molecule in a triplet state ($S_{dioxygen} = 1$). The main difference among spin states is the Fe-O distance (Table 4), which correlates with the local spin state of Fe(III). Quartet and doublet states ($S_{heme} = 1/2$) show a shorter iron-water distance (2.08-2.07 Å, respectively) compared to sextet (Fe-O = 3.29 Å, $S_{heme} = 3/2$) and octet (Fe-O = 2.55 Å, $S_{heme} = 5/2$). Regardless, for all spin states the water molecule is hydrogen bonded to the distal His, but not to the distal Asn (Figure 19). On the contrary, in the X-Ray structure of the native enzyme (Loewen, 2004) the pocket water is hydrogen bonded to both distal residues (Figure 20).

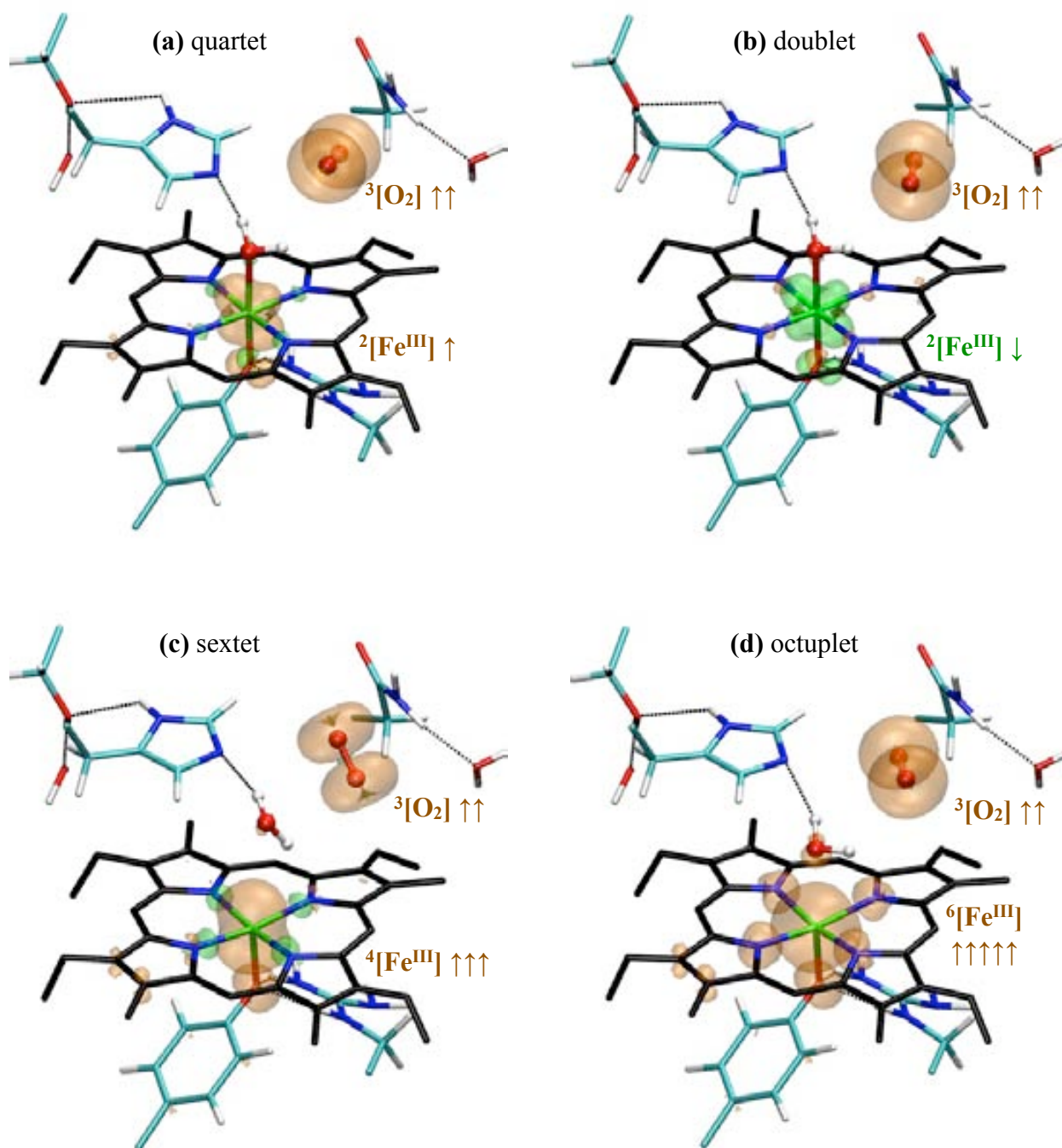


Figure 19. Optimized structures of the products (native enzyme + H_2O + O_2) in all the possible spin states. Only the QM atoms are displayed. Spin isodensity surfaces at $0.004 \text{ e } \text{\AA}^{-3}$ are also shown in orange (spin-up unpaired electrons) and green (spin-down).

Table 4. Main distances^a defining the optimized structure of the products (native enzyme + H₂O + O₂) in the different spin states, together with the X-Ray structure of the resting state of HPC.

distance (Å)	quartet	doublet	sextet	octet	X-Ray ^b
Fe-O _{Wat}	2.07	2.08	3.29	2.55	4.22-4.10
Fe-N _{Por}	1.99-2.01	1.99-2.01	1.98-2.00	2.03-2.08	2.04-2.12 / 2.03-2.10
Fe-O _{Tyr}	1.86	1.93	2.04	2.02	1.85-1.79
Fe out-of-plane	0.06	0.06	0.18	0.20	0.17-0.21
(O-O) _{oxygen}	1.25	1.24	1.23	1.23	–
O _{wat} -H _{wat}	0.98-1.02	0.98-1.02	0.99-1.01	0.99-1.01	–
N _{ε,His} -O _{wat}	2.81	2.69	3.29	2.97	2.65-2.67
N _{ε,His} -H _{wat}	1.70 ^c	1.84 ^c	1.86 ^c	2.04 ^c	–
O _{wat} -N _{δ,Asn}	7.48	7.44	6.67	7.30	3.39-3.51
O _{wat} -H _{δ,Asn}	7.44	7.33	6.63	7.21	–
N _{Por} -H _{wat}	2.65-2.67	2.71-2.71	2.32-3.57	2.80-2.97	–
O _{oxygen} -H _{wat}	2.84 ^c	2.78 ^c	3.01 ^c	2.97 ^c	–
O _{oxygen} -H _{δ,Asn}	3.41 ^c	3.16 ^c	2.85 ^c	3.09 ^c	–

^a For atom names see Figure 20. ^b PDB entry 1QWL. Values corresponding to the two independent subunits are given.

^c For simplicity, only the shortest hydrogen bond between the distal His and the pocket water (N_{ε,His}-H_{wat}), between the oxygen molecule and the pocket water (O_{oxygen}-H_{wat}), or between the oxygen molecule and the distal Asn (O_{oxygen}-H_{δ,Asn}) is indicated.

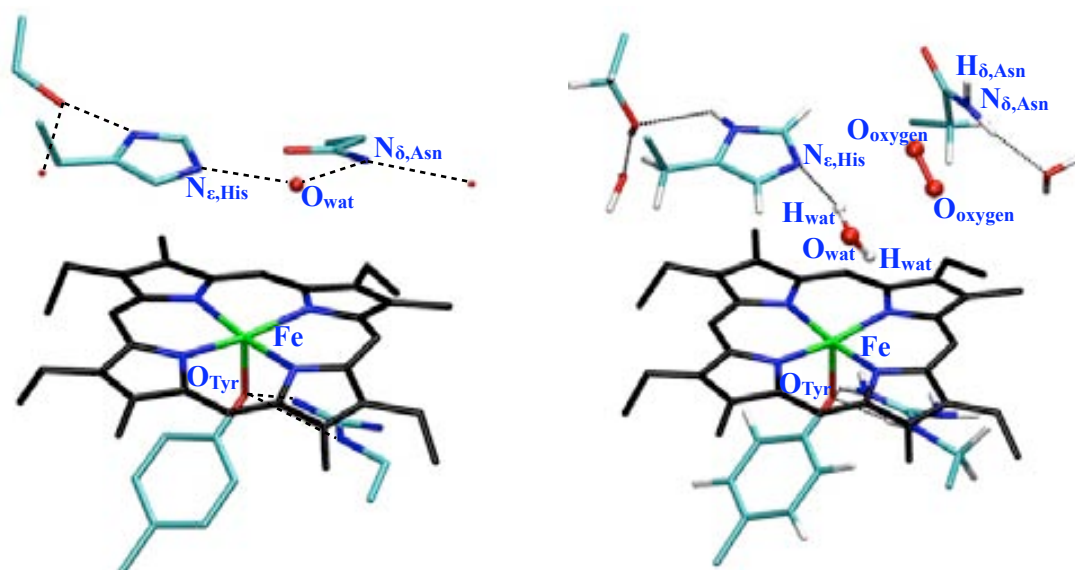


Figure 20. X-Ray structure of the resting state of HPC (*left*, PDB entry: 1QWL) (Loewen, 2004), compared to the optimized structure of the products in the sextet state (*right*).

Even though the spin state of the products is not known experimentally, it would be expected that the local spin at the heme is the same as in the resting enzyme, i.e., a high spin iron ($S_{heme} = 5/2$) (Sharma, 1989). However, our calculations predict that the ground state of the products is globally a sextet, with an intermediate spin iron ($S_{heme} = 3/2$). Two possible explanations may account for this discrepancy. First, the prediction of an intermediate spin electronic configuration (i.e. $S_{heme} = 3/2$) as the ground state of Fe(III) is a well known deficiency of GGA functionals (Schöneboom & Thiel, 2004; Ghosh, 2006). Alternatively, it could be that the spin state changes when O₂ is still in the heme pocket. As explained above, the optimized structure of the products in the sextet state shows an iron-water distance of 3.29 Å, whereas in the X-Ray structure of the native enzyme (Loewen, 2004) this distance is longer (4.10-4.22 Å). Most likely, the exit of the oxygen molecule from the active site may increase the available space in the pocket and allow the water molecule to become hydrogen bonded to the distal His and Asn, as in the crystal structure. This further increase in the iron-water distance would result in a smaller splitting of the d-orbitals of the iron and thus a larger stabilization of the high-spin iron.

6. DEPENDENCE OF THE BARRIERS FOR HYDROGEN ATOM TRANSFER ON THE DONOR-ACCEPTOR DISTANCE

To further investigate the effect of the distal His in Cpd I reduction, we performed gas-phase calculations² on a simplified model without distal residues, i.e. consisting of the bare porphyrin (with no substituents), the proximal tyrosinate (modeled as phenolate) together with the hydrogen bonded arginine (modeled as methyl guanidinium), and the hydrogen peroxide molecule. For fixed oxoferryl-peroxide distances ($d(\text{O}-\text{O}_a)$ or $d(\text{O}-\text{O}_b) = 2.5, 3.0, 3.5 \text{ \AA}$), the energetics for the transfer of H_a (or H_b) was calculated, optimizing all other degrees of freedom. Details of the DFT calculations are as for the QM/MM simulations described in section 1.

• *Transfer of H_a*

The transfer of H_a from hydrogen peroxide to the ferryl oxygen in the $\text{Por}^{\bullet+}\text{-Fe}^{\text{IV}}=\text{O} : \text{H}_2\text{O}_2$ complex was investigated at various fixed oxygen-oxygen distances. It was found that H_a is formally transferred as a hydrogen atom (H[•]), i.e. the species formed are Cpd II ($\text{Por-Fe}^{\text{IV}}\text{-OH}_a$) and a peroxy radical (H_bOO[•]). Figure 21a shows the obtained potential energy profiles. The process is exothermic and the barrier for the transfer shows a marked dependence on the $\text{O}_a \cdots \text{O}(\text{Fe})$ distance,

² These calculations were done by Dr. Pietro Vidossich in our group.

being smaller for shorter interoxygen distances. For very short $O_a \cdots O$ distances (2.5 Å), the process is almost barrierless.

- *Transfer of H_b*

The transfer of H_b from the peroxy radical to the hydroxoferryl unit in the $\text{Por-Fe}^{\text{IV}}\text{-OH} : \cdot\text{OOH}$ complex was also investigated at various fixed oxygen-oxygen distances. Like H_a , H_b formally transfers as a hydrogen atom, generating triplet dioxygen and a low spin iron(III) coordinated to a water molecule. The energy profiles are shown in Figure 21b. Again, the barrier decreases for short interoxygen distances, the transfer being barrierless for very short $O_b \cdots O(\text{Fe})$ distances.

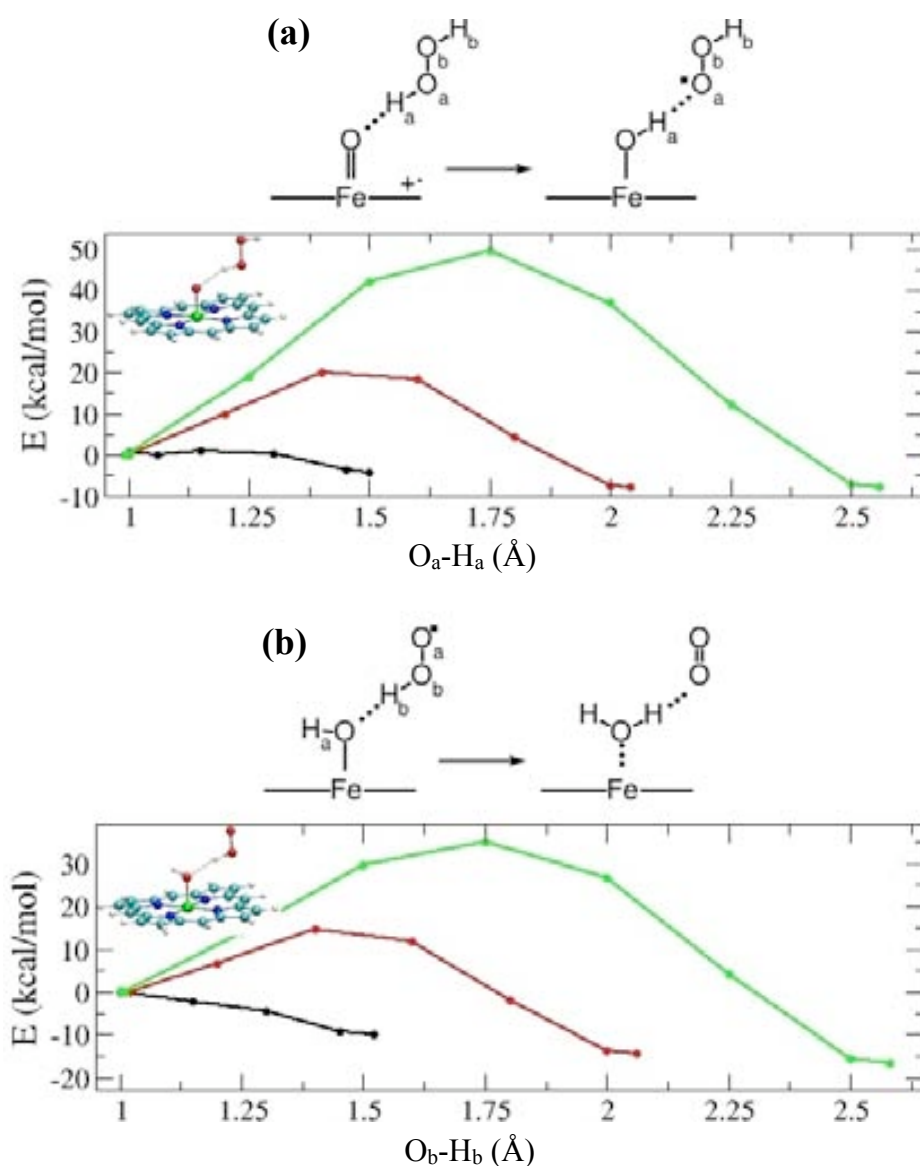


Figure 21. Energy profile for (a) the transfer of H_a and (b) the transfer of H_b in a gas-phase catalase model, for various $O_{\text{Fe}} \cdots O_{a/b}$ distances: $d(O\text{-}O_a)$ or $d(O\text{-}O_b) = 2.5$ (black), 3.0 (red), 3.5 Å (green).

7. INFLUENCE OF THE EXCHANGE-CORRELATION FUNCTIONAL

• Reaction energy barriers

GGA functionals, like the Becke-Perdew one used here, usually underestimate energy barriers of hydrogen abstraction reactions (Pu, 2005; Perdew, 2008; Aguilera-Iparagirre, 2008). Therefore, we also computed the energy barrier for the transfer of H_a with a hybrid functional (B3LYP)³, which is known to be less affected by the self-interaction error than the Becke-Perdew functional (Lundberg & Siegbahn, 2005). The energy barriers computed with the B3LYP functional (Table 5) reproduce the dependency on the O_a⋯O(Fe) distance (i.e. the shorter the distance, the lower the barrier), although the hybrid functional predicts a 4 kcal/mol barrier at short (2.5 Å) interoxygen distance, compared to the barrierless process found for BP86.

Table 5. Energy barrier (in kcal/mol) for the transfer of one hydrogen atom (H_a) from H₂O₂ to the oxoferryl oxygen, for various O_{Fe}⋯O_a distances (see Figure 21a).

method	O _{Fe} ⋯O _a = 3 Å	O _{Fe} ⋯O _a = 2.5 Å
BP86 / PW ^a	21.0	1.2
B3LYP / BasisSet1 ^b	27.0	3.5
B3LYP / BasisSet2 // B3LYP / BasisSet1 ^c	19.5	4.4

^a CPMD calculation using a plane wave basis set (PW) with a 70 Ry cutoff.

^b BasisSet1: LanLDZ in all atoms.

^c BasisSet2: TZP (aug-cc-pVTZ) on Fe and all heteroatoms bonded to Fe, and DZP (cc-pVDZ) in all other atoms.

To assess the error in relative energies of the local minima of the FES of HPC (Chapter VI-Figure 5) due to the functional employed, we also performed single-point calculations with the B3LYP (Becke, 1988; Lee, 1988; Becke, 1993) and PBE (Perdew, 1996) exchange correlation functionals, using the same PW basis set (Todorova, 2006). The energy difference between two stationary points (Cpd II-like^{HPC} and B1^{HPC}) changed by +0.21 / -2.6 kcal/mol with PBE / B3LYP. Thus we estimate an upper bound of 2.6 kcal/mol for the dependence of the relative energies on the functional employed.

• Spin density distributions

Figure 22 shows the spin density distribution for some of the stationary points found for HPC (the Cpd I : H₂O₂ complex, the Cpd II-like species, the B1 intermediate and the products). They are

³ These calculations were done by Dr. Pietro Vidossich in our group.

identical to the corresponding BP86 spin density distributions (see Chapter VII-Figures 2a, 3a and 7). Although this result does not exclude completely that the SIE may be present in our calculation, the electronic configuration of the Cpd II-like and the B1 intermediates at the heme is the same as that of Cpd II or Cpd I*, which have been experimentally detected for catalase (see Chapter I, section 3.3.). Therefore, it is not surprising that Cpd II is formed via hydrogen atom transfer from H₂O₂ to Cpd I.

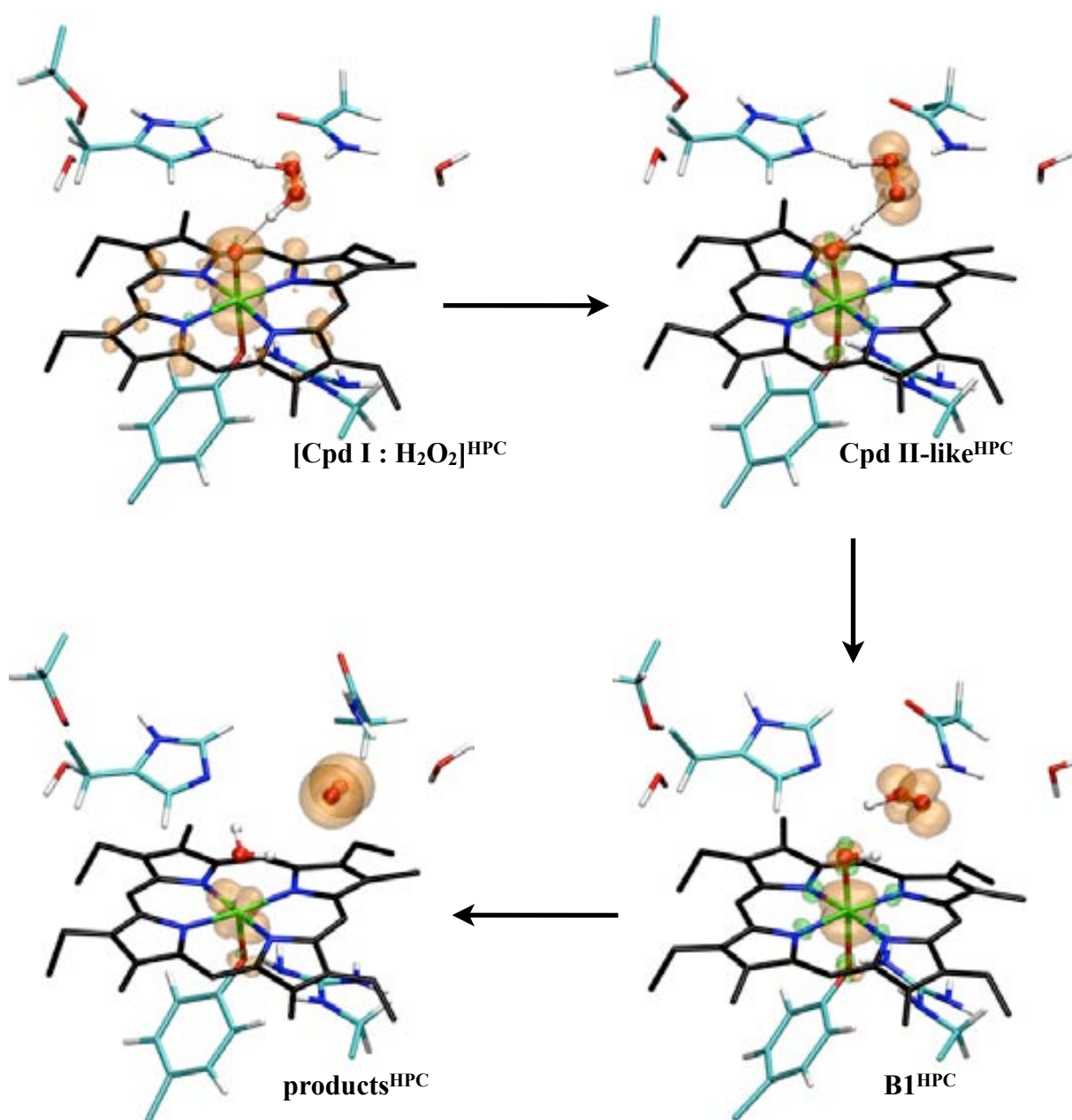


Figure 22. B3LYP spin density distributions for the Cpd I : H₂O₂ complex, the Cpd II-like species, the B1 intermediate and the products of HPC. Only the QM atoms are shown. Spin isodensity surfaces are plotted at 0.007 e Å⁻³.

BIBLIOGRAPHY

BIBLIOGRAPHY

- Abashkin, Y. G. & Burt, S. K. (2005) *Inorg. Chem.* 44: 1425-1432.
- Abrahams, S.C.; Collin, R.L. & Lipscomb, W.N. (1951) *Acta Cryst. D.* 4: 15-20.
- Adam, W.; Kazakov, D. V. & Kazakov, V. P. (2005) *Chem. Rev.* 105: 3371-3387.
- Aguilera-Iparagirre, J.; Curran, H. J.; Klopper, W. & Simmie, J. M. (2008) *J. Phys. Chem. A* 112: 7047-7054.
- Alfonso-Prieto, M.; Borovik, A.; Carpena, X.; Murshudov, G.; Melik-Adamyanyan, W.; Fita, I.; Rovira, C. & Loewen, P. C. (2007) *J. Am. Chem. Soc.* 129: 4193-4205.
- Alfonso-Prieto, M., Vidossich, P., Rodríguez-Forteza, A., Carpena, X., Fita, I., Loewen, P. C. & Rovira, C. (2008) *J. Phys. Chem. A* 112: 12842-12848.
- Alia; Mohanty, P. & Matysik, J. *Amino Acids* (2001) 21: 195-200.
- Altun, A., Shaik, S. & Thiel, W. (2007) *J. Am. Chem. Soc.* 129: 8978-8987.
- Altun, A.; Kumar, D.; Neese, F. & Theil, W. (2008) *J. Phys. Chem. A* 112 (50): 12904-12910.
- Amashukeli, X.; Gruhn, N. E.; Lichtengerger, D. L.; Winkler, J.R. & Gray, H.B. (2004) *J. Am. Chem. Soc.* 126: 15566.
- Andreoletti, P.; Gambarelli, S.; Sainz G.; Stojanoff, V.; White, C.; Desfonds, G.; Gagnon, J.; Gaillard, J. & Jouve, H.M. (2001) *Biochemistry* 40 (45): 13734-13743.
- Andreoletti, P.; Pernoud, A.; Sainz G.; Gouet, P. & Jouve, H. M. (2003) *Acta Crystallogr., Sect. D: Biol. Crystallogr.* 59: 2163-2168.
- Ayala, M.; Roman, R. & Vazquez-Duhalt R. (2007) *Biochem. Biophys. Res. Comm.* 357: 804-808.
- Ayala, R. & Sprik, M. (2008) *J. Phys. Chem. B* 112: 257-269.
- Bader, R. F. W. (1990) *Atoms in Molecules: A Quantum Theory*; Oxford University Press: New York.
- Baker, N. A.; Sept, D.; Joseph, S.; Holst, M. J. & McCammon, J. A. (2001) *Proc. Natl. Acad. Sci. U. S. A.* 98: 10037-10041.
- Banci, L.; Gori-Savellini, G. & Turano, P. (1997) *Eur. J. Biochem.* 249, 716.

Bibliography

- Barbara P.F., Meyer T. J. & Ratner, M. A. (1996) *J Phys Chem* 100, 13148-13168.
- Barea, G.; Maseras, F. & Lledós, A. (2003) *J Mol Struct: Theochem* 632: 323-333.
- Barrows, T. P.; Bhaskar, B. & Poulos, T. L. (2004) *Biochemistry* 43: 8826-8834.
- Bassan, A.; Blomberg, M.; Borowski, T. & Siegbahn, P. E. M. (2006) *J. Inorg. Biochem.* 100: 727-743.
- Bathelt, C. M.; Mulholland, A. J. & Harvey, J. N. (2005) *Dalton Trans.* 3470-3476.
- Bathelt, C. M.; Zurek, J.; Mulholland, A. J. & Harvey, J. N. (2005) *J. Am. Chem. Soc.* 127: 12900-12908.
- Bayly, C. I.; Cieplak, P.; Cornell, W. D. & Kollman, P. A. (1993) *J. Phys. Chem.* 97: 10269-10280.
- Becke, A. D. J. (1986) *Chem. Phys.* 84: 4524-4529.
- Becke, A. D. (1988) *Phys. Rev. A* 36: 3098-3100.
- Becke, A. D. J. (1993) *Chem. Phys.* 98: 5648-5652.
- Behan, R. K. & Green, M. T. (2006) *J. Inorg. Biochem.* 100: 448-459.
- Behan, R. K.; Hoffart, L.M.; Stone, K.L.; Krebs, C. & Green, M. T. (2006) *J. Am. Chem. Soc.* 128 (35): 11471-11474.
- Benecky, M. J.; Frew, J. E.; Scowen, N.; Jones, P. & Hoffman, B. M. (1993) *Biochemistry* 32: 11929-11933.
- Berglund, G. I.; Carlsson, G. H.; Smith, A. T.; Szoke, H.; Henriksen, A. & Hajdu, J. (2002) *Nature* 417: 463-468.
- Bhaskar, B.; Bonagura, C. A.; Li, H. Y. & Poulos, T. L. (2002) *Biochemistry* 41: 2684-2693.
- Biarnés, X.; Nieto, J.; Planas, A. & Rovira, C. (2006) *J. Biol. Chem.* 281: 1432-1441.
- Biarnés, X.; Ardèvol, A.; Planas, A.; Rovira, C.; Laio, A. & Parrinello, M. (2007) *J. Am. Chem. Soc.* 129: 10686-10693.
- Biarnés, X. (2007) *PhD thesis: Mecanismes de preactivació de substrat en 1,3-1,4-b-glucanasa. Modelització mitjançant dinàmica molecular de primers principis.* Barcelona: Universitat de Barcelona. Departament de Química Física, Química. <http://www.tdx.cat/TDX-0212108-120856>
- Bikiel, D. E., Boechi, L., Capece, L., Crespo, A., De Biase, P. M., Di Lella, S, Gonzalez Lebrero, M. C., Mart, M. A., Nadra, A. D., Perissinotti, L. L., Scherlis, D. A. & Estrín, D. A. (2006) *Phys. Chem. Chem. Phys.* 8: 5611-5628.

- Bishop, G. R. & Davidson, V. L. (1995) *Biochemistry* 34: 12082-12086.
- Blodig, W.; Smith, A. T.; Winterhalter, K. & Piontek, K. (1999a) *Arch. Biochem. Biophys.* 370: 86-92.
- Blodig, W.; Doyle, W.; Smith, A. T.; Winterhalter, K. & Piontek, K. (1999b) *J. Inorg. Biochem.* 74: 266.
- Blomberg, M.R.A; Siegbahn, P.E. & Babcock, G.T. (1998) *J. Am. Chem. Soc.* 120(34): 8812-8824.
- Blumberger, J.; Tateyama, Y. & Sprik, M. (2005) *Comp. Phys. Comm.* 256-261.
- Blumberger, J.; Ensing, B. & Klein, M. L. (2006) *Angew. Chem. Int. Engl. Ed.* 45: 2893-2897.
- Blumberger, J. & Klein, M.L. (2006) *J. Am. Chem. Soc.* 128 (42): 13854-13867.
- Blumberger, J. *Phys. Chem. Chem. Phys.* (2008), 10, 5651-5667.
- Blumberger, J. & Lamoreaux, G. (2008) *Mol. Phys.* 106 (12-13): 1597-1611.
- Boero, M. ; Ikeda, T. ; Ito, E. & Terakura, K. (2006) *J. Am. Chem. Soc.* 128: 16798-16807.
- Boero, M.; Ikeshoji, T.; Liew, C. C.; Terakura, K. & Parrinello, M. (2004) *J. Am. Chem. Soc.* 126: 6280-6286.
- Bonagura, C. A.; Bhaskar, B.; Shimizu, H.; Li, H.; Sundaramoorthy, M.; McRee, D. E.; Goodin, D. B. & Poulos, T. L. (2003) *Biochemistry* 42: 5600-5608.
- Bonagura, C. A.; Sundaramoorthy, M.; Pappa, H. S.; Patterson, W. R. & Poulos, T. L. (1996) *Biochemistry* 35: 6107-6115.
- Car, R. & Parrinello, M. (1985) *Phys. Rev. Lett.* 55: 2471-2474.
- Carlioni, P.; Röthlisberger, U. & Parrinello, M. (2002) *Acc. Chem. Res.* 35: 455-464.
- Carpenna, X.; Loprasert, S.; Mongkolsuk, S.; Switala, J.; Loewen, P. C. & Fita, I. (2003) *J. Mol. Biol.* 327: 475-489.
- Carpenna, X.; Wiseman, B.; Deemagarn, T.; Singh, R.; Switala, J.; Ivancich, A.; Fita, I. & Loewen, P. (2005) *EMBO Rep.* 6: 1156-1162.
- Chance, B. (1947) *Acta Chem. Scand.* 1: 236-267.
- Chance, M.; Powers, L.; Poulos, T. & Chance B. (1986) *Biochemistry* 25: 1266-1270.
- Chang, C.J.; Chang, M. C. Y.; Damrauer, N. H. & Nocera, D. G. (2004) *Biochim. et Biophys. Acta.* 1655: 13-28.

Bibliography

- Cheatham, T. E.; Cieplak, P. & Kollman, P. A. (1999) *J. Biomol. Struct. Dyn.* 16: 845-862.
- Chelikani, P.; Fita, I.; Loewen, P. C. (2004) *Cell. Mol. Life Sci.* 61: 192-208.
- Chelikani, P.; Carpena, X.; Perez-Luque, R.; Donald, L. J.; Duckworth, H. W.; Switala, J.; Fita, I.; & Loewen, P. C. (2005) *Biochemistry* 44, 5597-5605.
- Cho, K.-B.; Derat, E.; Shaik, S. (2007) *J. Am. Chem. Soc.* 129: 3182-3188.
- Chouchane, S.; Lippai, I.; Magliozzo, R. S. (2000) *Biochemistry* 39: 9975-9983.
- Chuang, W.J. & Van Wart, H.E. (1992) *J. Biol. Chem.* 267: 13.
- Colin, J.; Wiseman B.; Switala, J.; Loewen, P.C. & Ivancich, A. (2009). *J Am Chem Soc.* 131: 8557-8563.
- Collins, J. R.; Camper, D. L. & Loew, G. H. (1991) *J. Am. Chem. Soc.* 113: 2736-2743.
- Cornell, W. D.; Cieplak, P.; Bayly, C. I.; Gould, I. R.; Merz, K. M., Jr.; Ferguson, D. M.; Spellmeyer, D. C.; Fox, T.; Caldwell, J. W. & Kollman, P. A. (1995) *J. Am. Chem. Soc.* 117: 5179-5197.
- Coulter, E. D.; Cheek, J.; Ledbetter, A. P.; Chang, C. K.; Dawson, J. H. (2000) *Biochem. Biophys. Res. Comm.* 279(3): 1011-1015.
- CPMD program, <http://www.cpmd.org/>, Copyright IBM Corp 1990-2008, MPI für Festkörperforschung Stuttgart 1997-2001
- Daiber, A.; Herold, S.; Schöneich, C.; Namgaladze, D.; Peterson, J.A. & Ullrich V. (2000) *Eur. J. Biochem.* 267: 6729-6739.
- Dal Peraro, M., Ruggerone, P., Raugei, S., Gervasio, F. L. & Carloni, P. (2007) *Curr. Opin. Struct. Biol.* 17: 149-156
- Dal Peraro, M., Spiegel, K., Lamoureux, G., De Vivo, M., DeGrado, M. & Klein, M. L. (2007) *J. Struct. Biol.* 157, 444-453.
- Dawson, J. H. (1988) *Science* 240, 433-439.
- Daz, A., Valdes, V.-J., Rudio-Piera, E., Horjales, E. & Hansberg, W. (2009) *J. Mol. Biol.* 386: 218-232.
- De Biase, P. M.; Doctorovich, F.; Murgida, D. H.; Estrín, D. A. (2007) *Chemical Physics Letters* 434(1-3): 121-126.
- Decker, A.; Rohde, J. U.; Klinker, E. J.; Wong, S. D.; Que, L., Jr. & Solomon, E. I. (2007) *J. Am. Chem. Soc.* 129: 15983-96.

- Deeth, R. J. (1999) *J. Am. Chem. Soc.* 121: 6074-6075.
- de Groot, H.; Auferkamp, O.; Bramey, T.; de Groot, K.; Kirsch, M.; Korth, H.G.; Petrat, F., Sustmann, R. (2006) *Free Radic Res.* 40(1): 67-74.
- Deiseroth, A. & Dounce, A. L. (1970) *Physiol. Rev.* 50: 319-375.
- Derat, E.; Cohen, S.; Shaik, S.; Altun, A. & Thiel, W. (2005) *J. Am. Chem. Soc.* 127: 13611-13621.
- Derat, E. & Shaik, S. (2006a) *J. Phys. Chem. B* 110: 10526-10533.
- Derat, E. & Shaik, S. (2006b) *J. Am. Chem. Soc.* 128: 8185-8198.
- Derat, E. & Shaik, S. (2006c) *J. Am. Chem. Soc.* 128: 13940-13949.
- Derat, E. & Shaik, S. (2007) *J. Am. Chem. Soc.* 128: 13940-13949.
- Derat, E.; Shaik, S.; Rovira, C.; Vidossich, P. & Alfonso-Prieto, M. (2007) *J. Am. Chem. Soc.* 129: 6346-6347.
- Deterding, L.J.; Ramirez, D.C.; Dubin, J.R.; Mason R.P. & Tomer, K.B. (2004) *J. Biol. Chem.* 279(12): 11600-11607.
- de Visser, S. P.; Shaik, S.; Sharma, P. K.; Kumar, D. & Thiel, W. (2003) *J. Am. Chem. Soc.* 125: 15779-15788.
- de Visser, S. P. (2006) *Inorg. Chem.* 45: 9551-9557.
- DiCarlo, C. M.; Vitello, L. B. & Erman J.E. (2007) *J Inorg Biochem* 101, 603-613.
- DiLabio, G.A. & Johnson, E.R. (2007) *J. Am. Chem. Soc.* 129 (19): 6199-6203.
- Dounce (1983) *Theor. Biol.* 105: 553-567.
- Dunford, H. B. (1999) *Heme Peroxidases*; Wiley: New York.
- English, A.M. & Tsaprailis, G. (1995). *Catalytic structure-function relationships in heme peroxidases*. In *Advanced Inorganic Chemistry*; Sykes, A. G., Mauk, G., Eds.; Academic Press: New York; Vol. 43, pp. 79-125.
- Ensing, B., Laio, A., Parrinello, M. & Klein, M. L. (2005) *J. Phys. Chem.* 109: 6676-6687.
- Ensing, B., De Vivo, M., Liu, Z. W., Moore, P. & Klein, M. L. (2006) *Acc. Chem. Res.* 39: 73-81.
- Essman, U.; Perera, L.; Berkowitz, M. L.; Darden, T.; Lee, H. & Pedersen, L. G. (1995) *J. Chem. Phys.* 103: 8577-8593.
- Evans, D. R. & Reed, C. A. (2000) *J. Am. Chem. Soc.* 122: 4660-4667.

Bibliography

- Faller, P.; Goussias, C.; Rutherford, W. & Un, S. (2003) *Proc. Natl. Acad. Sci. U. S. A.* 100(15): 8732-8735.
- Fecenko, C.J.; Meyer, T.J. & Thorp, H.H. (2006) *J. Am. Chem. Soc.* 128(34): 11020-11021.
- Fenton, H. J. H. (1894) *J. Chem. Soc.* 65: 899-910.
- Fielding, A.J.; Singh, R.; Boscolo, B.; Loewen, P.C.; Ghibaudi, E.M. & Ivancich, A. (2008). *Biochemistry.* 47: 9781-92.
- Filatov, M.; Harris, N. & Shaik, S. (1999) *Angew. Chem., Int. Ed.* 38: 3510-3512.
- Fiorin G.; Pastore A.; Carloni P. & Parrinello M. (2006) *Biophys. J.* 91: 2768-2777.
- Fita, I. & Rossmann, M. G. (1985) *J. Mol. Biol.* 185: 21-37.
- Frisch, M. J.; Trucks, G. W.; Schlegel, H. B.; Scuseria, G. E.; Robb, M. A.; Cheeseman, J. R.; *et al.* (2004) *GAUSSIAN 03*, Gaussian Inc., Wallingford, CT.
- Gao, B.; Boeglin, W. E. & Brash, A. R. (2008) *Arch. Biochem. Biophys.* 477(2): 285–290.
- Ghosh, A.; Almlöf, J. & Que, L. (1994) *J. Phys. Chem.* 98: 5576-5579.
- Ghosh, A. (1997) *J. Phys. Chem. B* 101(16): 3290-3297.
- Ghosh, A.; Vangberg, T.; Gonzalez, E. & Taylor, P. (2001) *J. Porphyrins Phthalocyanines* 5: 345.
- Ghosh, A. (2006) *J. Biol. Inorg. Chem.* 11: 712-724.
- Ghot, L. & Eaton, J. W. (2000) *The Lancet* 356 (9244): 1820-1821.
- Gouet, P.; Jouve, H. M.; Williams, P. A.; Andersson, I.; Andreoletti, P.; Nussaume, L. & Hajdu, J. (1996) *Nat. Struct. Biol.* 3: 951-956.
- Gray, H.B. & Winkler, J.R. (2003) *Quart. Rev. Biophys.* 36: 341-372.
- Green, M. T. (2001) *J. Am. Chem. Soc.* 123: 9218-9219.
- Green, M. T.; Dawson, J. H. & Gray, H. B. (2004) *Science* 304: 1653-1656.
- Green, M. T. (2006) *J. Am. Chem. Soc.* 128: 1902-1906.
- Groves, J. T., Haushalter, R. C., Nakamura, M., Nemo, T. E. & Evans, B. J. (1981) *J. Am. Chem. Soc.* 103: 2884-2886.
- Guallar, V. & Friesner, R. A. (2004) *J. Am. Chem. Soc.* 126: 8501-8508.
- Guallar, V. & Olsen, B. (2006) *J Inorg Biochem* 100 (4): 755-760.

- Guallar, V. (2008) *J. Phys. Chem. B* 112: 13460-13464.
- Gubelmann, M.H. & Willimas, A.F. (1983) *Struct. Bonding*. 55: 1.
- Gunaydin, H. & Houk, K. N. (2008) *J. Am. Chem. Soc.* 130 (31): 10036–10037.
- Haber, F. & Weiss, J. (1934) *Proc. R. Soc. London. Ser. A* 147: 332-351.
- Halliwell, B. & Gutteridge, J. M. C. (1984) *J. Biochem.* 219: 1-14.
- Hamann, D. R. (1989) *Phys. Rev. B.* 40, 2980-2987.
- Hanson L. K., Chang C. K., Davis M. S., Fajer J. (1981) *J. Am. Chem. Soc.* 103 (3): 663-670.
- Harris, D. & Loew, G. (1995) *J. Am. Chem. Soc.* 117: 2738-2746.
- Harvey, J. N., Bathelt, C. M. & Mulholland, A. (2006) *J. J. Comput. Chem.* 27: 1352-1362.
- He, B.; Sinclair, R.; Copeland, B. R.; Makino, R.; Powers, L. S. & Yamazaki, I. (1996) *Biochemistry*. 35 (7): 2413-2420.
- Henkelman, G.; Arnaldsson, A. & Jonsson, H. (2006) *Comput. Mater. Sci.* 36: 354-360.
- Hersleth, H. P.; Dalhus, B.; Görbitz, C. H. & Andersson, K. K. (2002) *J. Biol. Inorg. Chem.* 7: 299-304.
- Hersleth, H. P.; Ryde, U.; Rydberg, P.; Görbitz, C. H. & Andersson, K. K. (2006) *J. Inorg. Biochem.* 100: 460-476.
- Hersleth, H. P.; Uchida, T.; Røhr, A. K.; Teschner, T.; Schnemann, V.; Kitagawa, T; Trautwein, A. X.; Görbitz, C. H.; Andersson, K. K. (2007) *J. Biol. Chem.* 282: 23372-23386.
- Hersleth, H. P.; Hsiao, Y.-W.; Ryde, U.; Görbitz, C.H. & Andersson, K. (2008) *Chem. Biodivers.* 5: 2067-2089.
- Herzberg, G. (1950) *Molecular Spectra and Molecular Structure*; 2nd ed.; Van Nostrand: New York, 1950.
- Hillar, A.; Nicholls, P.; Switala, L. & Loewen, P. C. (1994) *Biochem. J.* 300: 531-539.
- Hiner, A. N. P.; Raven, E. L.; Thorenley, R. N. F.; Carcia-Canovas, F. & Rodriguez-Lopez, J. N. (2002) *J. Inorg. Biochem.* 91: 27-34.
- Hirao, H.; Shaik, S. & Kozlowski, P. M. (2006) *J. Phys. Chem. A* 110: 6091-6099.
- Hoare, J. P. (1985) In *Standard Potentials in Aqueous Solution*; Bard, A. J., Parsons, R. & Jordan, J., Eds.; Marcel Dekker: New York, Ch. 4.

Bibliography

- Hoganson, C.W. & Tommos, C. (2004) *Biochim. et Biophys. Acta* 1655, 116-122.
- Hohenberg, P. & Kohn, W. (1964) *Phys. Rev. B: Condens. Mater. Phys.* 136: 864-871.
- Horner, O.; Oddou, J. L.; Mouesca, J. M. & Jouve, H. M. (2006) *J. Inorg. Biochem.* 100: 477-479.
- Horner, O.; Mouesca, J. M.; Solari, P. L.; Orio, M.; Oddou, J. L.; Bonville, P. & Jouve, H. M. (2007) *J. Biol. Inorg. Chem.* 12: 509-525.
- Hubbard, S.R.; Hendrickson, W.A.; Lambright, D.G. & Boxer, S.G. (1990) *J. Mol. Biol.* 213: 215-218.
- Huber, K. P. (1972) In *American Institute of Physics Handbook*; Mc-Graw Hill: New York; section 7g.
- Humphrey, W.; Dalke, A. & Schulten, K. (1996) *J. Mol. Graphics* 14: 33-38.
- Hünenberger, P. (2000) *J. Chem. Phys.* 113: 10464-10476.
- Iannuzzi, M., Laio, A. & Parrinello, M. (2003) *Phys. Rev. Lett.* 90: 238302.
- Imlay J. A. (2008) *Annu. Rev. Biochem.* 77: 755-776.
- Irebo, T.; Reece, S.Y.; Sjödin, M.; Nocera, D. G. & Hammarström, L. (2007) *J. Am. Chem. Soc.* 129(50): 15462-15464.
- Irebo, T.; Johansson, O. & Hammarström, L. (2008) *J. Am. Chem. Soc.* 130 (29): 9194-9195.
- Islam, K. N., Kayanoki, Y., Kaneto, H., Suzuki, K., Asahi, M., Fujii, J. & Taniguchi, N. (1997) *Free Radical Biol. Med.* 22: 1007-1017.
- Ivancich, A.; Jouve, H. M. & Gaillard, J. (1996) *J. Am. Chem. Soc.* 118: 12852-12853.
- Ivancich, A.; Jouve, H. M.; Sartor, B. & Gaillard, J. (1997) *Biochemistry* 36: 9356-9364.
- Ivancich, A.; Artz, K.; Williams, J. C.; Allen, J. A. & Mattioli, T. A. (1998) *Biochemistry*, 11812-11820.
- Ivancich, A.; Mattioli, T.A. & Un, S. (1999) *J. Am. Chem. Soc.* 121(24): 5743-5753
- Ivancich, A.; Jakopitsch, C.; Auer, M.; Un, S. & Obinger, C. (2003) *J. Am. Chem. Soc.* 125: 14093-14102.
- Ivanov, I.; Chen, B.; Raugei, S. & Klein, M. L. (2006) *J. Phys. Chem. B* 110: 6365-6371.
- Jacob, H. S.; Ingbar, S. H. & Jandl, J. H. (1965) *J Clin Invest.* 44(7): 1187-1199.

- Jakopitsch, C.; Auer, M.; Regelsberger, G.; Jantschko, W.; Furtmuller, P. G.; Ruker, F. & Obinger, C. (2003) *Biochemistry* 42: 5292-5300.
- Jakopitsch, C.; Ivancich, A.; Schmuckenschlager, F.; Wanasinghe, A.; Poltl, G.; Furtmuller, P. G.; Ruker, F. & Obinger, C. (2004) *J. Biol. Chem.* 279: 46082-46095.
- Jakopitsch, C.; Wanasinghe, A.; Jantschko, W.; Furtmuller, P. G. & Obinger, C. (2005) *J. Biol. Chem.* 280: 9037-9042.
- Jakopitsch, C.; Obinger, C.; Un, S. & Ivancich, A. (2006) *J. Inorg. Biochem.* 100: 1091-1099.
- Jakopitsch, C.; Vlasits, J.; Wiseman, B.; Loewen, P. C. & Obinger, C. (2007) *Biochemistry* 46: 1183-1193.
- Jarnagin, R. C. & Wang, J. H. (1958) *J. Am. Chem. Soc.* 80, 786-787.
- Jayaraj, K.; Gold, A.; Austin, R. N.; Mandon, D.; Weiss, R. ; Turner, J.; Bill, E.; Muether, M.; Trautwein, A. X. (1995) *J. Am. Chem. Soc.* 117 (35): 9079-9080.
- Jensen, G. M.; Bunte, S. W.; Warshel, A. & Goodin, D. B. (1998) *J. Phys. Chem.* 102: 8221.
- Jensen, K. P. & Ryde, U. (2001) *Mol. Phys.* 101(13): 2003-2018
- Jeong, Y. J., Kang, Y., Han, A.-R., Lee, Y.-M., Kotani, H.; Fukuzumi, S.; & Nam, W. (2008) *Angew. Chem. Intl. Engl. Ed.* 47: 7321-7324.
- Jones, P. & Perkins, P. G. (1967) *Nature* 215: 129-132.
- Jones, P. & Suggett, A. (1968) *Biochem. J.* 110: 621-629.
- Jones, P. & Middlemiss D. N. (1972) *Biochem. J.* 130: 411-415.
- Jones, P. & Dunford, B. (2005) *J. Inorg. Biochem.* 99: 2292-2298.
- Jones, P. & Dunford, H. B. (2006) *J. Bioinorg. Chem.* 99: 2292-2298.
- Jorgensen, W. L.; Chandrasekhar, J. D.; Madura, J. D.; Impey, R. W. & Klein, M. L. (1983) *J. Chem. Phys.* 79: 926-935.
- Jouve, H. M.; Andreoletti, P.; Gouet, P.; Hajdu, J. & Gagnon, J. (1997) *Biochimie* 79: 667-671.
- Jovanovic, S.V.; Steenken, S. & Simic, M.G. (1991) *J.Phys.Chem.* 95(2): 684.
- Kanamori, D.; Furukawa, A.; Okamura, T.; Yamamoto, H. & Ueyama, N. (2005) *Org. Biomol. Chem.* 3: 1453-1459.
- Kanofsky, J. R. (1984) *J. Am. Chem. Soc.* 106: 4278-4279.

Bibliography

- Kato, S.; Ueno, T.; Fukuzumi, S.; Watanabe, Y. *J. Biol. Chem.* (2004) 279 52376-52381.
- Khan, A. U.; Gebauer, P. & Hager, L. P. (1983) *Proc. Natl. Acad. Sci. U.S.A.* 80: 5195-5197.
- Kikuchi-Torii, K.; Hayashi, S.; Nakamoto, H. & Nakamura, S. (1982) *J. Biochem.* 92: 1449-1456.
- Kirkman, H. N. & Gaetani, G. F. (2007) *Trends. Biochem. Sci.* 32: 44-50.
- Kitagawa, T.; Mizutani, Y. (1994) *Coord. Chem. Rev.* 135-136: 685-735.
- Kleywegt, G. J.; Jones, T. A. (1994) *Acta Crystallogr., Sect. D: Biol. Crystallogr.* 50: 178-185.
- Klinker, E. J., Kaizer, J., Brennessel, W. W., Woodrum, N. L., Cramer, C. J. & Que, L., Jr. (2005) *Angew. Chem., Int. Ed. Engl.* 44: 3690-3694.
- Klotz, M. G. & Loewen, P. C. (2003) *Mol. Biol. Evol.* 20: 1098-1112.
- Kohn, W. & Sham, L. (1965) *J. Phys. Rev. A: At., Mol., Opt. Phys.* 140: 1133-1138.
- Kuramochi, H.; Noodleman, L.; Case, D. A. (1997) *J. Am. Chem. Soc.* 119: 11442-11451.
- Kuta, J.; Patchkovskii, S.; Zgierski, M. Z. & Kozlowski, P. M. (2006) *J. Comput. Chem* 27: 1429-1437.
- Lai, W.; Chen, H. & Shaik, S. (2009) *J. Phys. Chem. B.* 113 (22): 7912-7917.
- Laio, A.; vandeVondele, J. & Röthlisberger, U. (2002a) *J. Chem. Phys.* 116: 6941-6947.
- Laio, A.; VandeVondele, J. & Roethlisberger, U. (2002b) *J. Phys. Chem. B* 106: 7300-7307.
- Laio, A. & Parrinello, M. (2002) *Proc. Nat. Acad. Sci. U.S.A.* 99: 12562-12566.
- Laio, A.; Gervasio, F. L.; VandeVondele, J.; Sulpizi, M. & Rothlisberger, U. (2004) *J. Phys. Chem. B* 108: 7963-7968.
- Laio, A., Rodriguez-Forteza, A., Gervasio, F. L., Ceccarelli, M. & Parrinello, M. (2005) *J. Phys. Chem. B* 109: 6714-6721.
- Laio, A. & Gervasio, F. L. (2008) *Rep. Prog. Phys.* 71(12): 126601.
- Lardinois, O. M. & Rouxhet, P. G. (1994) *Free Radical Res.* 20 (1): 29-50
- Lardinois, O. M. (1995) *Free Radical Res.* 22 (3): 251-274.
- Lardinois, O. M. & Ortiz de Montellano, P. M. (2004) *Biochemistry* 43: 4601-4610.
- Latimer, W. M. (1938) *The Oxidation States of the Elements & their Potentials in Aqueous Solutions*, 1st ed.; Prentice-Hall, New York.

- Leach, A. R. (2001) *Molecular modelling*. Pearson Education Limited.
- Lee, C.; Yang, W. & Parr, R. G. (1988) *Phys. Rev. B* 37: 785-789.
- Liao, M.S. & Scheiner, S. (2002) *J. Chem. Phys.* 117, 205.
- Linstrom, P. J. & Mallard, W.G. (Eds) (2005) NIST Chemistry WebBook, NIST Standard Reference Database Number 69, National Institute of Standards and Technology, Gaithersburg, MD. Available from: <http://webbook.nist.gov>
- Lledías, F.; Rangel, P. & Hansberg, W. (1998) *J. Biol. Chem.* 273: 10630-10637.
- Loewen, P. C.; Switala, J.; von Ossowski, I.; Hillar, A.; Christie, A.; Tattrie, B. & Nicholls, P. (1993) *Biochemistry* 32: 10159-10164.
- Loewen, P. C.; Carpena, X.; Rovira, C.; Ivancich, A.; Perez-Luque, R.; Haas, R.; Odenbreit, S.; Nicholls, P. & Fita, I. (2004) *Biochemistry* 43: 3089-3103.
- Louie, S. G.; Froyen, S. & Cohen, M. L. (1982) *Phys. Rev. B* 26: 1738-1742.
- Lundberg, M. & Siegbahn, P. E. M. (2005) *J. Chem. Phys.* 122: 224103
- Marcus, R.A. & Sutin, N. (1985) *Biochim Biophys Acta* 811: 265-322.
- Markle, T.F.; Rhile, I.J.; DiPasquale, A.G. & Mayer, J.M. (2008) *Proc. Natl Acad. Sci. U.S.A.* 105(24): 8185-8190.
- Martonak R.; Donadio D.; Oganov, A. R. & Parrinello M. (2006) *Nature Materials* 5: 623-626.
- Martyna; G. J. & Tuckerman, M. E. (1999) *J. Chem. Phys.* 110: 2810.
- Marx, D. & Hutter, J. (2000) *Ab initio molecular dynamics: Theory & implementation*. In *Modern Methods & Algorithms of Quantum Chemistry*; Grotendorst, J., Ed.; John von Neumann Institute for Computing: Julich, Germany; pp 301-409.
- Maté, M. (1999) *PhD thesis: Determinación de la estructura tridimensional de catalasas*. Universitat de Barcelona.
- Maté, M.; Murshudov, G.; Bravo, J.; Melik-Adamyanyan, W.; Loewen, P. C. & Fita, I. (2001) *Heme-catalases*. In *Handbook of Metalloproteins*; Messerschmidt, A., Huber, R., Poulos, T., Wieghardt, K., Eds.; John Wiley & Sons: Chichester, U.K.
- Matsui, T., Ozaki, S., Liong, E., Phillips, G. N., Jr. & Watanabe, Y. (1999) *J. Biol. Chem.* 274: 2838-2844.
- Mayer, J. M. (2004) *Annu. Rev. Phys. Chem.* 55: 363-390.

Bibliography

- Medall, R.M.; Sanchís-Segura, C. & González-Aragón, C. M. (2002) *Psychopharmacology* 165: 51-59.
- Michán, S.; Lledías, F.; Baldwin, J. D.; Natvig, D. O. & Hansberg, W. (2002) *Free Radical Biol. Med.* 33: 521-532.
- Miller, V.P.; Goodin, D.B.; Friedman, A.E.; Hartmann, C. & Ortiz de Montellano, P.R. (1995) *J. Biol. Chem.* 270(31): 18413-18419.
- Miyamoto, T., Hayashi, M., Takeuchi, A., Okamoto, T., Kawashima, S., Takii, T., Hayashi, H. & Onozaki, K. (1996) *J. Biochem.* 120: 725-730.
- Mordasini, T.; Curioni, A. & Andreoni, W. (2003) *J. Biol. Chem.* 278: 4381-4384.
- Moser, C.C.; Page, C.C. & Dutton, P.L. (2006) *Phyl. Trans. R. Soc. B* 361: 1295-1305.
- Murshudov, G.N.; Grebenko, A.I.; Barynin, V.; Dauter, Z.; Wilson, K.S.; Vainshtein, B.K.; Melik-Adamyán, W.; Bravo, J.; Ferran, J.M.; Ferrer, J.C.; Switala, J.; Loewen, P.C. & Fita, I. (1996) *J. Biol. Chem.* 271(15): 8863-8868.
- Murshudov, G. N.; Grebenko, J. A.; Branningan, J. A.; Antson, A. A.; Barynin, V. V.; Dodson, G. G.; Dauter, Z.; Wilson, K. & Melik-Adamyán, W. R. (2002) *Acta Crystallogr., Sect. D: Biol. Crystallogr.* 58: 1972-1982.
- Narváez, A.J.; Kálmán, L.; LoBrutto, R.; Allen, J.P. & Williams, J.C. (2002) *Biochemistry* 41(51): 15253-15258.
- Narváez, A.J.; LoBrutto, R.; Allen, J.P. & Williams, J.C. (2004) *Biochemistry* 43(45): 14379-14384.
- Nelson, D. P. & Kiesow, L. A. (1972) *Anal Biochem.* 49: 474-478.
- Newcomb, M.; Halgrimson, J. A.; Horner, J.H.; Wasinger, E. C.; Chen, L. X. & Sligar (2008) *Proc. Natl Acad. Sci. U.S.A* 105(24): 8179-8184.
- Nicholls, P.; Fita, I. & Loewen, P. C. (2001) *Enzymology & structure of catalases*. In *Advanced Inorganic Chemistry*; Sykes, A. G., Mauk, G., Eds.; Academic Press: New York, Vol. 51, pp 51-106.
- Nilsson, K.; Hersleth, H. P.; Rod, T. H.; Andersson, K. K. & Ryde, U. (2004) *Biophys. J.* 87: 3437-3447.
- Noack, H. & Siegbahn, P. E. (2007) *J. Biol. Inorg. Chem.* 12, 1151-62.
- Obinger, C.; Maj, M.; Nicholls, P. & Loewen, P. C. (1997) *Arch. Biochem. Biophys.* 342: 58-67.
- Odenbreit, S.; Wieland, B. & Haas, R. (1996) *J. Bacteriol.* 178: 6960-6967.
- Oganov, A. R.; Martonak, R.; Laio, A.; Raiteri, P. & Parrinello, M. (2005) *Nature* 438: 1142-1144.

- O'Malley P.J. (1998) *J. Am. Chem. Soc.* 120(45): 11732-11737.
- Ozawa, S.; Fujii, H. & Morishima, I. (1992a) *J. Am. Chem. Soc.* 114 (5): 1548-1554.
- Ozawa, S.; Watanabe, Y. & Morishima, I. (1992b) *Inorg. Chem.* 31 (20): 4042-4043.
- Ozawa, S.; Watanabe, Y. & Morishima, I. (1994) *J. Am. Chem. Soc.* 116 (13): 5832-5838.
- Papoian, G. A.; DeGrado, W. F. & Klein, M. L. (2003) *J. Am. Chem. Soc.* 125: 560-569.
- Pearlman, D. A.; Case, D. A.; Caldwell, J. W.; Ross, W. S.; Cheatham, T. E.; Debolt, S.; Ferguson, D.; Seibel, G.; & Kollman, P. (1995) *Comput. Phys. Commun.* 91: 1-41.
- Perdew, J. P. (1986) *Phys. Rev. B.* 33: 8822-8824.
- Perdew, J. P., Burke, K. & Ernzerhof, M. (1996) *Phys. Rev. Lett.* 77: 3865-3868. Erratum: (1997) *Phys. Rev. Lett.* 78: 1396.
- Perdew, J. P., Staroverov, V. N., Tao, J. & Scuseria, G. E. *Phys. Rev. A* (2008), 78:052513.
- Petlicki, J. & van de Ven, T. G. M. (1998) *J. Chem Soc., Faraday Trans.* 94: 2763.
- Pfister, T.D.; Gengenbach, A.J.; Syn, S. & Lu, Y. (2001) *Biochemistry* 40(49): 14942-14951.
- Phillips, J. C.; Braun, R.; Wang, W.; Gumbart, J.; Tajkhorshid, E.; Villa, E.; Chipot, C.; Skeel, R. D.; Kale, L. & Schulten, K. (2005) *J. Comput. Chem.* 26: 1781-1802.
- Pipirou, Z.; Bottrill, A. R.; Metcalfe, C. M.; Mistry, S. C.; Badyal, S. K.; Rawlings, B. J. & Raven, E. L. (2007) *Biochemistry*. 46: 2174-2180.
- Poulos, T. L. & Kraut, J. (1980) *J. Biol. Chem.* 255, 8199-8205
- Poulos, T. L. (1996) *J. Biol. Inorg. Chem.* 1: 356-359.
- Poulos, T. L. (2007) *Nat. Prod. Rep.* 24: 504-510.
- Pu, J. & Truhlar, D. G. (2005) *J. Phys. Chem. A* 109: 773-778.
- Pujols-Ayala, I.; Sacksteder, C.A.; Barry, B.A. (2003) *J. Am. Chem. Soc.* 125(25): 7536-7538
- Putnam, C.D.; Arvai, A.S.; Bourne, Y. & Tainer, J.A. (2000) *J. Mol. Biol.* 296: 295-309
- Raiteri, P.; Laio, A.; Gervasio, F. L.; Micheletti, C. & Parrinello, M. (2006) *J. Phys. Chem. B* 110: 3533-3539.
- Ranguelova, K.; Giroto, S.; Gerfen, G. J.; Yu, S. W.; Suarez, J.; Metlitsky, L. & Magliozzo, R. S. (2007) *J. Biol. Chem.* 282: 6255-6264.

Bibliography

- Reece, S. Y.; Hodgkiss, J. M.; Stubbe, J. A. & Nocera, D. G. (2006) *Philos. Trans. R. Soc.* 361: 1351-1364.
- Reece, S. Y. & Nocera, D. G. *Annu. Rev. Biochem.*(2009) 78: 673-699.
- Rodríguez-Forteza, A.; Iannuzzi, M. & Parrinello, M. (2006) *J. Phys. Chem. B* 110: 3477-3484.
- Rodríguez-Forteza, A.; Iannuzzi, M. & Parrinello, M. (2007) *J. Phys. Chem. C* 111: 2251-2258.
- Rovira, C.; Kunc, K.; Hutter, J.; Ballone, P. & Parrinello, M. (1997) *J. Phys. Chem. A* 101: 8914-8925.
- Rovira, C. & Parrinello, M. (2000) *Biophys. J.* 78: 93-100.
- Rovira, C., Schulze, B., Eichinger, M., Evanseck, J. D.; & Parrinello, M (2001) *Biophys. J.* 81: 435-445.
- Rovira, C. & Fita, I. (2003) *J. Phys. Chem. B* 107: 5300-5305.
- Rovira, C. (2005) *The study of ligand-protein interaction by means of Density Functional Theory and first-principles molecular dynamics*. In *Methods in molecular biology* 305; Ullrich Nienhaus G. Ed.; Humana Press, Inc.
- Rovira, C. (2005) *Chem. Phys. Chem.* 6: 1-8.
- Rovira, C., Alfonso-Prieto, M., Biarnés, X., Carpena, X., Fita, I. & Loewen, P. C. (2006) *Chem. Phys.* 323: 129-137.
- Rovira, C. & Kozłowski, P. M. (2007) *J. Phys. Chem. B* 111: 3251-3257.
- Rydberg, P.; Sigfridsson, E. & Ryde, U. (2004) *J Biol Inorg Chem* 9: 203-223.
- Sandstrom, P. A. & Buttke, T. M. *Proc. Natl Acad. Sci. U.S.A.* (1993), 90, 4708-4712
- Scheidt, W. R. (2001) *J. Biol. Inorg. Chem.* 6: 727-732.
- Schlichting, I.; Berendzen, J.; Chu, K.; Stock, A.M.; Maves, S.A.; Benson, D.E.; Sweet, R.M.; Ringe, D.; Petsko, G.A. & Sligar, S.G. (2000) *Science*. 287(5458): 1615-1622.
- Schöneboom, J. C. & Thiel, W. (2004) *J. Phys. Chem. B* 108: 7468-7478.
- Schonbaum, G. R. & Chance, B. (1976) *Catalase*. In *The Enzymes*; Boyer, P. D., Ed.; Academic Press: New York; Vol. 13, pp 363-408.
- Schönemann, V.; Lenzian, F.; Jung, C.; Contzen, J.; Barra, A.-L.; Sligar, S. G. & Trautwein, A. X. (2004) *J. Biol. Chem.* 279: 10919-10930.
- Shaik, S.; Kumar, D.; de Visser, S. P.; Altun, A. & Thiel, W. (2005) *Chem. Rev.* 105: 2279-2328.

- Shaik, S.; Hirao, H. & Kumar, D. (2007) *Acc. Chem. Res.* 40: 532-542
- Shaik, S. (2008) *J. Am. Chem. Soc.* 130: 10128-10140.
- Sharma, K. D.; Andersson, L. A.; Loehr, T. M.; Turner, J. & Goff, H. M. (1989) *J. Biol. Chem.* 264: 12772-12779.
- Shelnutt, J.A.; Song, X.-Z.; Ma, J.-G.; Jia, S.-L.; Jentzen, W. & Medforth, C.J. (1998) *Chem. Soc. Rev.* (1): 31-42.
- Sicking, W., Korth, H. G., Jansen, G., de Groot, H. & Sustmann, R. (2007) *Chemistry* 13: 4230-4245.
- Siegbahn, P. E. M. (2001) *Theor. Chem. Acc.* 105: 197-206.
- Sigfridsson, E.; Olsson, M. & Ryde, U. (2001) *J Phys Chem B* 105: 5546.
- Silaghi-Dumitrescu, R. (2004) *J. Biol. Inorg. Chem.* 9: 471-476.
- Silaghi-Dumitrescu, R. & Cooper (2005) *Dalton Trans.* 3477-3482.
- Silaghi-Dumitrescu, R. & Reeder, B. J. & Nichols, P. (2007) *Biochem. J.* 403: 391-395.
- Singh, R.; Switala, J.; Loewen, P.C. & Ivancich A. (2007). *J Am Chem Soc.* 129: 15954-63.
- Sitter, A. J.; Shifflet, J. R. & Turner, J. (1988) *J. Biol. Chem.* 263(26): 13032-13038.
- Sivaraja, M.; Goodin, D. B.; Smith, M. & Hoffman, B. M. (1989) *Science.* 245: 738-740.
- Sjödin, M.; Styring, S.; Wolpher, H.; Xu, Y.; Sun, L. & Hammarström, L. (2005) *J. Am. Chem. Soc.* 127 (11): 3855-3863.
- Sjödin, M.; Irebo, T.; Utas, J.E.; Lind, J.; Mernyi, G.; Kermark, B. & Hammarström, L. (2006) *J. Am. Chem. Soc.* 128(40): 13076-13083.
- Smulevich, G.; Jakopitsch, C.; Droghetti, E. & Obinger, C. (2006) *J. Inorg. Biochem.* 100: 568-585.
- Sono, M. & Dawson, J. H. (1982) *J. Biol. Chem.* 257(10): 5496- 5502
- Spolitak, T.; Dawson, J.H. & Ballou D.P. (2005) *J. Biol. Chem.* 280(21): 20300-20309.
- Spolitak, T.; Dawson, J.H. & Ballou, D.P. (2006) *J.Inorg. Biochem.* 100, 2034-2044.
- Spolitak, T.; Dawson, J.H. & Ballou, D.P. (2008) *J. Biol. Inorg. Chem.* 13: 599-611.
- Steiner, T. (2002) *Biophys. Chem.* 95: 195-201.
- Stolzenberg, A. M.; Strauss, S. H. & Holm, R. H. (1981) *J. Am. Chem. Soc.* 103 (16): 4763–4778.

Bibliography

- Stone, K.L.; Behan, R.K. & Green, M.T. (2005) *Proc. Natl. Acad. Sci. U. S. A.* 102: 16563-16565.
- Stone, K.L.; Hoffart, L.M.; Behan, R.K.; Krebs, C. & Green, M.T. (2006a) *J. Am. Chem. Soc.* 128(18):6147-6153
- Stone, K.L.; Behan, R.K. & Green, M.T. (2006b) *Proc. Natl. Acad. Sci. U. S. A.* 103(33): 12307-12310
- Strich, A. & Veillard, A. (1981) *Theor. Chim. Acta* 60: 379.
- Strich, A. & Veillard, A. (1983) *Nouv. J. Chim.* 7: 347.
- Sulpizi, M. & Carloni, P. (2000) *J Phys Chem B* 104: 10087-10091
- Sulpizi, M.; Raugai, S.; VandeVondele, J.; Carloni, P. & Sprik, M. (2007) *J Phys Chem B* 111: 3969-3976.
- Svistunenko, D.A (2005) *Biochim. et Biophys. Acta* 1707: 127-155.
- Switala, J. & Loewen, P. C. (2002) *Arch. Biochem. Biophys.* 401: 145-154.
- Tateyama, Y.; Blumberger, J.; Ohno, T. & Sprik, M. (2007) *J Chem Phys* 126: 204506-10.
- Taube, H. (1965) *J. Gen. Physiol.* 49(2): 29-50
- Timkovich, R. & Bondoc, L.L. (1990) *Adv. Biophys. Chem.* 1: 203-247.
- Todorova, T.; Seitsonen, A. P.; Hutter, J.; Kuo, I-F. W. & Mundy, C. (2006) *J. Phys. Chem. B* 110: 3685-3691
- Tommos, C. & Babcock, G.T. (2000) *Biochim. et Biophys. Acta* 1458: 199-219.
- Troullier, M. & Martins, J. L. (1991) *Phys. Rev. B* 43: 1993-2006.
- Tsai, A.-L. & Kulmacz, R.J. (2009) *Arch. Biochem. Biophys.* (in press)
- Unno, M.; Chen, H.; Kusama, S.; Shaik, S. & Ikeda-Saito, M. (2007) *J. Am. Chem. Soc.* 129: 13394-13395
- Vainshtein, B. K.; Melik-Adamyan, W. R.; Barynin, V. V.; Vagin, A. A. & Grebenko, A. I. (1981) *Nature (London)*. 293: 411-412.
- VandeVondele, J. & Sprik, M. (2005) *Phys. Chem. Chem. Phys.* 7: 1363-1367.
- VandeVondele, J.; Ayala, R.; Sulpizi, M. & Sprik, M. (2007) *J. Electroanal. Chem.* 607 (1-2): 113-120.
- Vangberg, T. & Ghosh, A. (1999) *J. Am. Chem. Soc.* 121: 12154-12160.

- van Gunsteren W. F. (1996) *Biomolecular Simulation: The GROMOS96 Manual & User Guide*; Hochschulverlag AG der ETH Zuerich: Zuerich, Groningen.
- Veitch, G. & Smith, A. T. (2001) *Horseradish peroxidase*. In *Advanced Inorganic Chemistry*; Sykes, A. G., Mauk, G., Eds.; Academic Press: New York; Vol. 51, pp 107-162.
- Vidossich, P.; Alfonso-Prieto, M.; Carpena, X.; Loewen, P. C.; Fita, I. & Rovira, C. (2007) *J. Am. Chem. Soc.* 129:13436-13446
- Vlasits, J., Jakopitsch, C., Schwanninger, M., Holubar, P. & Obinger, C. (2007) *FEBS Lett.* 581, 320-324.
- von Lilienfeld, O. A.; Tavernelli, I.; Rothlisberger, U. & Sebastiani, D. (2005) *J. Chem. Phys.* 122: 013133 (1-6).
- Vuillame, M. (1987) *Mutat. Res.* 186: 43-72.
- Wagnerová, D.M. (2001) *Zeit. Phys. Chemie.* 215(1): 133-138.
- Wallrapp, F.; Masone, D. & Guallar, V. (2008) *J Phys Chem A* 112 (50): 12989-12994.
- Wallrapp, F. & Guallar, V. (2008) *J. R. Soc. Interface* 5: S233-S239.
- Wang, Y-N. & Eriksson, L.A. (2001) *Int. J. Quant. Chem.* 83: 220-229.
- Wang, J. M.; Wolf, R. M.; Caldwell, J. W.; Kollman, P. A. & Case, D. A. (2004) *J. Comput. Chem.* 25: 1157-1174.
- Wang, X., Li, S. & Jiang, Y. (2004) *Inorg. Chem.* 43: 6479-6489.
- Wang, J., Wang, W., Kollman P. A. & Case, D. A. (2006) *J. Mol. Graph. Model.* 25: 247260.
- Wang, R. & de Visser, S. P. (2007) *J. Inorg. Biochem.* 101: 1464-1472.
- Wang, Y., Chen, H., Makino, M., Shiro, Y., Nagano, S., Asamizu, S., Onaka, H. & Shaik, S. (2009) *J. Am. Chem. Soc.* 131: 6748-6762.
- Warshel A. & Levitt, M. (1976) *J. Mol. Biol.* 103: 227-249.
- Warshel A. (1982) *J Phys Chem* 86: 2218.
- Wasinger, E.C.; Davis, M.I.; Pau, M.Y.M; Orville, A.M.; Zaleski, J.M.; Hedman, B.; Lipscomb, J.D.; Hidgson, K.O. & Solomon, E.I. (2003) *Inorg. Chem.*42: 365-376.
- Watanabe, Y., Nakajima, H. & Ueno, T. (2007) *Acc. Chem. Res.* 40: 554-562.
- Wirstam, M.; Blomberg, M. R. A. & Siegbahn, P. E. M. (1999) *J. Am. Chem. Soc.* 121: 10178-10185.

Bibliography

- Witting, P.K.; Douglas, D.J. & Mauk, A.G. (2000) *J. Biol. Chem.* 275(27): 20391-20398.
- Wood, J.M.; Decker, H.; Hartmann H.; Chavan, B.; Rokos, H.; Spencer, J. D.; Hasse, S.; Thornton, M. J.; Shalhaf, M.; Paus, R. & Schallreuter, K. U. (2009) *FASEB J.* 23: 2065-2075.
- Wu, F.; Katsir, L.J.; Seavy, M. & Gaffney, B. J. (2003) *Biochemistry* 42 (22): 6871-6880.
- Yabuki, M., Kariya, S., Ishisaka, R., Yasuda, T., Yoshioka, T., Horton, A. A. & Utsumi, K. (1999) *Free Radical Biol. Med.* 26: 325-332.
- Yonetani, T. & Anni, H. (1987) *J. Biol. Chem.* 262(20): 9547-9554.
- Yshida, K.; Iizuka, T. & Ogura, Y. (1970) *J. Biochem.* 68(6): 849-857.
- Zámocky, M. & Koller, F. (1999) *Prog. Biophys. Mol. Biol.* 72, 19-66.
- Zámocky, M.; Furtmüller, P.G. & Obinger, C. (2008) *Antiox Redox Signal* 10(9), 1527-1547.
- Zhang, Y. & Huang, K. (2008) *J. Mol. Struct: Theochem* 864: 48-55.